Chapter 2 Power electronics from the view point of passive components

Section 1 Magnetism

1.1 Fundamentals of Magnetic Materials for Power Electronics

Keyword: Soft magnetic materials, Static magnetic properties, Dynamic magnetic properties, Magnetic property evaluation methods, Magnetic elements, Modeling, Steinmetz formula

In this section, the basic properties (static and dynamic magnetic properties) of soft magnetic materials that constitute magnetic elements such as transformers and inductors are outlined. Representative soft magnetic materials, magnetic property evaluation methods, magnetic elements using these materials, and modeling of elements based on the Steinmetz equation are also briefly reviewed.

1.1.1 Magnetostatic Properties of Magnetic Materials

Magnetic materials are "magnetized" when placed in a magnetic field. As the magnetic field *H* is gradually increased, the magnetization *M*saturates at a certain threshold value. The magnetization *M at* this point is called saturation magnetization M_s and the magnetic flux density *B* is called saturation flux density $_{Bs}$. Next, as the magnetic field *H* is weakened with respect to the saturated magnetization *M*, the magnetization *M* does not become zero where the magnetic field *H* is zero, but becomes zero at acertain magnetic field *H in* the opposite direction. The magnetization *M* at this zero magnetic field is called the residual magnetization M_r, the magnetic flux density *B* is called the residual flux density B_r, and the magnetic field *H* in which the magnetization *M*becomes zero is called the coercive force H_c. As shown in **Figure 2.1.1.1**, the magnetization *M* of a magnetic material follows different paths when the magnetic field *H* is made stronger and weaker, resulting in a characteristic loop. The magnetization curve obtained by alternately applying a magnetic field *H in* consideration of its direction is called a magnetic history curve (hysteresis curve). The relationship between the magnetization *M* and the magnetic flux density *B* of a magnetic material is expressed

$$B=\mu_0 H+M \qquad (2.1.1.1)$$

$$B=\mu_0 (H+M) \qquad (2.1.1.2)$$

As where μ_0 is the magnetic permeability of the vacuum. The difference between *E-H* and *E-B* is whether μ_0 is attached to magnetization *M* or not, and the unit of magnetization *M* is different. *B* is A/m in the SI unit system, the same as the magnetic field *H*. In this document, the units of magnetization *M* are generally the same as in equation (3) . In this document, the *E-H* correspondence is generally described using Equation (2.1.1.1), and the *E-B* correspondence using Equation (2.1.1.2) is also used depending on the contents. The magnetic permeability *μ* is the gradient of the magnetic history curve. The curve drawn by connecting the vertices of the magnetic history curve is called the normal magnetization curve, which is a static description of the

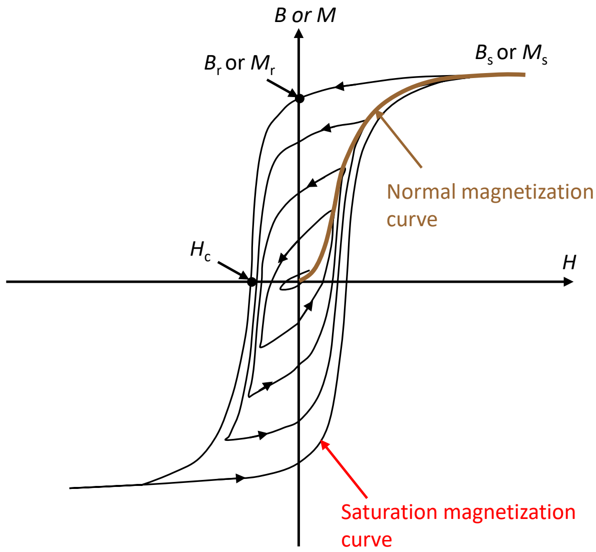

Figure 2.1.1.1 Magnetic history curve (hysteresis curve) and Magnetic Parameters

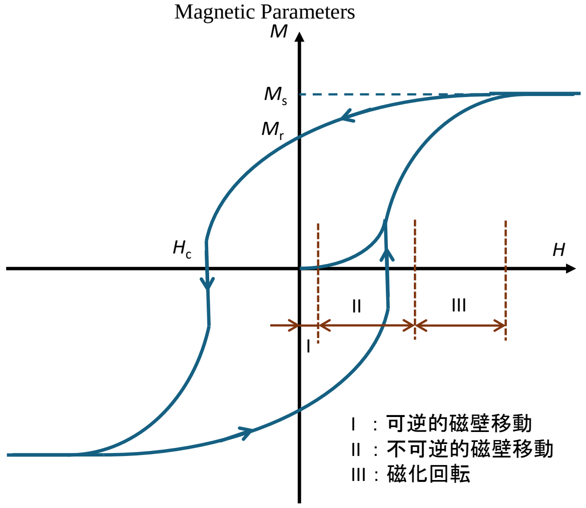

Figure 2.1.1.2 Magnetic history curve with mixed magnetic wall movement and magnetization rotation

curve known as the AC magnetization characteristic in the power electronics field. The curve drawn by connecting the midpoints of the width of the magnetic history curve is called the mean magnetization curve. The curve that gives the saturation flux density B_s, the residual flux density B_r, and the coercive force H_c in the magnetic history curve is called the saturation magnetization curve. The energy equivalent to the area confined by the magnetic history curve is supplied to the magnetic material from the external magnetic field and is converted into heat energy, resulting in loss [(1)-(4)].

In magnetic materials, when the magnet ization *M is* parallel to the direction of the external magnetic field, the magnetization process proceeds either by the movement of magnetic walls within the material or by magnetization rotation within the magnetic domain.

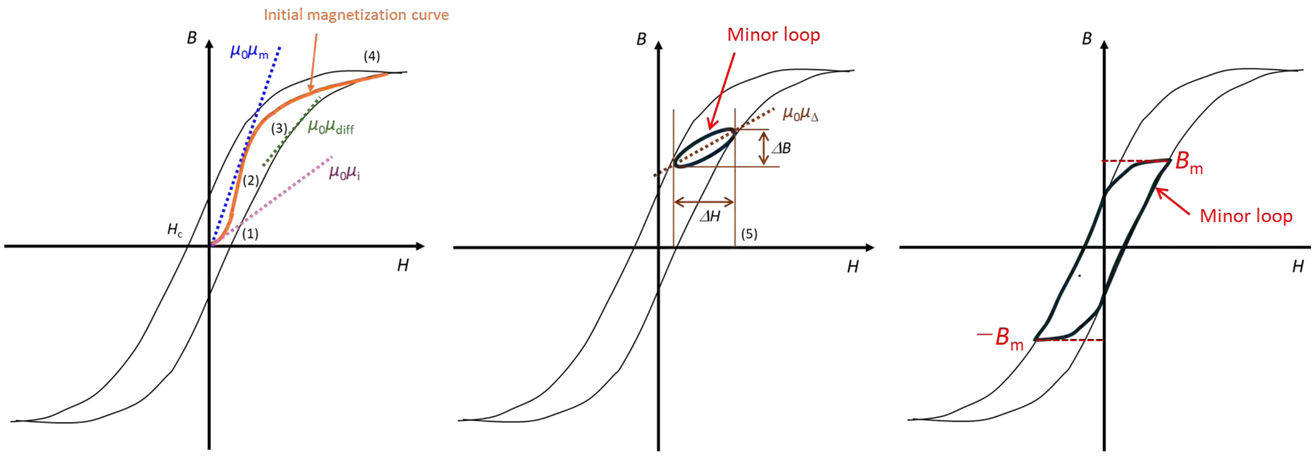

(a) (b) (c)

Figure 2.1.1.3 Initial magnetization curves and various permeabilities, minor loop

In soft magnetic materials, both wall movement and rotation are likely to occur. In the case of magnetization by wall movement, the magnetic walls within the material jump from one state to the next as the external magnetic field changes. The magnetization process that repeats this jump to the next state is irreversible, and a hysteresis curve is drawn. On the other hand, in the case of the magnetization process by magnetization rotation, the magnetization rotates so that it faces parallel to the direction of the applied magnetic field as it changes. In this case, a hysteresis curve is also drawn. However, the area enclosed by the curve is clearly smaller than that of the case of the magnetization process by wall shift. These magnetization processes are easy to separate when the magnetic domain structure is a simple thin film. On the other hand, in the case of thin films or powders, the magnetic domain structure in the material becomes complex, and these magnetization processes are mixed. In other words, as shown in **Figure 2.1.1.2**, in the weak magnetic field region, the magnetic wall migration is easy and the behavior is reversible (Process I). As the magnetic field becomes stronger, the magnetic wall jumps to the next state and becomes irreversible (process II). In stronger magnetic field regions, the magnetic domains disappear and magnetization rotation occurs (process III), resulting in a saturated state. This magnetization curve has hysteresis, in which the magnetization always changes with a delay with respect to changes in the external magnetic field [(1), (2), and (4)]. Since the specific permeability μ_r is normalized by the permeability μ_0 of the vacuum, its unit is dimensionless. The relationship between the specific magnetic permeability μ_r and the magnetic susceptibility χ is $\mu_r=1+\chi/\mu_0=1+\chi_r$. As shown in **Figure 2.1.1.3 (a)**, when the magnetic field H is increased gradually from zero, the magnetic flux density $B$of the magnetic material rises from zero, and when the magnetic field H is further increased, it increases from (1) to (4) and almost saturates. This curve from zero to (4) is the initial magnetization curve. In the initial magnetization curve, the rate of increase of magnetization near zero magnetic field is called the initial permeability μ_i, and the specific permeability μr reaches its maximum near (3), where μ_r is called the maximum permeability μ_m [(1)(2)(4)].

When the magnetic field H is varied slightly ΔH at the initial magnetization curve or at any point (5) of the hysteresis curve, the magnetic flux density Bchanges ΔB. The ratio between ΔB and ΔH is the incremental magnetic permeability μ_Δ. μ_Δ is the magnetic permeability when a small magnetic field is applied to the magnetic material with a bias DC magnetic field. The hysteresis curve with a bias DC magnetic field applied is the minor loop, which is the loop applied to the inductor (**Figure 2.1.1.3 (b)**). In contrast, the minor loop corresponding to the maximum flux density B_m symmetrical to the origin (zero field) as shown in **Figure 2.1.1.3 (c)** is the loop applied to a transformer with symmetrical AC excitation. In addition to this, when the tangent line is drawn at any point on the hysteresis curve, it becomes $(dB/dH)/\mu_0$, and the magnetic permeability at this point is called the differential permeability μ_{diff}. The maximum value of this permeability corresponds to the maximum differential permeability, but it is different from the maximum permeability μ_m, which is the slope of the tangent line drawn on the initial magnetization curve [(1),(2),(4)].

Table 2.1.1.1 summarizes the English notation, symbols, and definitions of the representative physical quantities and magnetic permeability used to evaluate the magnetostatic properties of the soft magnetic materials for power electronics mentioned above.

Finally, a note on units and the relationship between the specific magnetic permeability μ_r and the magnetic susceptibility χ is given. (5) In the SI unit system, μ has the same units of H/m as the magnetic permeability μ_0 of a vacuum. On the other hand, in actual permeability measurements, the dimensionless number specific permeability $\mu_r = \mu / \mu_0$ is often used. This is because the permeability μ^{cgs} in the cgs unit system is also a dimensionless number and has the same value as μ_r, and since the specific permeability of a vacuum is 1, using μ_r (= μ^{cgs}) has the advantage of facilitating comparison with a vacuum. However, adding a subscript *"r" for* relative to μ_i, μ_{diff}, and μ_Δ as defined above complicates the notation, and since the SI and cgs unit systems are sometimes used interchangeably, it often happens that the magnetic permeability and specific permeability are not distinguished. When using specific permeability in the SI unit system, it is necessary to pay attention to the units, for example, μ_i / μ_0 in these notations.

The magnetic flux density *B in* the SI unit system is expressed by equation (2.1.1.2), and if the magnetization *M is* proportional to the magnetic field *H*, then $M = \chi H$ if the proportionality constant is the magnetic susceptibility χ. From these equations, the relationship between μ_r and χ is $\mu_r = 1 + \chi$. Since $M >> H$ usually holds, we can ignore the magnetic field *H* and assume that the magnetic flux density *B* and the magnetic polarization $J = \mu_0 M$ are the same ($B = J$) and that the specific magnetic permeability μ_r and the magnetic susceptibility χ are the same ($\mu_r = \chi$).

Table 2.1.1.1 Typical physical quantities and permeabilities used to evaluate magnetostatic properties in soft magnetic materials for power electronics

Terminology	English (language)	symbol	Definition.	Measurements*.
Saturation flux density	Saturation flux density	*BS*	Maximum flux saturation density that can be reached by magnetic materials	1**, 2, 3, 4
Residual flux density	Residual flux density	*Br*	In the saturation magnetization curve Value of magnetic flux density *B*when magnetic field *H is* 0	1**, 2, 3, 4
Coercivity	Coercivity	*Hc.*	In the saturation magnetization curve Value of the magnetic field *H* for which the magnetic flux density *B*is zero	1**, 2, 3, 4
Initial permeability	Initial permeability	*mu*	Extreme value of the magnetic susceptibility when both the magnetic field strength and the magnetic flux density are as close to zero as possible (Slope at the origin of the initial magnetization curve	1**, 2, 3, 4, 5, 6, 7, 8
Incremental magnetic permeability	Incremental permeability	$\mu\Delta$	Under DC polarization conditions, if *B is* not zero, then Ratio of finite magnetic field strength change ΔH to corresponding magnetic flux density change ΔB	1**, 2, 3, 4, 6, 8
Differential magnetic permeability	Differential permeability	$\mu diff$	*B-H* Slope at a point on the curve (Note that it is not limited to saturation magnetization curves.	1**, 2, 3, 4, 5, 6, 8

* : The measurement method corresponding to each number is described in section 1.4.2 of this chapter.

** : Only magnetostatic characteristics can be measured

On the other hand, when the magnetization *M* is small and the magnetic field *H* is not negligible, it is necessary to use exact expressions for the magnetic flux density *B* and the specific permeability μ_r, and to distinguish between the magnetic flux density *B* and the magnetic polarization *J*, and between the specific permeability μ_r and the magnetic susceptibility χ.

In addition, the relationship between the magnetic flux density B^{cgs}, the magnetic field H^{cgs} and the magnetization M^{cgs} in the cgs unit system differs from equations (2.1.1.1) and (2.1.1.2) in that

$$B^{cgs} = H^{cgs} + 4\pi M^{cgs} \tag{2.1.1.3}$$

The magnetic flux density B^{cgs}, the magnetic field H^{cgs}, and the magnetization M^{cgs} are expressed as where the units of magnetic flux density B^{cgs}, magnetic field H^{cgs}, *and* magnetization M^{cgs} are gauss, Oe, and emu/cc, respectively. the magnetic susceptibility χ^{cgs} in the cgs unit system, is a proportionality constant such that $M^{cgs} = \chi^{cgs} H^{cgs}$, and substituting this, the relationship between magnetic permeability and magnetic susceptibility is $\mu^{cgs} = 1 + 4\pi \chi^{cgs}$. Comparing this with the relation between μ_r and χ in the SI system of units, we obtain $\chi = 4\pi\chi^{cgs.}$ Therefore, a material with magnetic susceptibility $\chi = 1$ in the SI unit system has $1 / 4\pi \approx 0.08$ in the cgs unit system. In summary, the permeability and magnetic susceptibility in the SI unit system and the permeability and magnetic susceptibility in the cgs unit system are all dimensionless numbers, and the permeability μ_r in the SI unit system and the permeability μ^{cgs} in the cgs unit system have the same value, but the magnetic susceptibility has different values in the SI and cgs unit systems.

1.1.2 Dynamic magnetic properties of magnetic materials

The magnetic parameters shown in section 1.1.1 are the magnetostatic properties of magnetic materials. For soft magnetic materials, low coercivity (low H_c), high saturation magnetization (high $4\pi M_s$) and high initial permeability (high μ_i) are mainly required as magnetostatic properties. The loss of magnetic materials caused by the excitation of an AC magnetic field is closely related to the magnetization process of soft magnetic materials and their frequency characteristics. The following is an overview of the magnetization process (dynamic magnetic properties) in AC magnetic fields.

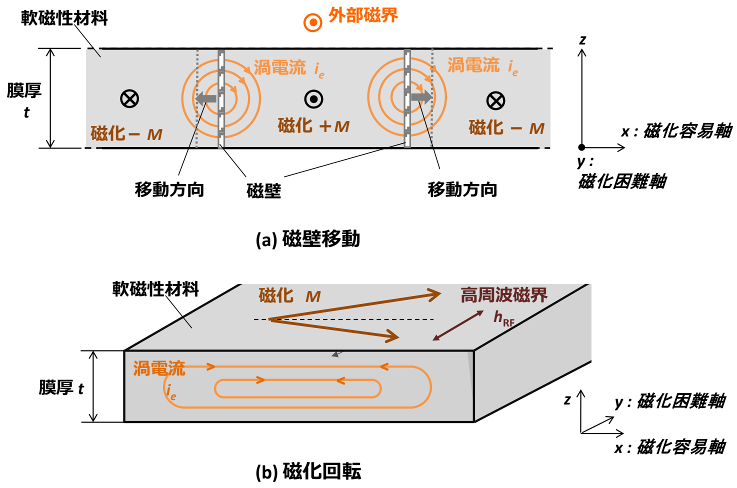

Figure 2.1.1.4 Magnetization process in an AC magnetic field (dynamic magnetic

The magnetization process by magnetic wall movement can cause a large-amplitude magnetization reversal when the frequency of the driving magnetic field is low and the magnetic field is weak. On the other hand, when the frequency of the driving magnetic field is high, the magnetic wall moves at high speed and a high-speed magnetization reversal occurs at the boundary of that area, resulting in a local concentration of heat loss due to eddy currents (eddy current loss) (**Figure 2.1.1.4 (a)**). The eddy current loss W_{eddy} due to the magnetic wall shift is proportional to the frequency of the driving magnetic field f

$$W_{\text{eddy}} = \frac{8.4 t w {B_{\max}}^2}{\pi \rho N} f^2 \tag{2.1.1.4}$$

[(6)-(8)], which is expressed as where t, w, ρ, N, and B_{max} are the thickness, width, and electrical resistivity of the material, the total number of magnetic walls in the material, and the amount of magnetic flux reversal per unit area (maximum flux density). This equation models the movement of magnetic walls in the material, meaning that a higher frequency f of the driving magnetic field and an increase in the flux reversal amount B_{max} are directly related to a rapid increase in eddy current loss W_{eddy}. Based on the equation (2.1.1.4) for eddy current loss due to magnetic wall movement and experiments, eddy current loss W_{eddy} can be sufficiently suppressed if the thickness *t of the* metallic magnetic material is less than several 10 μ m and the frequency *f*of the driving magnetic field is several 10 kHz. However, in order to use the material in a frequency range higher than this, it is important to reduce the material thickness t to a few μm or less (thinning), increase the electrical resistivity ρ of the material, or increase the total number of magnetic walls *N*in the material. In particular, in the case of thin films, there is an upper limit to the speed of magnetic wall movement due to inertia and heat loss, and the limit to the magnetization reversal speed (or frequency) due to magnetic wall movement is only a few MHz. Thus, although magnetic wall motion finds no application in the high-frequency region where the driving magnetic field is several MHz or higher, it is widely used in the low-frequency region where the driving magnetic field is low. In fact, in the case of metallic magnetic materials with a certain thickness, such as those used in power transformers, the eddy current loss W_{eddy} is kept low by increasing the total number of magnetic walls *N*and having each magnetic wall share the amount of magnetization reversal when causing a large magnetization reversal by magnetic wall movement [(4)].

The magnetization process due to magnetization rotation contributes predominantly in the high-frequency region above about 10 MHz, where the magnetic wall movement cannot be followed and the small amplitude operation near the initial permeability μ_i occurs. Magnetization reversal occurs uniformly throughout the material. As shown in **Figure 2.1.1.4 (b)**, the permeability μ, which is reduced by eddy current losses W_{eddy} when an AC magnetic field is applied in the direction of the magnetization difficulty axis, can be obtained from electromagnetism (Maxwell's equation) using the skin thickness δ and the initial permeability μ_i derived from the static magnetization process, assuming the material width is infinite

$$\mu = \mu_{\rm i} \tanh\left(\frac{t}{2\delta_e}\right) / \frac{t}{2\delta_e} = \mu_{\rm i} \tanh\left(\frac{(1+j)t}{2\delta}\right) / \frac{(1+j)t}{2\delta} \tag{2.1.1.5}$$

[(9)], where δ_e is called the effective epidermal thickness (complex number) . where δ_e is called the effective skin thickness (complex number), and its relationship to the general skin thickness δ is

$$\delta_e = \frac{1}{\sqrt{j2\pi f \mu_i/\rho}} = \frac{\delta}{1+j} \tag{2.1.1.6}$$

$$\delta = \frac{1}{\sqrt{\pi f \mu_i/\rho}} = \sqrt{\frac{2\rho}{\omega\mu_i}} \tag{2.1.1.7}$$

is expressed as As can be seen from these equations, the decrease in permeability μ depends on the ratio of material thickness t *to* skin thickness δ. If the material thickness t is less than a few μm and the skin thickness δ is sufficiently thick, the decrease in permeability μ is sufficiently suppressed up to several 10 MHz if the material thickness t is less than several μm. Therefore, if the material shape is thin enough, even metallic soft magnetic materials can suppress the loss up to higher frequencies. The upper limit of the frequency is closely related to the magnetic resonance phenomenon. This magnetic resonance phenomenon is a process in which the magnetization changes its direction while performing precessional motion, and is described by the Landau-Lifshitz-Gilbert (LLG) equation

$$\frac{\partial \vec{M}}{\partial t} = -\gamma[\vec{M} \times \vec{H}] + \frac{\alpha}{M}\left[\vec{M} \times \frac{\partial \vec{M}}{\partial t}\right] \tag{2.1.1.8}$$

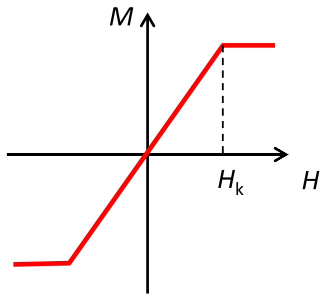

Figure 2.1.1.5 Magnetization curves of hard-to-magnetize axes in soft magnetic materials with

[10][11], which can be explained phenomenologically by where γ is the gyromagnetic constant, whose value is 8.7698 × 10-3g [Oe-1s-1] (g: g factor). α is the braking constant (damping constant). The first term in equation (2.1.1.7) is the precession term of magnetization and the second term is the braking term. The frequency at which this phenomenon occurs is determined by the intensity of the effective magnetic field (anisotropic magnetic field) H_k due to magnetization rotation (**Figure 2.1.1.5)** in a soft magnetic material when no static external magnetic field is given. In the case of a bulk-shaped soft magnetic material with uniaxial magnetic anisotropy, its resonance frequency is

$$f_{\mathrm{r}} = \frac{\gamma}{2\pi} H_{\mathrm{k}} \tag{2.1.1.9}$$

[12][13].

As described above, the magnetization process of soft magnetic materials is either wall movement or magnetization rotation. Which process is dominant depends on the material geometry, magnetization, size, and frequency range used. In power converters such as transformers, the magnetization process is dominant in the low frequency range near commercial frequencies, where magnetic wall movement is easy at low excitation currents. As shown in **Figure 2.1.1.6**, electromagnetic steel sheets that are close to the bulk shape are mainly used in the low frequency range from near commercial frequencies, while thin strips and a pressed core consisting of fine particles with large grain size are used in the frequency range from low frequency to around 100 kHz, and a pressed core consisting of smaller particles in the frequency range from 100 kHz to around several MHz. Mn-Zn ferrite is used over a wider frequency range. In the case of thin-film elements, the operating frequency is above several 10 MHz, and the magnetic wall movement is no longer followed, and the magnetization process is mainly based on magnetization rotation with a small amplitude close to the initial permeability.

1.1.3 Types of soft magnetic materials

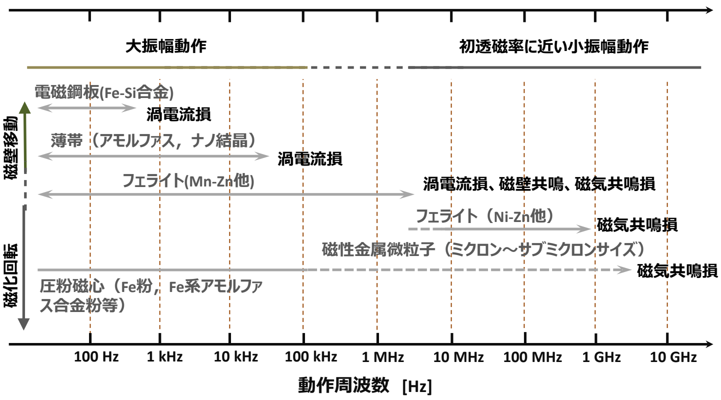

Figure 2.1.1.6 Typical frequency range of soft magnetic materials used

(Also consider the magnetization process by magnetic wall movement and

Typical soft magnetic materials include Fe-based alloy materials, amorphous alloy materials, nanocrystalline alloy materials, magnetic powder core materials, and ferrite materials. **Figures 2.1.1.7 (a)** and **(b)** show the relationship between the power capacity and excitation frequency of transformers using these materials and the relationship between the specific permeability of the materials and the excitation frequency, as well as an overview of these materials (14)(15).

Fe-Si alloy materials are called electromagnetic steel sheets (silicon steel sheets) and contain several percent Si. The Fe-Ni alloy material is an alloy made to increase the initial permeability μ_i, and is called permalloy from "permeability" and "alloy". Its magnetic properties vary depending on the Ni composition, especially the permeability is high around 78.5 wt.% Ni (78 Permalloy, Permalloy PC), and the saturation magnetization $4\pi M_s$ is high around 45 wt.% Ni (45 Permalloy, Permalloy PB). These Permalloys are used for transformers, winding cores, magnetic heads, magnetic shields, etc. Fe-Si-Al alloy materials are alloy systems with compositions in which crystal magnetic anisotropy and magnetostriction are simultaneously zero, and the magnetic permeability μ reaches a maximum around 9.6 wt.%Si and 5.5 wt.%Al. Sendust is an alloy that exhibits these excellent soft magnetic properties. This alloy is used for high-frequency magnetic cores.

Amorphous alloy materials are mainly Fe-based amorphous materials and Co-based amorphous materials in the form of thin strips of several 10 μm thickness. the magnetic properties of Fe-based amorphous materials are mainly used in power distribution transformers because of their high saturation magnetization $4\pi M_s$ and low coercive force H_c. Co-based amorphous materials have high permeability μ and low coercive force H_c, so they are used in saturable cores for magnetic amplifiers and magnetic sensors. Nanocrystalline materials are alloys consisting of crystal grains on a scale of a few to several 10 nm. Their magnetic properties are relatively high saturation magnetization $4\pi M_s$, high permeability, and low loss, and they are used in common mode chokes. Representative nanocrystalline materials include Fe-Si-B-Cu-Nb alloys and Fe-Zr-B alloys. Among them, Fe-Si-B-Cu-Nb alloys have a microstructure in which body center cubic (bcc) type Fe-Si crystal grains of about 10 nm are densely and uniformly dispersed in the ferromagnetic Fe-B-Nb amorphous phase, and have excellent soft magnetic properties.

Powdered magnetic core materials are soft magnetic powders with particle sizes ranging from a few to several tens of micrometers, the surfaces of which are insulated and molded into a specified shape. Its magnetic properties are as follows: although the initial permeability μ_i is not very high, it is resistant to magnetic saturation up to high magnetic fields, eddy current loss is low, and the specific permeability μ_r does not decrease up to high frequency regions as the particle size decreases. The main types of materials include carbonyl iron, pure iron, soft magnetic alloys such as Fe-Si, Fe-Ni, Fe-Si-Al (sendust), amorphous alloys and nanocrystalline alloys. These materials are mainly used as magnetic cores for noise filters and smoothing choke coils used in switching power supplies and small magnetic cores for power chokes in notebook PC applications.

Ferrite materials are magnetic materials consisting mainly of iron oxide. Mn-Zn or Ni-Zn ferrite materials with spinel-type crystal structure have low saturation magnetization $4\pi M_s$, but high electrical resistance and low loss up to high frequency range, and are used as magnetic cores in transformers, inductors, common mode noise filters, etc.

Further information on these materials is provided in Sections 2.1.2 and 2.1.3.

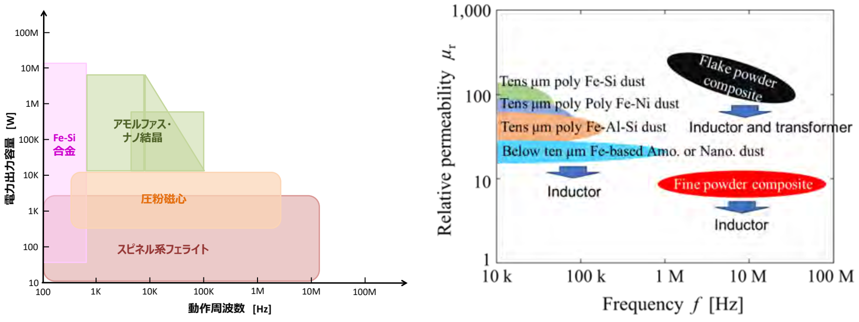

(a) (b)

Figure 2.1.1.7 Power capacity vs. frequency (a) and permeability vs. frequency (b) for typical

1.1.4 Magnetic Property Measurement Methods

To understand the magnetic properties of soft magnetic materials that constitute passive components, it is important to understand their magnetic property measurement methods. **Figure 2.1.1.8** summarizes the relationship between magnetic property measurement methods and measurement frequency ranges for soft magnetic materials. The main methods for measuring static magnetic properties are the Vibrating Sample Magnetometer (VSM), the Super-conducting Quantum Interference Device (SQUID) magnetometer, and the Alternating Gradient Magnetometer (AGM). Alternating Gradient Magnetometer (AGM), and DC *B*-*H* loop tracers. All of these measurement methods can measure the magnetization curves of soft magnetic materials. On the other hand, the main methods for measuring magnetic properties in AC are the Epstein test, two-dimensional vector magnetometer, one-coil method, two-coil method (including AC *B*-*H* loop tracer), inductive cancellation method, and capacitive cancellation method. These measurement methods can measure the dynamic magnetic properties of soft magnetic materials, but the parameters that can be evaluated are different for each. The Epstein test is the most basic magnetic measurement method for electromagnetic steel sheets, and can measure *B*-*H* curves and evaluate magnetic properties such as iron loss and magnetic permeability. The two-dimensional vector magnetic measurement system can evaluate the magnetic flux density *B and* magnetic field *H* of the iron core material as vector quantities. The two-coil method can measure *B*-*H* curves in magnetic core materials and thin strips, and can evaluate the frequency characteristics of their high-frequency losses. In addition to these measurement methods, the AC magnetic susceptibility method, which enables *M*-*H* measurement of soft magnetic materials in the high-frequency region of several MHz, and time-resolved magnetic imaging (magneto-optical Kerr effect microscopy), which can observe the dynamic behavior of the magnetic domain structure in soft magnetic materials, have recently been developed. Details on these magnetic property measurement methods are described in section 2.1.4.

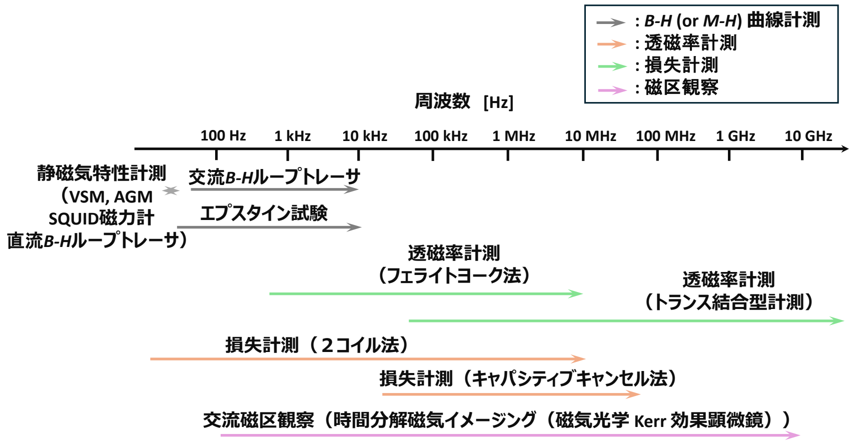

Figure 2.1.1.8 Typical magnetic property measurement methods vs. frequency

1.1.5 Magnetic elements (transformers, inductors)

For magnetic elements such as transformers and inductors, **Figure 2.1.1.9** shows the classification of transformers and inductors using soft magnetic materials by operating frequency and power band. Specifically, for transformers, typical topologies such as forward converters, full bridge converters, and Dual Active Bridge (DAB) converters are listed as converters for operating frequency ranges below 10 kHz and power above 1 kW, for these converters, inner and outer iron type transformers are used as shown in Figure **2.1.1.10** [16]. The soft magnetic materials used are mainly Fe-Si alloy materials, nanocrystalline materials (Finemet), and spinel ferrite materials (Mn-Zn ferrite). In the operating frequency range of 100 kHz-1 MHz and power of 100 W-1 kW, flyback converters and resonant converters are used as converters. In this case, spinel ferrite (Mn-Zn ferrite) is mainly used as the soft magnetic material. In addition, for operating frequency ranges above 1

MHz and power bands below 100 W, resonant converters are mainly used as converters. In this case, spinel ferrite material (Ni-Zn ferrite) and iron composite (fine particles (fine spherical powder and flat powder composite magnetic cores)) are used as soft magnetic materials.

As for inductors, there are many examples of inductors used as DC smoothing inductors in energy storage devices in all operating frequency ranges and power bands, but the soft magnetic materials used differ in the operating frequency range and power band. For operating frequency

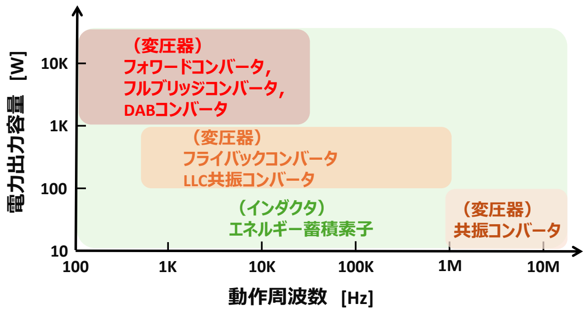

Figure 2.1.1.9 Power output capacity in transformers and inductors and Relationship between operating frequency

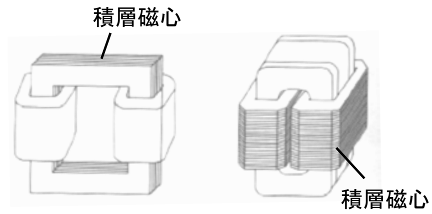

(a) Inner iron type (b) Outer iron type

Figure 2.1.1.10 Stacked iron core geometry of a transformer [15]

ranges of less than 10 kHz and power of 1 kW or more, soft magnetic materials such as Fe-6.5 wt.% Si alloy materials, nanocrystalline materials (Finemet), magnetic powder core materials (polycrystalline) and spinel ferrite materials (Mn-Zn ferrite) are used, and all materials are mainly used with a gap All materials are mainly used with gaps. In the operating frequency range of 100 kHz-1 MHz and power range of 100 W-1 kW, soft magnetic materials such as magnetic powder core materials (polycrystalline, amorphous/nanocrystalline) and gapped spinel ferrite materials (Mn-Zn ferrite) are used. In addition, the operating frequency range of 1 MHz or higher is also used. In addition, in the operating frequency range of 1 MHz or higher and power of 100 W or lower, magnetic core materials (Fe-based convojit (fine particles)) and spinel ferrite materials (Ni-Zn ferrite) are used as soft magnetic materials.

In addition to these factors, as the operating frequency increases, the number of windings can be reduced and miniaturized, but the AC resistance due to skin effect and proximity effect increases. Therefore, it is essential to reduce AC resistance in order to suppress heat generation in the windings and improve power conversion efficiency. The main methods for reducing copper loss include copper loss reduction by wire, interleaved winding structure, and magnetic circuit structure.

For details on magnetic elements, specific application examples of transformers/inductors and converters using the soft magnetic materials mentioned above and their issues, as well as technologies to reduce AC resistance, will be organized and explained in Section 2.1.5.

1.1.6 Modeling of magnetic elements

Although modeling is intended to mathematically express measured iron loss, excitation waveforms, *B-H* curves, etc., its meaning differs greatly depending on whether it is based on the physical mechanism or not. From the standpoint of circuit system design, the top priority is to be able to mathematically express the behavior of magnetic elements under circuit (excitation) conditions in a concise manner and to be able to measure them easily, and it is not easy to go into the physical mechanism of magnetic materials. On the other hand, little attention has been paid to this dilemma in the field of magnetism. A typical mathematical expression in iron loss modeling is the Steinmetz Equation (SE: Steinmetz Equation), where the iron loss P [$\mathrm{W/m^3}$] in sinusoidal excitation is

$$P = kf^{\alpha}{B_{\mathrm{m}}}^{\beta} \tag{2.1.1.10}$$

is given by the Beki function of the excitation frequency f and the amplitude of the maximum flux density B_m as where k, α, and β are material parameters. This prototype was proposed by Steinmetz in 1892 [17] as an expression for iron loss, and has been used for more than 130 years. On the other hand, Steinmetz himself did not use equation (2.1.1.10) as a mathematical expression of iron loss, but discussed the physical relationship between the α power of the excitation frequency fand the β power of the maximum flux density amplitude B_m and the iron loss separation (hysteresis loss P_h: $\alpha = 1$, $\beta = 1.6$, eddy current loss P_{cl}: $\alpha = 2$, $\beta = 2$) are discussed [17]. Later, an excess loss P_{exc} (or anomalous eddy current loss*) of $\alpha = 1.5$ was also added by Overshott, and the iron loss P ($\mathrm{W/m^3}$)

$$P = P_{\mathrm{h}} + P_{\mathrm{cl}} + P_{\mathrm{exc}} = C_{\mathrm{h}}f + C_{\mathrm{cl}}f^{2} + C_{\mathrm{exc}}f^{1.5} \tag{2.1.1.11}$$

It is expressed in a form that separates each component of loss as a "loss component" and is widely used in general [18].

Also, when discussing the physical origin of the loss, equation (2.1.1.11) is normalized by the excitation frequency f as an expression for the loss per cycle W ($= P/f$) [$\mathrm{J/m^3}$], where

$$W = W_{\mathrm{h}} + W_{\mathrm{cl}} + W_{\mathrm{exc}} = C_{\mathrm{h}} + C_{\mathrm{cl}} f + C_{\mathrm{exc}} f^{0.5} \tag{2.1.1.12}$$

It is more prospective to discuss using where C_{h}, C_{cl} and C_{exc} are the coefficients of the excitation frequency dependence of each loss component.

Furthermore, the generalized Steinmetz equation (GSE) is used to describe the iron loss when a square wave voltage is used as an example.

$$P = \frac{1}{T} \oint k_i \left| \frac{dB}{dt} \right|^{\alpha} |\Delta B|^{\beta-\alpha} dt \tag{2.1.1.13}$$

is now used [19]. It can be easily verified that substituting a sine wave for $B(t)$ in equation (2.1.1.13) is equivalent to equation (2.1.1.10). However, the relation between the coefficients k and k_1 is

$$k_i = \frac{k}{(2\pi)^{\alpha-1} \int_0^{2\pi} |\cos\theta|^{\alpha} 2^{\beta-\alpha} d\theta} \tag{2.1.1.14}$$

This is the case with the iGSE (improved GSE)(20). In addition, iGSE (improved GSE)[(20)], which is an improved version that also supports minor loop expressions, and i^2GSE (improved-improved GSE)[(21)], which introduces a relaxation term, have also been proposed and devised to handle arbitrary waveforms.

In addition to the modeling described above, a coupled Landau-Lifshitz-Gilbert (LLG) analysis, which enables us to understand the dynamic behavior of magnetization (high-frequency magnetic field response of magnetization) on a nanoscale, and a Maxwell analysis, which enables us to design magnetic elements such as transformers and inductors on a real scale and to analyze their electromagnetic properties clearly. Coupled analysis combining Landau-Lifshitz-Gilbert (LLG) analysis, which enables us to understand the dynamic behavior of magnetization (high-frequency magnetic field response of magnetization), and Maxwell analysis, which enables us to design magnetic elements such as transformers and inductors on a real scale and clarify electromagnetic property analysis.

Details on modeling are explained in section 2.1.7.

As explained in Section 2.1.7.2, it has recently become clear that the high-frequency loss component due to magnetostriction also behaves as $f^{1.5}$, and the $f^{1.5}$ loss component is the excess loss due to the combined contribution of eddy currents and magnetostriction.

[Yasushi Endo]

References

(1) Keizo Ohta: "Fundamentals of Magnetic Engineering I", Kyoritsu Shuppan, pp.30-35 (1973).

(2) Hiroshi Shimada, Koji Yamada, Shinichiro Hatta, Hirotoshi Fukunaga: "Magnetic Materials - Physical and Engineering Properties and Measurement Methods", Kodansha, pp.87-95 (1999).

(3) Hideo Saotome et al. and Magnetics Society of Japan (eds.): "Applied Electromagnetics for Power Magnetics", Kyoritsu Publishing, pp. 63-64 (2015).

(4) The Magnetics Society of Japan (ed.) : "Magnetism Handbook", Maruzen, pp. 199-203 (2016).

(5) Magnetics Society of Japan (ed.) : "Handbook of Magnetism", Maruzen, pp. 1-5 (2016).

(6) R. H. Pry and C. P. Bean : "Calculation of the energy loss in magnetic sheet materials using a domain model", Journal of Applied Physics, Vol. 29, No. 3, pp. 532-533, DOI: 10.1063/1.1723212 (1959).

(7) J.M.D. Coey : "Magnetism and Magnetic Materials", CAMBRIDGE Univ. Press, p.442 (2009).

(8) Technical Committee on Magnetics of The Institute of Electrical Engineers of Japan (ed.): "Revised: Fundamentals and Applications of Magnetic Engineering," Corona Sha, p.49 (2013).

(9) R. N. Bozorth : "Ferromagnetism", John Wiley & Sons. Inc. pp. 768-810 (2003).

(10) T.L. Gilbert : "A Lagrangian formulation of the gyromagnetic equation of the magnetic field", Physical Review, Vol. 100, No. 4, p. 1243 (1955). 4, p.1243 (1955), "A phenomenological theory of damping in ferromagnetic materials", IEEE Transactions on Magnetics, Vol. 40, No. 6, pp. 3443-3449, DOI: 10.1109/TMAG.2004.836740 (2004).

(11) L.D. Landau and E.M. Lifshitz : "On the theory of the dispersion of magnetic permeability in ferromagnetic bodies",. Physikakusche Zeitschrift der Sowjetunion, Vol.8, pp.153-169 (1935).

(12) Keizo Ohta: "Fundamentals of Magnetic Engineering II", Kyoritsu Shuppan, p.339 (1973).

(13) Satonobu Chikazumi: "Physics of Ferromagnetism (2)", Shokabo, p.324 (1994).

(14) Robert C. O'Handley : "Modern Magnetic Materials Priciples and Applications", John Wiley & Sons, inc. pp. 357-468 (2000).

(15) Magnetics Society of Japan (ed.): "Magnetism Handbook", Maruzen, pp. 204-260 (2016).

(16) Magnetics Society of Japan (ed.): "Magnetism Handbook", Maruzen, p.714 (2016).

(17) C. P. Steinmetz : "On the law of hysteresis", Transactions of the American Institute of Electrical Engineers, Vol. 9, No. 1, pp. .3-64, DOI: 10.1109/T-AIEE.1892.5570437 (1892).

(18) K. J. Overshott : "The causes of the anomalous loss in amorphous ribbon materials", IEEE Transactions on Magnetics, Vol. 17, No. 6, pp. 2698-2700, DOI: 10.1109/TMAG.1981.1061648 (1981).

(19) J. Li, T. Abdallah, and C. R. Sullivan : "Improved calculation of core loss with nonsinusoidal waveforms," Conference Record of the 2001 IEEE Industry Applications Conference, 36th IAS Annual Meeting, pp. 2203-2210, DOI: 10.1109/IAS.2001.955931 (2001).

(20) K. Venkatachalam, C. R. Sullivan, T. Abdallah and H. Tacca : "Accurate prediction of ferrite core loss with nonsinusoidal waveforms using only Steinmetz parameters", Proceedings of 2002 IEEE Workshop on Computers in Power Electronics, pp. 36-41, DOI: 10.1109/CIPE.2002. 1196712 (2002).

(21) J. Mühlethaler, J. Biela, J. W. Kolar, and A. Ecklebe : "Improved core-loss calculation for magnetic components employed in power electronic systems," IEEE Transactions on Power Electronics, Vol. 27, No. 2, pp. 964-973, DOI: 10.1109/TPEL.2011.2162252 (2012).

1.2 Thin strip, sintered

1.2.1 Applications of soft magnetic materials and *B-H* curves

Soft magnetic materials have different requirements depending on the application, and the required properties differ depending on the frequency. The energy that can be generated per unit volume of magnetic core is derived from the property that the electromotive force is proportional to the time derivative *dt* of the magnetic flux Φ, as stated in Faraday's law. The time variation can be taken as the reciprocal of the frequency *f*, which is approximately the period of the magnetic flux variation. In order to increase the energy that can be handled per unit volume, especially in the low frequency range, (1) the operating flux density B_m must be high and (2) the cross-sectional area *A* of the magnetic core must be large to increase the magnetic flux Φ, the product of A and B_m. To increase B_m, the *B-H* curve is used until near full loop. In such a usage of the *B-H* curve, it is more advantageous to have a high average permeability throughout the magnetization process than to have a high initial permeability μ_I. The magnetization process due to magnetic wall movement tends to occur, and the magnetization process due to magnetization rotation tends to lead to a decrease in permeability, especially in a material with high magnetostriction. This process is especially desirable in materials with large magnetostriction, as it tends to cause vibration and noise. Therefore, magnetic domains perpendicular to the magnetic path direction are a factor in the magnetization process due to magnetization rotation, and in many cases, magnetic domains are treated so that the magnetic walls are parallel to 180° by imparting stress-induced magnetic anisotropy by rolling or induced magnetic anisotropy by heat treatment in a magnetic field to the magnetic path direction.

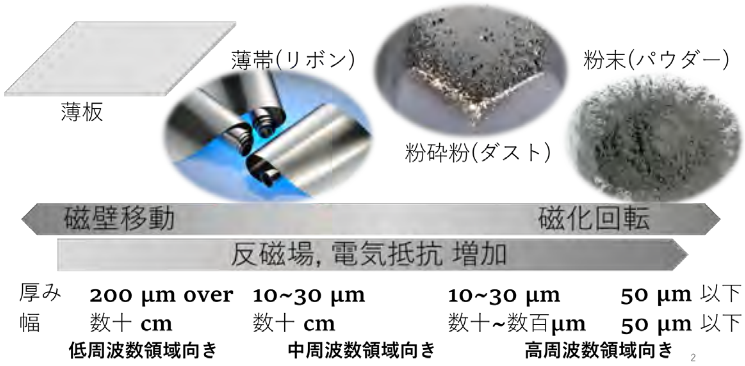

Figure 2.1.2.1 Changes in characteristics with changes in material form

Transformers and inductors used in power electronics equipment are not limited to 50 Hz or 60 Hz, but are used under various frequency conditions. higher $B_m f$ produces more electromagnetic energy, but the heat due to losses generated in the magnetic core also depends on B_m and *f*. This loss generated in the magnetic core material is called iron loss, and the iron loss *P* is constructed as follows

$$P = P_h + P_{cl} + P_{exc} \quad \text{(W)} \tag{2.1.2.1}$$

where P_h, P_{cl}, and P_{exc} are hysteresis loss, eddy current loss, and excess loss, respectively; P_h is proportional to frequency *f*, and P_h is lower when the coercive force H_c is low and the residual flux density B_r is low; P_{cl} and P_{exc} are losses appearing under AC magnetic fields. If a plate of thickness *t* is uniformly magnetized, the eddy current loss P_e is given by

$$P_{cl} = \frac{(\pi t f B_m)^2}{6\rho} \quad \text{(W)} \tag{2.1.2.2}$$

*A*s where ρ is the electrical resistivity.[(1)] P_{cl} is proportional to the square of *f*and is therefore an important factor, especially at high frequencies. The excess loss P_{exc} is a dynamic loss other than P_h and P_{cl}, and is considered to be a loss associated with the movement of magnetic walls, which is particularly noticeable when magnetic walls parallel to the magnetic path move in a direction perpendicular to the magnetic path. These three factors are the main causes of iron loss. Especially in the mid-frequency range (sub-kHz to several tens of kHz) to high-frequency range (several tens of kHz or higher), the suppression of eddy currents has a great significance in the suppression of heat generation and is an important requirement for material selection. From this point of view, ferrite cores are widely used. Paradoxically, however, if eddy current losses can be reduced to some extent, metal alloy materials with low electrical resistivity can also be effectively used in the mid to high frequency range. As a means of increasing electrical resistance, it is effective to reduce the thickness *t* of the conductor orthogonal to the magnetic path, as shown in Equation (2.1.2.2). As seen in **Figure 2.1.2.1**, thin strips (also called ribbons) made by liquid quenching are about

1/10th the thickness compared to steel plates. Liquid-quenched thin strips such as amorphous alloys and nanocrystalline alloys are advantageous. The thickness of general electromagnetic steel sheets, even thin ones, is about 200 μm, which is several tens to hundreds of times thicker than the P_{cl} of liquid-quenched thin strips. Therefore, liquid-quenched thin strips are an effective choice for Fe-based metal alloy core materials in the high frequency range. eddy current losses in thin strips of Fe-based amorphous alloys are comparable to hysteresis losses when $B_m f$ is about 20,000, according to Equation (2.1.2.2). For example, when B_{m} is 0.2 T, the eddy current loss exceeds the hysteresis loss at about 100 kHz, and the effect of eddy currents becomes apparent even at lower frequencies. Therefore, at frequencies above about 30 kHz, powder such as that shown in **Fig. 2.1.2.1**, which is made from crushed thin strips, is used. The reduction in the cross-sectional area of the conductor perpendicular to the magnetic flux increases the electrical resistance of the conductor, thereby suppressing eddy currents.

In the mid-frequency range, it is most important to suppress eddy current losses as mentioned above, but in liquid-quenched thin bands, where the ratio of eddy current losses is low, it is important to reduce excess losses. As shown in **Figure 2.1.2.2**, in the magnetization process by magnetic wall movement, there is a threshold before the magnetic wall begins to move, and the movement is irreversible to the magnetic field, like a damper. In crystalline systems, if there are grain boundaries, defects such as dislocations, or precipitates such as impurities on the direction of the magnetic wall, the magnetic wall is trapped and extra magnetizing force is required for further movement, and the magnetic field required to overcome this is expressed as a threshold value. On the other hand, the amorphous phase is generally isotropically random, so there should be fewer obstacles to magnetic wall migration. However, the rate of excess loss in thin bands of amorphous alloys is extremely large; for example, at 50 Hz and 1.4 T, the ratio of P_{h}:P_{cl}:P_{exc} is 6:0:4. Considering that P_{h} increases with f to the first power, while P_{exc} increases with f to the first.5 power, the effect of P_{exc} in the mid-frequency range is even larger (3). To reduce P_{exc}, it is effective to limit the travel distance of the magnetic wall, and domain segmentation is an effective measure. It has also been reported that there is a proportional relationship between P_{exc} and the saturation magnetostriction constant of magnetic materials λ_{s} in thin strips of quenched Fe-based alloys [(4)]. The magnetoelastic effect via magnetostriction is thought to provide resistance to magnetic wall movement like a viscous flow (damper), contributing to the increase in P_{exc}. λ_{s} of thin strips of Fe-based amorphous alloys is about 30×10^{-6}, which is one of the highest among soft magnetic materials. If the λs is low, further loss reduction will be possible, enabling the use of higher $B_{\mathrm{m}}f$, lower heat generation, and miniaturization of magnetic elements. From this viewpoint, nanocrystalline alloys in which nanocrystalline grains of Fe are precipitated in the Fe-based amorphous phase have been developed. From an alloy with zero magnetostriction and a saturation flux density B_{S} of about 1.2 T, λ_{s} is about 15×10^{-6}, half that of an amorphous alloy, and B_{s} is more than 1.75 T, etc., low magnetostriction by nanocrystallization has been confirmed [(5)]. As shown in the right side of **Figure 2.1.2.2,** P_{exc} is suppressed by making the easy direction of magnetization in the residual domain state orthogonal to the magnetic path by heat treatment, etc., so that the magnetization process by magnetic wall movement is suppressed and the magnetization process by magnetization rotation is dominant. In such a magnetization process, the average permeability is lower than that of the magnetic wall movement type, and a higher magnetic field is required to achieve magnetic saturation. In the mid-frequency range and above, the magnetization rotation type is easier to handle than the magnetic wall transfer type.

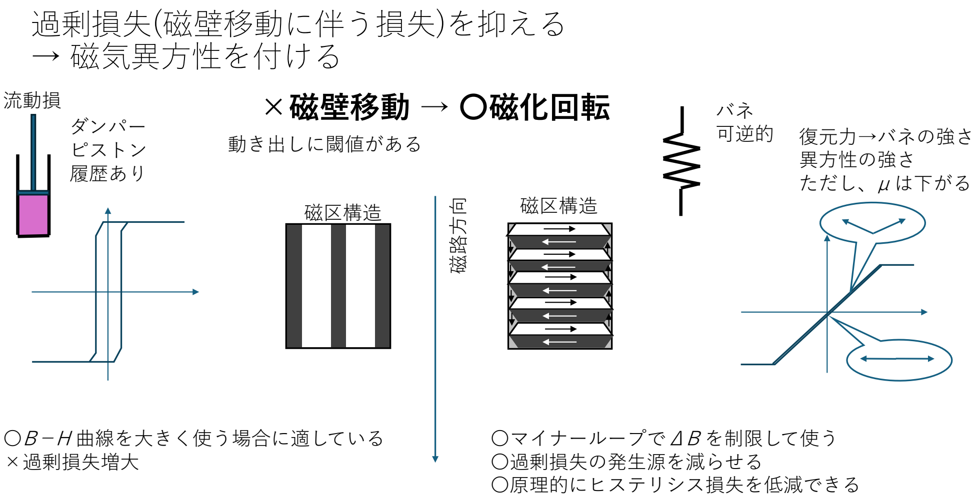

Figure 2.1.2.2 Magnetic Domain Structure and *B-H* Curve Shapes and Magnetization Processes

1.2.2 Medium to high frequency transformers

In medium- to high-frequency transformers, the voltage produced by switching includes a small DC voltage component in addition to the

AC component, which can cause the transformer to become magnetically polarized and deviate from the origin of the *B-H* plane. In such a case, if a material with high average permeability is used, the demagnetization causes magnetic saturation, and the excitation current supplied from the inverter that excites the transformer becomes excessive due to the decrease in excitation inductance, causing the inverter to break down or malfunction. Therefore, materials with low magnetic permeability, which are less likely to cause magnetic saturation even if some degree of demagnetization occurs, may be easier to use. The first requirement for medium- to high-frequency transformers is low iron loss to be able to drive at high *Bm f*. To suppress *Pe* and P_{exc}, thin walls and a magnetic domain structure perpendicular to the magnetic path must be controlled, and low P_h must be achieved due to the properties of the material itself. For this purpose, the initial magnetic permeability must be low. For this, a high initial permeability μ_i is an important requirement.

$$\mu_i \propto \frac{B_s^2}{K + \alpha\lambda_s\sigma} \tag{2.1.2.3}$$

For materials with high μ_i, K and λ_s must be as close to zero as possible [(2)]. In the 1980s, Fe-Cu-Nb-Si-B nanocrystalline alloys consisting of an amorphous phase and a nanocrystalline grain structure with an average grain size of a dozen nanometers were discovered. In the 1980s, Fe-Cu-Nb-Si-B nanocrystalline alloys consisting of an amorphous phase and a nanocrystalline grain structure with an average grain size of several tens of nanometers were discovered, and it was confirmed that the composite structure of the amorphous phase with positive magnetostriction and the nanocrystalline grain layer with negative magnetostriction provides high μ_i because the magnetostriction is canceled. The high μ_i and high B_s of the Fe-based nanocrystalline alloys are promising candidates for medium- to high-frequency transformers.

1.2.3 Inductor

One of the advantages of Fe-based metal alloy core materials over ferrite materials is their high saturation magnetic flux density B_s: Mn-Zn ferrite has a *Bs* of about 0.5 T, while the B_s of 6.5%Si-electromagnetic steel sheet, which is often used in mid-frequency applications, is about 1.85 T, Fe-based amorphous thin strips are about 1.6 T, and Fe-based nano crystal material is about 1.2 T [(1)]. Thus, inductors, rather than the transformers mentioned above, are a more suitable field of application where the high B_s of metal alloy cores can be utilized. In chopper circuits that step up or step down DC voltage, the circuit is relatively simple, consisting of an inductor made of magnetic core material and coil, a capacitor, and a switch, and the magnetic material and its shape are selected to satisfy the inductance and current capacity required by the circuit operating conditions. In the case of an inductor, since the load current is equal to the excitation current, the magnetic flux in the magnetic material increases in proportion to the increase in load current. The soft magnetic material used in the magnetic core has a higher permeability than the surrounding air, which means that magnetic flux passes through it more easily and is collected like a sponge. When the saturation flux density is reached, the permeability drops rapidly, causing an overcurrent in the circuit. As a method to prevent magnetic saturation, a gap or the like is provided in the magnetic core to lower the magnetic permeability, (incremental permeability $\mu\Delta$), when a magnetic field is applied, so that the magnetic flux density does not increase even in a large magnetic field *H*. The wider the gap, the higher the B_s. The wider the gap, the lower the permeability of the magnetic core, but the wider the gap, the more leakage flux increases, which causes eddy current loss and fringing loss due to the leakage magnetic field orthogonal to the coil near the gap. Since fringing loss increases when gaps are concentrated, some attempts are made to reduce the leakage flux in each gap by distributing the gaps. In the metal-alloy composite magnetic cores in which metal-alloy powders are solidified with resin, the space between magnetic materials is occupied by resin with low permeability, and narrow gaps are dispersed throughout the magnetic core to achieve both low permeability and low fringing loss. By reducing the grain size of the powder, the hysteresis loss P_h tends to increase, while the AC loss P_{cl}+ P_{exc} tends to decrease.

1.2.4 Applications and Material Specifications

Table 2.1.2.1 summarizes the magnetic characteristics and material specifications required for transformer and inductor core materials at each frequency. Transformers and inductors are required to have low loss, i.e., low hysteresis loss, eddy current loss, and excess loss. From this point of view, the magnetization rotation type of magnetization process is preferable to reduce hysteresis loss and excess loss when the frequency increases to some extent. As mentioned above, the ratio of each loss varies with frequency, so it is important to maximize the characteristics of the material by making it difficult for these losses to be manifested. In mid-frequency applications, the effect of eddy current losses can be greatly reduced by making metal alloy materials thinner, and if the magnetic permeability can be lowered, the high B_s characteristics can be utilized to take advantage of the high DC superposition property. At higher frequencies, the powder form of the material is used to suppress eddy currents and reduce hysteresis loss as high electrical resistance, so essentially, a high μ_I material with good magnetic field tracking of magnetization is an effective choice.

Table 2.1.2.1 Magnetic characteristics and material specifications required for transformer and inductor core materials for each frequency

	(power) transformer			inductor	
frequency (esp. of waveforms)	~0.1 kHz or less	Less than 0.1~100 kHz	100 kHz~	Less than 1~100 kHz	100 kHz~
B-H curve	Close to full loop	Near the origin hysteresis (behaviour) loop	Near the origin hysteresis loop	High-frequency minor loops superimposed on DC or low-frequency AC	High-frequency minor loops superimposed on DC or low-frequency AC
Qualities that materials should have	High μ_{max} High Br	High μ_i	High μ_i Low B_r	High B_s	High μ_i High electrical resistance
Shape of magnetic core	winding core	winding core sintered magnetic core	sintered magnetic core Metal alloy composite magnetic cores	cut magnetic core block core sintered magnetic core dust core	sintered magnetic core dust core Metal alloy composite magnetic cores
Material Example	directional magnetic steel plate Fe-based amorphous	ferrite Fe nanocrystals	ferrite Fe-based nanocrystals Co-based amorphous	6.5%Si electromagnetic steel plate Fe-based amorphous sendust ferrite	ferrite sendust Fe-based nanocrystals Co-based amorphous

1.2.5 Specifications and Material Selection

The needs of the world are changing, and there are more and more opportunities to use materials that have not been used in the past in order to meet the requirements, increasing the need to consider matching the required specifications and materials. The specifications include size, saturation flux density, frequency, temperature range, cost, and mechanical properties, etc. However, there is no material that covers all of these, and it is necessary to understand the characteristics of the material before making a selection. **Table 2.1.2.2** summarizes the relationship between the characteristics (size, saturation flux density, frequency used, temperature range, and cost) of thin strips of Fe-based nanocrystalline alloys and soft ferrite as examples. The high B_s and thin bandwidth of Fe-based nanocrystals enable miniaturization of devices when fabricated in the same way. In the frequency range of several hundred kHz or higher, ferrite cores with low eddy current losses are increasingly used. Recently, research has been conducted to utilize Fe-based nanocrystals in the high-frequency region, and under B_m = 20 mT, the iron loss of Fe-based nanocrystal alloys is about one-fifth that of Ni-Zn ferrites up to 2 MHz, where Ni-Zn ferrites have shown results [(6)].

Table 2.1.2.2 Characteristics (size, saturation flux density, frequency used, temperature range, cost) of thin Fe-based nanocrystalline alloy strips and soft ferrites

	Size	Saturation magnetic flux density (B_s)	Frequency (kHz)	Temperature range	cost
Fe-based nanocrystals	◎(Small size)	High (1.2 T)	ten - hundreds	○ (150 ℃ or higher OK)	weak
ferrite	×(large)	Low (0.5 T)	ten-thousand	× (100 ℃ or less)	'good work' (equiv. of silver star awarded to children at school)

1.2.6 Characteristics of Fe-based nanocrystalline alloys

As mentioned above, Fe-based nanocrystalline alloys are composite structures consisting of densely precipitated nanocrystalline grains in an amorphous phase; the Fe-based nanocrystalline phase is produced by freezing molten Fe- Cu-Nb-Si-B metal by liquid quenching to obtain an amorphous phase, followed by nanocrystalline heating treatment [(7)]. The amorphous phase and the nanocrystalline phase are thermally sensitive, magnetic field sensitive, and strain sensitive, respectively. The liquid quenching method is a casting method in which, as the name implies, a molten metal in a liquid state is pressed against copper alloy rollers rotating at high speed to obtain the amorphous phase, which is the initial phase, and then quenched and solidified. In this process, a cooling rate of-10^6 to 10^7 °C/s or higher is required to obtain an Fe-based amorphous alloy, and to achieve this cooling rate with Fe-Cu-Nb-Si-B alloy, the thickness of the thin strip must be controlled to 20 μm or less. The thinner the strip, the less weight is produced per unit time, but the advantage of a thin strip is also obtained. When a magnetic material is placed under an alternating magnetic field, the magnetic flux within the material is also changed by the external magnetic field. Eddy currents are generated to oppose this change. When the electrical resistivity of the material is high or the cross-sectional area where electricity flows is narrow because of its shape, the generation of eddy currents itself is suppressed and the eddy current loss associated with eddy current generation is also suppressed. The electrical resistivity of liquid quenched alloys is about 130 μΩcm [(1)], which is 2 to 4 times higher than that of soft magnetic plates such as electromagnetic steel plates, and the thickness of the plates is less than 1/10, thus suppressing eddy current losses compared to those soft magnetic materials. On the other hand, when comparing thin strips of Fe-based nanocrystalline alloys and ferrite, the electrical resistivity of ferrite is about 10^4 to 10^{10} times that of Fe-based nanocrystalline alloys [(1)], and in addition, since ferrite powder of several tens to several hundred μm is sintered to form the magnetic core, the eddy current loss suppression effect of the size effect is also added. This is a situation in which ferrite has an advantage.

1.2.7 Summary of thin body

As described above, magnetic core materials used in AC are strongly affected by eddy current losses, so the required form, saturation flux density B_s, magnetic permeability of the core, and other factors change with each frequency used. Therefore, materials are selected according to the application. By frequency, electromagnetic steel sheets with high maximum permeability and high B_s are often used at low frequencies. Especially in transformers, as a measure to reduce loss and increase the permeability of the magnetic core, the magnetization process by magnetic wall movement is treated as the main process. In the mid-frequency range from several kHz to several tens of kHz, both hysteresis loss and eddy current loss associated with magnetic wall movement affect the loss, so the magnetization process with large magnetic wall movement is not appropriate. In particular, in inductors, the permeability of the magnetic core is sometimes lowered by inserting an air gap in the magnetic path. When a DC voltage component is included in the voltage waveform input to a transformer, that is, when a magnetic circuit causes demagnetization, the use of a magnetic core with high permeability causes an extreme increase in the excitation current of the transformer. Another reason for lowering the permeability of inductors is that in circuits where DC is superimposed and voltage conversion is performed, a property is required that does not cause magnetic saturation even when a large DC current is input. In inductors in the low-frequency range (kHz or lower) to the mid-frequency range, Fe-based amorphous materials and Fe-based nanocrystalline materials are used along with electromagnetic steel sheets. The situation is the same in any frequency range, but especially in transformers in the mid-frequency range and above, B_s is not necessarily the main factor in determining the operating flux density B_m, but the heat generation associated with losses becomes important. For example, if the allowable heat generation is set at 100 W/kg, B_m must be set low for an iron core with large losses, resulting in a larger magnetic core. In this respect, Fe-based nanocrystalline alloys, for example, have extremely low losses at 10 kHz, about one-sixth to one-fifth those of Fe-based amorphous alloys and one-fifteenth to one-tenth those of 6.5% electromagnetic steel sheets, indicating that they are useful as iron cores for medium to high frequency transformers. Currently, ferrite cores are widely used in both transformers and inductors. As mentioned above, ferrite cores are made by sintering and solidifying ferrite powder, and the gaps are dispersed because the crystal grains act as narrow gaps between them, resulting in a magnetic permeability of about 5000 as a magnetic core. The permeability as a magnetic core can be reduced by adjusting the grain shape of the crystal grains. When using ferrite as the magnetic core of an inductor, it should be noted that the saturation magnetic flux density is low and that the performance changes with temperature.

[Motoki Ohta]

References

(1) Technical Committee on Magnetics of the Institute of Electrical Engineers of Japan (ed.): "Revised Fundamentals and Applications of Magnetic Engineering", Corona Publishing (2018).

(2) Motofumi Homma, Akira Nichiguchi: "Magnetic Discretionary Reader", Kogyo Chosakai (1998).

(3) N. Ito, H. Itagaki and M. Ohta: "Core loss reduction though a laser scribe on Fe-based amorphous ribbon surface for transformer cores *J. Magn. Magn. Mater.* 564 170168 (2022).

(4) H. Huang, H. Tshkahara, A. Kato, K. Ono and K. Suzuki: "Origin of excess core loss in amorphous and nanocrystalline soft magnetic materials *Phys. Rev. B*, 109, 104408 (2024).

(5) M. Ohta and R. Hasegawa: "Soft Magnetic Properties of Magnetic Cores Assembled with a High Bs Fe-Based Nanocrystalline Alloys. " *IEEE Trans. on Magn.*, 53

2000205 (2017).
(6) S. Kimura, K. Koike, M. Kanai, R. Miyata, T. Minamisawa, K. Miyaji, M. Sonehara and T. Sato: "Fabrication of Fe-based Nanocrystalline Spherical and Flake Powder Composite Magnetic Cores for Tens of MHz and their Application to Planar Power Inductor" *IEEJ Trans. on Fund. and Mater.* 144, pp. 199-206 (2024).
(7) Y. Yoshizawa, S. Oguma and K. Yamauchi: "New Fe-based Soft Magnetic Alloys Composed of ultrafine grain structure," *J. Appl. Phys.* 64, 6044 (1988).

1.3 Powdered magnetic cores and fine-particle composite magnetic cores

1.3.1 summary

(1) Relation between specific magnetic permeability and applicable frequency of magnetic cores made of pressed magnetic powder and fine-particle composite magnetic cores

Figure 2.1.3.1 shows the frequency vs. specific permeability map for the magnetic cores of the pressed powder and fine-particle composite cores.

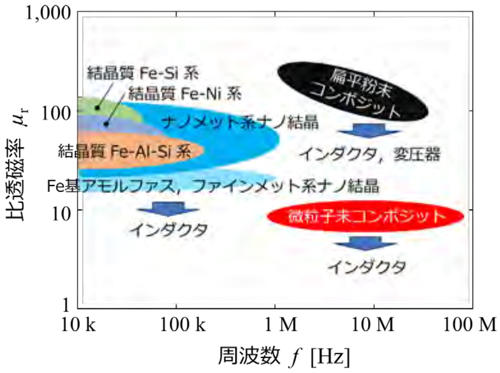

Fig. 2.1.3.1 Frequency vs. specific permeability map of a magnetic core of a magnetic powder core and a

Powdered magnetic cores are generally fabricated by press forming magnetic powders together with binders. As shown schematically in **Figure 2.1.3.2**, the binder behaves as a nonmagnetic gap spatially distributed in the magnetic core and the permeability of the core decreases due to the residual antimagnetic field effect of the powder, but the change in permeability under a DC bias magnetic field is small (constant permeability property) and is mainly used in inductors.

For frequencies below 100 kHz, crystalline Fe-Si, crystalline Fe-Ni, and crystalline Fe-Si-Al materials with a grain size of several tens of microns are generally used, while pure iron materials are also used below a few kHz in expectation of high saturation magnetization. For frequencies above 100 kHz, magnetic powder cores using Fe-based amorphous or Fe-based nanocrystalline powders with higher electrical resistivity than the crystalline materials mentioned above have been developed, and the use of 10 to 20 μm powders, together with their high electrical resistivity, has opened the door to applications in converters at several hundred kHz. The details will be described later, but the recently developed Nanomet-based nanocrystalline powder core has the features of high saturation magnetization, specific permeability of around 100, and ultra-low iron loss, and is very promising as a next-generation magnetic core.

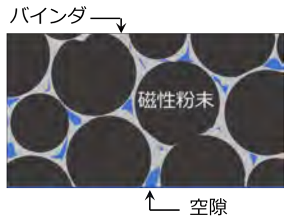

(a) Schematic diagram of the interior

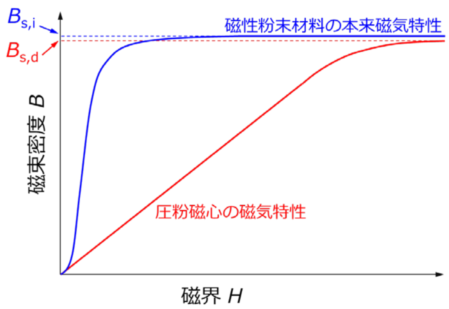

(b) Magnetic properties

Figure 2.1.3.2 Schematic diagram of the inside of a

At frequencies higher than 1 MHz, the greatest challenge is to reduce eddy current losses. There are fine particle composite cores using ultra-fine spherical magnetic powders of generally 5 μm or less in diameter, and flat powder composite cores made by layering flattened powders of several μm or less in diameter, which are used in transformers and inductors at frequencies above 1 MHz. They are used in transformers and inductors at frequencies above 1 MHz.

(2) Mounting form on power electronics circuit boards

Toroidal-shaped bulk pressed cores are mounted on circuit boards as inner-iron type inductors with the windings placed outside the core, whereas outer-iron type inductors with the windings embedded in the pressed core are surface-mounted on circuit boards. On the other hand, fine-particle composite cores targeting high frequencies exceeding 1 MHz are designed to be built into circuit boards, and the form of mounting on circuit boards differs depending on the type of magnetic core.

1.3.2 Dust core

(1) manufacturing process

Figure 2.1.3.3 shows the manufacturing process of a pressed magnetic core by die compression molding. Each process from the starting powder to the pressed magnetic core is described in turn.

a. Atomized magnetic powder

As mentioned above, magnetic powder cores using crystalline powders such as pure iron, Fe-Si, Fe-Ni, and Fe-Si-Al are generally used at frequencies below 100 kHz, except for electrolytic iron powder, which is obtained by grinding electrolytic refined pure iron**.** As shown in **Figure 2.1.3.4**, atomized powder is obtained by grinding and pulverizing molten alloys with a gas jet or water jet and then cooling them. Similarly, amorphous, metallic glass, and nanocrystalline alloy powders are also produced by atomization.

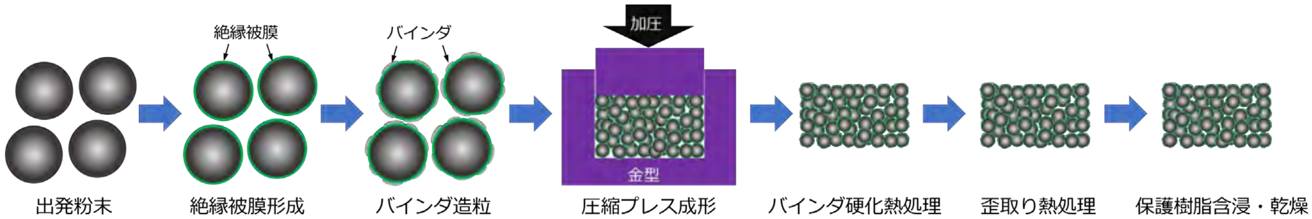

Fig. 2.1.3.3 Manufacturing Process of Powder Core (Die Compression Molding Method)

b. Insulating film formation

In order to avoid increased eddy current loss due to contact between powders in a magnetic powder core, metallic magnetic powders are treated with an insulating film on the surface of the powder. Various types of insulating films are available, including inorganic and organic, but a highly heat-resistant film that can withstand high-temperature strain removal heat treatment after press forming, as described below, is desirable.

Sugimura et al. (1) reported the formation of silica (SiO_2) film on carbonyl iron powder (CIP) by ammonia-catalyzed hydrolysis of TEOS (tetraethoxy-silane; Si（OC_2H_5）$_4$). The reaction equation is as follows.

$$Si(OC_2H_5)_4 + 2H2O + NH3 \Rightarrow SiO_2 + NH_3 + 4C_2H_5OH \qquad (2.1.3.1)$$

When treated with 0.32 ml of TEOS per 1 g of carbonyl iron powder, a silica film of about 100 nm is formed. Silica has excellent electrical insulation and heat resistance, but its wettability with epoxy resin binders is poor, requiring surface treatment with a silane coupling agent.

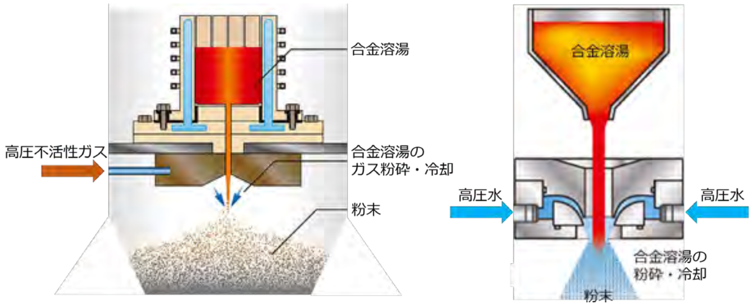

(a) Gas atomization method (b) Water atomization method

Fig. 2.1.3.4 Powder preparation by atomization method

As an example of spinel ferrite thin films on powder surfaces, Mori et al. (2) reported the formation of Mn-Zn-O ferrite plating films on Fe-Si-Cr powder surfaces with an average grain size of 10 µm by an ultrasonic excited ferrite plating method. $Mn_{0.54}Zn_{0.24}Fe_{2.32}O_4$ film on the surface of Fe-Si-Cr powder core after strain-relief heat treatment at 500 ℃ for 15 min, the electrical resistivity of the core was 0.0911 Ω-m, 57 times higher than that without the film, and the iron loss was reduced to 1/6 of the value without the film.

Spinel ferrite thermally decomposes into magnetite (Fe_2O_3), wustite (FeO), and other compounds when exposed to high temperatures, limiting the temperature of heat treatment for strain removal purposes. Huang et al. (3) focused on fayalite (Fe_2SiO_4) as an insulator that has a high electrical resistivity of 10^5 Ω-m and is stable at temperatures above 1,000 ℃. They found that spinel ferrite is a stable insulator at high temperatures. The electrical resistivity of the iron powder core with spinel ferrite coating before and after high-temperature heat treatment was evaluated. The results showed that the electrical resistivity of the core after heat treatment at 800 ℃ (1073 K) dropped to 10 µΩ-m, while the core with Fayalite coating maintained a high electrical resistivity of 10^4 to 10^5 µΩ-m after high-temperature heat treatment. In contrast, the electrical resistivity of the magnetic core after heat treatment at 800 ℃ (1073 K) drops to 10 µΩm.

c. Granulation process

The magnetic powders in a magnetic powder core are bound together by a binder to maintain the core shape. The fixing of the binder to the powder surface is called the granulation process. **Figure 2.1.3.5** shows the binder granulation process using a stirring-mixing granulator. A predetermined amount of binder precursor solution is fed into the magnetic powder, and the binder precursor is fixed to the powder surface by stirring and mixing. However, it is difficult to form a uniform film, and voids without binder and areas where the powders come into contact with each other occur inside the magnetic core.

Resin-based binders include epoxy, silicone, and polyimide. The heat resistance of the adhesive strength of resin-based binders is generally determined by the glass transition temperature, which is generally 100 to 200 ℃ for two-component epoxy resins consisting of a main agent and a curing agent. However, the thermal decomposition temperature is 250-350 ℃, and the thermal treatment temperature for the purpose of strain removal after powder molding, as described below, is limited by the thermal decomposition temperature of the epoxy resin, so strain removal may be insufficient for some materials. Silicone resin has a glass transition point below the freezing point and is flexible and rubbery at room temperature. As **shown in Figure 2.1.3.6**, at temperatures above 500 ℃, silicone resin gradually denatures to inorganic silica, mainly due to the decomposition of methyl and phenol groups. [5] Even at 500 ℃, the weight change from room temperature is about 10 % . The weight change from room temperature is about 10 % even at 500℃, enabling high-temperature strain-relieving heat treatment after powder molding using silicone resin as binder. P olyimide resin has high heat resistance with a thermal decomposition temperature of 400℃. However, there are few examples of its use as a binder because of its high cost.

Figure 2.1.3.5 Binder granulation proc

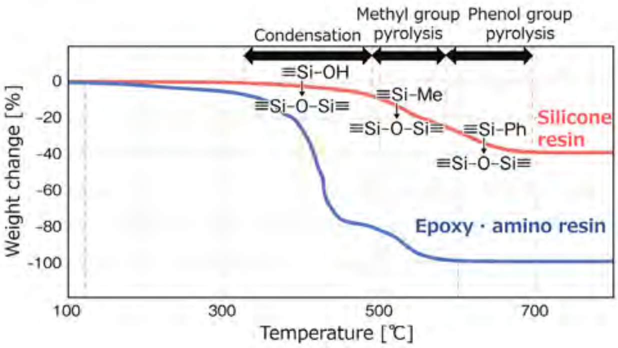

Figure 2.1.3.6 Thermogravimetric Change of Silicone and Epoxy Resins, Based on Reference (5)

There is a method of granulation using a precursor solution containing dispersed micro- or nanoparticles of alumina, zirconia, etc., and heat treatment after press molding to produce an inorganic ceramic binder, but the heat treatment temperature is high and the powder is prone to oxidation and sintering. On the other hand, low melting point glass with a softening point of about 300 ℃ is promising as an inorganic binder, but there is not much data on its wettability and adhesive strength with magnetic powders, which is an issue for the future.

Although not discussed in detail here, lubricants are added during the granulation process to improve the powder filling rate by improving the sliding between powders during pressing and molding, and mold release agents to facilitate release from the mold.

d. Powder molding

In many cases, the cold press method is used for powder forming of magnetic cores. High strength is required for press forming dies, and cemented carbides such as die steel and tungsten carbide are used. There is a lot of know-how involved in fabricating dies with complex shapes, and since dies are generally expensive and consumable, long life is also an important point.

In the mold compression molding method, the maximum applied pressure is about 2,000 MPa even when cemented carbide is used for the mold, and 1,300 MPa is considered the limit for mass production in consideration of mold life [6]. Generally, the higher the applied pressure, the higher the compacting density of the powder, but this not only shortens die life but also increases the size of the press equipment and makes it more expensive.

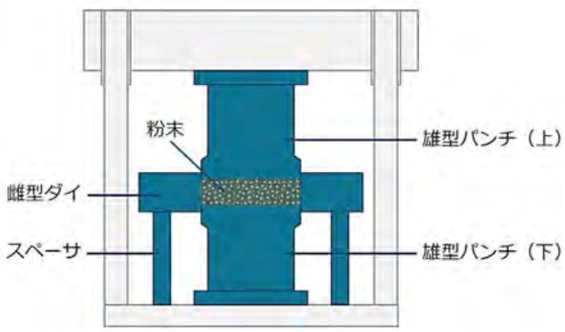

Fig. 2.1.3.7 Overview of dual-spindle press forming

Figure 2.1.3.7 shows an overview of the biaxial press forming equipment. Powder filled in the female die is pressurized by the male punch. Of the pair of upper and lower punches, the upper punch presses from above, and the method of pressurizing and compressing by the upper and lower punches is called biaxial press forming. When powder is molded in a die, biaxial pressure forming is often employed, in which the powder to be processed is filled into a female die and pressurized from the top and bottom. In the method where the powder is pressurized uniaxially from one side, friction with the inner wall of the die causes a pressure difference in the powder, making it difficult to maintain a uniform density of the compacted product. If the density of the compact is not uniform, cracks will occur during subsequent heat treatment.

Another method is the hot press method in which the powder is heated and compacted, but there are not many examples of its use in magnetic powder cores due to the large scale of the equipment. In addition, there is a prototype of a nanocrystalline magnetic core made by mixing magnetic powder and inorganic insulators and forming them by the discharge plasma sintering method [7], but it is difficult to increase the size of the core.

e. Binder curing heat treatment

To obtain powder-to-powder adhesion after press forming, a heat treatment is performed to harden the binder precursor on the surface of the magnetic powder fixed in the granulation process. The hardening heat treatment temperature depends on the binder material.

Polymerization reaction of thermosetting two-component epoxy resins starts at approximately 100 ℃, and they cure for a short time at curing temperatures of 120-150 ℃. In the case of silicone resins, standard products can cure at approximately the same temperature as epoxy resins. Standard silicone resins can be cured at approximately the same temperature as epoxy resins, but the curing temperature tends to be higher for high heat-resistant products exceeding 200℃. Polyimide resins undergo an imidization reaction at 350-400 ℃, so they can be cured in a short time at 120-150 ℃. Polyimide resins have a high curing temperature and excellent heat resistance because the imidization reaction occurs at 350-400 ℃. However, as mentioned above, they are expensive, and there are few examples of their use in magnetic powder cores.

Inorganic ceramic binders have a very high hardening temperature, and as mentioned above, there is a risk of oxidation and sintering of the magnetic powder, so there are few examples of application, except for pure iron-based magnetic powder cores used in the low frequency range where eddy current loss is not a problem. There is a type of magnetic powder core that is manufactured by mixing magnetic powder and low-melting-point glass, press forming, heating at the softening point of the low-melting-point glass to bond the powders together, and then cooling. The heating temperature in this case is about 350 ℃. Depending on the conditions, it may be possible to release the distortion of the magnetic powder caused by press forming, but there is a risk of an increase in the internal stress of the powder due to the difference in linear expansion coefficient between the low-melting-point glass and the magnetic powder.

f. Distortion heat treatment

In the crystalline-type pressed powder core described below, the powder filling ratio increases with plastic deformation of the powder during press forming, and the use of high saturation magnetization powder can achieve a pressed core with high saturation magnetization. However, in powder materials with large magnetostriction, the coercive force increases due to residual crystal distortion, leading to increased hysteresis loss. Similarly, in the case of a pressed core using Fe-based amorphous (including metallic glass) powder with poor ductility and ductility and large magnetostriction, the coercive force increases due to the internal stress induced during press forming. Distortion heat treatment is performed to reduce the coercive force on the binder-hardened heat-treated pressed magnetic powder core after pressing molding, regardless of whether it is crystalline or amorphous.

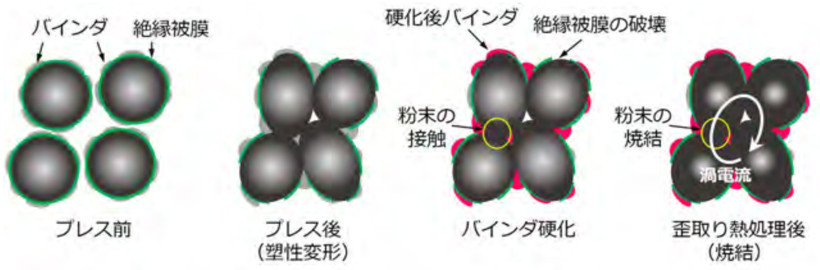

Figure 2.1.3.8 Sintering of powders by high-temperature distortion heat treatment

Even if a highly heat-resistant epoxy resin with a glass transition temperature exceeding 200 ℃ is used as a binder and heat-treated at a temperature exceeding 200 ℃, residual stress cannot be sufficiently released depending on the magnetic powder material. Furthermore, heat treatment at a temperature near or above the pyrolysis temperature promotes the release of residual stress, but the loss of the binder that binds the powders together makes it difficult to maintain the magnetic core shape itself. When silicone resin is used as a binder, the weight loss is only about 10 % even at 500 ℃, and the powder begins to denature into silica, making it possible to perform strain removal heat treatment at higher temperatures.

When the insulating film on the powder surface is destroyed by plastic deformation of the powder during press forming and the powders come into direct contact with each other, high-temperature strain removal heat treatment causes powder sintering, which increases eddy current losses due to macro eddy currents flowing across the multiple powders. **Figure 2.1.3.8** shows this schematically. If the temperature of the heat treatment for strain removal is increased in anticipation of a decrease in hysteresis loss, eddy current loss increases due to powder sintering. This is the reason why it is difficult to achieve low iron loss in a pressed magnetic core.

(2) Crystalline Powder Core

a. Magnetic powder materials

The Fe-Si, Fe-Ni, and Fe-Si-Al systems are typical of crystalline magnetic powder cores.

In Fe-Si alloys, the saturation magnetization decreases with increasing Si content, but the magnetostriction becomes small. 6.5 wt.% Si content increases the electrical resistivity, but the plastic deformation during pressing becomes small due to the increase in hardness. Fe-Si superimposed core with DC superposition characteristics is often used with 3 wt.% Si-Fe powder having saturation magnetization close to 2 T. Fe-Si superimposed core is characterized by high saturation magnetization and is often used at frequencies below several tens of kHz with low iron loss.

In the Fe-Ni system, the powder composition of 35 to 65 %-Ni and the rest Fe is selected. 50 % Fe-Ni is a particularly high permeability composition. The saturation magnetization is 1.4 to 1.6 T for the powder. The high ductility of this alloy allows for easy plastic deformation during press forming.

In the Fe-Si-Al system, there is a composition [9] in which both magnetostriction and crystal magnetic anisotropy are zero, and in this alloy composition, low coercivity and high magnetic permeability can be obtained. In the Fe-Si-Al system, both the magnetostriction constant and crystal magnetic anisotropy are temperature dependent.[10][11] If an alloy composition is selected in which both are zero at room temperature, there is a risk of thermal runaway, in which iron loss increases with increasing temperature. [12] The saturation magnetization of Fe-Si-Al system magnetic powder cores is not high, around 1 T, but the hysteresis loss is low. However, together with low hysteresis loss, it has lower iron loss than Fe-Si or Fe-Ni magnetic powder cores in the frequency range from low frequency to several hundred kHz, and is widely used especially in frequencies above 100 kHz.

In crystalline alloys, in addition to the coercive force generation mechanism due to magnetostriction and crystal magnetic anisotropy, the coercive force is also generated by grain boundaries that serve as pinning sites for magnetic wall movement, and the smaller the grain size, the greater the coercive force and the greater the hysteresis loss. In crystalline systems, heat treatment releases residual stress, which is expected to reduce the coercive force, and grain growth by merging of adjacent crystal grains in the powder reduces the grain boundaries that serve as pinning sites for magnetic wall movement, which in turn reduces the coercive force.

Magnetic powders for magnetic powder cores are often prepared by atomization, in which molten alloy is injected and cooled with water or gas.

b. Example of strain-removal heat treatment in Fe-Si type magnetic powder core

Daido Bunseki Research Inc. reported the relationship between the heat treatment temperature, plastic strain, and coercive force of Fe-Si magnetic powder cores. [13] The sample was press-formed from Fe-Si powder with a grain diameter (median diameter; D_{50}) of 27 μm using silicone resin as binder, and after resin hardening, it was subjected to strain removal heat treatment at three different temperatures: 500 ℃, 700 ℃, and 750 ℃. Because silicone resin was used as binder, the sample was subjected to strain removal heat treatment at three different temperatures. Since silicone resin is used as the binder, it is assumed that the silicone resin is modified to silica by heat treatment at the three different temperatures. According to the inverse pole figure (IPF) map, the crystal grains in the Fe-Si powder are almost randomly oriented, and the crystal grains become coarser as the heat treatment temperature increases. According to the KAM (Kernel Average Misorientation) map analysis, the coercive force decreases with increasing heat treatment temperature due to the decrease in plastic strain, but it is 265 A/m (3.3 Oe) even at 750 ℃ heat treatment, which is not a dramatic decrease in coercive force.

The above shows that although high-temperature heat treatment is effective in reducing hysteresis loss, there is concern about increased eddy current loss due to powder sintering, and the conditions are set considering the tradeoff between the two.

c. Suppression of plastic deformation during press forming in pure iron-based pressed magnetic cores

While it is easy to increase the density of pure iron-based magnetic powder cores, the sliding of the powder on the die surface during press forming causes plastic flow, which leads to the destruction of the insulating film . Ishihara et al. [14] developed an insulating solid lubricant for die pressing that suppresses plastic flow of powder. **Figure 2.1.3.9** shows a conceptual diagram of the proposed method to avoid plastic flow of pure iron-based powder. Insulating oxide particles are dispersed in the lubricant as an additive aid. The developed lubricant suppresses the sliding forces on the mold surface and between powders to lubricate them, thereby preventing plastic flow of the powders, and the oxide particles as an additive agent selectively bind to the powder surface to protect the insulating film. Pure iron-based magnetic powder cores for photovoltaic power conditioners and automotive DC-DC converters have been developed using this method.

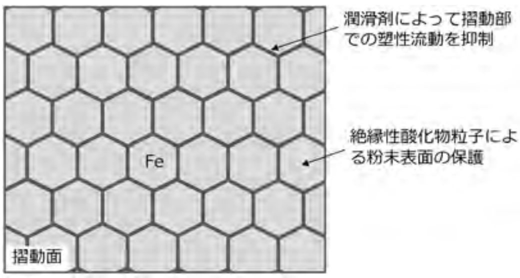

Figure 2.1.3.9 Lubricants for press forming to avoid plastic flow of pure iron-based powders, based on reference (14)

d. Improvement of the temperature characteristics of iron loss in Fe-Si-Al based magnetic powder cores

He stated that Fe-Si-Al alloys have temperature dependence of both magnetostriction constant and crystal magnetic anisotropy, and there is a risk of thermal runaway, in which iron loss increases with temperature rise.

Aikawa et al. [12] fabricated Fe-Si-Al magnetic powder cores using powders of various alloy compositions and investigated the temperature characteristics of iron loss in detail. They used powders prepared by gas atomization, and after granulating classified powders with a median diameter of 106 μm with a silicone resin precursor, they were mold-pressed at an applied pressure of 980 MPa and subjected to strain-relieving heat treatment at 700 ℃. **Figure 2.1.3.10** shows an example of the temperature dependence of the iron loss of a magnetic powder core when two types of Fe-Si-Al composition powders, Fe-8.8Si-6.0Al wt.% and Fe-9.9Si-5.9Al wt.%, are used. The temperature coefficient is positive in the temperature range from 20 to 120 ℃, indicating that there is a significant risk of thermal runaway. On the other hand, the iron loss of Fe-8.8Si-6.0Al wt.% composition powder-compacted magnetic cores decreases slowly with increasing temperature. Although the iron loss separation was not performed in Ref.(12), assuming that the temperature dependence of iron loss is due to the temperature dependence of magnetostriction and crystal magnetic anisotropy, the hysteresis loss is considered to be dominant in this case. In the case of the Fe-Si-Al compact core, the temperature coefficient of iron loss is inverted by a slight deviation in composition, so precise composition control is necessary.

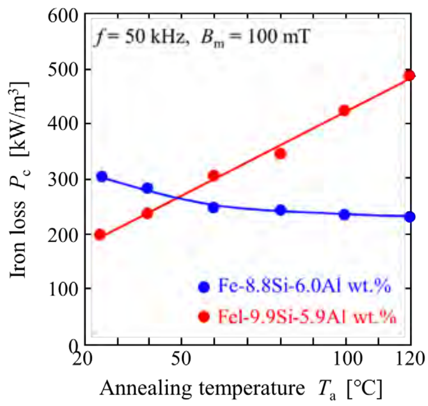

Fig. 2.1.3.10 Temperature dependence of iron loss in a magnetic powder core with two types of Fe-Si-Al composition powders,

e. Iron loss characteristics of crystalline-type pressed core

Figure 2.1.3.11 evaluates the iron loss of commercially available Fe-Si, Fe-Ni, and Fe-Si-Al crystalline-type piezoelectric cores. The frequency dependence of iron loss shows that hysteresis loss proportional to frequency is dominant in the range of approximately 50 to 100 kHz, and the iron loss of Fe-Si-Al and Fe-Ni type cores with low coercivity is 1/4 to 1/3 of that of Fe-Si type. On the other hand, above several hundred kHz, the iron loss increases with a dependence close to the square of the frequency, and eddy current loss becomes dominant, and the iron losses of the three systems approach each other.

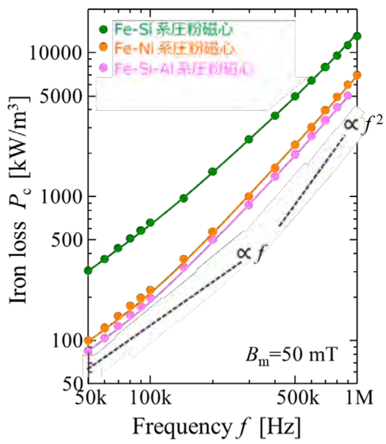

Fig. 2.1.3.11 Frequency characteristics of iron loss in commercially available Fe-Si, Fe-Ni, and Fe-Si-Al magnetic powder cores

(3) Fe-based amorphous, Fe-based glass, and Fe-based nanocrystalline magnetic powder cores

Fe-based amorphous, Fe-based glass, and Fe-based nanocrystalline materials are expected to have low coercivity, high electrical resistivity, and reduced eddy current loss.

a. Magnetic powder materials

Fe-based amorphous powder

In general, it is difficult to obtain a low coercivity powder comparable to roll-quenched thin strip by atomization. During atomization, water decomposes and generates oxygen gas and oxygen ions, which oxidize the surface of the powder, causing partial crystallization of the powder. In many cases, a small amount of Cr is added to improve corrosion resistance in order to suppress oxidation during atomization. The gas atomization method has a lower cooling rate than the water atomization method, resulting in a lower yield of amorphous powder. In the metal-semimetal amorphous system, the yield can be increased by increasing amorphous forming elements such as Si and B, but the saturation magnetization decreases and it is difficult to produce amorphous powder with the same composition as roll-quenched thin strip.

The SWAP method (Spinning Water Atomization Process) using a rotating water flow has been developed and put into practical use as a method to dramatically increase the cooling rate and improve the yield of amorphous powder without significantly increasing the amount of amorphous forming elements [15]-[17]. The SWAP method can also be used to produce amorphous powders with nanocrystalline compositions, as described below. Even in these cases, Cr is often added to improve corrosion resistance during atomization, and C is often added to reduce the viscosity of the molten alloy.

Amorphous powders for pressed magnetic cores are mostly Fe-Si-B based, and although they have the advantage of having a smaller coercive force than the aforementioned crystalline powders due to the disappearance of crystalline magnetic anisotropy, they have the disadvantage of having a large magnetostriction constant. Even if the powder coercive force is small, the residual stress induced by pressure forming increases the coercive force of the magnetic core, and since the strain removal heat treatment temperature is limited by the crystallization temperature, a dramatic reduction in coercive force is difficult.

Fe-based glass powder

Inoue et al. [18] discovered a new amorphous alloy that undergoes a glass transition and succeeded in fabricating a bulk amorphous alloy. Unlike conventional amorphous materials, this material was named metallic glass because it has a glass transition point. When cooled from the molten state, the alloy passes through the supercooled liquid temperature range (generally around 60% of the melting point), eliminating the need for superquenching as with conventional amorphous alloys. Subsequently, Fe-B-Si-Zr materials with high saturation magnetization of 1.53 T and low coercivity of 2.3 A/m [19] and Fe-Si-B-P materials with high glass-forming ability [20] were developed. Metallic glass powders have also been developed and commercialized [21] and are expected to be used in high-frequency magnetic powder cores [22].

Fe-based nanocrystalline powder

Yoshizawa et al. [23] presented Fe-based nanocrystalline alloy thin strips, which were named FINEMET because of their ultrafine crystalline structure with Fe in solid solution. The roll-quenched Finemet composition (Fe-Si-B-Nb-Cu system) thin strip is as-quenched and amorphous, and Cu nanoparticles are first deposited during heat treatment, and Fe-Si nanocrystal grains are deposited in the Nb-B rich matrix phase with high crystallization temperature to form the nanocrystal structure. Since the nanocrystal grains and the matrix phase have positively and negatively inverted magnetostriction, the magnetostriction constant can be reduced to about 1 ppm by properly balancing the two. However, optimization of heat treatment conditions is necessary to achieve an optimum nanocrystalline structure that produces low magnetostriction, and in the case of FINEMET, nanocrystallization heat treatment is performed in the range of 500 to 560 °C. Thin strips of FINEMET have a saturation magnetization of 1.24 T. Combined with low magnetostriction of about 1 ppm and the disappearance of crystal magnetic anisotropy due to the nanocrystalline structure, the coercive force is as low as several A/m and the specific permeability is as high as several tens of thousands or more.

A number of companies have introduced Fe-Si-B-Nb-Cu atomized powders for magnetic powder cores.[16][21] SWAP method Fe-Si-B-Nb-Cu-C-Cr spherical powders [24] are close to spherical and have extremely smooth surfaces. In addition, the Fe-Si-B composition of the atomized powder is different from that of the roll-quenched Finemet thin strip, and the coercive force is more than 10 times higher than that of the thin strip.

Makino et al. [25] developed Nanomet, a nanocrystalline soft magnetic alloy composed of Fe-Si-B-P-Cu with a high saturation magnetization of 1.8-1.9 T, comparable to silicon steel plates, and a low coercivity of 5.8 A/m. The magnetostriction constant is 2.3 ppm, which is slightly larger than that of Finemet. The magnetostriction constant is 2.3 ppm, which is slightly larger than that of Finemet, but the magnetostriction is remarkably low for a material with a high saturation magnetization of nearly 2 T. P has a high amorphous forming ability and can be amorphized even at high Fe concentrations, but the nanocrystallization mechanism is different from that of the Finemet system and the optimal nanocrystal structure is Rapid heating at several hundred °C per minute is required to obtain a uniform structure consisting of α-Fe crystal grains of about 10 nm.[26] Due in part to the high Fe concentration, the nanocrystallization heat treatment temperature is more than 100 °C lower than that of the FINEMET system. Recently, various multi-system nanomet alloys have been developed based on the nanomet composition, such as Fe-Co-Si-B-P-Cu, Fe-Ni-Si-B-P-Cu, and Fe-Si-B-P-C-Cu [27]. Nanomet-based powders for pressed magnetic cores have also been developed by several organizations. For example, an atomized Fe-Si-B-P-C-Cu powder [28] has a saturation magnetization of 1.76 T.

In 2015, Tohoku Magnet Institute, a Tohoku University venture established by Tohoku University, started mass production and commercialization of Nanomet materials, and has succeeded in mass production of powders as well as thin strips. The company developed a modified water atomization method named HPWA/YK method [29] and succeeded in producing amorphous single-phase powder with Nanomet composition. Magnet Institute was dissolved on May 2, 2025, but Tohoku University and Tokin are continuing the research and development of nanomet-based thin strips and powders. For example, Kuno et al. [30] developed a $Fe_{84.3}B_6P_9Cu_{0.7}$ at. % powder characterized by low coercivity of 30-40 A/m as a magnetic core powder for inductors with a saturation magnetization of about 1.7 T. Tokin also presented a nanomet powder magnetic powder core for next-generation power electronics jointly developed with Tohoku University.[31] Differential thermal (DSC) analysis of amorphous powder with an as-atomized nanomet (Fe-B-P-Cu) composition showed that α-Fe nanocrystals precipitate in the amorphous matrix phase at a temperature Tx The nanocrystalline powder after heat treatment at 410 °C of the as atomized amorphous powder shows saturation magnetization of 1.74 T and coercivity of 31 A/m. The powder has excellent properties of both high saturation magnetization and low coercivity. The nanocrystalline powder after heat treatment at 410 °C shows saturation magnetization of 1.74 T and coercivity of 31 A/m.

b. Examples of prototype Fe-based amorphous, Fe-based glass, and Fe-based nanocrystalline magnetic powder cores

Improved powder filling rate

Amorphous, metallic glass, and nanocrystalline alloys are not ductile, and as with crystalline magnetic powders, plastic deformation of the powder during pressing almost does not occur, making it difficult to achieve a high packing ratio, especially for near spherical powders.

In the usual cold press method, a composite powder densification technique is employed, in which an appropriate amount of multiple size

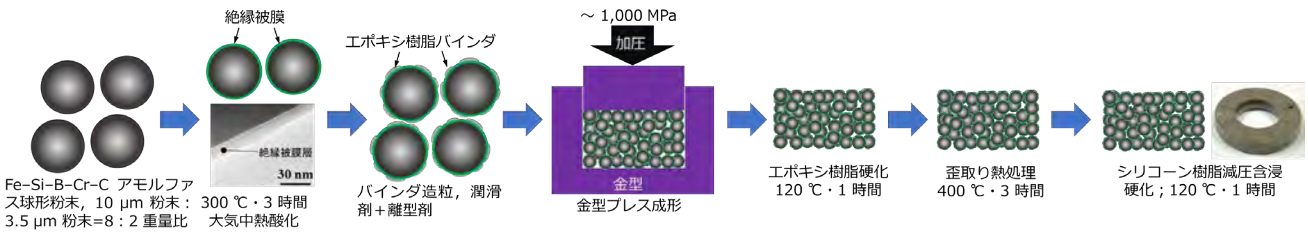

Fig. 2.1.3.12 Prototype of SWAP method Fe-Si-B-Cr-C amorphous spherical powder core, based on Ref. (32)

powders with different grain size distributions are mixed together. For example, in an example of a magnetic powder core using Fe-Si-B-Cr-C spherical powders with average median diameters of 10 μm and 3.5 μm produced by the SWAP method, when both were mixed at a weight ratio of 8:2 The highest powder fill factor of 75 % was obtained when both were mixed in a weight ratio of 8:2 (32).

Since metallic glasses have a glass transition point, the hot pressing method, in which powders are heated to the glass transition point and compacted, contributes to an improvement in the filling ratio due to deformation of the powder. In fact, in an example of hot press forming of $Fe_{77} P_7 B_{13} Nb_2 Cr_1$ at. powder (33), the filling ratio was improved to 91 %, saturation magnetization of 1.13 T, and coercivity of 50 A/m were achieved. However, in the case of a pressed core heat-treated by strain removal at 500 ℃, the specific permeability reached 1,200 at a frequency of 1 kHz, and the iron loss was 1,400 kW/m^3 at a frequency of 50 kHz and a flux density amplitude of 100 mT, which is not a low iron loss compared with a conventional crystalline-type pressed core.

There is an example of a nanocrystalline powder core in which low melting point glass (Li_2O-B_2O_3-SiO_2-CaO-Al_2O_3; LBSCA) is used as binder and heat hardening and powder forming are done by hot press method (34). The iron loss was 178 kW/m^3 at a frequency of 100 kHz and a flux density amplitude of 50 mT, which is slightly lower than the iron loss of 200 kW/m^3 under the same excitation conditions of a commercial Fe-Si-Al magnetic powder core shown in **Figure 2.1.3.11**.

Example of Fe-based amorphous powder core

Amorphous spherical powder with poor ductility is hardly deformed by high-pressure press forming. (32), a mixture of powders with a median diameter of 10 μm and a thermally oxidized insulating film of 3.5 μm in a weight ratio of 8:2, which results in the highest filling ratio, and mold forming at approximately 1,000 MPa resulted in a filling ratio of only 75 %. In this example, as shown in **Figure 2.1.3.12**, epoxy resin is used as the binder for molding, and nearly 30% of the epoxy resin for the binder decomposes thermally after strain removal heat treatment at 400℃, about 100℃ lower than the crystallization temperature of the powder, after the core is molded (see **Figure 2.1.3.6**). Therefore, after strain removal heat treatment, the silicone resin precursor is impregnated under reduced pressure and cured to make the final magnetic core. The saturation magnetization of the core is 0.93 T, the coercive force is 177 A/m, and the specific permeability is about 36, which is almost constant up to 3 MHz. The frequency characteristics of the iron loss are shown in **Figure 2.1.3.13.** The iron loss at a frequency of 100 kHz and a flux density amplitude of 50 mT is about 150 kW/m3, and at 100 mT it is about 505 kW/m^3, lower than the commercial Fe-Si, Fe-Ni, and Fe-Si-Al magnetic powder cores shown in **Figure 2.1.3.11**.

Example of Fe-based glass powder core

In 2008, Alps Electric Co., Ltd. announced the development of a magnetic core using Fe-based glass powder under the trade name Liqualloy^{TM}. (22) Liqualloy powder does not require ultra-quenching, and can be produced using ordinary water atomization equipment, which is a major advantage. Liqualloy powder cores are used in toroidal cores and chip inductors (35), but the specific fabrication method of these cores has not yet been published. According to reference (22), the saturation magnetization is 1.2 T, the electrical resistivity of the core is 3.07×10^3 Ω-m, the coercive force is undisclosed, the decrease in permeability with respect to DC magnetomotive force is the same as that of Fe-Si-Al type core (however, the specific magnitude of the permeability is unknown), the iron loss is almost the same as that of Mn-Zn ferrite core, and the iron loss is 1/3 that of Fe-Si-Al Al-based magnetic powder cores. However, the magnetic flux density amplitude at the time of iron loss measurement was not specified, making quantitative comparison of iron loss with magnetic cores other than Mn-Zn ferrite and Fe-Si-Al type pressed cores difficult. Later, Alps Electric changed its name to Alps Alpine, and later the inductor business featuring Liqualloy was transferred to the Delta Electronics Group of Taiwan.

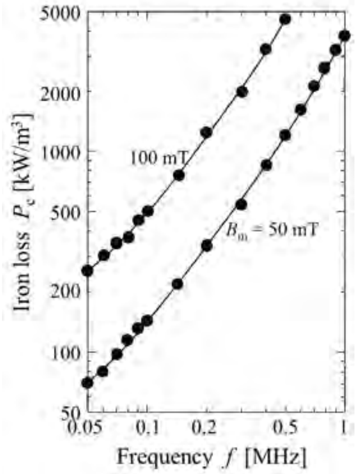

Figure 2.1.3.13 Frequency characteristics of iron loss of Fe-Si-B-Cr-C amorphous spherical powder core, based on reference (32)

Example of Fe-based nanocrystalline magnetic powder core

Both as-atomized amorphous powder and heat-treated nanocrystallized powder are available, but by using as-atomized amorphous powder for press forming and post-nanocrystallization heat treatment, nanocrystallization as well as internal strain release can be expected. By using As atomized amorphous powder for press forming and post-nanocrystallization heat treatment, it is expected to release the internal strain at the same time as nanocrystallization. The post-nanocrystallization heat treatment temperature is more than 100 ℃ higher than the strain-relieving heat treatment temperature (400 ℃) of Fe-Si-B-Cr-C amorphous spherical powder compacts, which enables more effective release of internal strain. more effectively.

Pressing amorphous powders under high pressure before nanocrystallization hardly changes the spherical powder shape. Therefore, Kanaya et al. (24) employed Fe-Si-B-Nb-Cu-Cr-C composition amorphous powders with median diameters of 10 μm and 3.5 μm, and fabricated Fe As with the Fe-Si-B-Cr-C amorphous spherical powder core, the 10 μm and 3.5 μm diameter powders were mixed in a weight ratio of 8:2 to achieve the highest powder filling ratio, cold pressed in a metal mold at about 1,000 MPa, and then formed into a nanocrystalline core at After cold press molding at approximately 1,000 MPa, the powder was subjected to nanocrystallization and strain removal heat treatment at 510 ℃ for 3 hours to produce a prototype SWAP Fe-Si-B-Nb-Cu-Cr-C nanocrystalline spherical powder magnetic core. As with the SWAP Fe-Si-B-Cr-C amorphous spherical powder core, epoxy resin was used as the molding binder and silicone resin as the impregnating resin after nanocrystallization and strain removal heat treatment. The powder filling rate is as high as that of amorphous spherical powder core. The powder filling ratio is 74 %, almost equivalent to that of the amorphous spherical powder core, and the saturation magnetization is 0.91 T. The coercive force is 123 A/m, which is smaller than that of the amorphous spherical powder core of 177 A/m. The specific permeability is about 33, which is almost constant up to a frequency of 4 MHz. **Figure 2.1.3.14** compares the frequency characteristics of iron loss with those of the Fe-Si-B-Cr-C amorphous spherical powder core. B-Nb-Cu-Cr-C nanocrystalline spherical powder core has an iron loss of about 105 kW/m3 at a frequency of 100 kHz and a flux density amplitude of 50 mT, and about 380 kW/m^3 at 100 mT. -Si-B-Cr-C amorphous spherical powder core at a frequency of 100 kHz and a flux density amplitude of 50 mT is approximately 105 kW/m^3 and 380 kW/m^3 at 100 mT, respectively, which is about 70 to 75% of the iron loss of Fe

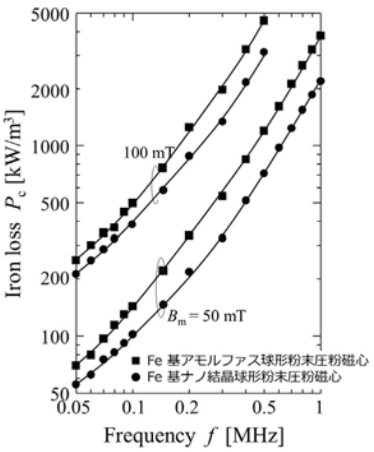

Figure 2.1.3.14 Frequency characteristics of iron loss of Fe-Si-B-Nb-Cu-Cr-C nanocrystalline spherical powder core, based on

As mentioned above, Tokin, in collaboration with Tohoku University, has developed an ultra-low-loss, high-saturation magnetization nanomet powder core.(31) DSC analysis of amorphous powder with As atomized nanomet (Fe-B-P-Cu) composition shows that α-Fe nanocrystals precipitate in the amorphous matrix phase at temperatures Tx1 and Hot pressing is performed at a temperature between T_{x1}, at which α-Fe nanocrystals precipitate in the amorphous matrix phase , and T_{x2}, at which the residual amorphous phase crystallizes. Although it is difficult to improve the powder filling ratio in the cold pressing method, the powder filling ratio of the hot pressed 17 μm diameter powder core was improved to 89 % after hot pressing at a temperature of 460 ℃ and an applied pressure of 784 MPa. It is interpreted that the nanocrystallization of α-Fe and the plastic deformation caused by the thermoplasticity of the powder during the hot press forming process simultaneously cause the densification of the core. The saturation magnetization and coercive force estimated from the saturation magnetization and *B-H* curves of the magnetic powder core evaluated by a sample vibration magnetometer are 1.54 T and 16 A/m. The saturation magnetization is close to that of crystalline Fe-Si and Fe-Ni magnetic powder cores and is about twice that of Fe-Si-Al magnetic cores. The coercive force is the smallest among all the commercially available pressed cores. It should be noted that the specific initial permeability, which is close to 100, is almost constant up to frequencies close to 10 MHz. As for iron loss, hysteresis loss is dominant below 10 kHz, and the iron loss is 146 kW/m^3 at a frequency of 100 kHz and a flux density amplitude of 100 mT, where eddy current loss is negligible, showing the lowest value for a pressed core under the same excitation conditions.

The magnetic powder core prototyped in reference (31) is a toroidal size with an outer diameter of 13 mm and an inner diameter of 8 mm (the height is unknown), and the scale of the hot press equipment must be expanded in order to expand it to a size conducive to actual application in inductors.

Comparison of iron loss of various types of magnetic powder cores

Figure 2.1.3.15 summarizes the relationship between iron loss and saturation magnetization of crystalline, amorphous, and nanocrystalline type magnetic powder cores with reference to the data in Reference (31). With some exceptions, it is clear that the nanocrystalline type pressed core has low iron loss. In particular, the hot-pressed nanomet type pressed core listed in reference (31) has both high saturation magnetization and low iron loss, and the iron loss of the pressed core using the aforementioned 17-μm-diameter nanomet powder is lower than that of the amorphous type (Fe (Fe-Si-B-Cr-C) spherical powder core [32] under the same excitation conditions, while the iron loss of the Finemet (Fe-Si-B-Nb-Cu-Cr-C) nanocrystalline spherical powder core [24], and the saturation magnetization is 1.7 times higher than that of the Fe-Si-B-Nb-Cu-Cr-C) spherical powder core.

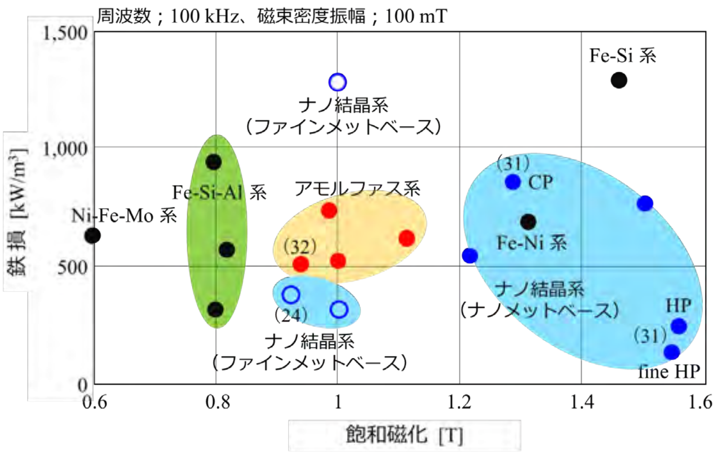

Fig. 2.1.3.15 Comparison of iron loss of various types of pressed cores, prepared by organizing the relationship between iron loss and saturation magnetization of crystalline, amorphous, and nanocrystalline powdery magnetic cores, with reference to the data in Ref. (31)

Traditionally, the greatest challenge for pressed magnetic cores has been to achieve low coercivity, and compatibility with high saturation magnetization has been strongly demanded. Hot press-formed nanomet powder pressed magnetic cores are now thought to offer a promising option for inductors that can achieve both high saturation magnetization and low iron loss.

1.3.3 Powder core Fine particle composite core for Beyond MHz

(1) Challenges of Ni-Zn ferrite cores in the Beyond MHz band benchmark

For magnetic core materials used at frequencies above 1 MHz, an important indicator is how to reduce the effects of eddy current losses and residual losses that are problematic in the high-frequency range. In this paper, we will discuss the challenges of Ni-Zn ferrite cores, which have been regarded as the benchmark for magnetic cores in the Beyond MHz band.

Bulk Ni-Zn ferrite has very low eddy current losses due to its high electrical resistivity (several hundred ohm-m) compared to metallic magnetic materials, but the upper frequency limit for use is limited by natural resonance.

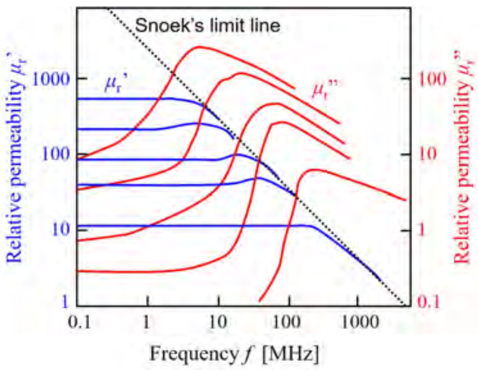

Figure 2.1.3.16 Complex specific permeability of bulk Ni-Zn ferrite, based on reference (36)

Figure 2.1.3.16 shows the frequency response of the complex specific permeability of bulk Ni-Zn ferrite [36]. By adjusting the ferrite composition, the specific permeability can be changed from around 10 to several hundred or more, but there is a relationship between the specific permeability and its cutoff frequency called the Snoek's limit, which follows equation (2.1.3.2).

$$\mu_{\mathrm{static}} \cdot f_{\mathrm{r}} \propto M_{\mathrm{s}} \qquad (2.1.3.2)$$

Here, μ_{static} is the static permeability, f_{r} is the natural resonance frequency, and M_{s} is the saturation magnetization.

It has been shown that Mn-Zn ferrite, which is also classified as a spinel ferrite, generates much larger magnetic loss than that predicted from the complex permeability when AC excitation is performed at large amplitude [37]. **Figure 2.1.3.17 shows** the frequency dependence of the dynamic loss (eddy current loss, residual loss), which is the iron loss W_{c0} minus the hysteresis loss W_{h0} per cycle measured for a Mn-Zn ferrite core for switching power supplies in the range 100 kHz to 10 MHz, plotted with the flux density amplitude B_{m} as a parameter. The solid line in the figure shows the frequency dependence of the dynamic loss (eddy current loss, residual loss). The solid line in the figure is the calculated value of dynamic loss W_{d} using the actual measured value of complex permeability under micro AC excitation conditions measured in the range of initial permeability, which is calculated based on the following equation. where tanδ (= μ"/μ') is the loss coefficient.

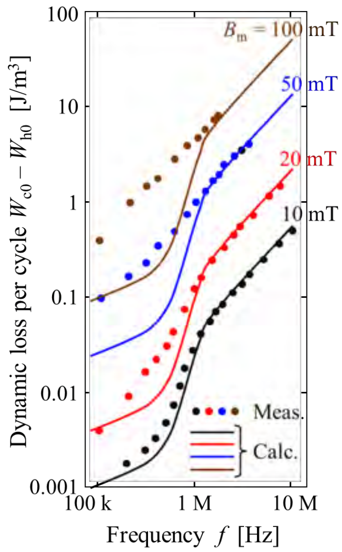

Figure 2.1.3.17 Frequency dependence of dynamic loss of Mn-Zn ferrite cores for switching power supplies, based on reference (37)

$$W_{\mathrm{d}} = \pi \, \frac{\tan\delta}{\mu'} \cdot \frac{1}{1+\tan^2\delta} \, B_{\mathrm{m}}^2 \quad [\mathrm{J/m^3}] \qquad (2.1.3.3)$$

Under conditions where the magnetic flux density amplitude B_{m} is small, the calculated and measured values of dynamic loss using the above equation with small amplitude parameters (μ', tanδ) agree well, but as B_{m} increases, the difference between the calculated and measured values increases, especially at frequencies below 1 MHz. The dynamic loss can be regarded as a linear loss proportional to the square of the magnetic flux density amplitude B_{m}, and it is assumed to be a reversible magnetization process. On the other hand, below 1 MHz, the dynamic loss generation mechanism is different between the micro-excitation level and the large-amplitude excitation of the magnetic core, indicating a significant nonlinearity in the loss. It is difficult to attribute such nonlinearity to eddy current losses, and it is necessary to consider the influence of residual losses other than eddy current losses, but the mechanism of generation of residual losses is still unresolved. The Mn-Zn ferrite described in reference (37) was developed with a view to application at several hundred kHz, and it can be said that it is greatly affected by the nonlinearity of dynamic loss in the large amplitude excitation state of actual operation.

It is assumed that the above phenomenon also occurs in Ni-Zn ferrites, and if the nature of the residual loss generation mechanism of spinel ferrites, including Mn-Zn ferrites, is clarified and guidelines for loss suppression are found in the future, the possibility of new low-loss ferrites is expected to expand.

(2) Various fine particle powders

a. Fine spherical powder

The greatest challenge for fine powder composite cores at frequencies higher than 1 MHz is the reduction of dynamic losses including eddy current losses, which requires the use of fine powders with high electrical resistivity and diameters of a few μm or less for metallic cores.

Carbonyl iron powder

Carbonyl iron powder is prepared by evaporation and precipitation of pentacarbonyl iron ($Fe(CO)_5$). For example, in BASF's lineup of carbonyl iron powders, as-made powders are called "hard grade" [38] and contain small amounts of impurities such as O, N, and C, but their saturation magnetization is close to that of pure iron. Because the particle size distribution of As-made powder with a median diameter of 1 to 2 μm is peaky [39] (see **Fig. 2.1.3.18**), it is difficult to increase the powder filling ratio in composite magnetic cores.

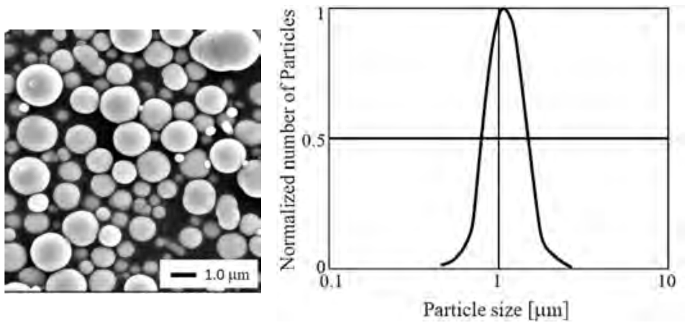

(a) SEM photograph (b) Particle size distribution

Figure 2.1.3.18 As made carbonyl iron powder, based on reference (39)

According to Koeda et al. [40], As made carbonyl iron powders have a nanocrystalline structure, which greatly reduces the crystalline magnetic anisotropy, and the powder interior has a Vortex magnetic structure reflecting its spherical shape. The powder becomes single crystal instead of Fe purity, and the sintering of the powder results in a larger powder size and higher coercive force.

Atomized powder

It is difficult to produce powders smaller than a few μm in diameter in high yield by conventional atomization methods, and fine powders are usually obtained by classification. Since fine powders are located at the left end of the particle size distribution, yields are low and costs are high, but Fe-Si-Cr, Fe-based amorphous, and Fe-based nanocrystalline powders with diameters of several μm are now on the market. In general, the coercive force of powders tends to increase as the powder size becomes finer, but Fe-based amorphous and Fe-based nanocrystalline powders have a lower coercive force and higher electrical resistivity than crystalline powders. Therefore, they are considered to be suitable as fine powders for fine composite magnetic cores targeting frequencies higher than 1 MHz.

To improve the yield of fine powder, it is effective to increase the temperature of molten alloy to reduce the viscosity of molten metal. However, conventional gas atomization and water atomization systems have not been able to easily increase the temperature of molten metal due to the life of refractory materials and operational safety. Tohoku University and Iwate University have jointly developed an atomization device using a high-speed combustion flame called the counter flame jet atomization (CFJA) method [40]. Trial production of Fe-Si-B-Cr-C amorphous powder has been achieved using this method, and an increase in the yield of nearly spherical fine powder less than 5 μm has been achieved.

Soft ferrite fine powder

In many cases, milled powders of 10 μm diameter or larger are employed for Mn-Zn and Ni-Zn bulk ferrite cores. On the other hand, Mn-Zn and Ni-Zn ferrite powders with a few μm diameter for composites with resin are now on the market [41]. Compared to powders for bulk ferrite cores, these powders have lower saturation magnetization and higher coercive force. The specific permeability of composite cores with 60 vol.% of these ferrite powders dispersed in resin is about 7 to 10, but the specific permeability drops significantly above 1 MHz. On the other hand, low- temperature co-fired ceramic (LTCC) chip inductors, which are used in various applications at frequencies higher than 1 MHz, use fine Ni-Cu-Zn ferrite powder with a sub-μm diameter [41].

Wet-synthesized magnetite fine particle powder and hydrogen-reduced fine iron powder

Magnetite (Fe_2O_3) fine particles of sub-μm diameter or smaller can be synthesized by wet processes such as coprecipitation, and until now, large coercivity exceeding 1,000 kA/m has been an issue [42], but recently, fine particle powders with low coercivity of around 400 A/m have also been developed [43]. Sub-μm -diameter iron fine powder can be obtained by heat-treating wet-synthesized magnetite fine powder in a hydrogen reduction atmosphere, but as with carbonyl iron powder, monocrystallization and sintering occur.

Chemically synthesized amorphous powder

Shimada et al. [44] and Murata et al. [45] prepared Fe-B amorphous fine powder by a wet chemical synthesis method. The powder synthesis was carried out using a drop solution consisting of an Fe-based reaction solution and a B-based reducing agent. The Fe-B amorphous fine powder with a median diameter of 490 nm has a uniform grain size and a smooth powder surface, and its saturation magnetization is higher (130-150 emu/g) than that of sub μm diameter magnetite powder prepared by coprecipitation because of its Fe-B binary composition. The coercive force of the powder is almost inversely proportional to the median diameter, and is as high as about 1 kA/m for 490 nm diameter powder and about 2.2 kA/m for 300 nm diameter powder. It has been reported that wet synthesis in a magnetic field can produce a chain structure of individual fine powder particles, and the longitudinal direction of the chain becomes the easy axis of magnetization due to shape magnetic anisotropy, resulting in high magnetic permeability, which may lead to the realization of an oriented fine powder chain anisotropic composite core.

b. Flat powder

In general, it is difficult to increase the powder filling ratio of composite magnetic cores using fine spherical powder targeting frequencies higher than 1 MHz, and it is difficult to achieve higher permeability than that of a pressed core for several hundred kHz due to residual antiferromagnetic field effects. In addition, it is difficult to achieve both high permeability and low loss in Ni-Zn ferrite, which is the benchmark magnetic core for high frequency range above 1 MHz, due to the limitation of Snoek based on natural resonance. Composite magnetic cores consisting of horizontally oriented and vertically stacked flat powders with thicknesses of a few μm or less may be able to achieve both high permeability and low loss by utilizing the high permeability in the flat plane due to the shape magnetic anisotropy of the flat powders. Various types of flat powders developed so far are shown below.

Fe-Si-Al flat powder

The application of flat powder began with its use in quasi-microwave band (300 MHz to 3 GHz) noise suppression sheets (product name: Bastareid) [by] Sato et al. For the application of noise suppression by energy absorption of unwanted electromagnetic waves, magnetic loss (complex permeability; the imaginary part μ'' in $\mu^{*}=\mu'-j\mu''$) should be dominant, so the thickness of the flat powder in the quasi-microwave band should be reduced to a minimum. The thickness of the flat powder in the quasi-microwave band should be about the thickness of the epidermis, and the realization of sub-μm -thick flat powder was targeted. The Fe-Si-Al flattened powder was prepared by flattening water-atomized Fe-Si-Al spherical powder with an average grain size of 14 μm and an oxide film by attritor milling.

The thickness of the powder remained almost the same at 1 μm even when the flattening time was increased beyond 7.2 ks (2 h) using an attritor mill. The powder coercive force already exceeds 5,000 A/m even after a short processing time of 1.8 ks (0.5 h), and increases to 7,500 A/m after 14.4 ks (4 h). The increase in the powder coercive force with increasing processing time is assumed to be due to processing strain. Subsequently, reduction of impurities and oxygen content in the raw powder, heat treatment after flattening, and other measures have resulted in low coercivity of Fe-Si-Al (sendust) flat powders, and flat powders with a low coercivity of about 300 A/m are now on the market [(48)].

Composite magnetic cores using Fe-Si-Al flat powders were first put to practical use as quasi-microwave band noise suppression sheets, and later, their application as magnetic cores for inductors in high-frequency DC-DC converters was promoted by TOKIN [(49)].

Fe-based amorphous flat powder

Fe-based amorphous flat powders for flat powder composite magnetic cores have been developed targeting application in magnetic components for MHz switching DC-DC converters [(50)]. **Figure 2.1.3.19** shows the preparation procedure for Fe-based amorphous flat powder. SWAP Fe-Si-B-Cr-C amorphous spherical powder with a median diameter of 12.8 μm and a saturation magnetization of 1.26 T was used. After flattening by vibration milling, the powder was heat treated in air at 380 ℃ to remove strain and to form a thermal oxide film. The footprint of the flattened powder after processing ranges from several tens of μm to 70 μm, and the thickness is approximately 1 μm. The coercive force of the amorphous spherical powder before flattening was 203 A/m, which increased rapidly to 3,980 A/m by flattening with a vibration mill and decreased to 438 A/m by heat treatment in air at 380 ℃. This is nearly 1.5 times larger than that of the heat treated Fe-Si-Al flat powder made from high-purity powder described above, 300 A/m. The crystallization temperature of Fe-Si-B-Cr-C amorphous spherical powder is about 450 ℃. It is difficult to increase the temperature of strain removal heat treatment, and the large internal strain caused by the flattening process was not fully released by the 380℃ heat treatment.

Qian et al. [(51)] investigated a wide range of flattening conditions by ball milling and post-processing heat treatment conditions using atomized Fe-Si-Me amorphous spherical powders (Me; Zr, B, P, etc.) as starting materials with the aim of achieving Fe-based amorphous flat powders with high saturation magnetization. The results of many experiments show that Fe-Si-P amorphous spherical powder flattened to a thickness of less than a few micrometers after 18 hours of ball milling and heat treatment at 380 ℃ has a saturation magnetization of 1.48 T and a coercive force of 600 A/m, which is twice that of the Fe-Si-Al The coercivity is twice that of the Fe-Si-Al flat powder.

Fe-based nanocrystalline flat powder

Although there are not many examples of the development of Fe-based nanocrystalline flat powders, Ying et al. [(50)] fabricated a prototype Fe-Si-B-Nb-Cu flat powder using roll-quenched thin strips as a starting material and achieved a low coercivity of 119 A/m, less than half that of Fe-Si-Al flat powders. As-quenched amorphous thin strips of Finemet composition were embrittlement heat-treated, milled, and flattened by a vibrating mill, and finally nanocrystallized by heat treatment at 560 ℃ for 1 hour in air to form a thermal oxide film. Similarly to the case of Fe-based amorphous flat powder, the coercivity of the powder increases rapidly to 3,311 A/m after flattening by vibration milling, but after heat treatment in air at 560 ℃, the coercivity decreases to 119 A/m due to nanocrystallization and release of processing strain.

Table 2.1.3.1 Comparison of magnetic properties of flat powders

Flat Powder	Saturation magnetization Ms	Coercive force Hc	Reference
Fe-Si-Al system	1.0 T	300 A/m	48
Fe-Si-B-Cr-C amorphous	1.26 T	438 A/m	50
Fe-Si-P amorphous	1.48 T	600 A/m	51
Fe-Si-B-Nb-Cu nanocrystal	1.24 T	119 A/m	50

Comparison of magnetic properties of flat powders

Table 2.1.3.1 compares the magnetic properties of Fe-Si-Al, Fe-based amorphous, and Fe-based nanocrystalline flat powders.

(3) Fine particle composite magnetic cores

a. Composite bulk magnetic cores

Carbonyl iron powder composite bulk magnetic cores

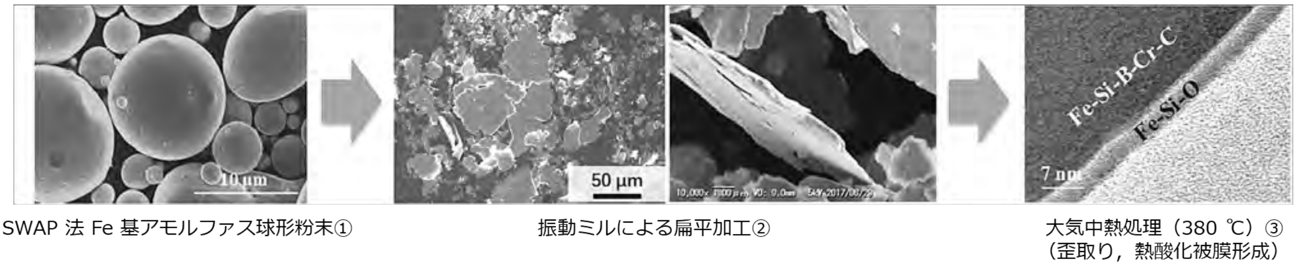

Fig. 2.1.3.19 Preparation procedure for Fe-based amorphous flat powder, based on Ref.

As mentioned above, As made carbonyl iron powder has a large powder coercivity of 700 to 800 A/m, but it is a fine spherical powder with a diameter of 1 to 2 μm, and has been put to practical use as a low permeability composite bulk core for high-current inductors that are difficult to magnetically saturate. For example, Micrometals' Carbonyl iron powder core has a lineup of magnetic cores with specific permeability ranging from 4 to 35, depending on the maximum frequency used [(52)]. The maximum operating frequency for a core with a permeability of 10 is 45 MHz, and the DC bias field at which the permeability drops by 20% is about 56 kA/m. According to Oliver [(53)] of the company, hysteresis loss accounts for most of the iron loss of a carbonyl iron powder core with a specific permeability of 10 up to about 10 MHz, and even above 10 MHz, the increase in eddy current loss is small, and above 20 MHz, the iron loss is lower than that of the benchmark Ni-Zn ferrite core. lower iron loss than the benchmark Ni-Zn ferrite core above 20 MHz.

Composite bulk magnetic cores by casting method

A casting method composite bulk magnetic core has been developed in which a mixed slurry of fine magnetic powder less than a few μm dispersed in a resin precursor solution by a vacuum mixer is poured into a mold and hardened to form a composite bulk magnetic core. **Figure 2.1.3.20** shows the fabrication procedure of a composite bulk magnetic core by the casting method.

Sugimura et al. [(54)] fabricated a composite bulk core using 2.56-μm-diameter SWAP Fe-Si-B-Cr-C amorphous powder with a saturation magnetization of 1.26 T and compared its magnetic properties with those of a Ni-Zn ferrite core. The Fe-Si-B-Cr-C amorphous powder is composed of fine powders with a diameter of 1-3 μm. The powder coercive force decreased from 132 A/m (1.65 Oe) before heat treatment to nearly 80 A/m (1 Oe) after heat treatment at 300 ℃ for 3 hours due to the release of internal strain remaining in the as-atomized state and the relaxation of the amorphous structure, and a 10 nm-thick oxide film of Fe-Si-O is formed. The saturation magnetization of the Fe-Si-B-Cr-C amorphous powder composite bulk core prepared using epoxy resin as binder is about 0.84 T, and the powder packing ratio of the core estimated by the saturation magnetization of the powder is about 67 %. The coercive force of the composite bulk core was 128 A/m, 1.6 times higher than that of the amorphous powder with oxide film, which is about 80 A/m. This is presumably due to the hardening stress of the epoxy resin used as the binder. The specific permeability of the amorphous powder composite bulk core is constant up to 100 MHz at about 10, and the loss factor tanδ estimated from the real part μ_r' and imaginary part μ_r'' of the complex specific permeability is on the order of 10^{-3} in the MHz band, which is comparable to that of Ni-Zn ferrite with specific permeability of 20. **Figure 2.1.3.21** shows the flux density amplitude dependence of the iron loss of the prototype Fe-Si-B-Cr-C amorphous powder composite bulk core at 2 MHz, together with the iron loss of commercially available Ni-Zn ferrites with permeabilities of 20 and 40. For both the amorphous powder composite bulk core and the two types of Ni-Zn ferrites, the iron loss shows more than a square dependence on the magnetic flux density amplitude B_m, indicating that the iron loss varies nonlinearly with the excitation level, similar to the dynamic loss in the Mn-Zn ferrite described above. The iron loss of the amorphous powder composite bulk core at 2 MHz frequency and 20 mT flux density amplitude is 0.94 W/cc (940 kW/m^3), which is about 1/6 of Ni-Zn ferrite with a specific permeability of 20 and 1/3 of Ni-Zn ferrite with a specific permeability of 40. It shows low permeability in the MHz band and low iron loss characteristics surpassing those of the benchmark Ni-Zn ferrite.

b. Printed and coated fine-particle composite cores

Printing method carbonyl iron powder composite core

Magnetic cores can be fabricated by the printing method by mixing magnetic particle powder and resin precursor to form a paste Yazaki et al. A prototype composite core for a built-in inductor was produced by the printing process. **Figure 2.1.3.22** shows a cross-section of the printed carbonyl iron powder composite core. The carbonyl iron powder composite core was fabricated using a mixed paste whose viscosity was adjusted to a metal mask printable by adjusting the amount of carbonyl iron powder. The upper limit of the powder filling ratio of the magnetic core was 54 % when the paste viscosity was adjusted to a metal mask printable viscosity. The saturation magnetization and coercive

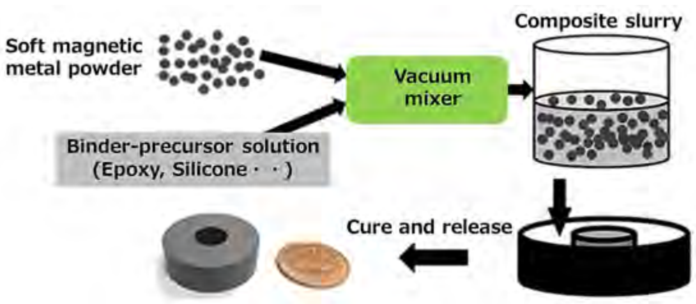

Fig. 2.1.3.20 Fabrication procedure of composite bulk magnetic cores by casting method

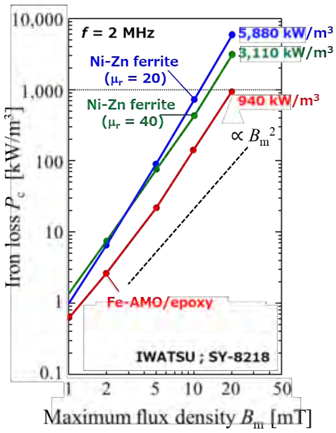

Figure 2.1.3.21 Dependence of iron loss of Fe-Si-B-Cr-C amorphous powder composite bulk magnetic cores on magnetic flux density amplitude, based on Ref.(54)

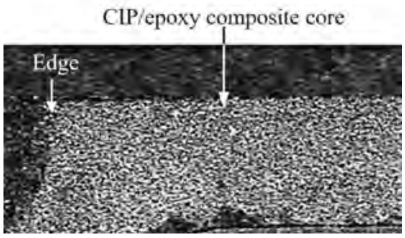

Figure 2.1.3.22 Cross section of a printed carbonyl iron powder composite core, based on Ref. (55)

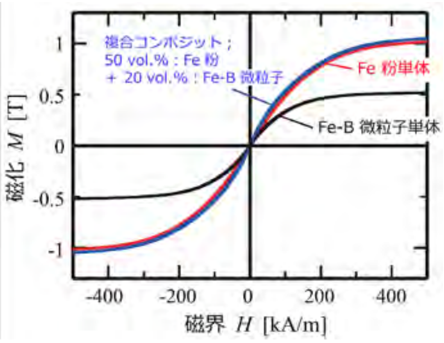

Fig. 2.1.3.23 Static magnetization characteristics of composite magnet cores made of Fe powder alone, Fe-B fine particles alone, and 50 vol.% Fe powder and 20 vol.% Fe-B fine particles, based on Ref.

force at the upper limit of 54 % powder filling ratio are 1.08 T and 2,000 A/m, respectively, and the upper limit of the magnetic field of constant magnetic susceptibility is about 80 kA/m. The specific permeability is about 7.5, which is almost constant up to 500 MHz, and the tanδ is about 0.03 at 100 MHz and 0.2 at 1 GHz, which means that it can be used as a low permeability and low loss magnetic core up to several hundred MHz.

Composite core of soft magnetic particle composite with composite orientation by coating method

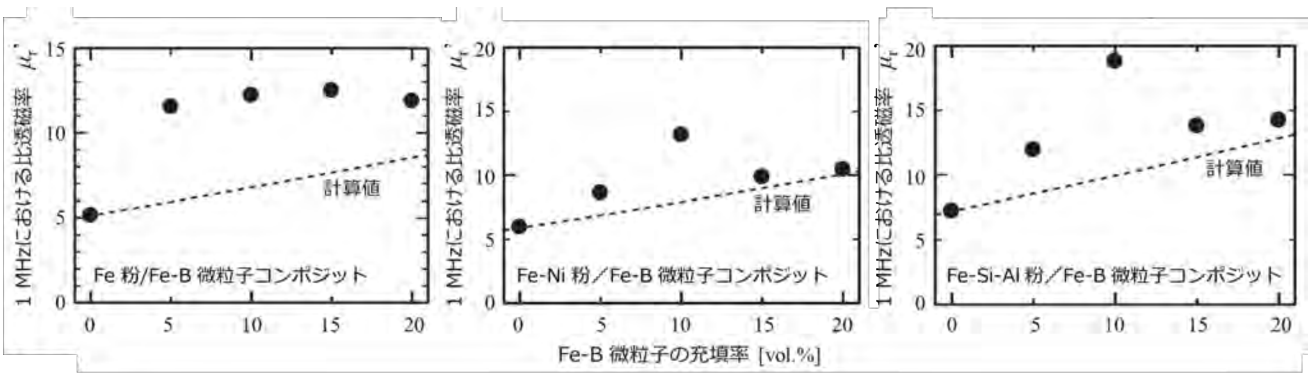

Figure 2.1.3.24 Relationship between magnetic permeability and Fe-B particle filling ratio of composite composite magnetic cores made of μm-class Fe, Fe-Ni, and Fe-Si-Al powders and sub-μm diameter Fe-B amorphous particles, μm-class powder filling ratio; 50 vol. % constant, based on reference (56)

Wakabayashi et al. of Tohoku University [56] fabricated a composite magnetic core using three kinds of μm -class powders (electrolytic iron powder with a grain size of 12 μm, Fe-Si-Al and Fe-Ni powders with a grain size of 3 to 5 μm) and sub μm -diameter amorphous Fe-B fine particle powder [45], and reported detailed magnetic properties. The core was fabricated by a coating method similar to the printing method, in which μm-class powder and sub μm -diameter amorphous Fe-B fine particles were dispersed and mixed in resin, coated on a polyimide resin substrate, and then oriented by applying a maximum magnetic field of 300 mT using an electromagnet until the resin hardens. When the Fe-B particle filling ratio is 5 vol.%, the Fe-B particles follow the magnetic flux flow generated between the Fe powders and enter the gaps between the Fe powders. On the other hand, when the filling ratio of Fe-B fine particles is 20 vol.%, Fe-B fine particles agglomerate not only between Fe powders but also among Fe-B fine particles. **Figure 2.1.3.23** shows the magnetostatic properties of composite magnetic cores made of Fe powder alone, Fe-B fine particles alone, and 50 vol.% Fe powder and 20 vol.% Fe-B fine particles. Similar results are obtained when Fe-Si-Al powder is used as a μm class powder, although the saturation magnetization is lower. **Figure 2.1.3.24** plots the change in specific permeability at 1 MHz for 50 vol.% Fe powder, Fe-Ni powder, and Fe-Si-Al powder with varying the Fe-B particle content from 0 to 20 vol.%. The dashed line in the figure is derived from Bruggeman's equation [57] and represents the estimated value when the filling ratio of μm-class powder alone is increased; the addition of Fe-B fine particles reduces the antimagnetic field of μm-class powder, resulting in a higher specific magnetic permeability than the value estimated by Bruggeman's equation for μm-class powder alone. In all cases, the maximum permeability is generally observed around 10 vol.% Fe-B fine particles.

These results indicate that the application of a magnetic field during resin hardening causes the Fe-B fine particles to move in a direction that reduces the antimagnetic field of the μm-class powder (in the direction of reducing the static magnetic energy), contributing to an improved powder fill ratio and higher magnetic permeability of the composite magnetic core.

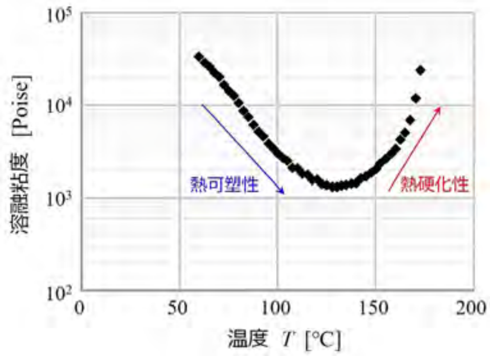

Figure 2.1.3.25 Relationship between melt viscosity and heating temperature of As made composite sheet with 3.5 μm diameter nanocrystalline powder 70 vol.% and 0.7 μm diameter Fe-Si-Cr particles 5 vol.% as filler, based on reference (58)

c. Fine particle composite sheet magnetic cores

Fine spherical powder composite sheet core

Oyama et al. [58] developed a fine spherical powder composite sheet core for organic interposers. The build-up sheet of the organic interposer is a 50-100 μm thick film of several μm diameter silica (SiO_2) filler dispersed in epoxy resin. We have fabricated composite sheet magnetic cores using various combinations of fine magnetic powders, including 3 to 5 μm-diameter crystalline Fe-Si-Cr, Fe-Si-B-Cr amorphous, Fe-Si-B-Nb-Cu-Cr nanocrystalline, Fe-Si-Cr and Mn-Zn ferrite as sub-μm-diameter particles to improve filling ratio. We are developing prototypes of composite sheet magnetic cores.

A specially prepared epoxy resin common to silica filler build-up film ABF for organic interposers is employed. **Figure 2.1.3.25** shows the relationship between melt viscosity and heating temperature for an as-made composite sheet with 70 vol.% 3.5 μm diameter nanocrystalline powder and 5 vol.% 0.7 μm diameter Fe-Si-Cr particles as filler. As made composite sheet with a filler of 5 vol.

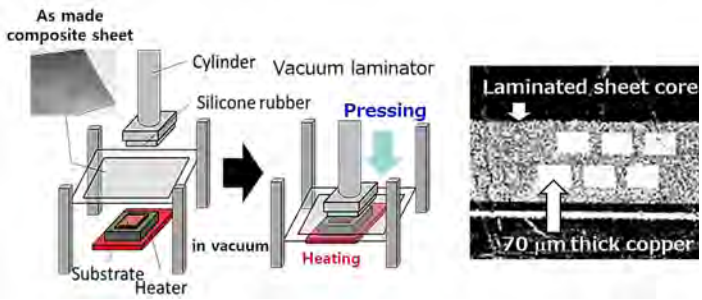

Figure 2.1.3.26 Example of forming a composite sheet magnetic core using a vacuum hot press laminator and cross sectional structure of a double-layer conductor embedded in a composite sheet magnetic core, based on Ref. (59)

Figure 2.1.3.26 shows an overview of forming a composite sheet magnetic core using a vacuum hot press laminator [59]. The sheet is heated at the temperature at which the sheet viscosity is minimized in a vacuum and decompressed atmosphere, and pressure is applied to soften the sheet and flatten the irregularities in the wiring conductor. Finally, the epoxy resin is cured by heat treatment (e.g., 190 °C) to complete the process. The cross-sectional structure of a two-layer conductor embedded in a composite sheet magnetic core using this method is shown in the figure.

Table 2.1.3.2 shows the specifications of the magnetic powders employed in the fine-grained composite sheet magnetic cores [58]. Saturation magnetization and coercive force have a trade-off relationship, and the nanocrystalline system has the lowest saturation magnetization (1.25 T) but the lowest coercive force.

Table 2.1.3.3 shows the magnetic properties of composite sheet magnetic cores fabricated with three different fine particle powders in an organized manner [58]. The cores were fabricated with three different powder fillings of 70, 75, and 80 vol.%. The coercive force of the composite sheet core is slightly smaller than that of the powder permeability, but reflecting the relationship between the permeability of the powder and the composite sheet core, the coercive force of the Fe-Si-Cr crystalline powder composite sheet core is the largest and that of the nanocrystalline powder composite sheet core is the smallest. The permeability at 100 MHz does not differ greatly among the three, being approximately 10, and is almost constant from the low-frequency region to 100 MHz. The loss factor tanδ of the composite sheet core using amorphous and nanocrystalline powders is less than half that of the Fe-Si-Cr crystalline powder composite sheet core, which is assumed to reflect the difference in electrical resistivity of the powders, considering that the powder sizes are almost the same.

Table 2.1.3.2 Specifications of magnetic powders employed in particulate composite sheet magnetic cores, based on Ref. (58)

fine powder	Fe-Si-Cr crystalline	Fe-Si-B-Cr-C amorphous	Fe-Si-B-Nb-Cu-Cr nanocrystal
Median diameter *D50*	3.2 μm 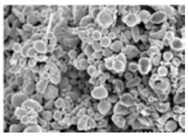	3.2 μm 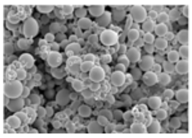	3.5 μm 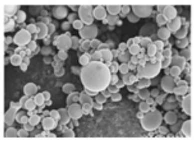
Saturation magnetization *Ms*	1.8 T	1.3 T	1.25 T
Coercive force *Hc*	1,482 A/m	148 A/m	92 A/m

Table 2.1.3.3 Magnetic properties of particulate composite sheet magnetic cores, based on Ref. (58)

Powder used	3.2 μm diameter Fe-Si-Cr crystalline			3.2 μm diameter Fe-Si-B-Cr-C amorphous			3.5 μm diameter Fe-Si-B-Nb-Cu-Cr nanocrystal		
Powder Fill Rate	70 vol. %, and	75 vol. %.	80 vol. % of	70 vol. %, and	75 vol. %.	80 vol. % of	70 vol. %, and	75 vol. %.	80 vol. % of
Coercive force *Hc*	1,080 A/m	1,120 A/m	1,180 A/m	141 A/m	151 A/m	180 A/m	72 A/m	76 A/m	78 A/m
Specific permeability μ_r' (100 MHz)	9.7	10.2	10.8	9.1	9.7	10.2	9.3	10.1	10.5
Loss coefficient tan δ (100 MHz)	0.1	0.105	0.105	0.04	0.045	0.046	0.038	0.039	0.042

Fe-Si-Al flat powder composite sheet core

As mentioned above, Fe-Si-Al flat powders with a coercive force of about 300 A/m have been put on the market [47][48] and are expected to be applied not only as quasi-microwave band noise suppression sheets but also as low-loss magnetic cores for magnetic elements.

Mikoshiba et al. [49] developed a composite sheet magnetic core for high-frequency inductors using Fe-Si-Al flat powder. The average diameter and thickness of the Fe-Si-Al flat powder are 40 μm and 1.5 μm, respectively. The powder filling ratio of the composite sheet core is 70 vol.%, and the horizontal orientation/perpendicular stacking of the flat powder is generally realized. **Figure 2.1.3.27** shows the frequency characteristics of the complex specific permeability of the Fe-Si-Al composite sheet core. The specific permeability in the horizontally oriented direction is approximately 280 and remains constant up to around 5 MHz. Chata'ni has developed a prototype thin inductor using a Fe-Si-Al flat powder composite sheet magnetic core [60], and has demonstrated a 12 V input -3.3 V and 18 A inductor developed at the Center for Power Electronics Systems (CPES) at Virginia Tech, USA [61]. -3.3 V, 18 A output 1 MHz step-down chopper DC-DC converter developed by the Center for Power Electronics Systems (CPES) at Virginia Tech in the U.S. [61].

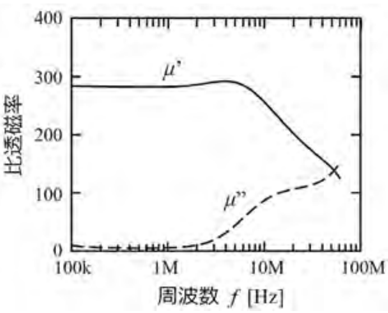

Figure 2.1.3.27 Frequency characteristics of complex specific permeability of Fe-Si-Al flat powder composite sheet magnetic cores, based on Ref. (49)

Fe-based nanocrystalline flat powder composite sheet magnetic cores

As mentioned above, Fe-Si-B and Fe-Si-P amorphous flat powders have a problem that the release of flat working strain is not sufficient even after strain removal heat treatment at temperatures close to the crystallization temperature, and the powder coercive force is about 1.5

to 2 times larger than that of Fe-Si-Al flat powders.

As mentioned above, Ying et al. [50] fabricated a prototype Fe-Si-B-Nb-Cu flat powder using roll-quenched thin strips as the starting material, and showed that the flat powder after nanocrystallization has a low coercivity of less than half that of Fe-Si-Al flat powder. It was shown that the flat powder after nanocrystallization has a low coercivity, less than half that of Fe-Si-Al flat powder, and that it may surpass the magnetic properties of Fe-Si-Al flat powder composite sheet magnetic cores when used in composite sheet magnetic cores. However, when flat powder laminated composite sheet cores are fabricated using low-coercivity nanocrystalline powders, the coercivity of the final composite sheet core increases due to residual distortion caused by pressurization during the process, and the characteristics of low-coercivity nanocrystalline alloys cannot be utilized.

Koike et al. [62] used amorphous flattened powder before nanocrystallization using a Finemet composition roll-quenched thin strip as the starting material, and employed a nanocrystallization heat treatment at the end of the fabrication process as a fabrication method for nanocrystalline flattened powder composite sheet magnetic cores. This method is almost the same as the aforementioned method of making Finemet-based Fe-based nanocrystalline magnetic powder cores [24], and is based on the idea that the internal strain in the material accumulated in the roll-quenched thin strip flattening and composite sheet core fabrication process is released in the final nanocrystallization heat treatment. The starting material, a thin strip of amorphous Finemet composition immediately after roll quenching, is 18 μm thick and 5 cm wide, and has some ductility and ductility (however, rolling is difficult), making it difficult to obtain flattened powder directly from the thin strip. After the brittle heat treatment at 400 ℃ for 3 hours, the powder is coarsely ground to 150 μm or less, and then flattened by a vibration mill (target thickness: 1 to 3 μm) to obtain a flat powder. **Figure 2.1.3.28** shows SEM photographs and X-ray diffraction patterns of the flattened powder. The footprint of the flattened powder is 100-200 μm, and the thickness is 1-3 μm, which is not shown here. The flat powder shows a halo XRD pattern characteristic of amorphous materials and retains its amorphous state after processing.

The fabrication process of Fe-based nanocrystalline flat powder composite sheet magnetic cores is as follows [62]. Shin-Etsu Chemical's two-component thermosetting silicone (KE-1031) was used as the binder, and toluene, which is highly compatible and volatile with silicone

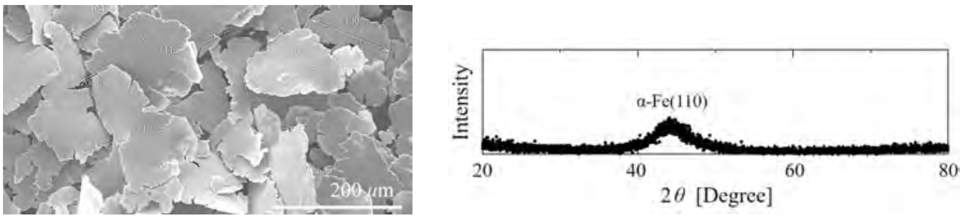

(a) SEM photograph (b) X-ray diffraction pattern

Fig. 2.1.3.28 SEM photograph of Finemet (Fe-Si-B-Nb-Cu) flat powder after flattening by vibrating mill, and X-ray diffraction pattern, based on Ref.

resin, was used as the diluent for viscosity adjustment. Flat powder paste for sheet forming was prepared.

The mixed paste was formed into sheets by metal mask printing using a 50 μm thick SUS303 metal mask, and then the toluene diluent was volatilized at 40 ℃-25 min on a hot plate. After that, pressure was applied using a 15-ton hot press for the purpose of horizontal orientation of the flat powder and removal of excess binder resin, and the silicone resin was thermally cured at 80 ℃ for 2 hours while the pressure was still applied. Nanocrystallization heat treatment was performed in five different ways using a muffle furnace at 515 ℃, 530 ℃, 545 ℃, 560 ℃, and 575 ℃. At all heat treatment temperatures, flattening was performed. The grain size of the flat powder was estimated to be approximately 14 nm at all heat treatment temperatures. Since heat treatment at 500 ℃ or higher causes the silicone resin binder to denature into silica and embrittle the composite sheet core, the silicone resin is impregnated and hardened under reduced pressure to obtain the flat powder composite sheet core. **Figure 2.1.3.29** shows a cross-sectional SEM photograph of the fabricated Fe-based nanocrystalline flat powder composite sheet core. The saturation magnetization of the Fe-based nanocrystalline flat powder composite sheet core is approximately 0.5 T, which is 45 vol.% in terms of powder filling ratio. **Figure 2.1.3.30** shows the relationship between the final nanocrystallization heat treatment temperature and the coercive force of the magnetic core. Therefore, the increase in coercive force with increasing heat treatment temperature is assumed to be due to the increase in magnetostriction. **Figure 2.1.3.31** shows the frequency characteristics of the specific permeability of Fe-based nanocrystalline flat powder composite sheet magnetic cores heat-treated at various temperatures. For example, heat treatment at 530 ℃ produces a permeability close to 500, which is not achieved with Fe-Si-Al flat powder,

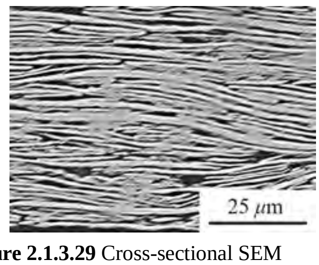

Figure 2.1.3.29 Cross-sectional SEM photograph of Fe-based nanocrystalline flat powder composite sheet magnetic core,

but after 3 MHz, the permeability decreases as the frequency increases. Composite sheet cores at heat treatment temperatures of 560 ℃ and 575 ℃ have permeabilities of 100 and 50, respectively, which are almost constant up to 10 MHz. **Figure 2.1.3.32** shows the frequency characteristics of iron loss at a flux density amplitude of 20 mT for an Fe-based nanocrystalline flat powder composite sheet core at a nanocrystallization heat treatment temperature of 560 ℃. For comparison, a Fe-Si-Al flat powder composite sheet core, Fair Rite's Ni-Zn The Fe-based nanocrystalline flat powder composite sheet core has lower iron loss over a wider frequency range than the other two.

Subsequently, the Fe-based nanocrystalline flat powder composite sheet magnetic core was employed in a surface-mount coupled inductor for a 24 V input-12 V, 2.5 A output 12 MHz switching two-phase Buck converter for USB PD [63].

Flat powder-laminated composite sheet magnetic cores after nanocrystallization heat treatment are not flexible and can only be used in sheet form, but the use of flexible pre-nanocrystallized sheets can be applied to a variety of core shapes such as toroidal-wound cores.

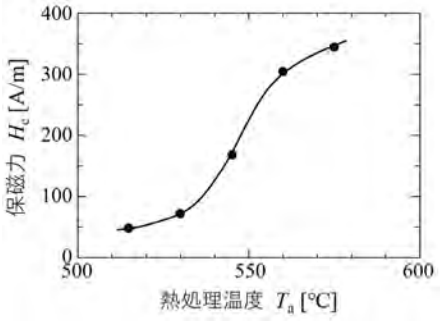

Figure 2.1.3.30 Relationship between final nanocrystallization heat treatment temperature and magnetic coercive force of Fe-based nanocrystalline flat powder composite sheet magnetic cores, based on Ref.(62)

1.3.4 Summary and Future Issues

Although there are various options for magnetic powder cores, such as crystalline, Fe-based amorphous, and Fe-based nanocrystalline, the most promising, apart from cost, is Fe-based nanocrystalline powder core, which has both high saturation magnetization and low iron loss, which are required for inductors. In particular, nanocrystalline powder cores are expected to make a significant contribution to the realization of innovative power electronics that take advantage of the characteristics of WBG power semiconductors such as SiC and GaN. In the future, it is desirable to establish mass production technology through further investigation of hot press forming methods.

Although there have been examples of composite magnetic cores using fine metallic powders that surpass Ni-Zn ferrite, which is the benchmark for Beyond MHz band magnetic cores, there are not many examples of practical applications, except for carbonyl iron powder composite bulk cores that are already on the market. In particular, low-cost fabrication of fine alloy powders with diameters ranging from a few micrometers to sub-μm is a major challenge. In the future, in addition to the establishment of low-cost fabrication technology for fine powder, further improvement of the properties of fine composite cores in the Beyond MHz band is desired.

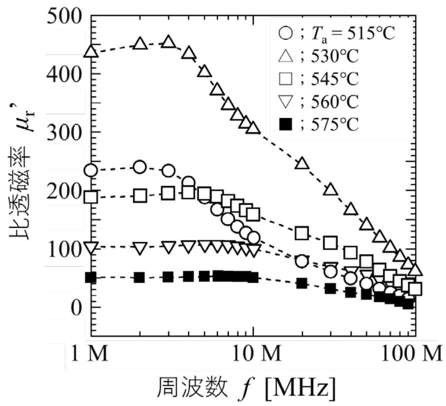

Figure 2.1.3.31 Frequency characteristics of specific permeability of Fe-based nanocrystalline flat powder composite sheet magnetic cores, based on Ref. (62)

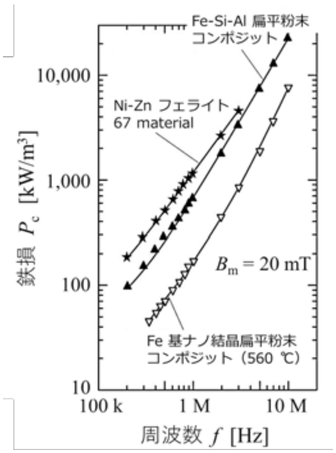

Figure 2.1.3.32 Frequency characteristics of iron loss of Fe-based nanocrystalline flat powder composite sheet magnetic cores with nanocrystallization heat treatment temperature of 560° C ($_{Bm=20}$ mT), based on Ref. (62)

[Toshiro Sato]

References

(1) K. Sugimura, Y. Miyajima, M. Sonehara, T. Sato, F. Hayashi, N. Zettsu, K. Teshima, and H. Mizusaki : "Formation of high electrical resistivity thin surface layer on carbonyl-iron powder (CIP) and thermal stability of nanocrystalline structure and vortex magnetic structure of CIP ", *AIP Advances*, Vol. 6, 055932, 8 pages. doi: 10.1063/1.4944705 (2016).

(2) Satoshi Mori, Takeshi Mitsuoka, Kanako Sugimura, Ryosuke Hirayama, Makoto Sonehara, Toshiro Sato, Nobuhiro Matsushi: "Core-shell structured Mn-Zn-Fe ferrite/Fe-Si-Cr particlesfor magnetic composite cores with low loss ", *Advanced Powder Technology*, Vol.29, No.6, pp.1481-1486. pp.1481-1486., DOI : 10.1016/j.apt.2018.03.012 (2018).

(3) Huang, H., M. Utsuno, S. Matsubara, and M. Mitomi: "Formation of Fayalite Used as Insulating Film for Magnetic Powder Core," Powder and Powder Metallurgy, Vol. 71, No. 2, pp. 47-50. DOI : 10.2497/jjspm.23-00057 (2024).

(4) Press Release: "Development of High Tg Epoxy Encapsulating Material for Next Generation SiC Power Module", Sumitomo Bakelite Company, Limited: http

s://www.sumibe.co.jp/topics/2024/it-materials/0522_01/index.html (2024).
(5) Shin-Etsu Silicone : "Raw materials for room temperature curing coatings", https://www.silicone.jp/guide/casestudy/06/.
(6) Shin Tajima: "Magnetic Composite Materials: Powder Core and Bonded Magnet", Corona, pp. 235-236, First edition, 1st printing (2023).
(7) Hiroki Hamakake, Shigeo Fujii: "Development of Nanocrystalline Magnetic Powder Core by Discharge Plasma Sintering", Hitachi Metals Technical Review, Vol.21, pp.39-44 (2005).
(8) Takahiro Isohata: "Low Melting Point Glass Vaneetect Series VS-1298M," Hitachi Chemical Technical Report, No.62, pp.23-24(2019).
(9) T. Masumoto and T. Yamamoto: "On the Magnetic and Electrical Properties of New Alloys 'Sendust' and Fe-Si-Al Alloys," Journal of the Japan Institute of Metals, Vol.1, No.3, pp.127-135 (1937).
(10) K. Takahashi, H. Arai, J. Tanaka, and N. Wakiyama: "Regular structure and crystal magnetic anisotropy of sendust alloy single crystals," Journal of the Magnetics Society of Japan, Vol. 10, No. 2, pp. 221-224. DOI.org/10.3379/jmsjmag.10.221 (1986).
(11) K. Takahashi, H. Arai, and N. Wakiyama: "Magnetostriction of Sendust alloy single crystals," Journal of the Magnetics Society of Japan, Vol. 11, No. 2, pp. 251-254., DOI.org/10.3379/jmsjmag.11.251 (1987).
(12) Yoshikazu AIKAWA and Nobuyuki KATO: "Effect of Composition on Loss of Fe-Si-Al Powder Core," Sanyo Tokushu Steel Technical Report, Vol.7, No.1, pp.29-34 (2000).
(13) Daido Bunseki Research Inc.: "Effect of Annealing Temperature on Coercivity of Soft Magnetic Powder Cores," https://daido-dbr.com/dbr/products/soft_magnetism.html (2025).
(14) Chio Ishihara, Tetsuya Ogawa, and Noriyuki Nakayama: "Powder Metallurgy Powder Core for Reactor and Motor," Hitachi Chemical Technical Report, No.62, pp.15-16(2019).
(15) Isamu Otsuka, Kimio Wada, Yu Maeta, Takeshi Kadomura, Masaaki Yagi: "Magnetic Properties of Fe-Based Amorphous Powders With High- Saturation Induction Produced by Spinning Water Atomization Process (SWAP) ", *IEEE Transactions on Magnetics*, Vol.44, No.11, pp.3891- 3894, DOI: 10.1109/TMAG.2008.2002249 (2008)
(16) Epson Atmix website: https://www.atmix.co.jp/products.html#products-powder.
(17) Isamu Otsuka, Masaru Maeda, Kazushi Ishiyama, Masaaki Yagi: "Properties of high flux density Fe-based amorphous soft magnetic powders and shaped magnetic cores," Powder and Powder Metallurgy, Vol. 56, No. 9, pp. 563-567, DOI.org/10.2497/jjjspm.56.563 (2009).
(18) Akihisa Inoue, Tao Zhang, and Tsuyoshi Masumoto: "Zr-Al-Ni Amorphous Alloys with High Glass Transition Temperature and Significant Supercooled Liquid Region", *Materials Transactions, Japan Institute of Metals*, Vol. 31, No. 3, pp. 177-183, DOI.org/10.2320/matertransans DOI.org/10.2320/matertrans1989.31.177 (1990).
(19) Akihisa Inoue, Baolong Shen: "Formation and Soft Magnetic Properties of Fe-B-Si-Zr Bulk Glassy Alloys with High Saturation *Materials Transactions, Japan Institute of Metals*, Vol. 43, No. 9, pp. 2350-2353, DOI.org/10.2320/ materialstrans.43.2350 (2002).
(20) Akihiro Makino, Takeshi Kubota, Chuntao Chang, Masahiro Makabe, Akihisa Inoue: "FeSiBP Bulk Metallic Glasses with Unusual Combination of High Magnetization and High Glass-Forming Ability *Materials Transactions, Japan Institute of Metals*, Vol.48, No.11, pp.3024-3027 MRP2007198, DOI.org/10.2320/matertrans.MRP2007198 (2007).
(21) Sintokogio Website: https://www.sinto.co.jp/product/magnetic-metal-powder/
(22) Takao MIZUSHIMA, Hisato KOSHIBA, Yutaka NAITO and Akihisa INOUE: " Magnetic Properties and Applications of Fe-Based Glass Liqualloy ™ Powder Cores," Powder and Powder Metallurgy, Vol.55, No.2, pp.146-148, DOI.org/10.2497/jjjspm.55.146 (2008).
(23) Y. Yoshizawa, S. Oguma, K. Yamauchi: "New Fe-based soft magnetic alloys composed of ultrafine grain structure", *Journal of Applied Physics*, Vol. 64, pp. 6044-6046, DOI.org/10.1063/1.342149 (1988).
(24) Takanori Kanaya, Ryosuke Ohta, Makoto Sonehara , and Toshiro Sato: "Fabrication of Fe-Based Nanocrystalline Powder-Pressed Magnetic Core and Application to Planar Reactor for Hundreds of kHz or Beyond", *IEEE Transactions on Magnetics*, Vol. 59, No. 11, 2801006, DOI:10. 1109/TMAG.2023.3286026 (2023).
(25) Akihiro Makino, He Men, Takeshi Kubota, Kunio Yubuta, Akihisa Inoue: "New Excellent Soft Magnetic FeSiBPCu Nanocrystallized Alloys With High *Bs* of 1.9 T From Nanohetero-Amorphous Phase", *IEEE Transactions on Magnetics*, Vol. 45, No. 10, pp. 4302-4305, DOI:10.1109/TMAG.2009 .2023862 (2009).
(26) Parmanand Sharma, Xin Zhang, Yan Zhang, Akihiro Makino: "Competition driven nanocrystallization in high Bs and low coreloss Fe -Si-B-P-Cu soft magnetic alloys", *Scripta Materialia*, Vol. 95, pp. 3-6, DOI.org/ 10.1016/j.scriptamat.2014.08.023 (2015).
(27) E.Dastanpour, M.H.Enayati, A.Masood V.Strom: "Crystallization behavior, soft magnetism and nanoindentation of Fe-Si -B-P-Cu alloy on Ni substitution", *Journal of Alloys and Compounds*, Vol. 851, 156727, DOI.org/ 10.1016/j.jallcom.2020.156727 (2021).
(28) T. Takahashi, K. Yoshida, Y. Shimizu, A. D. Setyawan, M. Bito, M. Abe, A. Makino: "Fe-Si-B-P-C-Cu nanocrystalline soft magnetic powders with high Bs and low core loss", *AIP Advances*, Vol. 7, 056111, DOI.org/10.1063/1.4978408 (2017).
(29) Takuoki Hozoku : "Development of New Atomization Technology", Materia, Vol.58, No.6, pp.336-337 (2019).
(30) Masato Kuno, Naoto Onishi, Makoto Yamaki, Yosuke Imano, Akiri Urata: "Magnetic Properties of High-Bs Fe84. 3B6P9Cu0.7 Nanocrystalline Alloy Powder", *Abstract of* 2023 *IEEE International Magnetic Conference*, DOI:10.1109/INTERMAG50591.2023.10265097 (2023).
(31) M. Kuno, N. Ono, Y. Imano, A. Urata, H. Oikawa, S. Okamoto: "Ultra-low core loss and high core saturation magnetization of nanocrystalline Fe-B-P-Cu powder cores fabricated by using a hot-press process", *Acta Materialia*, Vol. 294, 121159, DOI.org/10.1016/j.actamat.2025. 121159 (2025).
(32) Takanori KANAYA, Toshiro SATO, Makoto SONEHARA: "Fabrication of Magnetic Powder Core for High Frequency Charge Force Conversion with Low Coercive Force and Low Iron Loss," IEEJ Magnetics Research Meeting Materials, MAG-23-008, pp.39-43 (2023).
(33) Yaqiang Dong, Qikui Man, Jijun Zhang, Chuntao Chang, Run-Wei Li, Xin-Min Wang: "Fabrication of FePBNbCr Glassy Cores With Good Soft Magnetic Properties by Hot Pressing", *IEEE Transactions on Magnetics*, Vol. 51, No. 11, 2006704, DOI:10.1109/TMAG.2015.2446998 (2015).
(34) Peng Cao, Ying Liu, Jun Li, Jiao Du, Renquan Wang, Tingchuan Zhou: "Enhanced Magnetic Properties of Hot-Pressed Fe-Based Nanocrystalline Powder Cores With Low-Melted Glass-Modified Insulating," *IEEE Transactions on Magnetics*, Vol. 57, No. 4, 2800407, DOI:10.1109/TMAG. 2021.3057878 (2021).
(35) TECHNO-FRONTIER 2016: "Power Inductors Using Alps Electric and Other Companies' Proprietary Material Liqualloy," https://news.mynavi.jp/techplus/article/20160422-technofrontier2016_5/
(36) Keizo Ohta: "Fundamentals of Magnetic Engineering II", Kyoritsu Shuppan, First edition, 6th printing, p.363 (1976).
(37) Y. Sakaki and T. Sato: "Relationship between large amplitude loss and small amplitude parameter (tan δ) of magnetic cores for high frequency," IEICE Transaction C, Vol.J68-C, No.6, pp.462-467 (1985).
(38) BASF: "CARBONYL IRON POWDER", https://electronics-electric.basf.com/global/en/electronics/products/carbonyl_ iron_powder
(39) Yuichiro Sugawa, Kazuma Ishidate, Makoto Sonehara, and Toshiro Sato: "Carbonyl-Iron/Epoxy Composite Magnetic Core for Planar Power Inductor Used in Package-Level Power Grid", *IEEE Transactions* on *Magnetics*, Vol. 49, No. 7, pp. 4172-4175, DOI:10.1109/TMAG.2013. 2250925 (2013).
(40) M. Koeda, A. Harada, H. Ono, T. Ishikura, T. Kuroda, and E. Shigero: "Study on carbonyl iron powder for development of power inductors for high frequency," Journal of the IEEJ Basic, Material and Common Division, Vol. 131, No. 11, pp. 949-954, DOI.org/10.1541/ieejfms .131.949 (2011).
(41) Yoshihiko Yokoyama, Yousuke Suenaga, Torao Yamagata: "New atomization technology products fine amorphous metal powders". , *Powder Injection Moulding*, Inovar Communications Ltd.
(42) Toda Kogyo Web Site:https://www.todakogyo.co.jp/product/img/Resin_composite_soft_ferrite_powder-Flyer.pdf, https://www.todakogyo.co.jp/ product/img/ Electronic_parts_soft_ferrite_powder-Flyer.pdf

(43) Ibid: https://www.todakogyo.co.jp/rd/wet.html

(44) Y. Shimada, Y. Endo, M. Yamaguchi, S. Okamoto, O. Kitakami, Y. Imano: "Production of Magnetically Soft Submicron Particles From Aqueous Solutions and Characterization", *IEEE Transactions on Magnetics*, Vol. 45, No. 10, pp. 4298-4301, DOI:10.1109/TMAG.2009.202495 (2009).

(45) Keita Murata, Takamichi Miyazaki, Hiroshi Masumoto, and Yasushi Endo: "Static and dynamic magnetic properties of amorphous Fe-B soft magnetic particles," Special Transactions of the Magnetics Society of Japan, Vol. 5, No. 1, pp. 1-5, doi.org/10.20819/msjtmsj.21TR310 (2021).

(46) M. Sato, E. Yoshida, H. Sugawara, and H. Shimada: "Permeability and electromagnetic wave absorption properties of flattened sendust-polymer composites," Journal of the Magnetics Society of Japan, Vol. 20, No. 2, pp. 421-424, doi.org/10.3379/jmsjmag.20.421 (1996).

(47) Yoshikazu AIKAWA and Masaru YANAGIMOTO: "Effects of Powder Grain Size and Plastic Processing on Electromagnetic Wave Absorption Characteristics," Sanyo Tokushu Steel Technical Report, Vol.9, No.1, pp.59-63 (2002).

(48) Product Introduction: "Soft Magnetic Flat Powder for Noise Suppression Sheet," Sanyo Special Steel Technical Report, Vol. 23, No. 1, pp. 34-35 (2016).

(49) Shun Mikoshiba, Hiroshi Shima, Ken-ichi Chatani: "Development of Thin Magnetic Core Material for High Frequency Power Supply Using Soft Magnetic Metal Flat Powder," Proceedings of the 42nd Annual Meeting of the Magnetics Society of Japan, 13aC-3 (2018).

(50) Ying Yuan, Inagaki Yutaro, Nomata Ryu, Sonehara Makoto, Sato Toshiro: "Fabrication of Fe-based soft magnetic flake powders for flake- IEEJ Magnetics Society, MAG-21-046, pp.17-22 (2021).

(51) Kun Qian, Alexander S. Sokolov, Qifan Li, Chins Chinnasamy, Samuel Kernion, and Vincent G. Harris : "High Performance Metallic Amorphous Magnetic Flake-based Magnetodielectric Inductors," https://arxiv.org/pdf/1806.02486 (2018).

(52) Micrometals Home Page: https://www.micrometals.com/products/materials/rf/

(53) Christopher G. Oliver: "Powder Core Materials for Magnetic Components in GaN and SiC Power Devices", *2016 Applied Power* Electronics *Conference* (APEC2016), Industry Session, IS09.6, Long Beach, CA, USA (2016).

(54) Kanako Sugimura, Daisuke Shibamoto, Naoki Yabu, Tatsuya Yamamoto, Makoto Sonehara, Toshiro Sato: "Surface-Oxidized Amorphous Alloy Powder/Epoxy-Resin Composite Bulk Magnetic Core and Its Application to Megahertz Switching LLC Resonant Converter", *IEEE Transactions on* Magnetics *on Magnetics*, Vol. 53, No. 11, #2801406, DOI:10.1109/TMAG.2017.2718042 (2017).

(55) Yuichiro Yazaki, Kazuma Ishidate, Kazuhiro Hagita, Yuta Kondo, Saki Hattori, Makoto Sonehara, Toshiro Sato, Tetsuro Watanabe, Yuto Seino, Nobuhiro Matsushita: "Embedded planar power inductor in an organic interposer for package-level dc power gird", *IEEE Transactions on* Magnetics , Vol. 50, No. 1, pp. 3-24, 1985 . *on Magnetics*, Vol. 50, No. 11, #8401304, DOI: 10.1109/TMAG.2014.2327965 (2014)

(56) K. Wakabayashi, K. Murata, T. Miyazaki, H. Masumoto, and Y. Endo: "Study on Magnetic Properties of Composite Oriented Soft Magnetic Particle Composite Materials," Special Transactions of the Magnetics Society of Japan, Vol. 7, No. 1, pp. 11-15, doi.org/10.20819/msjtmsj.23TR513 (2023).

(57) R. Ramprasad, P. Zurcher, M. Petras, and M. Miller: "Magnetic properties of metallic ferromagnetic nanoparticle composites ", *Journal of Applied Physics*, Vol. 96, No. 1, pp. 519-529, doi.org/10.1063/1.1759073 (2004).

(58) Hideki Oyama, Nanami Kawada, and Toshiro Sato: "Magnetic Properties of Soft Magnetic Powder/Epoxy Composite Sheet", *IEEE Transactions on Magnetics*, Vol. 59, No. 11, # 2001205, DOI:10.1109/TMAG.2023.3288912 (2023).

(59) Toshiro Sato: "Fe-based Metal Composite Magnetic Core and Its Application to High-frequency Switching DC-DC Converter",. *2018 International Workshop on Power Supply on Chip*, NCTU, Hsinchu, Taiwan (2018).

(60) Ken'ichi Chata'ni: "Soft magnetic metal-flake composite material suitable for highly integrated power Modules", *2018 International Symposium on* 3D Power Electronics Integration *and* Manufacturing (3D PEIM2018), College Park, MD, USA (2018).

(61) Dongbin Hou, Yipeng Su, Qiang Li, Fred C. Lee: "Improving the Efficiency and Dynamics of 3D Integrated POL", *Proceedings of the 2015* Applied *Power* Electronics *Conference and* Exposition (APEC2015), pp. 140-145, Charlotte, NC, USA (2015).

(62) Kota KOIKE, Takanori KANAYA, Tomoya TADA, Makoto SONEHARA, Toshitaka MINAMISAWA and Toshiro SATO: "Magnetic properties and nanocrystallization heat treatment temperature dependence of magnetic properties of Fe-based nanocrystalline alloy flat powder laminated sheet cores," IEEJ Magnetics Research Meeting Materials, MAG-21-129, pp.39-44 (2021).

(63) Soichi Kimura, Kota Koike, Motohiro Kanai, Ryohei Miyata, Toshitaka Minamisawa, Kousuke Miyaji, Makoto Sonehara, and Toshiro Sato:" Fabrication of Fe-based Nanocrystalline Spherical and Flake Powder Composite Magnetic Cores for Tens of MHz and Their Application to Planar Power Inductor", IEEJ *Transactions on Fundamentals and Materials*, Vol. 144, No. 6, pp. 199-206, doi.org/10.1541/ieejfms.144.199 (2024).

1.4 Magnetic Property Measurement Methods

Keyword: Iron loss measurement, Minor loop, DC superposition characteristics

1.4.1 Magnetization curve and permeability

Measurement techniques for evaluating the dynamic properties of soft magnetic materials play an important role in the research and development of magnetic passive components for power electronics. The dynamic characteristics of soft magnetic materials are generally expressed by the magnetic permeability μ. However, as shown in Section 1.1 of this chapter, the value of μ is not uniquely determined, but varies depending on the magnetic field application history and measurement conditions because magnetic materials exhibit complex behaviors such as dependence on the magnetic field application history (magnetic hysteresis), frequency dispersion, and nonlinearity that depends on the operating point and excitation amplitude. It varies depending on the magnetic field application history, measurement conditions, and other factors. Among them, the μ values that are particularly important in power electronics technology are summarized in **Table 2.1.1.1** in Section 1.1 of this chapter. In addition, it is difficult for a single measurement technique to cover all the measurement conditions required for the development of power electronics technology in permeability measurement, so different measurement techniques must be used depending on the measurement conditions. Therefore, in the dynamic characterization of soft magnetic materials, it is essential to understand the principle of each measurement technique, the measurement conditions that can be covered, and the results obtained, and to comprehensively evaluate multiple measurement results for physical interpretation of the behavior of the sample to be measured.

(1) Classification of permeability in "Magnetization Dynamic Properties

Since the definition of the physical quantity to be measured is fundamental to the discussion of measurement technology, this section first discusses each μ value used to evaluate" magnetization dynamics" in power electronics technology. Section 1.1 of this chapter lists three μ values that are important in power electronics technology: initial permeability μ_i, incremental permeability μ_Δ, and differential permeability μ_{diff}. Their definitions are based on static magnetization curves, as described in Section 1.1.1, and are therefore entirely rigorous as "magnetostatic properties," i.e., magnetic permeability in the low-frequency limit. However, since this paper discusses permeability in AC excitation and their measurement techniques, it is necessary to consider two excitation conditions: a DC excitation field to determine the operating point and an AC excitation field to obtain magnetization dynamic characteristics. Therefore, as shown in **Table 2.1.4.1**, each μvalue is defined under different DC and AC excitation conditions, and it is especially important to note that there are two possible differential permeability μ_{diffs} with different physical meanings and purposes. In this paper, we distinguish between differential permeability 1 (μ_{diff1}) and differential permeability 2 (μ_{diff2}), and discuss the definition of each μ value shown in the table and the excitation conditions for the measurement.

Table 2.1.4.1 Typical permeability and excitation conditions used to evaluate "magnetization dynamics" in soft magnetic materials for power electronics

magnetic permeability	measured value	DC excitation field	AC excitation field		high-frequency magnetic permeability Measurement Technique*.
			amplitude (of vibration)	frequency (esp. of waveforms)	
Initial permeability (μ_i)	complex number	0	microscopic	broadband	2, 3, 4, 5, 6, 7, 8
Incremental permeability (μ_Δ)	complex number	any	finite	Below excitable frequency	2, 3, 4, 6, 8
Differential permeability1(μ_{diff1})	real number	any	finite	Below excitable frequency	2, 3, 4, 6, 8
Differential permeability2(μ_{diff2})	complex number	any	microscopic	broadband	2, 3, 4, 5, 6, 8

* : The measurement method corresponding to each number is described in section 1.4.2 of this chapter.

μ_i in magnetostatic characteristics is defined as the slope *dB/dH* at the origin of the initial magnetization curve, as shown in **Figure 2.1.1. 3**. The same mathematical definition applies to μ_i in AC excitation. Therefore, at the time of measurement, the sample is demagnetized, the DC excitation field is 0, and the amplitude of the AC excitation field, *dH*, is ideally infinitesimal, and in actual measurement, a small amplitude is used as long as sufficient detection sensitivity is obtained. On the other hand, the frequency can be measured over a wide bandwidth. At high frequencies, μ_i is generally complex because of the phase delay in the magnetization response.

Next, μ_Δ in magnetostatic characteristics is defined as the ratio $\Delta B/\Delta H$, where ΔB is the average change in magnetic flux density with respect to ΔH under the condition that the sum of a DC excitation field and a quasi-static excitation field ΔH with finite amplitude is applied. μ_Δ in AC excitation also follows the same definition except that ΔH is AC. Therefore, in actual measurement, in order to simulate the excitation conditions in actual operation of a power electronics circuit, a DC excitation field and an AC excitation field of finite amplitude are superimposed and applied, and $\mu\Delta=\Delta B/\Delta H$ is estimated by determining the average ΔB from the acquired minor loop. However, if this procedure is simply followed, the magnetic loss exhibited by the sample, i.e., the area of the minor loop, cannot be expressed. Therefore, in power electronics technology, μ_Δ is often expanded to a complex number by approximating the minor loop with an ellipse, and used as a physical quantity that includes the loss. The frequency is limited to the AC excitation field below which a finite ΔH can be generated.

Finally, the differential permeability is basically defined as the slope *dB/dH* of the tangent line at a point on the magnetization curve.

However, in AC excitation, there are two possible methods: software differentiation and hardware differentiation. First, μ_{diff1}, like μ_{Δ}, obtains a minor loop under excitation conditions that simulate actual operation and determines the slope at a point in the loop by software. Therefore, the measurement method used is the same as μ_{Δ}, and μ_{Δ} and μ_{diff1} can be considered as different minor loop analysis methods. However, μdiff1 is always a real number by definition and cannot represent losses. In power electronics technology, μdiff1 is often used as a parameter for analyzing the minor loop shape, for example, or as the permeability at a point on the magnetization curve, which is necessary to estimate the back EMF in large amplitude excitation. It should also be noted that μ_{Δ} and μ_{diff1} are often used synonymously in actual measurements.

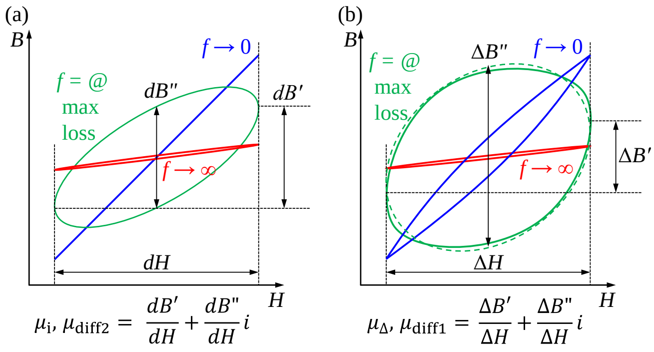

Figure 2.1.4.1 Examples of the variation of the minor loop shape with frequency and the correspondence of permeability μ with the loop shape. (a) for infinitesimal excitation amplitude dH and (b) for finite amplitude ΔH. In both figures, blue, green, and red correspond to frequencies $f \rightarrow 0$, f at maximum loss, and $f \rightarrow \infty$. The green dotted line in (b) is an elliptical approximation of the green solid minor loop

On the other hand, μdiff2 follows the same definition as μ_{diff} in mathematical terms, but in actual measurement, differentiation is performed by hardware. Specifically, a DC excitation field and an AC excitation field of small amplitude, *dH*, are superimposed and applied, and μ *is* estimated from the small-signal impedance. Therefore, as with μ_i, it can be measured over a wide bandwidth, and its value is generally complex. Because of this excitation condition, μ_{diff2} is not used in the evaluation of materials for magnetic passive components with large AC currents, but small-signal impedance with DC superposition may be required for EMI countermeasure components such as inductors for noise filters, and is important as an evaluation index It is important as an evaluation index of materials for such applications.

(2) Change in magnetization curve

In measurement techniques for measuring magnetic permeability in AC excitation, the excitation amplitude *dH* (at infinitesimal) or ΔH (at finite) and the frequency *f* are two particularly important parameters. The various measurement techniques described in this section measure μ *over* different excitation amplitudes and frequencies, and the results obtained depend on these parameters. In this section, we discuss the influence of these parameters on the measurement results. For simplicity of discussion, we assume only the magnetization process due to magnetic wall movement and do not consider other magnetization processes such as magnetization rotation.

First, consider μ_i or μ_{diff2} using **Figure 2.1.4.1 (a).** Since they are defined as the differential coefficient dB/dH, we can assume that *dH* is infinitesimal, in which case *dB is* proportional to *dH*. At low frequencies (f→0), the magnetic wall follows the magnetic field without delay, so the minor loop is a straight line as shown by the blue line, and μ is a real number. as *f*increases, the response of the magnetic wall to the magnetic field is delayed due to eddy currents and other dynamic behaviors described in section 1.1.2, and the resulting minor loop shape is an ellipse as shown by the green line. As a result, the minor loop shape becomes an ellipse as shown by the green line. In this case, *dB* becomes a complex number, and the change in *B*when *dH* is at its maximum amplitude and 0, that is, *dB'* and *dB" in* **Fig. 2.1.4.1 (a)**, are the real and imaginary parts. Therefore, μ is also a complex number, and its imaginary part corresponds to the loss term. As *f*increases, the magnetic walls stop responding to the magnetic field and only the vacuum contribution remains, so the minor loop collapses as shown by the red line, and μ approaches 1 asymptotically. In reality, however, as *f* increases, the mechanism of magnetization changes from magnetic wall movement to magnetization rotation and then to spontaneous resonance, and each mechanism shows a different frequency dispersion, so μ often does not monotonically approach 1.

Next, consider μ_{Δ} or μ_{diff1} using **Figure 2.1.4.1 (b).** As *f*increases, the loss due to dynamic behavior such as eddy currents is added , as in (a), and the hysteresis loss becomes larger. As f increases, losses due to dynamic behavior such as eddy currents are added as in (a), and the area of the minor loop increases, as shown by the green line. As *f*increases further, the minor loop collapses as shown by the red line because the magnetic wall becomes unresponsive. Since loss cannot be expressed by simply following the definition of μ_{Δ} as described above, in power electronics technology, in a series of minor loop shapes such as those shown in **Figure 2.1.4.1 (b)**, when loss is finite, as in the blue and green lines, μ_{Δ} can be expanded to a complex number by approximating it with an ellipse of the same internal area. This is often used as a physical quantity that includes the loss. This is the same as expressing magnetic loss as the phase lag component of magnetization at the fundamental frequency of the excitation field. On the other hand, as is clear from the shapes of these curves, minor loops generally take a shape different from an ellipse due to the nonlinearity of the magnetization characteristics, which means that there is a loss contribution due to harmonic components. Therefore, when analyzing the details of the loss mechanism, it is necessary to go back to the minor loop shape itself rather than a single complex value of μ_{Δ}.

(3) Effect of antimagnetic field

Before introducing the various measurement techniques, we will briefly discuss the influence of antimagnetic fields as a generally applicable point to note. In all permeability measurements, a magnetic field is applied to the sample to be measured to magnetize it, and the resulting magnetic flux change is detected. However, when a magnetic material is magnetized, an antimagnetic field is generated inside the sample in the direction opposite to that of magnetization, which reduces the magnetic field actually felt by the sample, resulting in a smaller magnetic flux change. This means that the effective magnetic permeability μ_{eff} actually measured is smaller than the original μ of the material. The ratio of magnetization to antimagnetic field in a uniformly magnetized sample is called the antimagnetic field coefficient, N_{D}, and is a second-order tensor, or matrix, determined by the sample geometry; N_{D} is constant regardless of the position inside the sample when the sample geometry is ellipsoidal and is a diagonalized matrix along its three principal axes. When the sample is not ellipsoidal, N_{D} varies with the position inside the sample. If the antimagnetic field coefficients along the three principal axes are N_x, N_y, and N_z, respectively, then $N_x + N_y + N_z = 1$ [(1)]. As an example, when a thin strip sample of thickness t is cut into a thin disk of diameter d (>> t) and magnetized in the transverse direction, the antimagnetic field coefficient Nz is approximately given by the following equations [(2) (3)].

$$N_z \approx 1 - \frac{3\pi}{4} \cdot \frac{t}{d} \tag{2.1.4.1}$$

Next, the in-plane antimagnetic field coefficient N_x is given by the following equation, since $2N_x + N_z = 1$ due to symmetry of the geometry.

$$N_x = 0.5(1 - N_z) \approx \frac{3\pi}{8} \cdot \frac{t}{d} \tag{2.1.4.2}$$

On the other hand, the effective permeability μ_{eff} of the sample for the magnetic susceptibility χ of the material and the antimagnetic field coefficient N_{D} in the direction of the applied magnetic field is given by the following equation

$$\mu_{\mathrm{eff}} = \frac{\chi}{1 + \chi N_{\mathrm{D}}} + 1 \tag{2.1.4.3}$$

This formula indicates that if $|\chi \mathrm{ND}| >> 1$, μ_{eff} converges to $\mu_{\mathrm{eff}} \to 1 / N_D + 1$ regardless of the original μ *of* the material, i.e., μ_{eff} is determined by the shape of the sample. Therefore, in order to correctly estimate the original μ of the material, it is necessary, for example, to prepare a sample with a size that satisfies $|\chi N_{\mathrm{D}}| \approx |\chi| \cdot 3\pi/8 \cdot t/d \ll 1$ the above-mentioned thin disk shape, or to accurately calculate the value of N_{D} and back-calculate μ from μ_{eff}. However, as for the sample shape, the typical thickness t of a thin strip sample produced by the melt span method is about several 10 µm, and to satisfy this condition for a soft magnetic material with a high μ of several 100 or more, the diameter d of the sample must be very large. In addition, as mentioned above, the antimagnetic field coefficient N_{D} varies depending on the position inside the sample when the sample shape is other than an ellipsoid, making it difficult to calculate the coefficient accurately. Therefore, in order to accurately measure high-μ materials without the influence of antimagnetic field, it is necessary to form a closed magnetic path so that the sample to be measured has $N_{\mathrm{D}} = 0$. Among the measurement methods described in Section 1.4.2 of this chapter, 1 and 8 can only measure the effective permeability μ_{eff} because the sample geometry is in principle impossible to form a closed magnetic path, and 6 can only measure the effective permeability μ_{eff} because it does not form a closed magnetic path if the magnetic core is not toroidal. 4 and 5 can only measure the magnetic resistance μ_{eff} because the return yoke forms a part of the magnetic path and its magnetic 3 can be measured by assembling the sample to be measured in a well-shaped configuration, 2 and 7 are usually toroidal samples, and 6 can be measured if the magnetic core is toroidal, since the sample forms a closed magnetic path, $N_{\mathrm{D}} = 0$ in both cases, and the intrinsic μ of the material can be measured without being affected by the antimagnetic field. The difference between the two methods is that each method is based on a different magnetic field. These differences will be explained in more detail in the overview of each measurement technique.

1.4.2 Magnetic permeability measurement method

Figure 2.1.4.2 shows the rough ranges of frequency and excitation field strength covered by the measurement techniques introduced in this section. Although it is desirable for magnetic passive components for power electronics to operate at higher frequencies and larger amplitudes, permeability measurement generally becomes more difficult with higher frequency and larger amplitude excitation, so various measurement techniques are used depending on the measurement conditions and purpose. In this section, the following eight measurement techniques are outlined as basic measurement techniques.

1. Vibrating sample magnetometer (VSM) [(4)-(6)]
2. 2-coil method (*M-H* loop tracer, *B-H* analyzer) [(7)(8)]
3. Epstein test (JIS C 2550-1) [(9)]
4. Single plate magnetic property test (JIS C 2556) [(10)(11)]
5. Ferrite Yoke Method [(12)]

6. Inductive method 1 [13]
7. Inductive method 2 [14]
8. AC magnetic susceptibility measurement method [15][16]

These measurement methods can be roughly classified according to their operating principles: 1 is mechanically vibrated and the electromotive force due to the velocity change is measured; 2, 3, 4, and 8 belong to the two-coil method, in which an alternating current is applied to the excitation coil to vibrate the magnetization of the sample and the electromotive force due to the magnetic flux change is measured using independent detection coils; 5, 6 and 7 belongs to the one-coil method, in which the magnetization of the sample is oscillated by an alternating current and the electromotive force due to the magnetic flux change is detected by the same coil. However, as shown in **Table 2.1.4.1** and **Figure 2.1.4.2** in this section, the measurement range and physical quantities that can be measured vary depending on the actual device configuration and sample shape, even if the measurement methods are based on the same principle.

(1) Vibrating sample magnetometer (VSM)

VSM is the most common measurement technique for measuring the static magnetization curve of a sample. **Figure 2.1.4.3** shows the principle diagram [4]-[6]. The sample is fixed to a rod and inserted between the poles of an electromagnet. When the sample is magnetized by applying a magnetic field generated by the electromagnet, a magnetic flux proportional to the magnetization of the sample is chained to the detection coil. When the rod is vibrated up and down by a shaker to change the chained magnetic flux, an induced electromotive force is generated in the detection coil, and a signal proportional to the magnetization of the sample can be obtained with high sensitivity by lock-in detection of the vibration frequency component. By performing this measurement while sweeping the applied magnetic field, a static magnetization curve is obtained, from which the various permeabilities defined in Section 1.1.1 of this chapter can be determined. Typical vibration frequencies for commercially available VSMs are around several 10 Hz. Note that this is the mechanical vibration frequency of the sample and not the vibration of the magnetization, so care should be taken not to confuse the two. In order to convert the detection signal to the absolute value of magnetization of the sample, the proportionality constant between the detection signal and magnetization is required, which is determined by measuring a standard sample whose saturation magnetization is known in advance (pure Ni is most commonly used).

VSM can measure not only solid samples, but also various types of samples by enclosing liquid or powder samples in the cell. The applied magnetic field can be up to 3 T for room temperature magnets and up to 18 T for superconducting magnets. The VSM has high sensitivity because it eliminates external noise by lock-in detection, and it is capable of measuring magnetization at a low magnetic field of up to 10 The VSM has high sensitivity due to its lock-in detection that eliminates external noise, and magnetization measurements with a magnitude of about 10^{-9} A-m^2 ($=10^{-6}$ emu) have been reported. Therefore, VSMs are used not only for ferromagnetic materials but also for extremely weakly magnetized materials such as paramagnetic and antimagnetic materials.

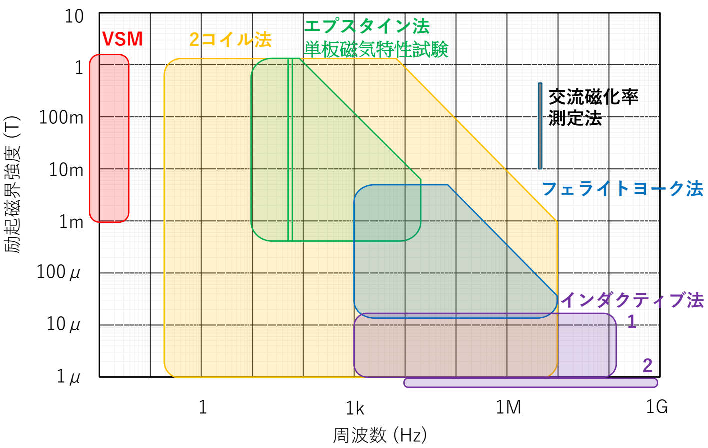

Figure 2.1.4.2 Rough measurement ranges for various permeability measurement methods

As mentioned above, the VSM is extremely versatile in the measurement of static magnetization curves, but there are some points to note when measuring soft magnetic materials for power electronics. First, the magnetic field sweep speed of the VSM depends on the time constants of the electromagnet and lock-in detection, and takes several tens of seconds per sweep at the fastest, making it almost impossible to obtain the dynamic behavior of magnetization. Another point is that it is impossible for the sample to form a closed magnetic path due to the structure of inserting the sample between the poles of an electromagnet, and since the pole spacing of a VSM is usually a few centimeters and the sample size must be smaller than that to be inserted, the influence of antimagnetic fields is inevitable for a sample with high μ and thickness. Specifically, the coercive force H_c is not affected by the antimagnetic field

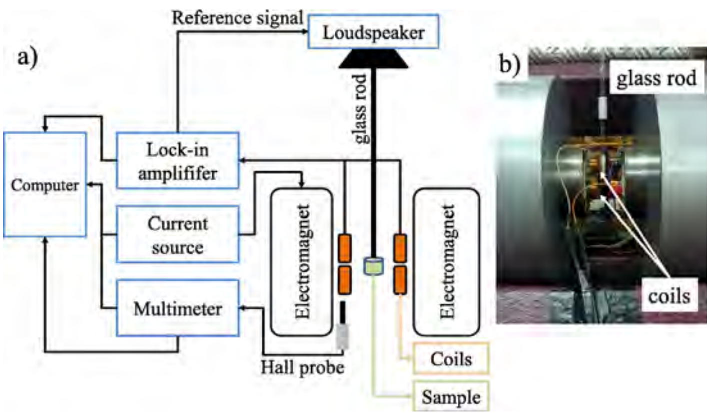

Figure 2.1.4.3 Block diagram of the VSM and photographs around the

because it does not occur if the magnetization of the sample is zero. If a sufficiently strong magnetic field is applied so that the sample is completely saturated, the saturation flux density B_s can also be correctly evaluated. However, since the shape of the *B-H* curve is affected by the antimagnetic field, the residual flux density B_r and various permeabilities such as μ_i, μ_{diff}, and μ_Δ are affected. To measure the initial magnetization curve, the sample must be demagnetized, and the AC demagnetization method, in which a damped oscillating magnetic field is applied, is usually used. However, it is not possible to generate such a magnetic field with the electromagnets of the VSM, so it is difficult to measure the initial magnetization curve and μ_i with the VSM alone.

(2) Two coil method (*M-H* loop tracer, *B-H* analyzer)

Commercial measurement devices based on this method are generally called *M-H* loop tracers or *B-H* analyzers [7][8]. As shown in the principle diagram in **Figure 2.1.4.4**, an excitation coil and a detection coil are wound around a toroidal-shaped sample, and a magnetic field *H* given by the following equation is applied in the circumferential direction to the sample by passing a current *i*through the excitation coil.

$$H = \frac{N_1 i}{l} \tag{2.1.4.4}$$

This magnetizes the sample and generates a voltage proportional to the time derivative of the magnetic flux at the detection coil, which is integrated by an integrating circuit consisting of an operational amplifier, resistor *R* and capacitor *C*. The magnetic flux density *B* of the sample is estimated from the output voltage V_{OUT} of the integrating circuit by the following equation.

$$B = \frac{CR}{N_2 A} V_{\mathrm{OUT}} \tag{2.1.4.5}$$

Therefore, by measuring *B* while changing *i*, a *B-H* curve can be obtained. Since both excitation and detection are purely electrical and do not use large electromagnets or shakers as in VSM, this measurement method can cover the widest range of measurement conditions, from low to high frequency and from small to large amplitude excitation. For example, with high-μ materials such as permalloy and sendust, a static magnetization curve similar to that of VSM can be obtained by applying a low-frequency, low-amplitude current to the excitation coil to slowly magnetize the sample and detecting the resulting magnetic flux change. On the other hand, it is also possible to measure the *B-H* curve of a sample under conditions similar to actual operation in a power electronics circuit, such as applying a high-frequency, large-amplitude current to the excitation coil or a superposition of AC and DC currents. When the sample has a toroidal shape, it is not affected by the antimagnetic field in principle, and therefore, the original μ *of the* material can be obtained, which is another advantage compared to VSM.

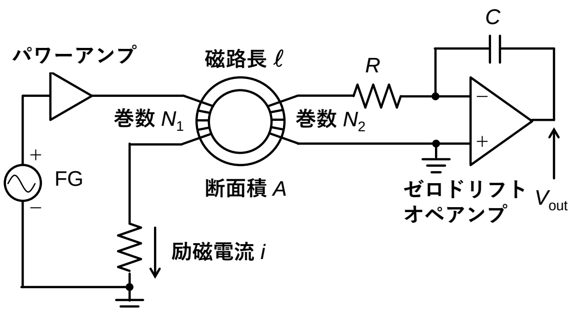

Figure 2.1.4.4 Principle of the two-coil method [8]

The following are some points to note about this method. First of all, it is time-consuming to prepare for the measurement because coils are wound around each toroidal-shaped sample to be measured. In addition, it is necessary to select the optimum wire diameter and number of coils depending on the measurement conditions. For example, if an AC current of large amplitude or a large DC current is applied to the excitation coil to measure DC superposition characteristics, it is necessarily necessary to use a large wire. Furthermore, when the AC current has a large amplitude and high frequency, a large induced electromotive force is applied to the excitation coil, so care must also be taken to insulate it. Conversely, when measuring characteristics at low frequencies, the induced electromotive force generated in the detection coil is proportional to the frequency and the number of windings, so it is difficult to detect signals with a sufficient signal-to-noise ratio unless the number of windings N_2 is increased to increase the detection voltage.

The voltage generated in the detection coil is proportional to the time variation of all flux linkages. If the μ*of* the sample is high and the cross-section of the sample occupies a sufficient proportion of the detection coil cross-section, there is no problem because the magnetic flux of the sample is dominant. However, if the μ of the sample is low and the cross-sectional area is much smaller than the detection coil cross-section due to the foil or thin film shape of the sample, the magnetic flux generated by the excitation coil and linked directly to the detection coil without passing through the sample must be subtracted . The contribution of the magnetic flux generated by the excitation coil and directly linked to the detection coil without passing through the sample should be subtracted. The magnetic field and flux distribution by the excitation coil depend on the winding method, but even if the sample geometry is the same, it is sometimes difficult to wind coils exactly the same way on multiple samples, which tends to reduce the reproducibility of measurement from sample to sample, especially for *low-micro* size samples.

(3) Epstein test

The Epstein test is the most basic magnetic measurement method for electromagnetic steel sheets, standardized by JIS C 2550-1 [9]. As shown in **Figure 2.1.4.5**, several 30 × 280 mm strip-shaped specimens are inserted into an Epstein measuring frame equipped with an excitation coil (primary coil) to excite the specimen and a detection coil (secondary coil) to detect magnetization, forming a closed magnetic path. The magnetic field intensity is obtained from the current value flowing in the excitation coil, and the magnetic flux of the sample is obtained from the voltage induced in the detection coil to measure the *B-H curve* and estimate various magnetic properties such as permeability and iron loss. Although this measurement method is, in principle, a two-coil method, it is a standard measurement method for soft magnetic materials and is used to obtain magnetic properties in commercial transactions because the Epstein measuring frame is pre-equipped with primary and secondary coils, there is no need to coil each sample, the sample size and number of coils are specified by the thickness of the sample to be measured, and the measurement is highly repeatable. This method is used to obtain the magnetic properties of soft magnetic materials during commercial transactions. This method is standardized for measuring magnetic permeability at 50 / 60 Hz, the frequency of commercial power supplies, but the frequency band can be extended to about 20 kHz. For details of this measurement method, see reference [9].

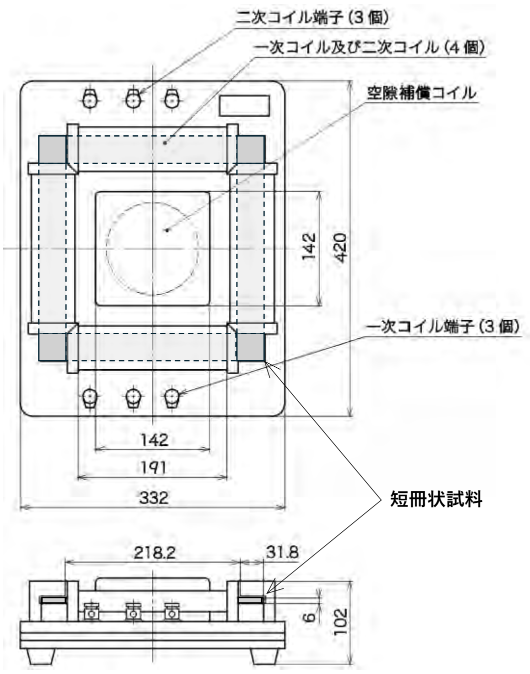

Figure 2.1.4.5 Epstein Tester [9]

In this figure, the sample is changed to gray and a label and arrow are added in the original figure (Figure JA.2 in Reference [9]) to clearly indicate the sample insertion position.

(4) Single plate magnetic property test

The Epstein test requires a large number of samples to be assembled in a well-shaped assembly, so it is not possible to evaluate variations among samples or to measure changes in magnetic properties when samples are subjected to stress. The single plate magnetic property test makes these things possible. As shown in **Figure 2.1.4.6**, the sample to be measured is inserted into the coil, and both ends are sandwiched by a yoke with high magnetic permeability and a cross-sectional area sufficiently larger than the sample to form a closed magnetic path. The coil is double-layered, and an electric current is applied to the excitation coil to magnetize the sample, and the magnetic flux change is detected by the detection coil. The basic principle of this measurement method is the two-coil method, and if the magnetic resistance of the yoke is sufficiently smaller than that of the sample, the original μ of the sample can be obtained. The structure and materials of the coil and yoke, sample size, and measurement conditions are specified in JIS C 2556, and this method is widely used as one of the standard measurements for magnetic materials [10]. However, measurement devices with various extensions are also used in the research and development of soft magnetic materials, such as extending the frequency band to higher frequencies, applying stress to the sample, and using a ferrite yoke to reduce loss and increase the accuracy of loss evaluation of the sample [11]. For details of this measurement method, please refer to references [10] [11].

(5) Ferrite yoke method

Of the measurement methods described above, (2) to (4) are two-coil methods, i.e., a measurement system in which the magnetization of the sample and the detection of the magnetic flux change are performed using independent excitation and detection coils, respectively. However, as a simpler method, a single coil can be used for both excitation and detection. In the ferrite yoke method, as shown in **Figure 2.1.4.7,** a ferrite yoke is

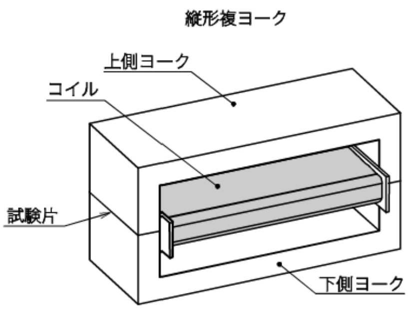

Figure 2.1.4.6 Single Plate Magnetic Property Tester [10]

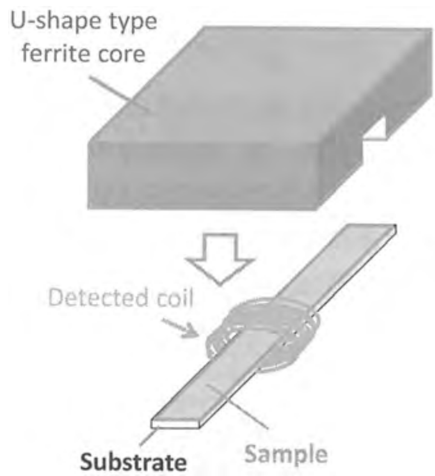

Figure 2.1.4.7 Principle of ferrite yoke method permeability measurement [12]

placed in contact with both ends of a strip sample to form a closed magnetic path by magnetically short-circuiting the sample, and μ is estimated by measuring the impedance of the ferrite or the coil wound around the sample. In principle, the coil can be wound on the ferrite yoke side or inserted into a pre-wound coil, but the latter is more common because it is easier to measure even if the ferrite yoke and sample are small. By using a ferrite yoke with high resistivity, eddy current loss is suppressed up to high frequencies, preventing a decrease in permeability. This method is often used for permeability measurements in the frequency range up to about 10 MHz, where eddy current losses in the ferrite yoke are not a problem.

This measurement method is often combined with an impedance analyzer or LCR meter, in which case the current flowing through the coil is small, at most several 10 to several 100 mA. If combined with a *B*-*H* analyzer or a high power high frequency amplifier, it is possible to measure μ_Δ and μ_{diff1} with high amplitude excitation, but in this case, the temperature of the ferrite yoke rises due to excitation, which may change its magnetic characteristics. In this case, however, the temperature of the ferrite yoke rises due to excitation, which may change its magnetic characteristics.

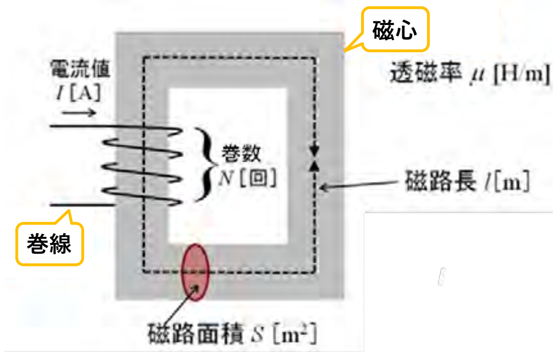

Figure 2.1.4.8 Principle diagram of inductive method 1 (13)

(6) Inductive method 1

The method of estimating the magnetic properties of a magnetic core by winding a coil around the magnetic core to be measured and measuring its inductance is generally called the inductive method. There are two main methods.

One method is to form an inductor by winding a coil around a magnetic core of the actual shape to be used, and measure its inductance using an LCR meter or an impedance analyzer (13). This method is the simplest and most direct when the purpose of the measurement is not to evaluate the material characteristics of the magnetic core but to evaluate the characteristics of the inductor as a passive element. General LCR meters and impedance analyzers can usually measure only μ_{i} and μ_{diff} by small-amplitude excitation, since the maximum AC current to the element under test is several 10 to several 100 mA and the measurable element voltage is several V. However, the measurement of a few to several 10 A is not possible with a direct current of several 10 A. However, there are models that can apply a DC bias current of several to several tens of A, so DC current superposition characteristics can be measured over a wide range by using such devices. If you wish to evaluate only the characteristics of the magnetic core, you can first saturate the core by applying a sufficiently large DC bias current and measure the inductance of the coil alone, then measure the inductance of the core when it is not saturated and subtract the inductance of the coil from it to separate the contribution of the magnetic core.

When the magnetic core forms a closed magnetic path as shown in **Figure 2.1.4.8**, $N_{\mathrm{D}} = 0$. If the contribution of the magnetic core to the inductance is L, the intrinsic permeability μ of the material can be estimated from the following equation.

$$\mu = \frac{Ll}{N^2 S} \tag{2.1.4.6}$$

This method is simple in principle, but because the excitation and detection coils are common, the voltage observed at the coil winding terminals includes not only the electromotive voltage caused by the magnetic flux change but also the voltage caused by the resistance component of the winding, making it difficult to separate the iron loss from the copper loss and limiting measurement accuracy. In addition, as mentioned above, ordinary LCR meters and impedance analyzers can only handle small-amplitude AC signals, and to measure large-amplitude excitation, it is necessary to construct a custom measurement device equipped with a high-output RF amplifier, which is not necessarily inexpensive or simple. When evaluating the dynamic characteristics of a magnetic core with high precision and large amplitude excitation, the two-coil method is often more advantageous. On the other hand, the one-coil method is often more advantageous above 10 MHz because the effect of interwinding capacitance becomes apparent at higher frequencies with the two-coil method.

(7) Inductive method 2

Another inductive method uses a short-circuit terminated coaxial-shaped jig as shown in **Figure 2.1.4.9** (14). The impedance of the toroidal sample is measured with and without the toroidal sample inserted at the tip of the jig, and the permeability μ of the sample is estimated from the difference using the following equation.

$$\mu = \frac{(Z_{\mathrm{m}} - Z_{\mathrm{sm}})2\pi}{j\omega h \ln(c/b)} + 1 \tag{2.1.4.7}$$

This measurement method is basically a one-coil method with only

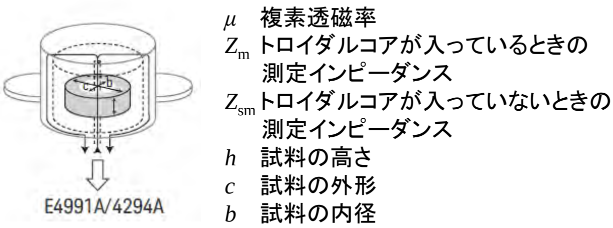

Figure 2.1.4.9 Jig Structure for Inductive Method 2 (14)

one turn of winding on the toroidal core, but it can also be considered as a system in which the end of a short-circuit terminated coaxial transmission line is filled with a medium having a finite permeability. At the short-circuit termination plane, the electric field is zero while the magnetic field is maximum, and their distribution follows a simple electromagnetic field theory, so the magnetic permeability of the medium can be calculated with high accuracy. The natural logarithm in the denominator of equation (2.1.4.7) is due to the fact that the magnetic field generated by a conductor passing through its center is inversely proportional to the radial distance from the center when the inner and outer diameters of the sample are very different, so the distribution is integrated from the inner to outer diameters of the sample. In the limit where the inner and outer diameters are close, i.e., the sample width is narrow and the magnetic field intensity can be considered constant, equation (2.1.4.7) converges to equation (2.1.4.6). Since the sample has a toroidal shape, N_D = 0. This has the advantage of eliminating the influence of the antimagnetic field and allowing the measurement of the sample's original μ with high precision. The measurement bandwidth depends on the size of the sample, but it can be up to 1 GHz when using an impedance analyzer, which is the usual combination.

However, because the number of windings is one turn and the output of the base impedance analyzer is as small as 1 dBm (1.3 mW) at maximum for a 50 Ω load, only μ_i can be measured with small amplitude excitation, and DC current superposition characteristics cannot also be measured. Also, due to the small number of windings, measurement accuracy is greatly reduced under conditions where impedance is low, such as low μ, thin samples, and low frequencies.

(8) AC magnetic susceptibility measurement method

As mentioned at the beginning of this section, magnetic materials exhibit inherently nonlinear behavior, so their dynamic magnetization response must be measured under actual operating conditions. If the sample is a toroidal core, the objective can be achieved by measuring it under the same conditions as an actual circuit using the (2) two-coil method or the (6) inductive method1. However, this means that the magnetic material needs to be finished to the shape of the component used in the actual power electronics circuit, which slows down the feedback in the material development process. The AC magnetic susceptibility measurement method [15][16] described in this section is currently under development for this purpose, because it has the advantage that feedback will be faster if measurements can be made at the material level under conditions close to actual operation. Since this measurement method is still under development and not commercially available, it is described in more detail in this section.

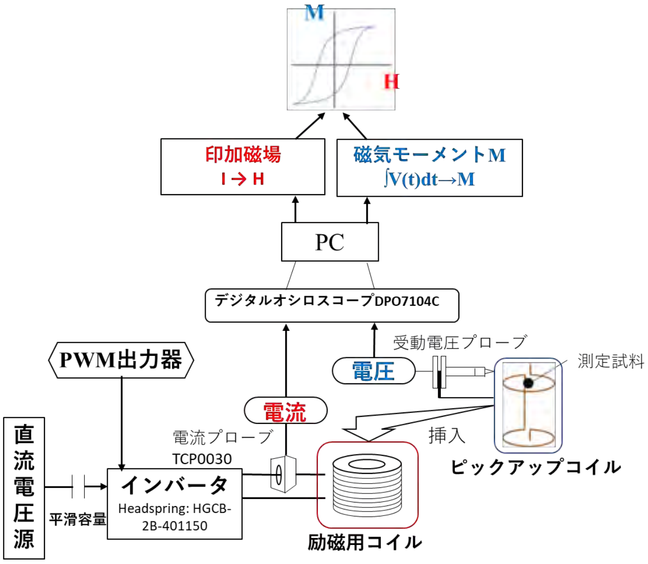

Figure 2.1.4.10 Schematic of AC magnetic susceptibility measurement system

iWhen making magnetic measurements $H = nI$, the magnetic field produced by the excitation coil is proportional to the number of turns N of the coil per unit length and the excitation current i. On the other hand, the voltage $v_L = 2\pi f_s Li$ applied to the coil is proportional to the operating frequency f_s, inductance L, and i. L is proportional to the volume of the excitation coil and N^2, the operating voltage can easily become unrealistic as the frequency increases under constant magnetic field amplitude conditions. In fact, in the two-coil method of measurement (*B*-*H* analyzer), which is now widely used to evaluate soft magnetic properties, it has become difficult to apply a magnetic field large enough to saturate as the measurement frequency increases. Therefore, we are developing the *m*-*H* measurement method as an alternative to the conventional *B*-*H* measurement method, as a device that can evaluate the magnetic response of magnetic materials by applying a sufficiently large alternating magnetic field in the high-frequency range of several MHz, for example. In order to suppress the increase in the operating voltage associated with high frequency, the excitation coil is made as small as possible, and the toroidal sample is replaced by a spherical sample of about 1 mm in diameter, which is designed to measure the magnetic moment *m* instead of the magnetic flux density *B*.

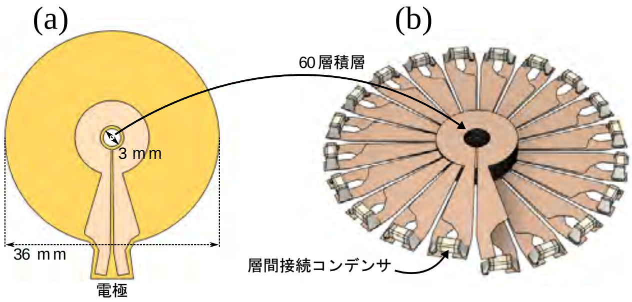

Fig. 2.1.4.11 Appearance of excitation coil

Figure 2.1.4.10 shows a schematic of the device and **Figure 2.1.4.11** shows a photograph of the excitation coil. The basic configuration of the device consists of (i) an excitation coil and power supply, (ii) a pickup mechanism, and (iii) a measurement system. Each of these is described below.

As mentioned above, to suppress the voltage applied to the excitation coil, the coil itself is made smaller. In order to suppress the power supply voltage for excitation, the coil and capacitor are connected in series to form an *LC* series resonant circuit. In addition, in order to suppress the voltage to an appropriate level even when a large current is applied, a multistage *LC* resonant circuit is used with a resonant capacitor between each turn of the excitation coil. 1-turn coils are fabricated on a flexible printed circuit board and laminated together, with an appropriate capacitor between the layers. The inner diameter of the coil is 3.1 mm, the length is 7.3 mm, and the number of turns is 60. The excitation coil is driven by a GaN inverter. At a maximum current i =52 A, the magnetic field amplitude at the center is $\mu_0 H = 0.49$ T

First-order differential coils with one turn each of right- and left-handed coils are used for the pickup. By placing the sample at the center of the coil on one side, the voltage signal associated with the time variation of the magnetic flux caused by the alternating magnetic field produced by the excitation coil is canceled, and only the voltage signal proportional to the change in the magnetic flux (change in magnetic moment) of the sample itself can be detected.

For the excitation magnetic field, the current flowing in the coil is monitored, and for the magnetic moment of the sample, the voltage produced in the pickup coil is recorded with an oscilloscope. As an example of the measurement, a YIG sphere with a diameter of 0.5 mm was measured under an AC magnetic field of 3.7 MHz, and the results are shown in **Figure 2.1.4.12.** The pickup coil signal, indicated by the blue line in the above figure, is converted to magnetic flux (∝ sample magnetic moment) by integration. Plotting the magnetic flux (magnetic moment) against the current signal (magnetic field), the figure below shows that since YIG is an ideal insulating soft magnetic material, the vertical and horizontal axes are calibrated using its saturation magnetization and saturation magnetic field. The magnetization curves measured by a vibrating sample magnetometer are also shown for comparison. It can be seen that both curves are in good agreement. The AC magnetization curve has some noticeable noise, which should be improved in the future. By placing this device in the gap of an electromagnet, it is easy to measure the AC magnetization process in a superimposed DC magnetic field, the so-called minor loop. If the sample is a sphere, the magnetic flux density B is related to the applied magnetic field H_{ex} and $B = \mu_0\left(H_{\mathrm{ex}} + \frac{2}{3}M\right)$ can be compared with the experimental results obtained by the two-coil method. In the future development of this measurement method, minor loop measurement and iron loss evaluation of various soft magnetic materials for power electronics will be promoted as well as noise reduction.

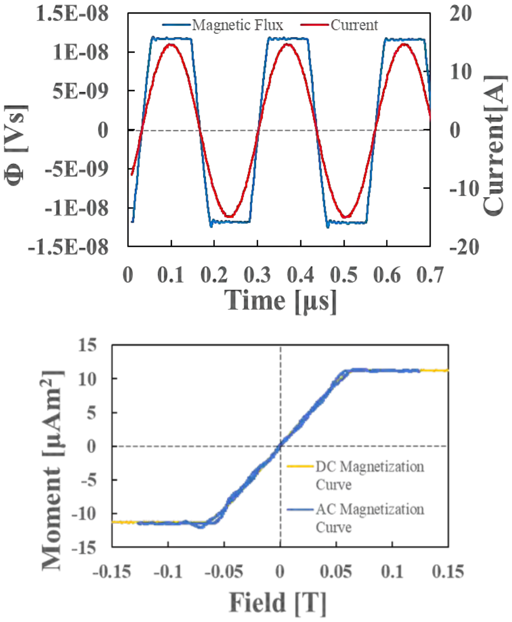

Figure 2.1.4.12 Measurements of a 0.5 mm diameter YIG sphere under a 3.7 MHz AC magnetic field. (top) excitation current and voltage waveforms generated in the pickup coil, (bottom) comparison of *M*-*H* loops of samples obtained by this measurement method (blue) and VSM (yellow).

[Shingo Tamaru, Hideto Yanagihara]

1.4.3 Basics and Issues of Iron Loss Measurement

Figure 2.1.4.13 shows aschematic diagram of the two-coil method. The red line in the figure represents the measurement target (Core Under Test: CUT), and a toroidal magnetic core with two windings as shown in **Figure 2.1.4.14 (a)** is generally used. Here, the primary winding is called the excitation coil (orange) and the secondary winding is called the sensing coil (blue). Note that the coupling between the two windings may not be 100% depending on the CUT and measurement conditions if there is a gap in the magnetic path where the magnetic flux is formed. The measurement accuracy based on the coupling coefficient between the two windings is described below.

In the two-coil method, when current is applied to the excitation coil, the following magnetic field H_m is excited during CUT according to Ampere's law.

$$H_m = \frac{N_1 i_1}{l} \tag{2.1.4.8}$$

where N_1 and l are the number of turns and magnetic path length of the primary winding, respectively. On the other hand, the amplitude of the magnetic flux density, B_m, is obtained using the open circuit voltage, v_2, induced by the sensing coil by the following equation

$$B_m = \frac{1}{2N_2 S}\int_0^{T/2} v_2 dt \tag{2.1.4.9}$$

where N_2, S and T are the number of turns of the secondary winding, the magnetic path cross-sectional area of the CUT, and the time of one cycle, respectively. Since iron loss is defined as the area of the magnetization curve shown in **Figure 2.1.4.1**, iron loss is calculated by the following equation

$$P_{cv} = \frac{1}{T}\int_c HdB = \frac{1}{TSl}\frac{N_1}{N_2}\int_0^T i_1 v_2 dt \tag{2.1.4.10}$$

From this formula, it can be seen that the iron loss is obtained by integrating the current i1 applied to the excitation coil and the open circuit voltage v_2 detected by the sensing coil in one cycle.

Consider the measurement sensitivity of the two-coil method. Let us assume that the excitation current i1 and the open circuit voltage v_2 to be detected are sinusoidal. In that case, the iron loss in equation（2.1.4.10）can be written as

$$P_{cv} = \frac{1}{TSl}\frac{N_1}{N_2} i_1^{rms} v_2^{rms}\cos\theta \tag{2.1.4.11}$$

where i_1^{rms} and v_2^{rms} are the rms values of the excitation current and open circuit voltage, respectively, and θ is the phase difference between i_1 and v_2. Considering the variants of Eq.（2.1.4.11）, we obtain

$$P_{cv} + \partial P_{cv} = P_{cv}\left(1 + \frac{\partial i_1^{rms}}{i_1^{rms}} + \frac{\partial v_2^{rms}}{v_2^{rms}} - \tan\theta\,\partial\theta\right) = P_{cv} + \Delta P_{cv}(\Delta i_1) + \Delta P_{cv}(\Delta v_2) + \Delta P_{cv}(\Delta\theta) \tag{2.1.4.12}$$

Here, if Δi_1 Δv_2 is very small, the measurement sensitivity depends on $\tan\theta$. **Figure 2.1.4.15** shows the dependence of $\Delta\theta$ on θ**.** Since the measurement sensitivity depends on $\tan\theta$, when θ is close to 90 deg, a small deviation of θ can cause a large measurement error. This means that the excitation rear of the CUT is not affected by the measurement error. In other words, measurement errors are more likely to occur at low power factor conditions where the excitation reactance of the CUT is extremely large compared to the loss component. Since the excitation reactance increases in proportion to the frequency, high-frequency measurements above several hundred kHz and measurements of low-loss soft magnetic materials, which have been developed in recent years, are prone to low power factor conditions and large measurement errors.

Another common problem in other iron loss measurements is the lack of established calibration/calibration methods and standard samples.

(a) Toroidal core (b) EI core

Figure 2.1.4.13 Circuit diagram of the

Figure 2.1.4.14. Example of CUT

In addition, since the coupling coefficient between two windings is assumed to be 100%, it may not be possible to measure the loss with high accuracy when using soft magnetic materials with low permeability or magnetic cores with voids such as EI and EE cores. Solutions to these problems are explained in Section 1.4.4.

(a) $0 \leq \theta \leq$ 90deg.

(b) 85 $\leq$ $\theta \leq$

Figure 2.1.4.15. θ dependency of

1.4.4 Iron Loss Measurement Method (1) - Resonance Method (Capacitive Cancellation Method)

(1) Overview of Iron Loss Measurement Methods

IEC 62044-3 specifies the digitizing method, the cross-power method, and the calorimetric method for measuring iron loss in magnetic materials.[19] The digitizing method calculates the loss by integrating the instantaneous power, the cross-power method calculates the loss by fast Fourier transforming the measured values corresponding to voltage and current, and the calorimetric method calculates the loss by measuring the temperature rise due to core loss and comparing it to the known heating resistance . The calorimetric method calculates the loss by measuring the temperature rise due to core loss and comparing it with the known heating resistance. The cross-power method is used in commercially available *B-H* analyzers (IWATSU SY-8218, etc.). A transformer is configured with the CUT to be measured, the excitation current i_1 in the primary winding and the induced voltage v_2 in the secondary winding are taken as time-domain waveforms, converted to a frequency spectrum, integrated without phase error, and the amplitude and phase error of the current detection resistance are compensated in the frequency domain to calculate the iron loss. However, in iron loss measurement for low power factor and low iron loss materials with a phase difference between i_1 and v_2 is close to 90˚, even a small measurement phase error has a significant effect on the accuracy of iron loss evaluation. Accurate evaluation of iron loss, particularly in high-frequency ranges of MHz and above, remains a challenge[20]. This section describes the resonance method (capacitive cancellation method) as an example of an iron loss measurement method that addresses this issue, and the inductive cancellation method is described in the next section.

(2) Basics of Resonance Method

To reduce the measurement error of the two-coil method in the previous section, the resonance method has been proposed [21][22]. In this method, iron loss is measured by connecting a capacitor C_r in series with the CUT as shown in **Figure 2.1.4.16**. In this case, the iron loss is

$$P_{cv} = \frac{1}{TSl}\frac{N_1}{N_2}\int_0^T i_1 v_3 dt \qquad (2.1.4.13)$$

can be obtained by the following equation. In this measurement method, since the open circuit voltage v_3 is referenced, θ in equation (2.1.4.13) is the phase difference between i_1 and v_3. If the inductance of the CUT and C_r are resonant at the measurement frequency, the phase difference between i_1 and v_3 is zero. Therefore, $\Delta\theta$ in **Fig. 2.1.4.15** only needs to refer to a phase difference near 0 deg. and the measurement sensitivity is significantly improved. Therefore, the resonance method is suitable for low permeability materials and high frequency measurements.

Figure 2.1.4.16. Circuit diagram of

On the other hand, although the resonance method is expected to reduce the measurement sensitivity of $\Delta\theta$ as much as possible, it is affected by the ESR of the capacitor and the parasitic resistance of the measurement jig. Therefore, it is important to select a capacitor with low ESR and to create a measurement jig with minimal parasitic resistance. However, even so, the influence of error factors cannot be completely eliminated in iron loss estimation. Therefore, a calibration method called R_0 plot has been proposed to check the influence of error factors in iron loss measurement systems [23][24]. In this method, the effective resistance $R_c = P_{cv}/i_1^{rms2}$ is first calculated from the iron loss P_{cv} measured by the two-coil or resonance method, and the following resistance values are obtained by extrapolation.

$$R_0 = \lim_{i_1 \to 0} \frac{P_c}{i_1^{rms\,2}} \qquad (2.1.4.14)$$

This R_0 is the effective resistance at the micro limit of the excitation current i_1 and includes the resistance derived from the iron loss, the ESR of the capacitor and the parasitic resistance of the measurement fixture. Thereafter, R_0 is compared with the resistance RVNA of the CUT, which is measured by an impedance analyzer or network analyzer (Vector Network Analyzer : VNA). However, in the case of the method using VNA, since the resistance value of the winding is included, it is necessary to remove the effect of the winding.

(a) (b) (c) (d)

Figure 2.1.4.17 Measurement samples (a) 18turnx2, (b) 8turnx4, (c) 5turnx6, (d) 3turnx1

Therefore, anonmagnetic toroidal core with the same shape and winding as the CUT is prepared, and its resistance is subtracted to calculate R_{VNA}. Finally, by comparing R_0 and R_{VNA}, it is checked whether the error component is included. In this method, if R_0 and R_{VNA} agree, the error factor can be ignored because the iron loss, which is the common term in the micro-limit, is the same. On the other hand, if there is a difference, the ESR of the capacitor and parasitic resistance of the measurement jig are on the measurement system, and it can be confirmed that improvement is necessary.

(3) Measurement example

An example of the application of this calibration method is shown below. The sample is a sendust pressed core material with a specific permeability of 30, and the CUT sample used for the measurement is shown in **Figure 2.1.4.17.** The outer diameter, inner diameter, and thickness of the magnetic core were 13 mm, 8 mm, and 1 mm, respectively, and four samples with different types of windings were prepared. **Figure 2.1.4.18** shows the curves of the effective resistance R_c in the resonance method in the low flux density region for these core samples. This time, the extrapolation to R_0 is a linear approximation. **Figure 2.1.4.19** shows a comparison of R_{VNA} and R_0 measured by VNA. From the figure, it can be confirmed that the R_{VNA} and R_0 measured by the VNA are in good agreement. It can be confirmed that the influence of ESR and measurement jig can be neglected in this iron loss measurement system. The advantage of this method is that the error factors can be estimated by comparing with the measurements of impedance analyzers and VNAs, for which calibration methods have been established. Therefore, this method can be used as a calibration method for general iron loss measurements.

Figure 2.1.4.18 Effective resistance R_c *and* extrapolated value R_0

Figure 2.1.4.19 Comparison of R_0 and R_{VNA}

(4) Correction for coupling between two windings

Finally, the coupling between the two windings of the CUT is discussed. The coupling between the two windings is an extremely important factor in two-coil-based measurement methods, including the resonance method. The equation (2.1.4.10) used to calculate iron loss assumes that there is no leakage flux and that all fluxes are linkedto the sensing coil, that is, that the coupling between the two windings is 100%. However, for materials with low magnetic permeability, which are increasingly used in the high-frequency range, the effect of leakage flux becomes non-negligible. In this case, the number of windings can be increased as a means of reducing leakage flux, but this results in an increase in parasitic capacitance between the windings, which lowers the resonance frequency and limits the measurement range.

Figure 2.1.4.20 Frequency response of coupling

Iron loss measurements were performed on samples with different couplings shown in **Figure 2.1.4.17.** Four types of windings were used for the loss measurements, and the frequency characteristics of their coupling coefficients are shown in **Figure 2.1.4.20.** It can be seen that the coupling coefficient is about 75% to 100% for the four types of magnetic cores. On the other hand, the resonance frequency of the magnetic cores with high coupling coefficients as mentioned above is in the low frequency region. **Figure 2.1.4.21** shows the results of iron loss measurements using these cores. The results in the figure are measured when the excitation amplitude of the magnetic flux density is B_m = 10 mT. It can be seen that the iron loss values differ greatly depending on the sample with different coupling. In particular, it can be confirmed that the value is greatly underestimated for sample (d) with 75% coupling. **Figure 2.1.4.22** shows the frequency response of the effective permeability obtained during the iron loss measurement at B_m = 0.25 mT. Here, the effective permeability was calculated as $\mu_{eff} = B_m/\mu_0 H_m$ using equations (2.1.4.8) and (2.1.4.9) obtained from the iron loss measurement. The black line in the figure is the frequency response of the real part of the specific permeability obtained by the transmission line method [25]. In the micro-excitation limit, the black line and each specific permeability curve should coincide, but it can be confirmed that they do not.

To verify the validity of these results, an analysis using electromagnetic field simulations was performed. **Figure 2.1.4.23** shows the vector distribution of the magnetic flux density simulating samples (a) and (d). It can be seen that in sample (a), the magnetic flux density passes uniformly through the core. On the other hand, in sample (d), the magnetic flux is not uniformly linkedthrough the core, and it can be confirmed that the magnetic flux lines form a magnetic path, especially around the excitation coil. This suggests that the magnetic path length *l in* equation (2.1.4.8) is actually effectively shortened. From this, the effective permeability in **Figure 2.1.4.22** is

$$\mu_{eff} = \frac{B_m}{\mu_0 H_m} = \frac{l}{2N_1 N_2 i_1 S}\int_0^{T/2} v_2 dt \qquad (2.1.4.15)$$

The effective permeability was overestimated because l is larger than the effective magnetic path length l_{eff}, as calculated in Eq. On the other hand, the iron loss is underestimated because l in Eq. (2.1.4.8) is large and the current value is not sufficient to make $B_m = 10$ mT. This indicates that the iron loss measurement cannot be performed accurately when the coupling between the two windings is insufficient.

On the other hand, the ratio of the effective magnetic path length to the actual magnetic path length can be used as a correction factor. From the above discussion, these ratios can be obtained by the ratio of the effective magnetic permeability to the true value of the magnetic permeability $\mu_{r.v.}$

$$\Delta = \frac{l_{eff}}{l} = \frac{\mu_{eff}}{\mu_{r.v.}} \qquad (2.1.4.16)$$

For example, $\mu_{r.v.}$ can use the permeability obtained by the transmission method shown in **Figure 2.1.4.22.** Finally, this ratio can be used to correct B_m or H_m as follows.

$$B_{cor} = \frac{1}{\Delta} B_m \ or \ H_{cor} = \Delta H_m \qquad (2.1.4.17)$$

Figure 2.1.4.24 shows the result of correcting **Figure 2.1.4.21** using the correction coefficients. It can be confirmed that the correction is correctly performed by using the correction using formula (2.1.4.17), and that the lines are on the same line.

The calibration and correction methods discussed in this section are applicable to all methods based on the general two-coil method, not just the resonance method. Therefore, it can be applied to iron loss measurements in the low-frequency range and for soft magnetic materials with high permeability. [Yuki Sato]

1.4.5 Iron Loss Measurement Method 2 - Inductive Cancellation Method

(1) Basics of the Inductive Cancellation Method

The inductive cancellation method consists of a transformer of the opposite phase with sufficiently small loss relative to the CUT, connected in series on both the primary and secondary sides, as shown in **Figure 2.1.4.25 (a)**, and by canceling the respective excitation inductances, the secondary side induced voltage generated only by the iron loss resistance is used for iron loss calculation [28]. While the resonance method is limited by its principle to sinusoidal excitation only [26], the inductive cancellation method can measure iron loss under arbitrary excitation conditions and can be applied to iron loss evaluation by simulating the excitation conditions of transformers and inductors in a power conversion circuit.

Figure 2.1.4.21 Iron loss measurement results for samples with different coupling

Figure 2.1.4.22 Frequency response of effective permeability obtained during iron loss measurement

(a) Sample (a)

(b) Sample (d)

Figure 2.1.4.23 Magnetic flux density distribution during iron loss measurement

Figure 2.1.4.24 Results of Loss Measurement with

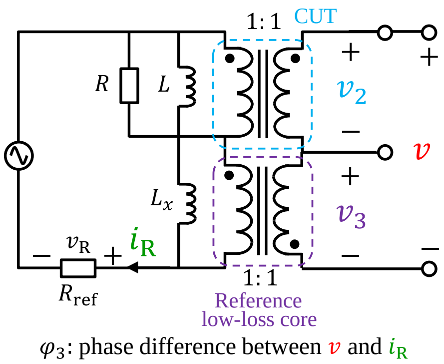

(a) Equivalent circuit of inductive cancel method

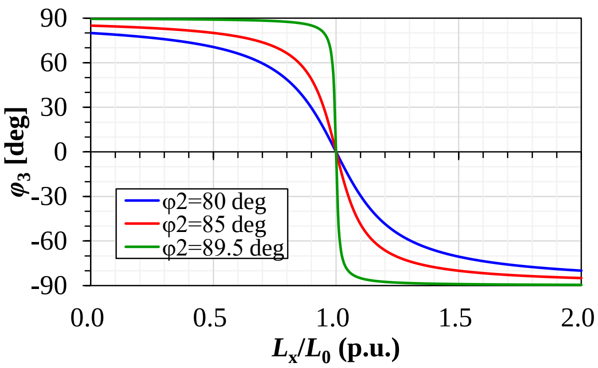

(b) Relationship between φ_3 and normalized inductance

Figure 2.1.4.25 Basic configuration and measurement accuracy of the inductive cancellation method

In the following description, the turn ratios of the CUT and the added low-loss transformer are considered to be 1:1 each. If the iron loss resistance R and excitation inductance L are as shown in **Figure 2.1.4.25 (a)**, the primary impedance Z of the CUT is expressed as follows

$$Z = \frac{\omega^2 L^2 R + j\omega L R^2}{R^2 + \omega^2 L^2} \tag{2.1.4.18}$$

Therefore, the following relationship holds for the induced voltage v_2 of the secondary winding and the phase difference between i_R and φ_2

$$v_2 = Z i_R = \frac{\omega^2 L^2 R + j\omega L R^2}{R^2 + \omega^2 L^2} i_R \tag{2.1.4.19}$$

$$\tan \varphi_2 = \frac{R}{\omega L} \tag{2.1.4.20}$$

On the other hand, the induced voltage v_3 in the added low-loss transformer can be expressed as $v_3 = j\omega L_x i_R$. Thus, the cancellation voltage can be expressed as $v_2 - v_3 (= v)$

$$v_2 - v_3 = \frac{1}{R^2 + \omega^2 L^2}\{\omega^2 L^2 R + j[\omega L R^2 - \omega L_x (R^2 + \omega^2 L^2)]\} i_R \tag{2.1.4.21}$$

Using the cancellation voltage and excitation current $i_R(t) = I \sin \omega t$, the iron loss P can be expressed as follows

$$P = I^2 \frac{R\omega L}{\sqrt{R^2 + \omega^2 L^2}} \frac{\cos \varphi_2}{2} \tag{2.1.4.22}$$

For the inductance L_x of a low-loss transformer, the condition of perfect cancellation is when the v_2 imaginary part expressed in equation (2.1.4.16) is equal v_3 to the inductance of the transformer, in which case the following relationship holds.

$$L_x = \frac{L R^2}{R^2 + \omega^2 L^2} \equiv L_0 \tag{2.1.4.23}$$

If the v phase difference between i_R and φ_3

$$\tan \varphi_3 = \frac{R}{\omega L}\left\{1 - \frac{L_x}{L_0}\right\} = \tan \varphi_2 \left\{1 - \frac{L_x}{L_0}\right\} \tag{2.1.4.24}$$

Figure 2.1.4.25 (b) plots the characteristics of the inductance versus $\frac{L_x}{L_0}$ the compensation ratio φ_2 based on Equation (2.1.4.24). Using the detected phase error $\Delta\varphi$ to express the error rate of

$$\left|\frac{\Delta P}{P}\right| = |\tan \varphi_3 \, \Delta\varphi| = \left|\tan \varphi_2 \left\{1 - \frac{L_x}{L_0}\right\} \Delta\varphi\right| \tag{2.1.4.25}$$

$\varphi_2 = L_x$This means that the inductance compensation ratio must be within the range of $\Delta\varphi = 1$. This result indicates that the inductance compensation factor should be within the range of

$$0.89 \leq \frac{L_x}{L_0} \leq 1.11$$

to keep the measurement error of iron loss within 10 % for a CUT that shows 89˚ when considered as less than ˚ (29).

(2) Example of measurement by inductive cancellation method

As an example of actual measurement and evaluation based on the inductive cancellation method, the following introduces the iron loss calculation results when multiple transformers with different excitation inductances (Types 1, 2, and 3) are applied to the CUT (30). Using a digital oscilloscope, the primary excitation current i_R, secondary induced voltage, and overall secondary voltage v_2 (cancellation voltage) v including the secondary winding of the transformer are measured and the iron loss is calculated. **Figure 2.1.4.26** shows i_R, v_2 and the time waveforms of v and obtained under the excitation conditions of 1 MHz frequency and maximum flux density B_m = 10 mT. When the excitation inductance of the transformer is almost equal to the perfect cancellation condition (Type 2), the amplitude of v is small and the phase difference between i_R is smaller than 90˚. When the excitation inductance of the transformer is smaller than this condition (Type 1), the amplitude of v is in phase with v_2. Conversely, if the excitation inductance of the transformer is too large (Type 3), the v phase is opposite to that v_2 of the CUT. In the case of the low power factor CUT, when the deviation from the perfect cancellation condition is large, it can be read from the results that the absolute value of the phase difference between i_R and v is almost 90˚ in all cases.

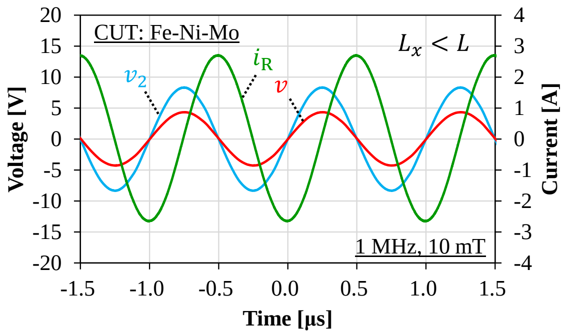

(a) Reference air-core: Type 1 ($L_x < L$)

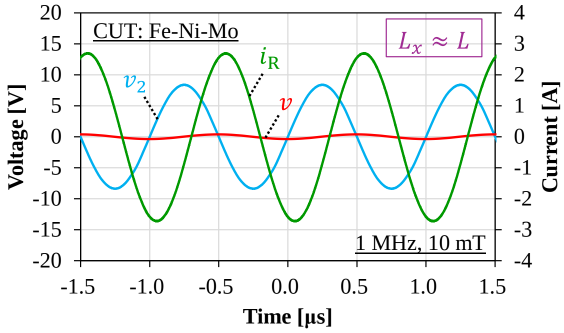

(b) Reference air-core: Type 2 ($L_x \approx L$)

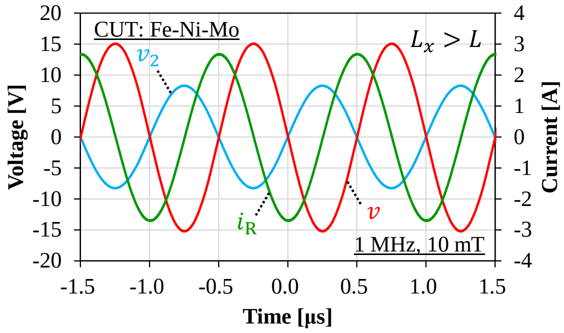

(c) Reference air-core: Type 3 ($L_x > L$)

Figure 2.1.4.26 Time response of voltage and current in the inductive cancellation method

Figure 2.1.4.27 shows the *B-H* curve and iron loss evaluation results obtained in the iron loss measurement system based on the inductive cancellation method under the excitation conditions of 1MHz and B_m = 10 mT (30). The *B-H* curve obtained based on the excitation current and the secondary side induced voltage of the CUT (**Figure 2.1.4.27 (a)**) corresponds to the *B-H* characteristics of the CUT obtained by the two-winding method and does not depend on the characteristics of the applied blank-core transformer. On the other hand, the *B-H* curve drawn from the excitation current and cancellation voltage (**Figure 2.1.4.27 (b)**) is not the *B-H* characteristic of the CUT itself, but the iron loss is obtained using the excitation current and cancellation voltage. When the excitation inductance L_x of the air-core transformer is small

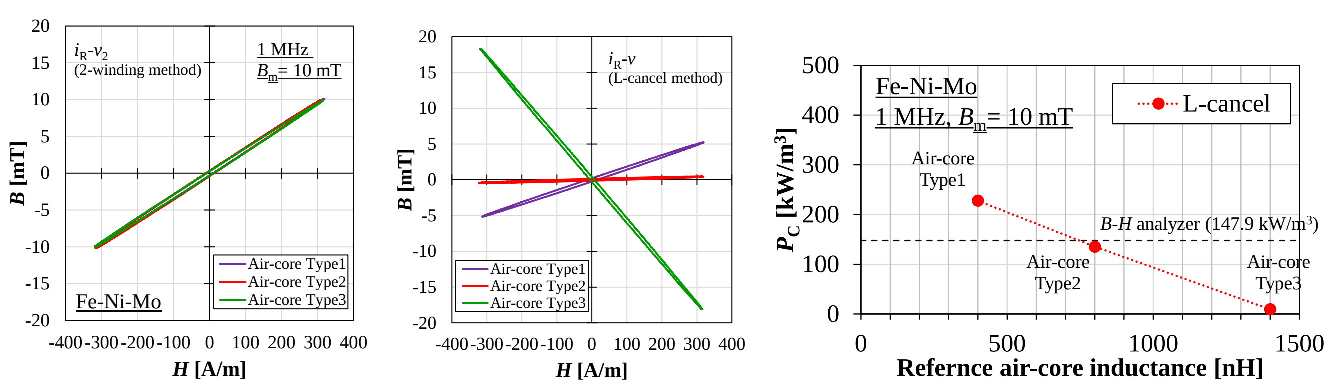

(a) B-H curve (2-winding method) (b) *B-H* curve (inductive cancel method) (c) Iron loss evaluation results

Figure 2.1.4.27 Iron loss evaluation results based on inductive cancellation method compared to the excitation inductance L of the CUT, in the case of $L_x < L$ (Type 1), the loop is right-shouldered up due to insufficient cancellation, whereas in the case of $L_x > L$ (Type 3), the loop is right-shouldered down due to excessive cancellation. In the case of $L_x \approx L$ (Type 2), which is close to the perfect cancellation condition, the shape of the loop is almost as if it were lying on its side. This corresponds to the small amplitude of the cancellation voltage caused only by the iron loss. **Figure 2.1.4.27 (c)** shows the measured iron loss of the CUT obtained based on the inductive cancellation method. For comparison, the iron loss measurements obtained using the *B-H* analyzer (IWATSU SY-8218) are also shown. In the iron loss measurements based on the inductive cancellation method, the measured iron loss values also differ depending on the type of transformer used, suggesting that it is important to design and apply a transformer that is as close as possible to the perfect cancellation condition where the phase difference between the primary side excitation current and the secondary side induced voltage generated only by the iron loss is almost 0˚.

(3) Partial cancellation method

As a method to mitigate the dependence of the iron loss calculation based on the inductive cancellation method on the characteristics of the additional transformer as described above, there is a partial cancellation method in which the iron loss is obtained by introducing a correction factor obtained by applying a phase perturbation in the excitation current measurement [27]. **Figure 2.1.4.28** shows the basic configuration of an iron loss measurement system based on the partial cancellation method. As with the inductive cancellation method, the primary-side excitation current $i_\mathrm{R}\left(=\dfrac{v_\mathrm{R}}{R_\mathrm{ref}}\right)$, the secondary-side induced voltage v_2 of the CUT, and the secondary-side induced voltage v_3 of the transformer with an empty core are measured with a digital oscilloscope, and the iron loss is calculated. The phase difference between i_R and v_2 is φ_2, and the transformer is determined as $i_\mathrm{R}=\dfrac{V_\mathrm{R}}{R_\mathrm{ref}}\sin\omega t$, $v_2=V_2\sin(\omega t+\varphi_2)$, $v_3=V_3\sin\left(\omega t+\dfrac{\pi}{2}\right)$.

The measured values i_R', v_2', v_3', taking into account the measurement phase error $\Delta\varphi_\mathrm{R}$, $\Delta\varphi_2$, $\Delta\varphi_3$ for each true value, are expressed as follows

$$i_\mathrm{R}'=\frac{V_\mathrm{R}}{R_\mathrm{ref}}\sin(\omega t+\Delta\varphi_\mathrm{R}) \tag{2.1.4.26}$$

$$v_2'=V_2\sin(\omega t+\varphi_2+\Delta\varphi_2) \tag{2.1.4.27}$$

$$v_3'=V_3\sin\left(\omega t+\frac{\pi}{2}+\Delta\varphi_3\right) \tag{2.1.4.28}$$

The true iron loss value P_core of the CUT, the error in iron loss measurement ΔP_core, and the true iron loss value of the air-core transformer $P_\mathrm{core}=0$, and the error in loss measurement ΔP_air.

$$P_\mathrm{core}+\Delta P_\mathrm{core}=\frac{f}{R_\mathrm{ref}}\int_0^T v_2'v_\mathrm{R}'dt\cong\frac{V_2I_\mathrm{R}}{2}\cos\varphi_2+\frac{V_2I_\mathrm{R}}{2}(\Delta\varphi_\mathrm{R}-\Delta\varphi_2)\sin\varphi_2 \tag{2.1.4.29}$$

$$\Delta P_\mathrm{air}=\frac{f}{R_\mathrm{ref}}\int_0^T v_3'v_\mathrm{R}'dt\cong\frac{V_3I_\mathrm{R}}{2}(\Delta\varphi_\mathrm{R}-\Delta\varphi_3) \tag{2.1.4.30}$$

Here, the modification factor k is defined as follows

$$k\equiv\frac{\Delta P_\mathrm{air}}{\Delta P_\mathrm{core}}=\frac{\frac{V_3I_\mathrm{R}}{2}(\Delta\varphi_\mathrm{R}-\Delta\varphi_3)}{\frac{V_2I_\mathrm{R}}{2}(\Delta\varphi_\mathrm{R}-\Delta\varphi_2)\sin\varphi_2} \tag{2.1.4.31}$$

Equation (2.1.4.31) depends on the measurement phase error $\Delta\varphi_\mathrm{R}$, $\Delta\varphi_2$, $\Delta\varphi_3$. However, when $\Delta\varphi_2=\Delta\varphi_3$

$$k=\frac{V_3}{V_2\sin\varphi_2} \tag{2.1.4.32}$$

The value k of the induced voltage is defined as a constant value, independent of any measurement phase error. In order to $\Delta\varphi_2=\Delta\varphi_3$ realize the actual measurement, voltage probes of the same model number with the same characteristics should be used for the secondary side

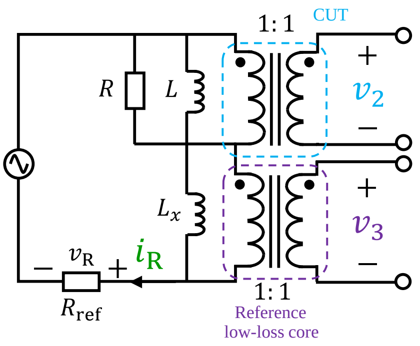

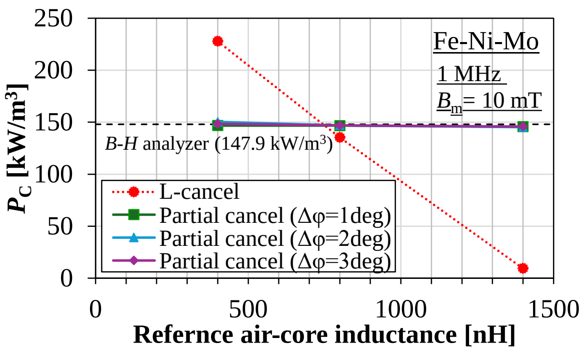

Figure 2.1.4.28 Basic configuration of partial cancellation method **Figure 2.1.4.29** Iron loss evaluation results based on partial cancellation method

induced voltage measurement.

P_{core} can be expressed from Equations (2.1.4. 29), (2.1.4. 30), and (2.1.4. 32) as follows

$$P_{\mathrm{core}} = \frac{f}{R_{\mathrm{ref}}}\int_0^T v_2{}'v_{\mathrm{R}}{}'dt - \Delta P_{\mathrm{core}} = \frac{f}{R_{\mathrm{ref}}}\int_0^T v_2{}'v_{\mathrm{R}}{}'dt - \frac{\Delta P_{\mathrm{air}}}{\mathrm{k}} = \frac{f}{R_{\mathrm{ref}}}\int_0^T v_2{}'v_{\mathrm{R}}{}'dt - \frac{1}{\mathrm{k}}\frac{f}{R_{\mathrm{ref}}}\int_0^T v_3{}'v_{\mathrm{R}}{}'dt \qquad (2.1.4.33)$$

Now, let us assume that we obtain a new $v_{\mathrm{R}}{}''$ by $v_{\mathrm{R}}{}'$ giving a phase perturbation to $\Delta\varphi_{\mathrm{R}}{}''$. In this case, each ΔP_{core}, ΔP_{air} is represented by $\Delta P_{\mathrm{core}}{}''$, $\Delta P_{\mathrm{air}}{}''$, but the modification factor is constant $\left(\frac{\Delta P_{\mathrm{air}}{}''}{\Delta P_{\mathrm{core}}{}''} = k\right)$.

$$P_{\mathrm{core}} = \frac{f}{R_{\mathrm{ref}}}\int_0^T v_2{}'v_{\mathrm{R}}{}''dt - \Delta P_{\mathrm{core}}{}'' = \frac{f}{R_{\mathrm{ref}}}\int_0^T v_2{}'v_{\mathrm{R}}{}'dt - \frac{\Delta P_{\mathrm{air}}{}''}{\mathrm{k}} = \frac{f}{R_{\mathrm{ref}}}\int_0^T v_2{}'v_{\mathrm{R}}{}''dt - \frac{1}{\mathrm{k}}\frac{f}{R_{\mathrm{ref}}}\int_0^T v_3{}'v_{\mathrm{R}}{}''dt \qquad (2.1.4.34)$$

kSince Equations (2.1.4.33) and (2.1.4.34) are equal, Equation (2.1.4.35) can be used to express

$$k = \frac{\int_0^T v_3{}'v_{\mathrm{R}}{}'dt - \int_0^T v_3{}'v_{\mathrm{R}}{}''dt}{\int_0^T v_2{}'v_{\mathrm{R}}{}'dt - \int_0^T v_2{}'v_{\mathrm{R}}{}''dt} \qquad (2.1.4.35)$$

Substituting the result k obtained from Equation (2.1.4.35) into Equation (2.1.4.33), we obtain P_{core}.

(4) Example of measurement by partial cancellation method

Figure 2.1.4.29 shows an example of iron loss evaluation results based on the partial cancellation method [31]. In contrast to the conventional inductive cancellation method, which gives results that vary greatly depending on the inductance of the transformer with an empty core, the partial cancellation method introduces a correction factor obtained by giving a phase perturbation in the excitation current measurement, which reduces the dependence of the iron loss calculation on the characteristics of the additional transformer and results in a The resultant variation is small. In addition, compared to the two-winding method, the partial cancellation method can mitigate the influence of phase error caused by the measurement system, and the measurement system constructed with general-purpose measuring instruments (oscilloscope, voltage probe) can achieve the same iron loss measurement accuracy (within 10 % difference) as the *B*-*H* analyzer using the cross-power method. Inductive Cancellation The inductive cancellation method described in this paper was proposed by a research group at Virginia Tech in the U.S. [27][28], and has been used in Japan to improve the accuracy of iron loss measurement based on gain-phase-frequency characteristics evaluation and correction [32][33] of voltage and current probes. And the separate evaluation of copper and iron losses in inductor losses under DC superposition and triangular wave excitation conditions [34].

1.4.6 DC superimposed characteristics

(1) Basic Concept of Measurement

A square wave voltage is applied to the magnetic elements in the power conversion circuit as a result of the switching operation of the power semiconductor devices, and a triangular wave-shaped excitation current flows. In addition, a load current flows through the inductor of the DC-DC converter, so the magnetic field strength H becomes a triangular waveform with a superimposed DC current. The waveform of the magnetic flux density B expressed by the integral value of the inductor voltage also has a triangular wave shape corresponding to the switching frequency, and does not have a positive-negative symmetrical excitation waveform. Considering this in the B-H plane, as shown in **Figure 2.1.4.1**, the minor loop is drawn at a biased position that includes the DC bias. The incremental permeability, defined as the ratio of the magnetic field strength ripple ΔH and the corresponding magnetic flux density ripple ΔB, changes depending on the operating point, and the inductance and loss when a DC bias magnetic field is applied are different from those under sinusoidal excitation conditions. In other words, it is important in circuit design to understand the magnetic element loss characteristics with respect to excitation frequency, magnetic flux density ripple, and DC bias magnetic field. In the following, we will introduce the results of a study on the evaluation of the characteristics of magnetic powder cores under DC superposition under small-signal and large-signal excitation conditions [35].

(2) Example of measurement under small-signal excitation conditions

Here, we show as an example the results of evaluation of five types of toroidal cores (manufactured by Magnetics) of the same size with an initial permeability of 60 and the same winding conditions (bifiler winding, number of turns 80). **Figure 2.1.4.30 (a)** shows the configuration of the measurement system for evaluating the DC superposition characteristics of inductance under small-signal excitation conditions. The DC current flows from the DC power supply to the excitation winding of the CUT through the Bias-Tee. The impedance measurement signal of the inductor is applied from a vector network analyzer (VNA), and the frequency characteristics of the impedance are measured by a 1-port measurement. The DC superimposed inductance characteristics (DC superimposed current: 0 to 10 A) evaluation results are shown in **Figure 2.1.4.30 (b)**. In general, the inductance of an inductor made of pressed materials shows a characteristic of gradual decrease with the magnitude of the DC superposition current. The inductance of Fe-Ni and Fe-Si shows a smaller decrease in inductance against the DC superposed current than that of Fe-Ni-Mo and Fe-Si-Al. Fe-Ni and Fe-Si-Al.

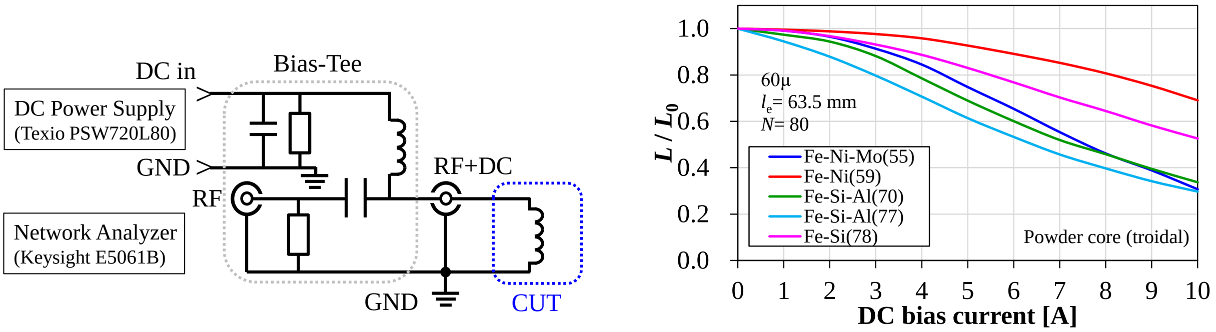

(a) Measurement system (b) DC bias current dependency of inductance

Fig. 2.1.4.30 Evaluation of DC superposition characteristics of a piezoelectric core (small-signal excitation)

(3) Example of measurement under high-signal excitation conditions

Next, **Figure 2.1.4.31 (a)** shows the configuration of the measurement system constructed for the evaluation of DC superposition characteristics under large-signal excitation conditions. The method of applying DC current is the same as in the case of small-signal excitation (**Figure 2.1.4.30 (a))**. The signal generator output is amplified in the RF power amplifier and applied to the primary winding of the CUT via Bias-Tee. Using a digital oscilloscope, the time responses of the primary-side excitation current and secondary-side induced voltage are measured to evaluate the B-H characteristic and iron loss. The evaluation results under sinusoidal excitation conditions are presented here. **Figures 2.1.4.31 (b)** and **2.1.4.31 (c) show** the B-H characteristics of Fe-Ni and Fe-Si-Al when the excitation frequency is 20 kHz and $ΔB$=

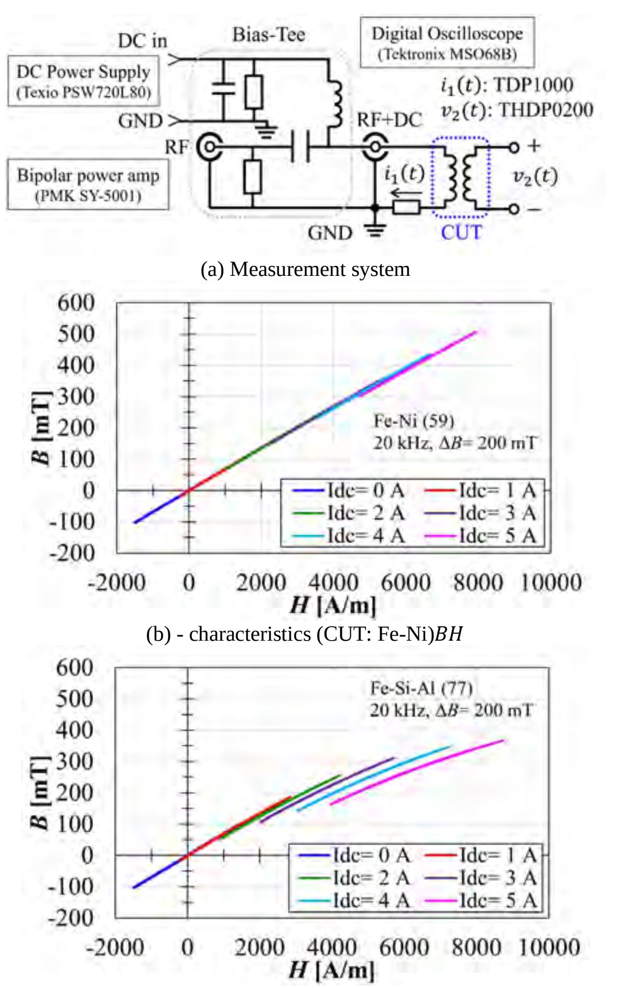

(a) Measurement system

(b) - characteristics (CUT: Fe-Ni)BH

(c) - characteristics (CUT: Fe-Si-Al)BH

BH**Fig. 2.1.4.31** Evaluation of the -characteristics of a magnetic powder core under DC bias excitation conditions

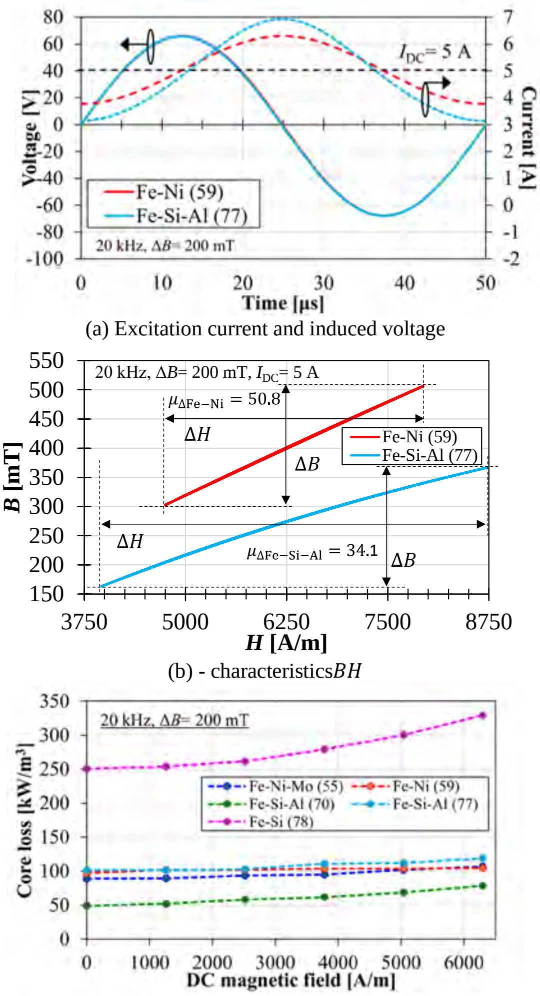

(a) Excitation current and induced voltage

(b) - characteristicsBH

(c) DC bias magnetic field dependency of core loss

Fig. 2.1.4.32 Evaluation results of time response of excitation current and induced voltage, B-H characteristics, and dependence of iron loss on DC bias magnetic field

200 mT and the DC superposition current is set from 0 to 5 A. In the case of Fe-Ni, the minor loop moves parallel to the upper right of the B-H plane as the DC bias magnetic field increases, while in the case of Fe-Si-Al, the minor loop gradually increases ΔH as the DC bias magnetic field increases under certain conditions ΔB, and the shape of the loop also changes. **Figures 2.1.4.32 (a) and 2.1.4.32 (b)** show the time response of the excitation current and induced voltage and the corresponding B-H characteristics of the Fe-Ni and Fe-Si-Al samples when the excitation frequency is 20 kHz, ΔB = 200 mT, and the DC superposition current is 5 A. The voltage waveforms of the two samples are identical, but the excitation current amplitudes are different, because the excitation currents of the two samples are measured ΔB as the same as the excitation currents of the Fe-Ni and Fe-Si-Al samples. The incremental permeability was calculated from the obtained B-H characteristics, and it was 80% or more of the initial permeability for Fe-Ni and 60% or less for Fe-Si-Al. These all correspond to the results of the DC superposition characteristics evaluation of inductance shown in **Figure 2.1.4.30 (b). Figure 2.1.4.32 (c)** shows the evaluation results of the DC bias magnetic field dependence of the iron loss exhibited by the five types of CUTs. It can be confirmed that each magnetic material has different iron loss characteristics with respect to the DC bias magnetic field. **Figure 2.1.4.32 (c)** shows the evaluation results for an excitation frequency of 20 kHz, ΔB= 200 mT. If the excitation frequency ΔB is increased for the same sample, the induced voltage amplitude also increases in proportion to the frequency.

In order to measure and evaluate iron loss under higher frequency, higher amplitude, and higher bias excitation conditions, various restrictions and corrections of characteristics caused by the measurement system, such as power capacity and bandwidth of bipolar amplifiers, gain and phase frequency characteristics of probes for high voltage and high current measurement, etc., will be required. Therefore, it is necessary to verify the accuracy of iron loss measurement evaluation and results obtained in response to these limitations.

[Takaaki Ibuchi]

Table 2.1.4.2 Materials used for superimposed property analysis

(a) CUTs of four different materials

Material	Fe-Si-Al (Sendust)	Fe-Si	Fe-Ni-Mo (Mo-Permalloy)	MnZn ferrite
Saturation magnetization $\mu_0 Ms$ (T)	1.0	1.8	0.75	0.5
Relative initial permeability μ_i	60			2,900
Outer diameter, inner diameter, height (mm)	42.9, 24.2, 16.3		12.7, 7.6, 4.8	13.0, 8.0, 5.0

(b) CUTs with different specific permeability

Material	Fe-Ni-Mo (Mo-Permalloy)				
Saturation magnetization $\mu_0 Ms$ (T)	0.75				
Relative initial permeability μ_i	26	60	125	300	550
Outer diameter, inner diameter, height (mm)	12.7, 7.6, 4.8				

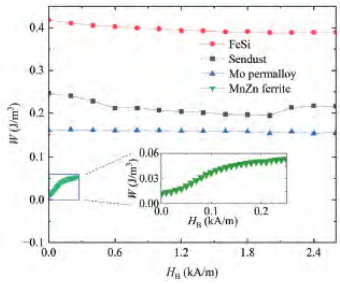

Figure 2.1.4.33 Loss characteristics for superimposed magnetic fields in four different materials

1.4.7 DC Superimposed Characteristic Analysis by Principal Component Analysis

In reference (36), a detailed analysis of iron loss behavior during DC superimposed excitation is performed using Principal Component Analysis (PCA), which analyzes the reasons why DC superimposed characteristics differ depending on the material type as described in Section 1.4.3 of Chapter 1.

Principal Component Analysis is a dimensionality reduction technique to represent the information contained in multidimensional data with a small number of variables with as little loss as possible. The same method is also used in the analysis in Chapter 4, Section 3 in general, and should be referred to in conjunction with this section. The materials used are listed in **Table 2.1.4.2**. In this analysis, in addition to (a) four different magnetic materials, (b) several samples with different specific initial permeabilities μ_i were used for the Fe-Ni-Mo system (Mo-Permalloy). First, **Figure 2.1.4.33** shows the results of iron loss measurements for each material listed in **Table 2.1.4.2 (a)**. The horizontal axis is the superimposed magnetic field H_B (A/m) and the vertical axis is the iron loss W (J/m^3). From the figure, it can be confirmed that the response of iron loss to the application of DC bias differs greatly depending on the material. For example, in Fe-Si, the iron loss decreases monotonically with increasing H_B, whereas in Mn-Zn ferrite, a sharp increase in iron loss is observed even at small H_B. In particular, Sendust showed an initial decrease in loss, followed by a slight increase in loss.

To quantitatively evaluate these differences in iron loss behavior, PCA was applied to the descending curves of the obtained *B*-*H* curves (see Reference (37) for detailed methodology). **Figure 2.1.4.34** shows the change in *B*-*H* curve shape for each material,

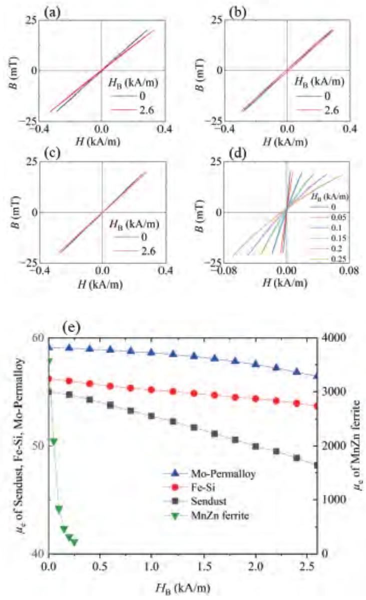

Figure 2.1.4.34 *B-H* curve and change in effective permeability when DC bias magnetic field is applied for each magnetic material

and **Figure 2.1.4.35** shows the extracted first principal component (PC1: slope) and second principal component (PC2: curvature); PC1 mainly corresponds to the slope of the B-H curve, or effective permeability, while PC2 reflects the curvature component, including nonlinearities and saturation effects PC2 reflects the curvature component including the effects of nonlinearity and saturation. The analysis shows that the PC1 score decreases with increasing H_B for all materials, a behavior consistent with the decrease in effective permeability μ_e. On the other hand, PC2 scores show different trends depending on the material, with Mn-Zn ferrite showing a significant increase, while Fe-Si shows a decreasing trend.

Next, similar measurements and PCA analysis were performed on several samples of Mo-Permalloy with varying specific permeability μ_i. **Figures 2.1.4.36** and **2.1.4.37** show the iron loss characteristics and PCA results for each sample. The samples with small permeability show a trend of decreasing iron loss with respect to H_B, but the higher the permeability, the more pronounced the trend of increasing loss becomes. This trend corresponds well with the previously observed analysis results between different materials, especially with the marked

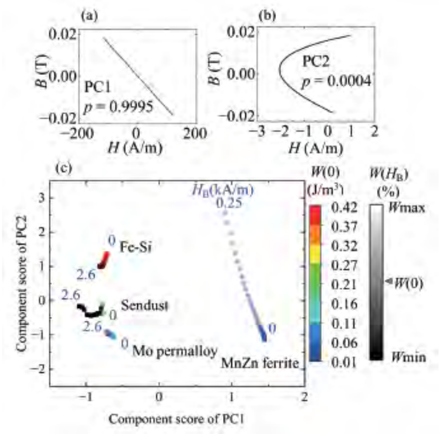

Figure 2.1.4.35 Results of feature extraction of *B-H* curve shape by Principal Component Analysis (PCA)

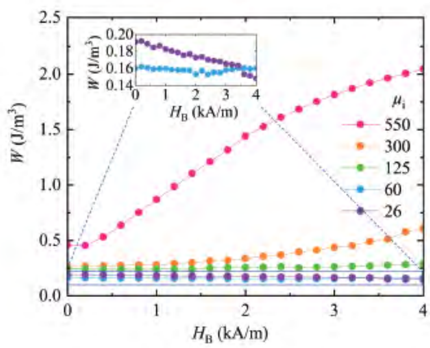

Figure 2.1.4.36 Iron loss characteristics of Mo-Permalloy cores with different permeability when a DC

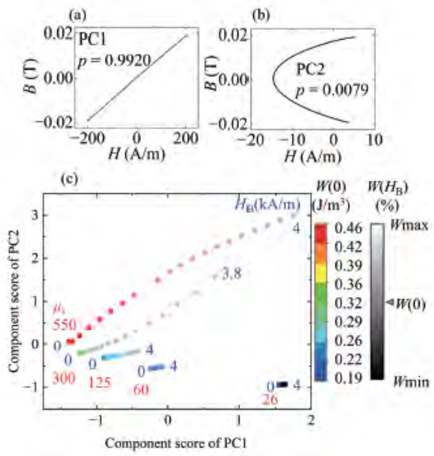

Figure 2.1.4.37 Relationship between principal component analysis results and iron

difference in PC2 scores between Mn-Zn ferrite, a high permeability material, and other materials (Fe-Si, Sendust, Mo-Permalloy). This is interpreted as an increase in the curvature of the *B-H* curve (PC2) as the saturation flux density is approached, and the contribution to iron loss becomes dominant.

These results indicate that the iron loss behavior under DC bias magnetic field can be consistently explained by the competition between two components of the *B-H* curve: the slope (PC1) and curvature (PC2). This shows that the nonlinear behavior of iron loss, which has conventionally been treated as a material-specific property, can be understood in a unified manner based on a general-purpose and quantitative shape index.

[Yuki Sato]

1.4.8 Time-resolved magnetic imaging (magneto-optical Kerr effect microscopy)

(1) Magnetic Domain Observation Technique

The occurrence of iron loss is closely related to the temporal and spatial motion of magnetization. For example, in a metallic magnetic material, if there are no magnetic domains in the material as shown in **Figure 2.1.4.38 (a)**, and uniform magnetic flux changes in the material due to magnetization rotation, eddy currents flow more near the surface of the magnetic material. Since the path of the current is longer, the electrical resistance becomes larger and the loss becomes smaller. On the other hand, when the magnetic flux change is caused by the movement of a single magnetic wall, as shown in **Figure 2.1.4.38 (b)**, the magnetic flux change is concentrated near the magnetic wall, and large eddy currents are generated around the magnetic wall, resulting in large losses. When the magnetic flux change is caused by the movement of multiple magnetic walls (N pieces) as shown in **Figure 2.1.4.38 (c)**, the overall eddy current loss is 1/N of that in **Figure 2.1.4.38 (b)** because the magnetic flux change per magnetic wall is 1/N. Although eddy current losses are not large in magnetic materials with high electrical resistance such as ferrite, resonance phenomena dependent on the magnetic domain structure, such as magnetic wall resonance, are thought to have a strong influence on the losses.

As shown in these examples, it is known that magnetic domain structure and its motion are strongly related to loss, and efforts have been made to reduce loss by controlling the generation of magnetic domains in various soft magnetic materials. However, the control of the magnetic domain structure has been based on the statically observed magnetic domain structure. In most cases, the analysis of iron loss, which is the basis for the development of magnetic materials, is also based on the model that the change in magnetization can be divided into two components, magnetic wall movement and magnetization rotation, without observing the actual change in magnetic domains. On the other hand, it has been pointed out experimentally that not only the motion of magnetic domains but also the structure of magnetic domains and the number of magnetic walls change when the excitation frequency is changed [(38)], and static magnetic domain observation alone is not sufficient. In order to understand the mechanism of iron loss generation in various magnetic materials and to develop low-loss materials and magnetic elements, time-resolved magnetic imaging technology that actually observes the temporal and spatial motion of magnetization is important.

Table 2.1.4.3 Comparison of main magnetic domain observation methods

	Magneto-Optical Microscope (MOKE)	Magneto Force Microscope (MFM)	Lorentz microscope (LTEM)	Scanning transmission X-ray microscope (STXM)	photoelectron microscope (XMCD-PEEM)
Spatial resolution	Several hundred nm	Several nm degree	a few nm	Around several tens of nm	Several tens of nm
Vector magnetization observation	Many things are possible.	Difficult	possible	It's possible. Not common	It's possible. Not common
Quantitative magnetization observation	possible	Difficult	possible	possible	possible
High-speed time-resolved observation	possible	Difficult	Difficult	possible	possible
Sample Constraints	Mirror surface and flatness required	not much	Thickness must be less than 100 nm	Must be less than a few microns thick.	Surface must be clean
Equipment size	Can be installed on tabletop	Can be installed on tabletop	Can be installed in a laboratory	Synchrotron radiation facilities are needed	Synchrotron radiation facilities are needed

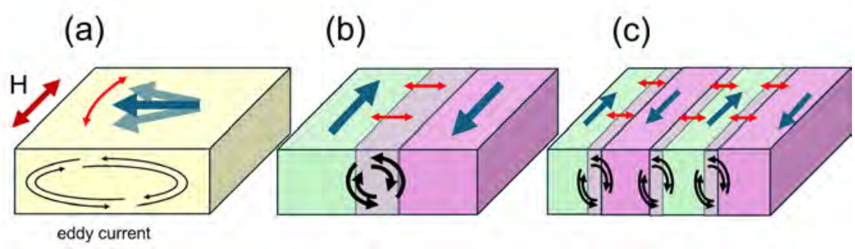

Figure 2.1.4.38 Relationship between magnetic domain structure and eddy current loss. (a) Change due to magnetization rotation. If the magnetic flux variation is spatially uniform, eddy currents are larger near the surface. (b) Change due to the movement of a single magnetic wall. Since the magnetic flux change is concentrated around the magnetic wall, large eddy currents are generated locally. (c) Change due to the movement of multiple magnetic walls. When the number of magnetic walls increases

The main observation techniques used to observe magnetic domains in magnetic materials include magneto-optical microscopy, magnetic force microscopy, Lorentz transmission electron microscopy, scanning transmission X-ray microscopy (STXM), and X-ray magnetic circular dichroism photoemission electron microscopy (XMCD-PEEM). The characteristics of these techniques are briefly summarized **in Table 2.1.4.3**[39-41]. Each technique has its advantages and disadvantages, and is used for different purposes. Important features of magnetic domain observation for the development of soft magnetic materials and magnetic elements for power electronics are the ability to observe magnetic domains in a shape close to that in use and time-resolved observation in the kHz to MHz bandwidth. Since the magnetic domain structure of soft magnetic materials is strongly affected by the shape of the sample, if the sample is shaved thin for transmission observation, the magnetic domain structure will be significantly different from that in actual use as a magnetic element, and the relationship between loss and magnetic domain structure cannot be correctly evaluated.

(2) Features of time-resolved magneto-optical Kerr effect microscopy

Magneto-optical Kerr effect microscopy is a technique for observing magnetic domains based on the fact that the polarization of light reflected from ferromagnetic materials changes slightly depending on the magnetization. Although this technique has been around for many years, it is still widely used today as an easy-to-use method for observing magnetic domains in the laboratory. It is a suitable method for the evaluation of soft magnetic materials because it does not require thinning of the sample for observation of the reflection configuration, it enables time-resolved observation, and it can observe a relatively large area. Furthermore, in recent years, spatial resolution has been improved, and three-dimensional vector magnetization observation and stroboscopic time-resolved observation have become relatively easy to use, making it a very powerful tool. In this subsection, we introduce the features of the recently developed time-resolved magneto-optical Kerr effect microscope and examples of observations of soft magnetic materials using it.

This magneto-optical Kerr effect microscope has higher spatial resolution than conventional magneto-optical microscopes and is characterized by its ability to observe three-dimensional vector magnetization and time-resolved observation up to about 10 GHz [42][43]. **Figure 2.1.4.39 (a)** shows a schematic diagram of this magneto-optical microscope. The light source is a semiconductor laser, which is introduced into the illumination optics of the microscope using an optical fiber. The illumination optics can be oriented 360 degrees by an automatic rotation stage. Since the magneto-optic effect is sensitive to the magnetization component in the direction of light travel, when observing magnetization in the in-plane direction of the sample with a magneto-optic microscope, the illumination light must be incident at an angle to the sample surface from the direction of magnetization to be observed (**Figure 2.1.4.39 (b))**. In this case, the spatial resolution in the direction perpendicular to the incident direction of the light (the direction of magnetization to be observed) is lower than that of a conventional optical microscope. With this magneto-optical microscope, magnetic domain images are taken by changing the incident direction of the illumination light from 8 to 16 directions, and these images are numerically superimposed to enable observation of the three components of the magnetization vector and to obtain images with no reduction in spatial resolution.

A method called the stroboscopic method is used for time-resolved observation. The stroboscopic method is an observation method that makes use of the fact that magnetic domains appear to stand still when periodically changing due to a periodic external magnetic field is illuminated by a pulsed light synchronized with this period (**Figure 2.1.4.39 (c))**. A pulsed semiconductor laser is used as the illumination source. The semiconductor laser used here can generate pulsed light of arbitrary width down to a minimum of about 30 picoseconds with an arbitrary period of 250 MHz or less, enabling the observation of dynamic phenomena from static magnetic domains up to about 10 GHz. (It is probably up to 10 MHz that will be important in the development of soft magnetic materials for power electronics.) Another advantage of semiconductor lasers is that their output is stable and does not require adjustment, so measurements can be started as soon as the power is

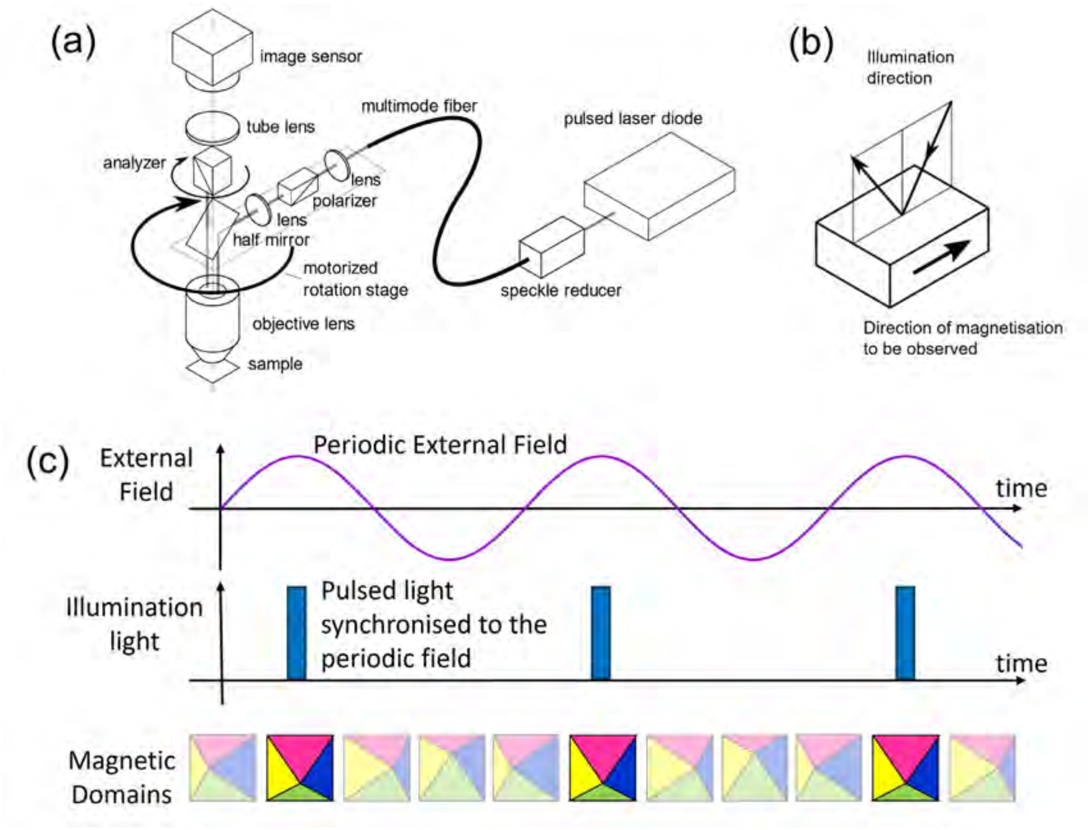

Figure 2.1.4.39 (a) Schematic of a time-resolved magneto-optical Kerr effect microscope. A semiconductor laser is used as the pulse light source. A number of magnetic domain images are acquired by changing the incident direction of the illumination light with a rotating stage, and then numerically synthesized to achieve high resolution and vector domain observation. (b) Relationship between the direction of magnetization to be observed and the incident direction of the illumination light. To observe magnetization in the in-plane direction, the illumination light must be incident obliquely on the sample surface. In ordinary magneto-optical microscopes, this causes a decrease in spatial resolution. (c) Principle of time-resolved observation by the

turned on.

(3) Observation example

Figures 2.1.4.40 and **2.1.4.41** show the motion of magnetic domains observed with this device due to AC excitation. Twenty-four time-resolved images were taken per cycle of the AC magnetic field (1 ms in this example), and although these images can usually be viewed as moving images, only a few of them are shown here. The AC magnetic field is applied in the left and right directions. **Figure 2.1.4.40** shows the change of magnetic domains when an amorphous thin band is excited by a 1 kHz AC magnetic field. The numbers at the top of the image indicate the time elapsed since the first image, and the arrows in the magnetic domain image indicate the direction of the magnetization vector in the plane. The red area in the lower left graph shows the corresponding position of the magnetic domain image in the magnetization curve, and the lower right image is a two-dimensional histogram showing the distribution of the magnetization vectors in the plane. The magnetic domain structure shows characteristic rippled magnetic domains, which are roughly divided into two groups: those with rightward magnetization (shown in red) and those with leftward magnetization (shown in green). The leftward magnetic field is also well corresponds

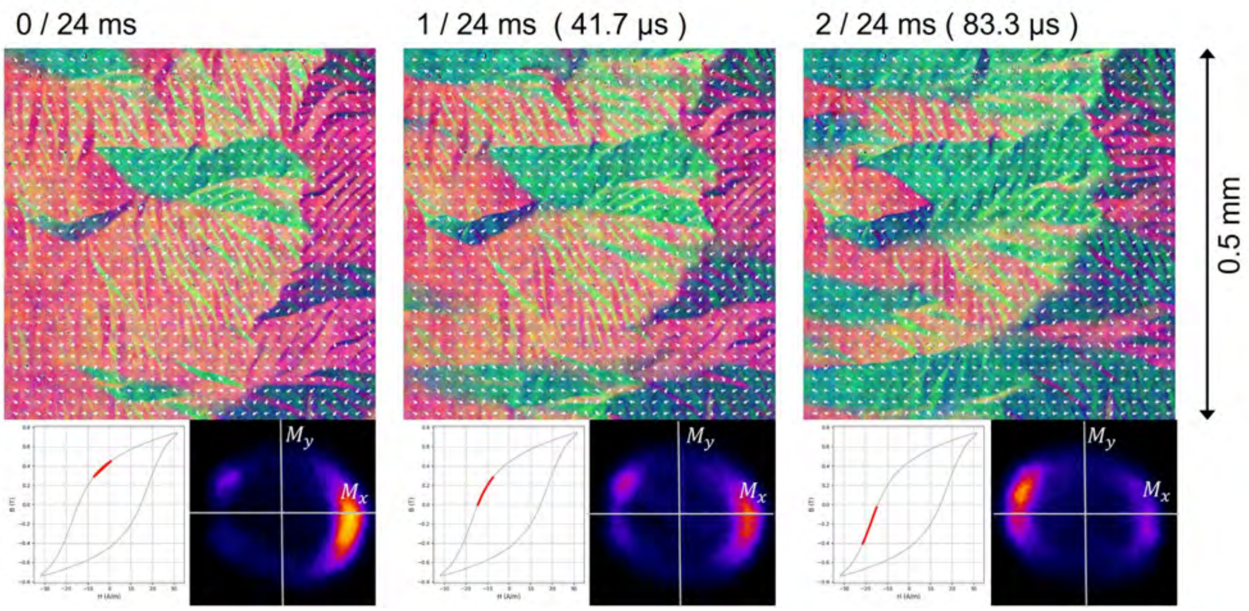

Figure 2.1.4.40 Time-resolved magnetic domain observation of an amorphous thin-band sample AC excited at 1 kHz. Arrows in the magnetic domain images indicate the direction of the in-plane magnetization vector. The lower left of each image shows the corresponding position on the magnetization curve, and the lower right is a histogram showing the distribution of magnetization vectors. As the leftward magnetic field becomes stronger, the leftward magnetic domain, shown in green, spreads. In the histogram showing the distribution of the magnetization vectors, only the weights of the left and right peaks change, and the positions of the peaks do

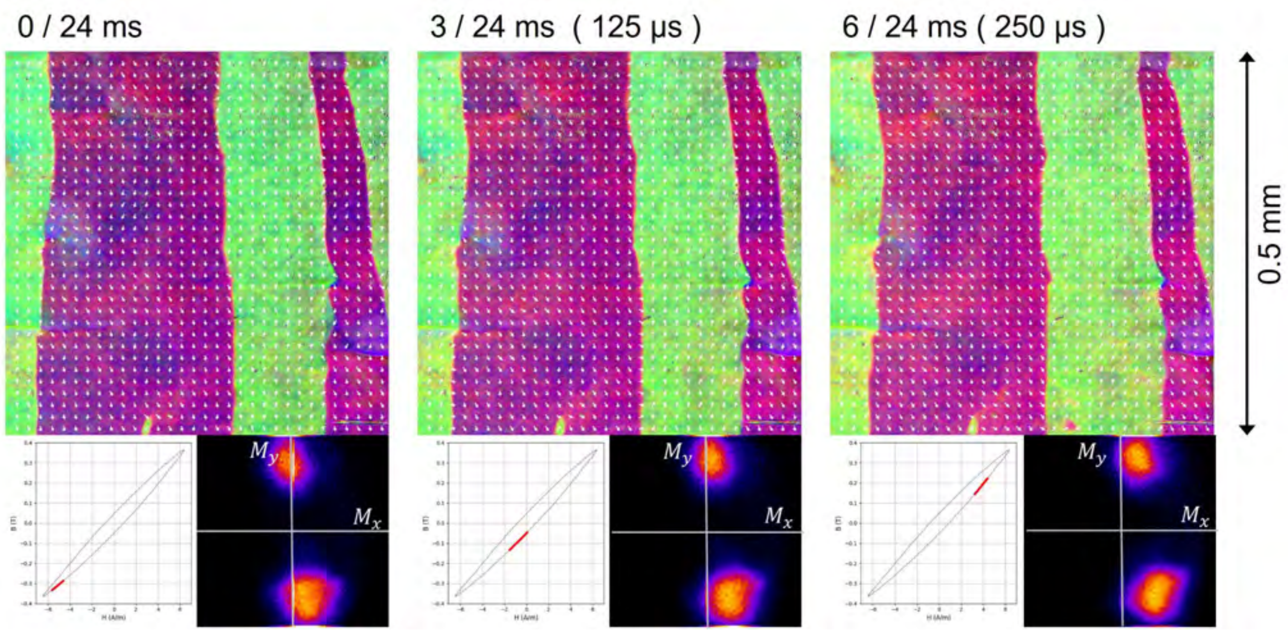

Figure 2.1.4.41 Time-resolved magnetic domain observation of a nanocrystal thin-band sample AC-excited at 1 kHz. Although the change in the magnetic domain structure is slight, the histogram showing the distribution of magnetization vectors shows that the top and bottom two peaks move from left to right, indicating that the overall magnetization changes due to the rotation of the magnetization direction in the upward and downward magnetic domains, respectively.

to the magnetization curves. The first two-dimensional histogram shows a strong peak on the right side and a weak peak in the opposite direction, corresponding to leftward and rightward magnetic domains, respectively. The stronger peak on the right side reflects the greater number of right-oriented magnetic domains. As the number of left-oriented magnetic domains increases, the right peak becomes weaker and the left peak becomes stronger, indicating an increase in the number of left-oriented magnetic domains. The change in the strength of the two peaks without a change in the position of the peaks indicates that a change in magnetization is occurring in this sample due to the movement of the magnetic wall.

On the other hand, **Figure 2.1.4.41** shows an example of observation when a wound core of a commercially available nanocrystalline thin strip is excited at 1 kHz. The sample has weak magnetic anisotropy in the vertical direction in the figure, and is divided into upward and downward magnetic domains when no magnetic field is applied. 2-D histograms show two peaks in the vertical direction, corresponding to upward and downward magnetic domains, respectively. Although the magnetization curve shows a change in magnetization with time, the change in the shape of the magnetic domains in the magnetic domain image is negligible. On the other hand, the histogram shows that the upper and lower peaks move to the left and right with time, indicating that the direction of magnetization rotates within the magnetic domains. Although the rotation of magnetization can be confirmed by observing the direction of the arrows in the magnetic domain image in detail, this kind of histogram analysis allows us to understand the motion of magnetization in a more visually comprehensible manner. In addition, although it is difficult to see from the still image, the movement of the magnetic wall can also be confirmed. Since the magnetization of each magnetic domain is oriented roughly perpendicular to the applied AC magnetic field, the magnetic wall movement in this case does not contribute much to the magnetization change in the direction of the magnetic field (left-right direction), but causes a large magnetization change locally in the direction perpendicular to the magnetic field, generating eddy currents around the magnetic walls. Therefore, it is thought that the loss in this material can be further reduced by suppressing the movement of the magnetic wall.

Because ferrite has low reflectivity and low magneto-optical effect compared to metallic magnetic materials, it has been difficult to observe magnetic domains using magneto-optical microscopy. **Figure 2.1.4.42 (a)** shows a magnetic domain image of a commercial Mn-Zn ferrite ring core. Grain boundaries are indicated by white lines. Each grain is divided into several magnetic domains, and vortex-like reflux domain structures can be seen in some places. **Figure 2.1.4.42 (b)** shows the distribution of the rotation angle of magnetization obtained from the dynamic magnetic domain observation when magnetized with an AC magnetic field at 100 kHz, and the frequency (histogram) for each angle is shown by the solid red line in **Figure 2.1.4.42 (c).** The areas with large rotation angles correspond to the areas where the magnetic wall shift occurred, but the percentage of the total is small, indicating that most of the shift occurred in the areas with rotation angles of 20 degrees or less. The blue dashed lines in **Fig. 2.1.4.42 (c)** show the contribution to the magnetization change from each rotation angle: the peak near 160 degrees and the weak peak near 70 degrees indicate the contribution from the 180 degree and 90 degree magnetic wall shifts, respectively. However, the largest contribution to the magnetization change is seen at a rotation angle of about 10 degrees.

Figure 2.1.4.43 shows an example of magnetic domain observation of an amorphous thin strip, a precursor to nanocrystalline materials. Here, the effect of the internal distortion caused by rapid cooling of the amorphous thin strip and the effect on the magnetic domains caused by surface scratches and distortion at the edge of the amorphous thin strip during cutting are clearly observed. Thus, it can be used to evaluate the effects of material processing (building factor) and other factors.

(4) Summary

As mentioned above, time-resolved magnetic imaging techniques can be used to determine the processes that produce changes in magnetization under AC excitation. Magnetic imaging with magneto-optical microscopes can be quantitatively measured with appropriate calibration, and quantitative analysis can be performed not only on how the shape of magnetic domains changes, but also on how much magnetization rotates and how much the movement of magnetic walls contributes to the change in magnetization. More information can be obtained by combining not only time-resolved magnetic imaging but also various other methods such as iron loss measurement, microstructural observation, and simulation. To reduce the loss of soft magnetic materials, a steady process of carefully removing detailed loss factors is required. To this end, it is necessary to confirm and understand the factors that cause loss for each material before proceeding

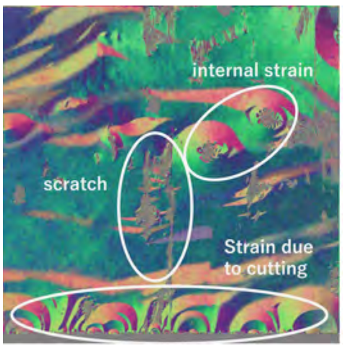

Figure 2.1.4.43 Effects of flaws and distortion during manufacturing and processing that appear in the magnetic domain image

with development. We hope that this method will be widely used in future research and development of soft magnetic materials and magnetic elements.

[Tsuyoshi Ogasawara]

1.4.9 Microstructure, composition, and atomic distribution analysis methods

In addition to the magnetic property measurements described above, scanning electron microscope (SEM) observation, transmission electron microscope (TEM) observation, and atom probe tomography (APT) analysis are also effective in the development of soft magnetic materials from the viewpoint of crystal structure analysis. Atom Probe Tomography (APT) analysis are also effective measurement methods. Here, we will give an overview of these measurement methods.

SEM observation is a technique for observing microstructures by irradiating a sample with an accelerated electron beam. The electron beam is focused and scanned two-dimensionally to detect secondary electrons and reflected electrons emitted from the specimen to obtain an image. It can also be used for crystal orientation analysis by Electron Backscatter Diffraction (EBSD).

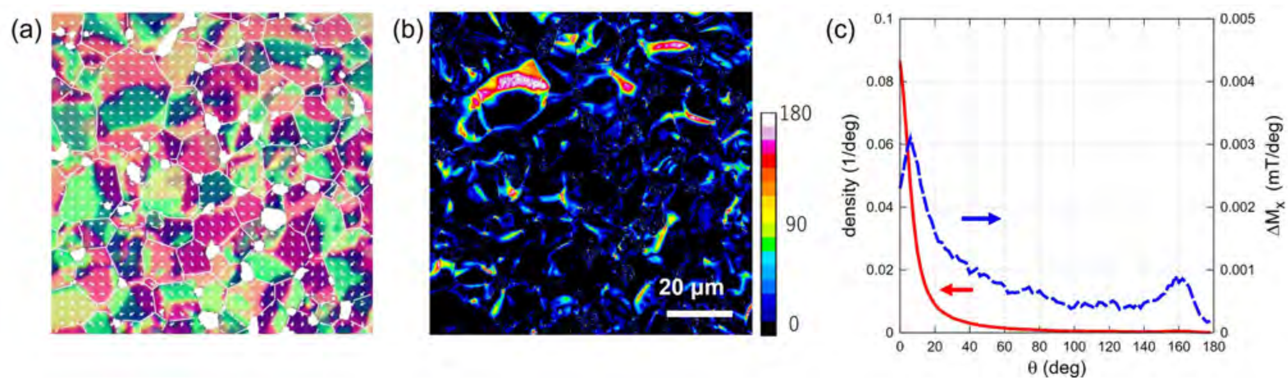

Figure 2.1.4.42 (a) Magnetic domain image of a commercial Mn-Zn ferrite ring core. White lines indicate grain boundaries and white spots indicate vacancies. (b) Distribution of the rotation angle of magnetization when excited by a 100 kHz AC magnetic field. The large rotation angle corresponds to the movement of the magnetic wall. (c) Histogram of the rotation angle distribution (solid red line) and the contribution of each rotation angle to the magnetization change (dashed blue line). The area where the magnetic wall shift occurred is very small compared to the whole area, and most of the area has a rotation angle of less than 20 degrees. The contribution of the magnetic wall shift to the magnetization change has a peak around 160 degrees, but the largest contribution is around 10 degrees rotation angle.

TEM observation, like SEM observation, is a scanning transmission electron microscope (STEM) observation in which electron beams are

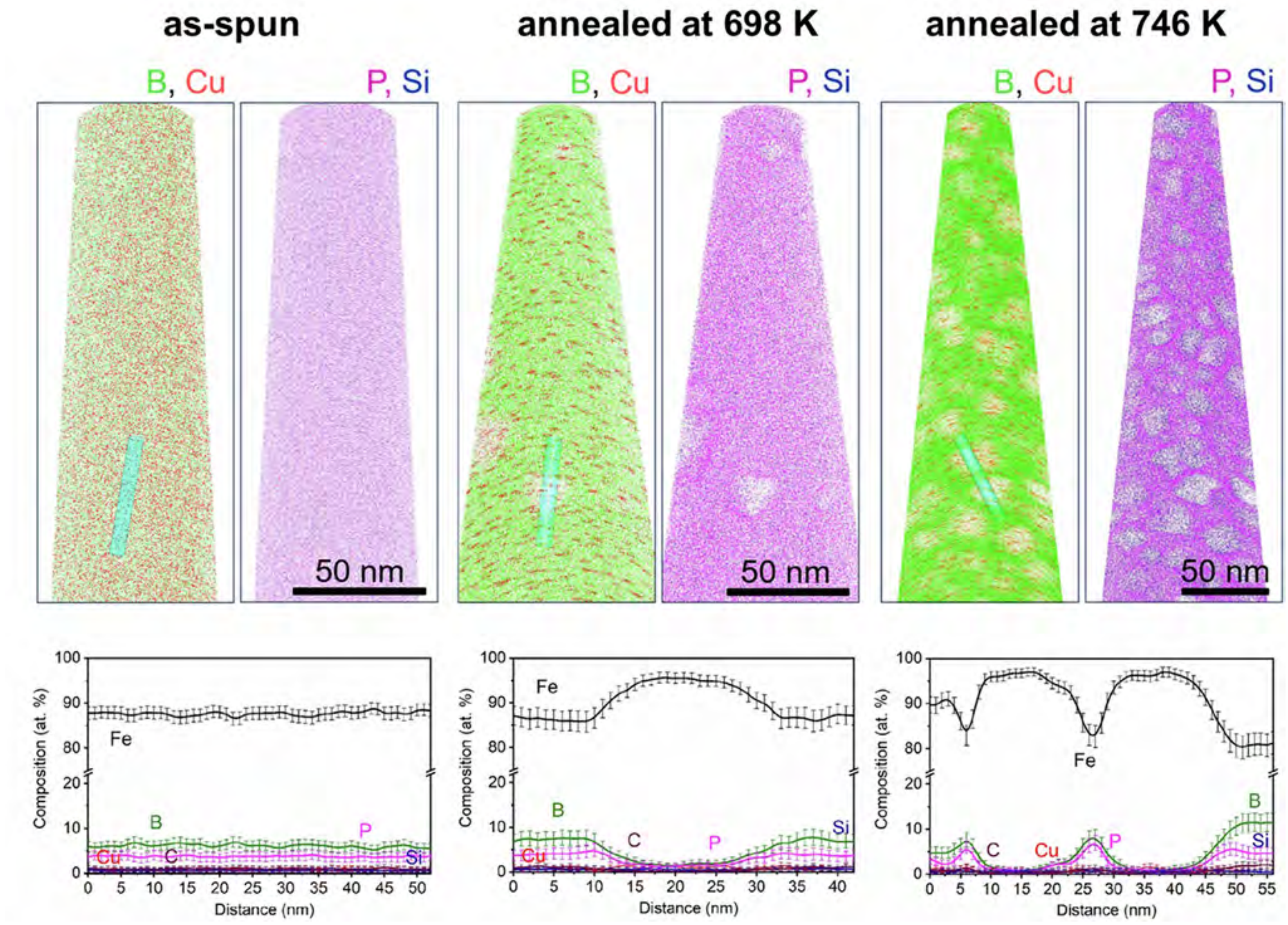

Figure 2.1.4.44 Examples of atomic maps and composition profiles in nanocrystalline alloy materials [44]

converged and scanned in two dimensions. Spherical aberration correction enables spatial resolution of less than the interatomic distance. In combination with EDS, elemental mapping at the atomic column level is also possible. Furthermore, the 4D-STEM (4 Dimensional-Scanning Transmission Electron Microscope) method, which obtains a two-dimensional map of a nanobeam electron diffraction image from a selected region of the STEM image, is effective for analyzing nano-scale phase separation. On the other hand, in ordinary TEM observation, in which electron beams are irradiated to a sample in a broadened state without convergence, bright-field and dark-field images can be obtained by selecting any spot in the diffraction image formed from the transmission wave. This is often used to confirm the shape and grain size of fine crystal grains. Both STEM and TEM can be combined with Electron Energy-Loss Spectroscopy (EELS) to analyze the bonding state in the selected region and the film thickness.

APT is an instrument that combines time-of-flight elemental analysis with a position-sensitive detector to obtain a three-dimensional atomic distribution in a sample, enabling the detection of all elements. For example, as shown in **Figure 2.1.4.44** (example of atomic map and composition profile of nanocrystalline alloy material [44]), APT is capable of elemental analysis that is impossible with TEM or STEM, such as the composition of fine crystal grains of several nm size and their interface composition with the matrix phase [45]. Focused Ion Beam (FIB) lift-out method can be used to prepare samples for analysis from arbitrary locations, which is useful for analysis of grain boundaries.

Regarding magnetic domain observation methods, the Lorentz method, which uses the Lorentz force from the magnetic domains of a sample to shift the electron beam to visualize the magnetic walls, which are the boundaries of the magnetic domains, using a TEM, has the disadvantage that the sample must be made thinner. On the other hand, it is also possible to change the applied magnetic field in the TEM, which can be used to study the effect of microstructure on the movement of magnetic walls [46].

[Tadakatsu Ohkubo.]

References

(1) R. Moskowitz, and E. Della Torre : "Theoretical aspects of demagnetization tensors," IEEE Trans. Magn. 2.4, pp. 739-744 (1966).

(2) E. H. Brandt : "Geometric edge barrier in the Shubnikov phase of type-II superconductors.", Low Temp. Phys. 27, pp. 723-731 (2001).

(3) R. Prozorov, and V. G. Kogan : "Effective demagnetizing factors of diamagnetic samples of various shapes," Phys. Rev. Applied 10, 014030 (2018).

(4) Magnetics Society of Japan (ed.): "Magnetic Handbook", Maruzen Publishing, ISBN 978-4-621-30014-5 (2016).

(5) V. Franco, and B. Dodrill, eds. : "Magnetic measurement techniques for materials characterization. ", Springer Nature, (2021).

(6) D. Jordán, et al. : "Detection of magnetic moment in thin films with a home-made vibrating sample magnetometer," J. Magn. Mater. 456, pp. 56-61 (2018)

(7) B-H Analyzer SY-8218 / SY-8219 Instruction Manual, IWATSU ELECTRIC CO.

(8) Yamada: "B-H Curve Measurement of Soft Magnetic Materials," Osaka Institute of Industrial Technology, Technical Sheet, No. 16011 (2017).

(9) JIS C 2550-1: "Testing methods for electromagnetic steel strip-Part 1: Methods for measuring magnetic properties of electromagnetic steel strip by Epstein tester", Japanese Standards Association (2011).

(10) JIS C 2556: "Method for Measuring Magnetic Properties of Electromagnetic Steel Strips by Single Plate Tester", Japanese Standards Association (2015)

(11) Higashi Daichi, et al: "Standardization of Fe-based amorphous alloys for transformers and their magnetic property measurement methods," Hitachi metals technical review/ GRIT, Global Technology Innovation Center, Technology Development Division, Hitachi Metals, Ltd. ed. 33, pp. 28-33 (2017).

(12) Yasushi Endo: "Development of Soft Magnetic Particle Materials with Different Particle Diameters," Magne, Vol. 19, No. 1, pp. 4-10 (2024).

(13) CQ Publishing Company: "Tragei Junior No. 29 (Spring 2017) Video Linked Corner, "Electric Science Experiments! Supplemental Information for "Uncontrollable Inductors: Magnetic Saturation Mechanisms of Inductors and Transformers," https://www.cqpub.co.jp/toragijr/article/2017/1704mov3.html (cited on 2025-05-06)

(14) Keysight Technologies : "Dielectric/permeability measurement solutions using LCR meters and impedance analyzers," Application Note 5980-2862JAJP (2015).

(15) T. Mannen, et al: "Flexible-Printed-Circuits Based Magnetizing Coil for a High-Frequency and Large-Amplitude Magnetic-Field Generator.", 2021 IEEE Applied Power Electronics Conference and Exposition (APEC), pp. 2870-2875, Jun. 2021, DOI: 10.1109/apec42165.2021.9487199

(16) H. Tanaka, et al: "Dynamic Magnetometer for Full M-H Loop Measurement in the Megahertz Range.", under review.

(17) R. Prozorov, and V. G. Kogan : "Effective demagnetizing factors of diamagnetic samples of various shapes", Phys. Rev. Applied 10, 014030 (2018).

(18) B-H Analyzer SY-8218 / SY-8219 Instruction Manual, IWATSU ELECTRIC CO. LTD, (2017).

(19) IEC 62044-3 : "Cores made of soft magnetic materials - Measuring methods - Part 3: Magnetic properties at high excitation level", Edition 2.0 (2023).

(20) T. Shimizu: "Loss Evaluation of Magnetic Devices Used in Power Converters", IEEJ Trans. Vol. 18, pp. 1728-1736 (2023).

(21) M. Mu, Q. Li, D. J. Gilham, F. C. Lee and K. D. T. Ngo: " New Core Loss Measurement Method for High-Frequency Magnetic Materials," in IEEE Transactions on Power Electronics, Vol. 29, No. 8, pp. 4374-4381, Aug. 2014, DOI: 10.1109/TPEL.2013.2286830.

(22) D. Hou, M. Mu, F. C. Lee and Q. Li: " New High-Frequency Core Loss Measurement Method With Partial Cancellation Concept," in IEEE Transactions on Power Electronics, Vol. 32, No. 4, pp. 2987-2994, April 2017, DOI: 10.1109/TPEL.2016.2573273.

(23) Yuji Uehara, Kenji Kono, Yuki Sato, Satoshi Okamoto: "High Frequency Loss Measurement of Powder Materials by Resonance Method," Transactions of the Institute of Electrical Engineers of Japan, A (Journal of the Division of Fundamentals, Materials and Common Technology), 143(12), pp.374-378.

(24) Y. Sato et al: " Accuracy Investigation of High-Frequency Core-Loss Measurement for Low-Permeability Magnetic Materials ", in IEEE Transactions on Magnetics, Vol. 59, No. 11, pp. 1-5, Nov. 2023, Art no. 6301105, doi: 10.1109/TMAG.2023.3283955.

(25) E. Ferrara et al: "Characterization and assessment of the wideband magnetic properties of nanocrystalline alloys and soft ferrites ", J. Mater. Res., Vol. 33(15), pp. 2120-2137, Aug. 2018.

(26) M. Mu, Q. Li, D. J. Gilham, F. C. Lee and K. D. T. Ngo: " New Core Loss Measurement Method for High-Frequency Magnetic Materials," in IEEE Transactions on Power Electronics, Vol. 29, No. 8, pp. 4374-4381, Aug. 2014, DOI: 10.1109/TPEL.2013.2286830.

(27) D. Hou, M. Mu, F. C. Lee and Q. Li: " New High-Frequency Core Loss Measurement Method With Partial Cancellation Concept," in IEEE Transactions on Power Electronics, Vol. 32, No. 4, pp. 2987-2994, April 2017, DOI: 10.1109/TPEL.2016.2573273.

(28) M. Mu, *et al*: "A high-frequency core loss measurement method for arbitrary excitation", Proc. APEC 2011, pp. 157-162 (2011).

(29) Ibuchi, Funaki: "A Study on the Influence of Parasitic Components in the Actual Iron Loss Evaluation Results of Magnetic Components Applied to Power Conversion Circuits," IEEJ Technical Report, MAG-22-055, LD-22-038, pp. 39-44 (2022).

(30) Ibuchi, Funaki: "Study on High Frequency Iron Loss Measurement Method of Magnetic Elements Applied to Power Conversion Circuits," IEEJ Technical Report, MAG-22-071, pp. 34-40 (2022).

(31) Ibuchi, Funaki: "Study on Iron Loss Measurement of Compacted Materials Based on Partial Cancellation Method," The Japan Institute of Metals, 174th SPSJ Annual Meeting, S3-6 (2024).

(32) Ibuchi, Funaki: "A Study on the Mounting Method and Measurement Accuracy of Coaxial Shunt Resistor in Switching Current Measurement," IEEJ Technical Report, SPC-21-122, MD-21-109, pp.91-96 (2021).

(33) Ibuchi, Funaki: "A Study on Performance Evaluation of Voltage and Current Probes Based on Gain-Phase Characteristics and Transient Response Measurement," IEEJ Technical Report, EMC-22-002, pp. 5-10 (2022)

(34) Y. Uehara, Y. Sato, S. Okamoto, T. Taniguchi, H. Tsukahara, and N. Ono: "Core loss measurements and loss separation of power inductor under triangular excitation", 49th Annual Conference on Magnetics in Japan, 18pD-5, pp.247 (2025).

(35) Ibuchi, Funaki: "Investigation on the Issues of Loss Evaluation in Real Circuit Operation of Magnetic Powder Core for High Frequency Switching Converter," IEEJ Technical Report, MAG-24-078, pp.31-36 (2024).

(36) T. Onuma, N. Ono, and S. Okamoto: "Feature analysis on iron loss behaviors of various soft magnetic cores under DC bias fields". , Journal of the Magnetics Society of Japan 49.1 (2025): 21-26.

(37) T. Onuma, Z. Li and S. Okamoto: " Feature Analysis on B-H Curves of Dust Cores Under the Application of DC Bias Field", in IEEE Transactions on Magnetics, Vol. 59, No. 11, pp. 1-5, Nov. 2023, Art no. 6000705, DOI: 10.1109/TMAG.2023.3281548.

(38) S. Flohrer, R. Schäfer, J. McCord, S. Roth, L. Schultz, and G. Herzer, "Magnetization loss and domain refinement in nanocrystalline tape wound cores," Acta Materialia, 54(12), 3253 (2006), DOI: 10.1016/j.actamat.2006.03.011.

(39) Magnetic Imaging Handbook", edited by Magnetics Society of Japan, Kyoritsu Shuppan K.K., 2010, ISBN 978-4-320-03468-6.

(40) Alex Hubert, Rudolf Schäfer, "Magnetic Domains - The Analysyses of Magnetic Microstructures", Springer- Verlag Berlin Heidelberg 1998, ISBN 978-3-540-64108-7.

(41) Ed, Akinobu Yamaguchi, Atsufumi Hirohata, and Bethanie Stadler, "Nanomagnetic Materials - Fabrication, Characterization and Application", Elsevier 2021, ISBN 9780128223499.

(42) T. Ogasawara, "Improvement in spatial frequency characteristics of magneto-optical Kerr microscopy," Japanese Journal of Applied Physics, 56(10), 108002 (2017), DOI: 10.7567/JJAP.56.108002.

(43) T. Ogasawara, and A. Yamaguchi, "Observation of frequency dependent resonances in magnetic vortex core gyration using time-resolved magneto-optical Kerr microscope with pulsed semiconductor laser illumination", Japanese Journal of Applied Physics, 61(1), 018001 (2022), DOI: 10.35848/1347-4065/ac3ea6.

(44) R. Gautam, S. Hiramoto, N. Kulesh, H. Mamiya, S. Okamoto, N. Ono, T. Ogasawara, T. Ohkubo and H. Sepehri-Amin : "Ultra-low core loss in Fe- enriched soft magnetic ribbons enabled by nanostructure and high-frequency domain engineering", Nat Commun, 16, 8022, https://doi.org /10.1038/s41467-025-63139-1, (2025).

(45) Taisuke Sasaki, Jun Uzumihashi, Tadakatsu Okubo, Kazuhiro Takarano: "Recent progress in 3D atom probe analysis method", Materia, vol.61, no.2, 61-72,

DOI :10.2320/materia.61.72, (2022).
(46) Y.M. Chen, T. Ohkubo, M. Ohta, Y. Yoshizawa and K. Hono : "Three-dimensional atom probe study of Fe-B-based nanocrystalline soft magnetic materials", Acta Materialia, Volume 57, Issue 15, Pages 4463-4472, DOI :10.1016/j.actamat.2009.06.008, (2009).

1.5 Transformers and inductors

Keyword: Soft magnetic materials, Magnetic circuit, Magnetic core, Winding, Iron loss, Copper loss, Circuit system, Efficiency

1.5.1 Summary

This section summarizes the typical characteristics required of transformers and inductors used in DC-DC converters.

(1) Circuit topology and magnetic components used in the operating frequency and power bands

Figure 2.1.5.1 shows the circuit topology and magnetic components used, corresponding to the switching frequency and power capacity of a DC-DC converter. Corresponding to the trade-off between rated voltage/current and frequency in power semiconductor devices, there is a similar trade-off relationship between switching frequency and power capacity in DC-DC converters. It should also be noted that the operating modes (e.g., excitation operation and winding current) of the transformers and inductors used in these converters are different for each circuit configuration.

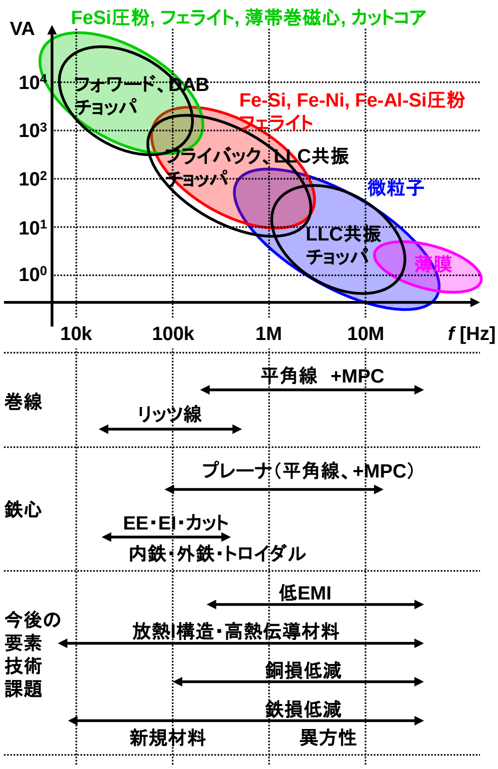

Figure 2.1.5.1 Circuit topology and magnetic components used in the switching frequency and power capacity of a DC-DC converter

In the frequency range of several kHz to 100 kHz, there are high-power (approximately several hundred kW to 1 kW) DC-DC converters using Si-IGBT and SiC power semiconductors, while bridge and forward types are used as isolated converters using transformers above 10 kHz. In particular, DAB (Dual Active Bridge) converters are capable of bi-directional power conversion by employing a full bridge configuration on the primary and secondary sides, and are also capable of soft switching. On the other hand, boost choppers are used in power conditioners for photovoltaic power generation systems and in the electric propulsion powertrains of hybrid and electric vehicles, and inductors for high voltage and high current are used.

Converters with operating frequencies from 100 kHz to 1 MHz employ Si power MOS-FETs or GaN-FETs and generally cover power ranging from several kW to several tens of watts. Flyback and LLC resonant are the most common isolated converters using transformers. In particular, LLC resonance is characterized by low noise and high efficiency due to zero-voltage soft switching of power semiconductors.

In the 1 MHz to 10 MHz operating frequency range, GaN-FETs are often used, resonant converters are the most common isolated type, and Ni-Zn ferrites are used in transformer cores. Chopper circuits are often used in point-of-load (POL) applications to supply low-voltage, high-current power to CPUs and GPUs. Ni-Zn ferrites and fine particle composite cores are used in inductors.

Although some resonant isolation type converters using Ni-Zn ferrite have been proposed for the ultra-high frequency range above 10 MHz, research and development of such converters is still in progress. Integrated voltage regulators (IVRs) for CPUs and GPUs are mostly used as step-down choppers, and multiphase converters employing soft magnetic thin-film coupled inductors or carbonyl iron powder (CIP) composite core inductor arrays as a replacement for air-core inductors have been put to practical use. The multiphase converters employing soft magnetic thin-film coupled inductors or composite iron-powder (CIP) core inductor arrays instead of air-core inductors are in practical use.

[Toshiro Sato]

(2) Typical characteristics required

a. Transformers and inductors in common

First, there are size and shape, such as volume, mounting area, and height. Magnetic components are typical components in power electronics that are difficult to reduce in size. In addition, since magnetic components are mainly made of metallic materials (magnetic metal and copper wire) and are the heaviest components in power electronics systems, weight is an equally important factor. Other factors include thermal conductivity and temperature coefficient. Although the thermal conductivity of the metal part is high, the thermal conductivity of the magnetic component as a whole depends on the coating material, adhesive, and shape, while the temperature coefficient must have good characteristics for high temperature operation resistance and thermal runaway resistance.

b. Transformer

The larger the excitation inductance, the lower the excitation current, which contributes to improving the efficiency of the conversion circuit. However, if the inductance is unnecessarily large, the loss increases due to increased winding resistance. However, if it is unnecessarily large, losses increase due to increased winding resistance. It also hinders miniaturization and weight reduction. The use of high permeability materials also greatly contributes to increasing the excitation inductance, but there is a trade-off with frequency characteristics. Next, except for coupled inductors, the coupling coefficient is a performance index that does not exist for inductors. Basically, a coupling coefficient as close to 1 as possible is ideal and desirable because it has no leakage inductance, but in some resonant circuit systems using leakage inductance, it may be intentionally set around 0.8 to 0.95. Losses, like inductors, can be largely divided into iron loss and copper loss, but the loss mechanisms and points to note differ due to differences in operating methods and structures. Iron loss depends greatly on the core material, magnetic flux density, and frequency. Forward and flyback converters operate in the first quadrant of the B-H plane, and flyback converters in particular must pay attention to magnetic saturation due to the DC superposed magnetic field. On the other hand, the bridge type operates in a loop that travels between the first and third quadrants, and the magnetic field amplitude can be increased. As for copper loss, transformers have no DC current, so they have AC copper loss. If the turn ratio is large, the current ratio between the primary and secondary windings differs greatly, so it is necessary to select an appropriate winding cross-sectional area according to the current value. In addition, the strength of the proximity effect and copper loss vary greatly depending on how the primary and secondary windings are wound. Furthermore, the inter-winding capacitance and self-resonant frequency are also important characteristics. In addition to the capacitance between the primary and secondary windings, there is also capacitance between the primary and secondary windings. The self-resonant frequency is determined by these capacitances and inductances, and must be set sufficiently higher than the switching frequency (approximately 10 times or more). In addition, unnecessary capacitive coupling must be avoided because the capacitance between the primary and secondary windings provides a conduction path for common-mode noise currents. Then there is the isolation performance. For isolated converters, the withstand voltage between the primary and secondary windings is particularly important, and compliance with the relevant standards is required. High isolation performance is basically a trade-off between size, inductance, coupling coefficient, and loss.

c. Inductors

The larger the inductance of an inductor, the lower the current ripple, which is effective in reducing power device losses. However, if the inductance is unnecessarily large, it tends to increase the inductor loss. It also hinders miniaturization and weight reduction. The use of high permeability materials also contributes greatly to increasing inductance, but there is a trade-off with frequency characteristics. DC superposition characteristics are also important for inductors. When DC current is present, a DC magnetic field component is always applied, so care must be taken to avoid inductance degradation and magnetic saturation, both of which require excellent characteristics. Since a sudden decrease in inductance due to magnetic saturation can lead to fatal operation failure, it is desirable for the inductance to decrease slowly. In many cases, magnetic materials with low magnetic permeability and magnetic path gaps are provided to prevent magnetic saturation. Next, we will discuss loss. Since the inductor current is equal to the excitation current, the iron loss tends to increase as the ripple current increases. As for copper loss, since DC current is included, conduction loss due to DC resistance accounts for a large proportion. Since materials with low magnetic permeability and gaps to reduce effective permeability are used, attention must be paid to the increase in AC copper loss due to leakage flux. The self-resonant frequency is determined by the inductor's own inter-winding capacitance and inductance. The self-resonant frequency should be set sufficiently higher than the switching frequency (approximately 10 times or more).

1.5.2 (Power) transformer

(1) For converters below 100 kHz (1 kW or more)

For DC-DC converters below 100 kHz and above 1 kW, typical topologies such as forward converters and half-bridge/full-bridge converters are discussed, and the internal and external iron type transformers used in these converters are described. The excitation of transformers used in forward converters operates using only the first quadrant of the B-H plane, while half-bridge and full-bridge transformers are excited to draw the entire B-H plane symmetrically at the origin. Therefore, the bridge configuration can provide high magnetic field amplitude and is suited for circuits with high circuit voltage and large power rating. However, the bridge type has the risk of accumulation of DC magnetic field components due to unbalanced excitation operation (polarization) and resulting magnetic saturation. In addition, magnetic saturation suppression by inserting a gap in the transformer is necessary.

a. Forward converter

First, the circuit and operating waveforms of the forward converter are shown in **Figure 2.1.5.2**. Power is transferred from winding n_1 to n_2 by turning on M_1. At this time, the primary winding n_1 of the transformer flows the primary equivalent of the excitation current of the magnetic core and the load current transferred to the secondary side. Since the magnetic flux for the load current cancels each other out on the primary and secondary sides, only the flux for the excitation current flows through the magnetic core. On the secondary side, the choke inductor L_1 is excited via D_2, and the current I_{L1} of L_1 increases like a chopper. When M_1 is then turned off, no current flows in winding n_1 because there is no current in M1, but winding n_3 is used as a path for the excitation current of the magnetic core. In other words, diode ${}_{D1}$ turns on and the excitation current flows through winding n_3 to the input power supply V_{IN}. The voltage of back EMF-V_{IN} is generated in the primary winding from the time of M_1 turn-off, and the excitation current gradually decreases until it eventually reaches zero, at which point the back EMF also disappears (called the resetting of the excitation current). The state is maintained until the next turn-on of M_1. During this time, the inductor ${}_{IL1}$ on the secondary side regenerates through diode D_3 as in a normal buck chopper, and the current decreases. Note that the transformer only needs to handle the magnetic flux for the excitation current, and the resetting of the excitation current prevents the excitation current from continuing to accumulate and causing the magnetic core to become unbalanced.

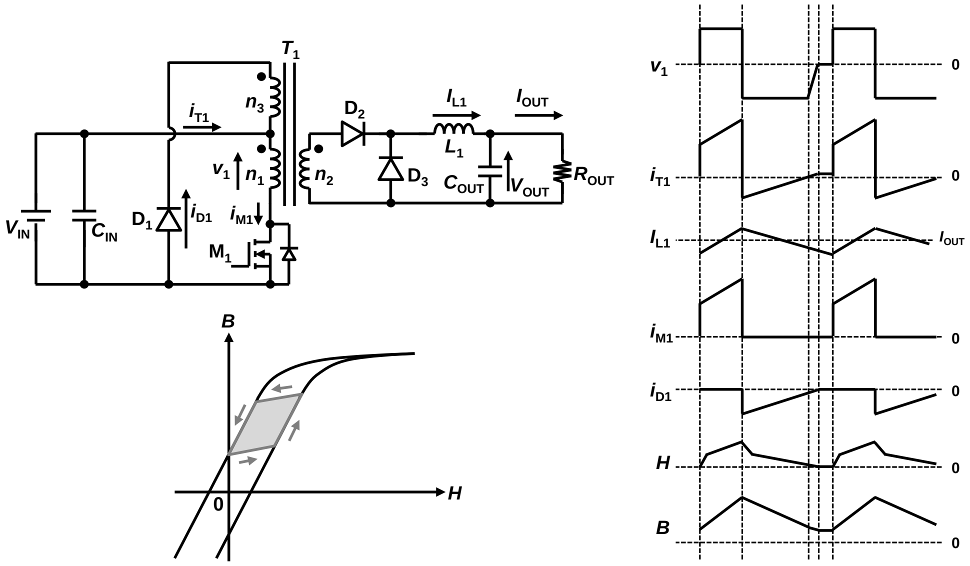

Figure 2.1.5.2 Forward Converter

b. Full bridge converter

A full-bridge converter is then shown in **Figure 2.1.5.3**. Since V_{IN} and-V_{IN} are alternately applied to the transformer, this circuit operates in the B-H plane over a wide range and is used when a large output power is required. On the other hand, because the amplitude of the B-H is large, the amount of iron loss generated tends to be relatively large. In this full-bridge converter operation, the excitation current often flows through the secondary side when the primary side switch is turned off. In addition, since the full-bridge converter actually generates demagnetization even when the switching timing is slightly shifted, capacitors are sometimes inserted in series with the transformer to cut the DC component. In a full-bridge converter, the excitation current flows through the secondary side during the period when v_1 is 0 V, and the conduction loss is an issue. The switching losses associated with turning the transistor on and off are also an issue.

c. DAB converter

Figure 2.1.5. 4 shows a DAB converter, which also employs the primary side full-bridge structure of **Figure 2.1.5.3** on the secondary side, and is attracting attention in high-power converters that require bidirectional power transmission, such as charging and discharging. By shifting the secondary side full-bridge operation by a phase difference φrelative to the primary side full-bridge operation, which is the reference, power is supplied from the phase advance side to the phase lag side. In the case of **Figure 2.1.5.4**, power is sent from the primary side to the secondary side. The output power is zero when φ is 0° and maximum at 90° . Under appropriate operating conditions, zero-voltage switching is possible and switching losses can be significantly reduced.

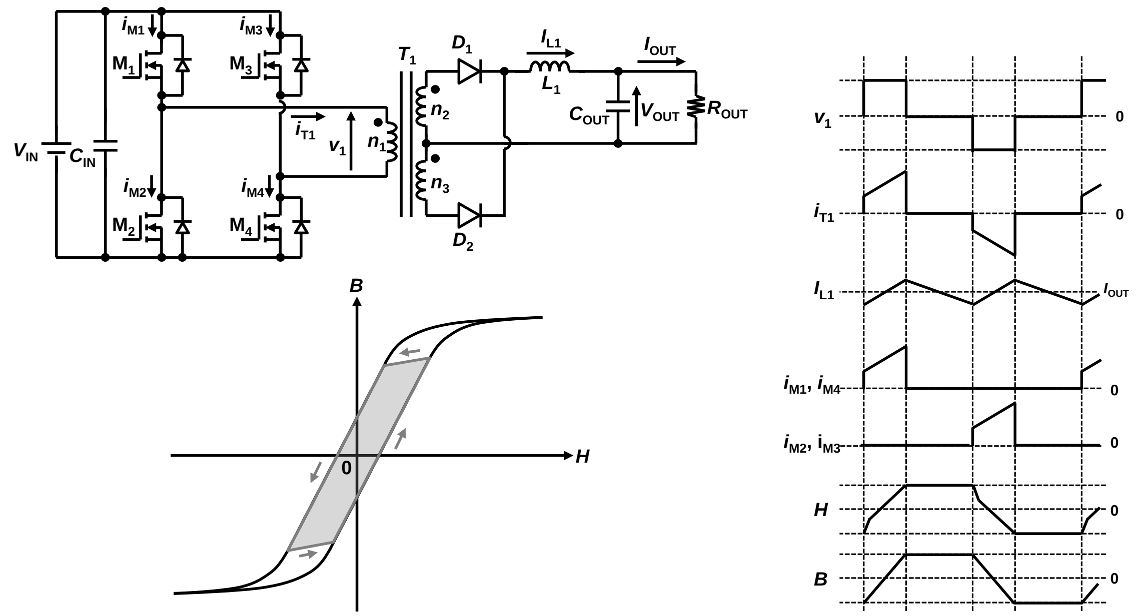

Figure 2.1.5.3 Full Bridge Converter

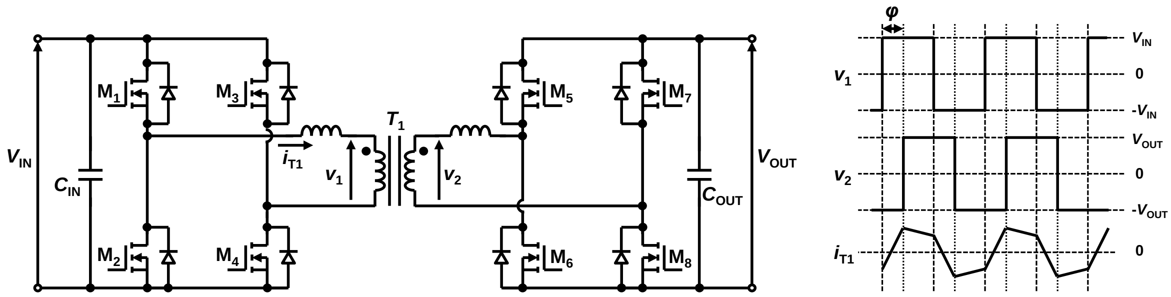

Figure 2.1.5.4 DAB Converter

d. Magnetic core material

While electromagnetic steel sheets are often used as the core material for transformers at frequencies up to several kHz, Mn-Zn ferrite, Fe-based amorphous and Fe-based nanocrystalline thin strips (e.g., FINEMET) are used for insulated converters in the frequency range of 10 kHz to 100 kHz for wound cores and laminated cut cores (**Figure 2.1.5.5**) [(1)]. The specific permeability is often between several thousand and several tens of thousands, and since Fe-based nanocrystalline thin strips have extremely low magnetostriction, they are suitable for low-noise magnetic cores in the audible band below 20 kHz. However, Fe-based nanocrystalline thin strips are more expensive than Fe-based amorphous materials. The saturation magnetic flux density of Fe-based amorphous material is about 1 T, while that of Fe-based nanocrystalline thin film material is as high as 1.5 T, making it suitable for large-capacity power supplies. On the other hand, Mn-Zn ferrite has lower loss above about 50 kHz. Since ferrite is inexpensive and easy to process, various core shapes are available as described below. On the other hand, since the saturation magnetic flux density is as low as 0.5 to 0.7 T, ferrite is often used in power supplies with small power capacity.

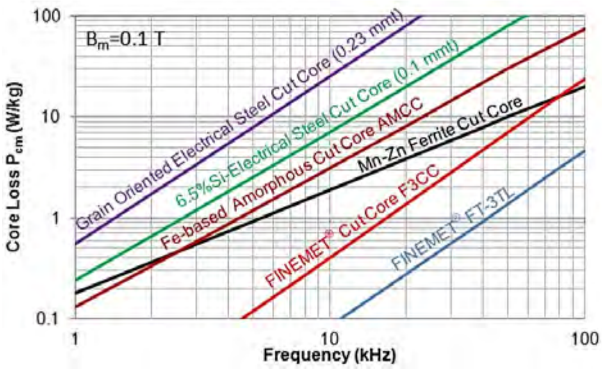

Figure 2.1.5.5 Iron Loss vs. Operating Frequency (1)

e. Structure and shape of the magnetic core

The structure of the transformer core can be divided into an inner-iron type and an outer-iron type transformer as shown in **Figure 2.1.5.6**. In the inner-iron type, the magnetic core is covered by the coils, while in the outer-iron type, the core covers the coils and the magnetic core is outside the coils. In the inner iron type, the primary and secondary windings can be wound on different legs, while in the outer iron type, the primary and secondary windings are wound on the same legs. In both cases, the core windings and magnetic cores are fastened with bands or tapes to secure the core, and lead terminals or insertion/removal terminals are provided for board mounting. Ferrite is particularly easy to form and is available in a variety of shapes.

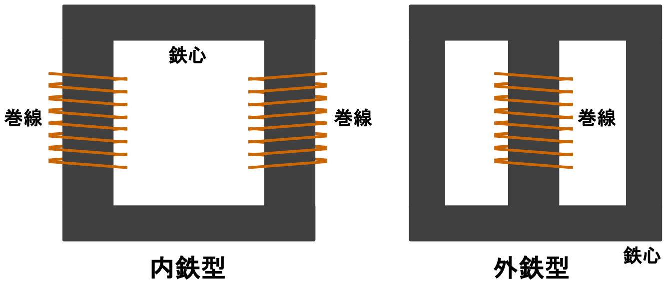

Figure 2.1.5.6 Inner- and outer-iron type magnetic core structures

As shown in **Figure 2.1.5.7**, there are various types of magnetic core shapes, with differences in the processing method depending on the material. (2) Among the characteristic internal iron types using Mn-Zn ferrite are toroidal, UU core, and UI core. The toroidal core is easy to realize a closed magnetic circuit structure with low leakage flux and a uniform magnetic path cross-section, making it easy to design. The gap between the contact surfaces of the two magnetic cores generates leakage flux, and the coupling coefficient is lower than that of a toroidal core made of the same material that realizes a completely closed magnetic circuit. In addition, by winding the primary and secondary windings on separate legs, it is possible to improve the dielectric strength and reduce the capacitance between the windings. However, in this case, it is necessary to deal with the proximity effect and other factors that increase AC copper loss and lower the coupling coefficient.

The EI and EE cores have prismatic legs and a uniform magnetic path cross-section, making magnetic circuit design easy and allowing for greater flexibility in how the cores are placed (vertically or horizontally). However, because of the low volume utilization due to gaps in the winding of thick windings, thin windings are often used, and they are relatively unsuitable for high currents. The EER core is an improved version of the EE core, in which the middle legs are cylindrical in shape. Therefore, even thicker windings can be wound efficiently, making it suitable for large currents. The PQ core is a further improved version of the EER core, with a larger cross-sectional area of the outer legs to suppress magnetic saturation. In addition, there are other complex core shapes, such as pot cores and RM cores, that are suitable for high-density mounting.

For strip-shaped materials (strip materials) such as Fe-based amorphous and Fe-based nanocrystalline thin strips that are not ferrite, wound cores (uncut cores) and cut cores are commonly used (see **Figure 2.1.5.8**) (3). The magnetic core is formed by winding the strip material into a die in a number of layers. The core is then annealed to remove distortion and nanocrystallize, bonded and adhered, cut, and polished on the cut surface. If no cutting is performed, a closed magnetic path structure called a wound core (non-cut core) is formed. A wrapped core is one in which the cut parts are overlapped and assembled into a coil without gluing or bonding, and then tightened with a band or the like. A core similar to a ferrite UU core is called an SC core, and one similar to an EE core is called an EC core. SCP cores and ECP cores also exist with slightly different cross-sections.

Figure 2.1.5.7 Typical Shape of Magnetic Core (2)

Figure 2.1.5.8 Thin Strip Material Cut Cores (3)

f. Winding

As described in detail in Section 1.5.4, round wire and Litz wire (described below) are generally used as the winding wire. As the operating frequency increases, the effective cross-sectional area of the copper wire decreases due to the skin effect, resulting in increased resistance and copper loss, so a thin winding with a small cross-sectional area is used to match the corresponding frequency, such as Litz wire. However, the problem with Litz wire is that its occupancy ratio is low. In addition, AC copper loss reduction due to the proximity effect can be achieved by interleaved winding, in which the secondary and primary windings are wired alternately. On the other hand, it should be noted that interleaved windings increase stray capacitance between the primary and secondary windings, contributing to the formation of common-mode current paths that can be a noise source. In winding schemes such as center-tap, the coupling symmetry of the primary and secondary windings is broken, resulting in current imbalance, so physical symmetry is important and symmetrical interleaved windings should be employed.

In transformers using such magnetic core materials, structures, and windings, the coupling coefficient without a gap is often 0.99 or higher due to high permeability, but the maximum value of the excitation flux density must be kept low to avoid magnetic saturation. On the other hand, when an air gap is provided to reduce the effective permeability, fringing magnetic flux is generated in the gap. This is a factor that reduces the coupling coefficient and increases the eddy current loss (AC copper loss) caused by the fringing magnetic flux linking with the winding.

(2) For 100 kHz to 1 MHz (100 W to 1 kW) converters

For the 100 kHz to 1 MHz (100 W to 1 kW) converters, flyback converters and LLC resonant converters are introduced. In this frequency range, PCB transformers, in which the windings are formed in a printed circuit board (PCB) pattern, are often used. PCB transformers have excellent low profile and high dimensional accuracy for good winding coupling. Thin and flat ER cores are also used for the magnetic cores. However, it is necessary to design the transformer at the same time as the circuit design, so it is difficult to change the transformer after the PCB is manufactured. In addition, although the flatness is high, the wiring width is wide and the area tends to expand.

a. Flyback converter

Figure 2.1.5.9 shows a simplified circuit diagram of a flyback converter and its operation. The flyback converter has the advantage of being able to configure an isolated power supply with a small number of elements. In operation, M_1 is first turned on, current flows through the transformer, and energy is stored in the magnetic core. At this time, no current flows on the secondary side because of the reverse voltage of the diode. Then, when M_1 is turned off, there is no current on the primary side, so the excitation current is released from the secondary side to the load. In other words, the excitation current is transferred, and unlike forward converters and full-bridge converters, current does not flow simultaneously in the primary and secondary windings. In addition, the DC current (magnetic field) component due to the load current is superimposed on the transformer. Therefore, although the converter uses a transformer, it operates similar to an inductor, which is described below, and has the disadvantage of being prone to magnetic saturation. Therefore, a high saturation magnetic flux density and DC superposition characteristics are important indicators. A high coupling coefficient is also required because a low coupling coefficient and leakage inductance will cause a large reverse voltage to be generated in the power device due to leakage inductance when switching. Because of these characteristics, the power supply is often used as a small-capacity isolated power supply of less than 100 W. Mn-Zn ferrite core material is the most common magnetic core material in this operating frequency band. Gaps are often used to prevent magnetic saturation, but consideration must be given to the winding, magnetic core, and gap shape to avoid generating a large amount of leakage flux. Although iron-based dust cores and pressed cores have high saturation magnetic flux density, their low magnetic permeability lowers the coupling coefficient, which is a problem. Round wire and Litz wire are used as the winding wire.

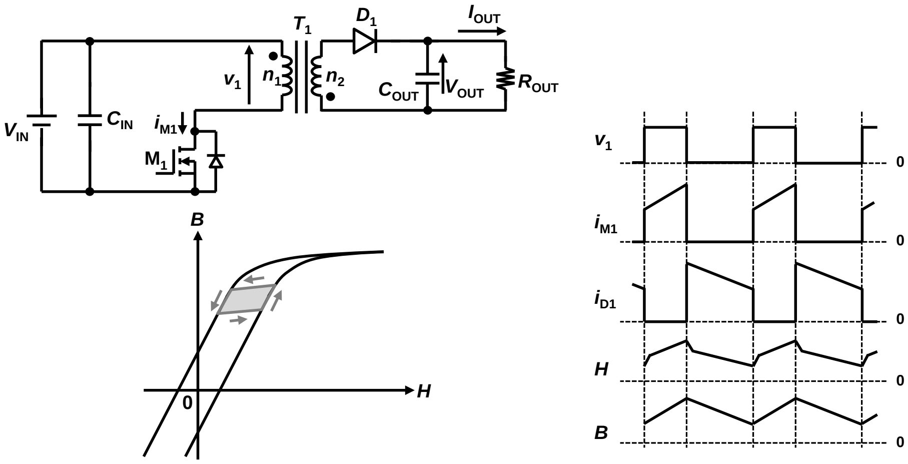

Figure 2.1.5.9 Flyback Converter

[Kousuke Miyaji]

b. LLC resonant converter

LLC resonant converters are often used for capacities from 100 W to around 1 kW, and they offer low noise, high efficiency, and high-frequency switching for smaller equipment with fewer components and soft switching (4). Because of these features, LLC resonant converters are used as server power supplies in data centers, and further improvements in efficiency are required as the information society develops (5).

To improve the efficiency of the LLC resonant converter, it is effective to reduce the primary current of the transformer. To achieve this, it is necessary to increase the excitation inductance and excitation frequency. However, since there is an upper limit to the excitation inductance due to soft switching conditions (6), the excitation frequency must be increased. Increasing the excitation frequency can be achieved by decreasing the transformer coupling coefficient. However, in the conventional method, the reduction of the coupling coefficient is accompanied by a significant reduction of the excitation inductance. Therefore, there is concern about increased losses due to the increase in excitation current (7). Therefore, a method to reduce the coupling coefficient while maintaining the excitation inductance is needed.

The use of magnetic tape-wound square wires in transformers has been investigated as a method to reduce the coupling coefficient while maintaining the excitation inductance (8).

c. Transformer case study of LLC resonant converter

Figure 2.1.5. 10 shows the circuit configuration of the LLC resonant converter, and **Figure 2.1.5.11** shows the gain characteristics of the LLC resonant converter with the coupling coefficient as a parameter. The coupling coefficients are 0.95, 0.9, 0.85, and 0.8, respectively. The required gain is determined by the specification of the LLC resonant converter; here the gain G = 1.26. The frequency that intersects the required gain is the excitation frequency. The figure shows that decreasing the coupling coefficient increases the excitation frequency, and that to improve the efficiency of the LLC resonant converter, it is necessary to decrease the primary current by decreasing the coupling coefficient.

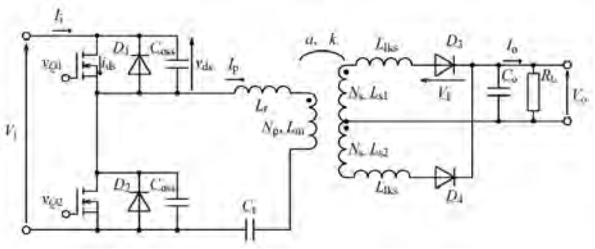

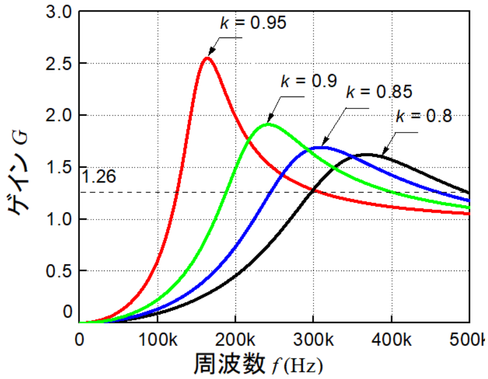

Figure 2.1.5.10 Circuit configuration of LLC resonant converter **Figure 2.1.5.11** Coupling factor k as a parameter

Gain-Frequency Response

($_{Po}$ = 800 W, $_{fsh}$ = 500 $_{kHz}$, Lm = 22 μH)

Figure 2.1.5.12 shows the method of increasing leakage inductance. In the conventional method of increasing leakage inductance by lengthening the gap, the excitation inductance decreases due to the decrease in the main magnetic flux. In addition, the fringing magnetic flux increases and the AC copper loss increases. By winding the magnetic tape around the square wire, the magnetic flux can be guided to the magnetic tape, increasing the leakage flux without decreasing the main flux and reducing the AC copper loss.

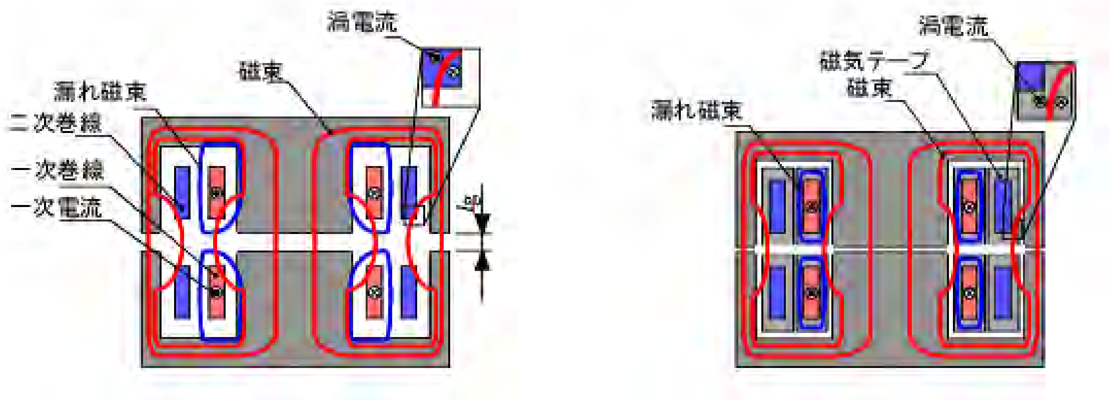

(a) Conventional method with a long air gap (b) Method using magnetic tape

Figure 2.1.5.12 Method of increasing leakage inductance

Figure 2.1.5.13 shows the transformer structure of the LLC resonant converter. The transformer core material is ML27D (PROTERIAL), which has excellent iron loss characteristics from 100 kHz to 500 kHz. The magnetic permeability is 2,900. The magnetic core has a PQ shape. The dimensions of the primary and secondary flat wires are 0.3 × 4 mm^2 and 0. 4 × 5 mm^2, respectively.

Table 2.1.5.1 shows the specifications of the LLC resonant converter.

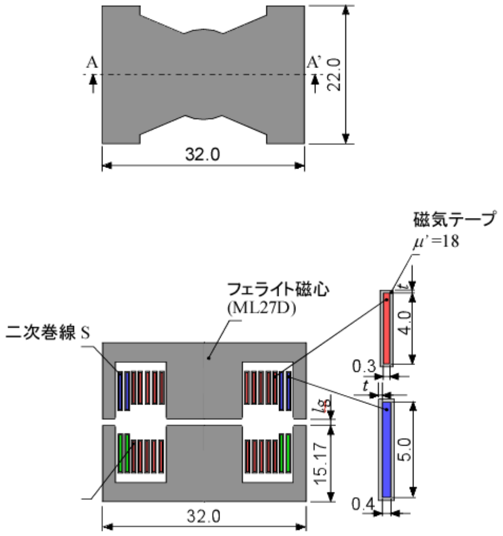

Figure 2.1.5.13 Transformer Structure (Unit: mm)

Table 2.1.5.1 LLC converter specifications

(data) item	numerical value
Input voltage V_i (V)	380
Output voltage V_o (V)	48
Output P_{o}(W)	800
Resonance frequency f_{sh} (kHz)	500
Coupling coefficient k	0.85～0.95
Volume ratio a	5
Number of primary windings N_p	10
Number of secondary windings N_s	2
Debt time t_{dead} (ns)	40-60
Excitation inductance L_m (μH)	19.7 to 29.5

Figure 2.1.5.14 shows the impedance characteristics of the transformer. The coupling coefficient decreased from 0.91 to 0.88 with the application of magnetic tape. The primary self-inductance increased from 23.8 μH to 24.6 μH with the application of magnetic tape. The excitation inductance was 21.7 μH and 21.6 μH before and after the magnetic tape was applied, respectively, and the excitation inductance was maintained. The AC resistance when the secondary side was open and when the secondary side was short-circuited was reduced by 18.8% from 282 mΩ to 229 mΩ and by 37.9% from 671 mΩ to 417 mΩ, respectively, by the application of magnetic tape. The coupling coefficient and AC copper loss were reduced by the magnetic flux induced in the magnetic tape as described above.

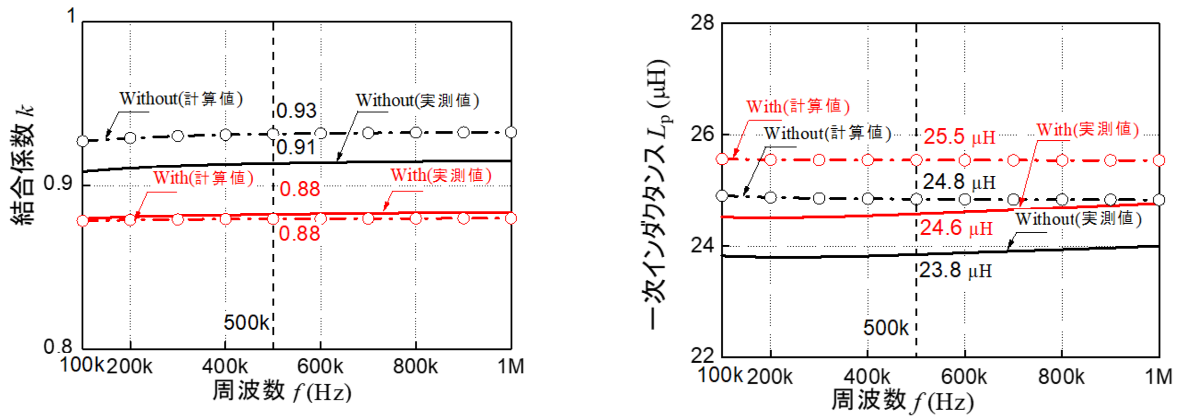

(a) Coupling coefficient (b) Primary inductance

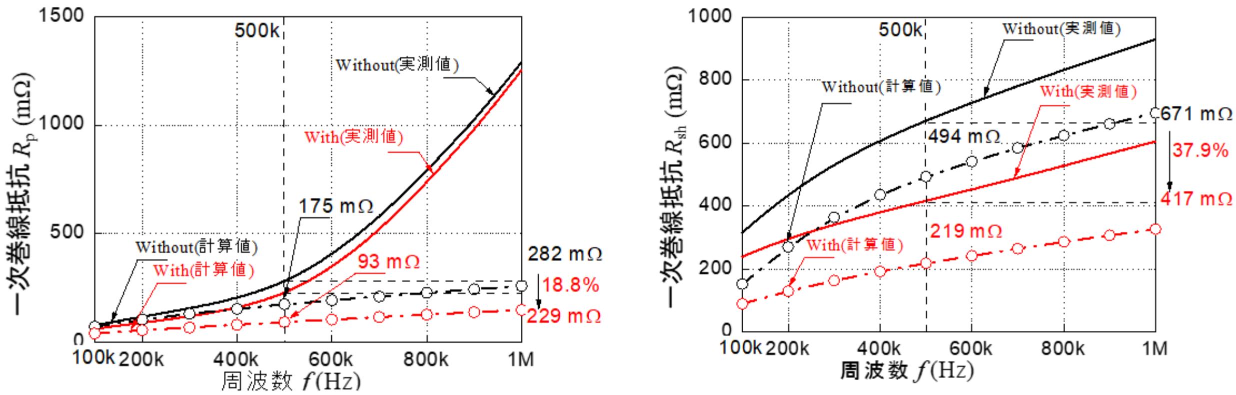

(c) AC resistance at open secondary (d) AC resistance at short secondary

Figure 2.1.5.14 Impedance characteristics of an LLC transformer

d. Converter application examples of LLC resonant converter transformers

The transformer was mounted on an LLC resonant converter and the excitation frequency characteristics, primary transformer voltage, efficiency characteristics, and heat generation characteristics were measured.

Figure 2.1.5.15 shows the efficiency characteristics of the converter. The efficiency of the converter improved by 0.54 percentage points to 94.16% and 94.7% before and after the application of magnetic tape at 600 W output, respectively. The loss was reduced by 3.92 W at 800 W output by the application of the magnetic tape.

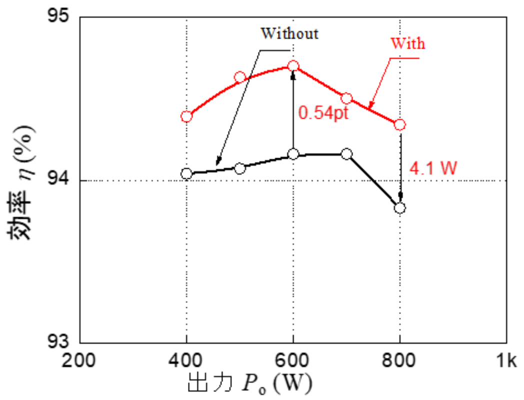

Figure 2.1.5.15 Converter Efficiency Characteristics

Figure 2.1.5.16 shows the appearance and temperature of the transformer during excitation of the LLC resonant converter. The temperatures of the windings were 58 ℃ and 102 ℃ with and without magnetic tape, respectively, a decrease of 34 ℃. This is due to a decrease in the AC copper loss in the windings. This is due to the reduction of AC copper loss in the windings. The temperatures of the magnetic cores with and without magnetic tape were 43.1 ℃ and 64.6 ℃, respectively, a decrease of 21.5 ℃. The temperatures of the magnetic cores with and without magnetic tape were 43.1 ℃ and 64.6 ℃, respectively, a decrease of 21.5 ℃. There was no increase in heat generation in the magnetic core with increasing excitation frequency.

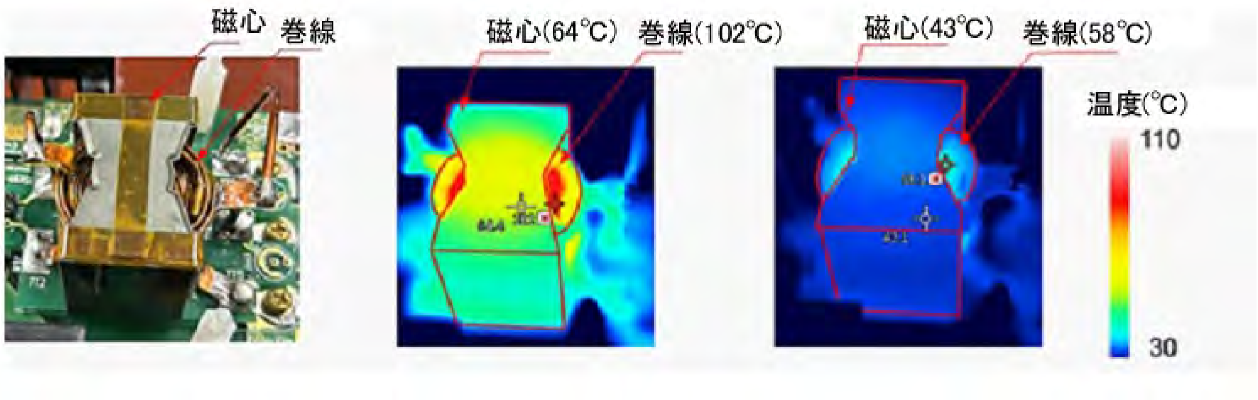

(a) Appearance of LLC transformer (b) Magnetic tape: No (c) Magnetic tape: Yes

Figure 2.1.5.16 Temperature of LLC transformer depending on appearance of LLC transformer and presence of magnetic tape (output 800 W, frequency 500 kHz)

[Tsutomu Mizuno]

(3) For converters above 1 MHz and below 100 W

As described in "1.2.2 Powder Cores and Fine-Particle Composite Cores," the specific permeability of low-loss soft magnetic materials in the Beyond MHz band is several tens or less, and when employed in a transformer, the generation of leakage inductance is unavoidable. Therefore, the mainstream is to implement them in resonant converters that utilize the leakage inductance for resonance. Here, we introduce the application of Ni-Zn ferrite and fine particle composite cores to transformers and examples of their implementation in converters, and also summarize the issues involved.

a. Ni-Zn ferrite transformers

Examples of Research and Development

Hanson et al. [9] benchmarked various power core materials for Beyond MHz at iron losses of less than 1,000 kW/m^3 and compared the $f \cdot B_m$ product (f: frequency, B_m: magnetic flux density amplitude, the larger the amplitude, the smaller the core with constant losses) at constant iron loss, or a modified $f \cdot B_m^{3/4}$ product. As a result of comparing the $f \cdot B_\mathrm{m}^{3/4}$ product, which is a modified version of the $f \cdot B_m^{3/4}$ product, Fair Rite's Ni-Zn ferrite (67 material, specific permeability: 40) is superior in the range of 2 to 20 MHz.

In fact, Sagneri [10] of Finsix constructed a transformer using 67 material and developed a Φ2 resonant isolation converter for a 65 W output AC adapter. **Figure 2.1.5.17** shows the main circuit topology of the Φ2 resonant isolation converter, and it has been confirmed that ZVS is achieved for both turn-on and turn-off of the GaN-FET in 50 MHz switching operation. In fact, the Φ2 resonant isolation converter employed in the AC adapter operates at 13.56 MHz, and the volume of the transformer magnetic core is 1.2 cm^3, which is 1/12 the size of the 100 kHz flyback transformer with Mn-Zn ferrite used in the conventional AC adapter. The transformer has a transmission power density of 680 W/inch3 (41.5 W/cm^3) and an efficiency of 96%.

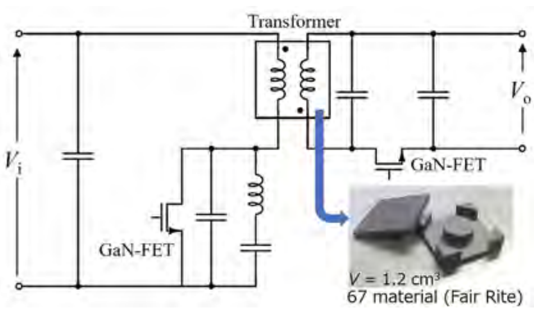

Figure 2.1.5.17 Main circuit topology of a Φ2 resonant isolated converter

As another example of applying Ni-Zn ferrite to MHz-band transformers, Hariya et al. [11] of TDK reported a 5 MHz switching PWM-controlled current resonant converter employing a Ni-Zn ferrite planar transformer as the main transformer, with PWM control of the primary side main switch and secondary side rectifier switch phase shift control. **Figure 2.1.5.18** shows the main circuit topology and an external view of the converter, with input voltage V_i: 42 to 53 V and output voltage V_o and current I_o: 12 V and 8 A (96 W). The footprint of the planar transformer is 19.4 x 8.9 mm, but the magnetic properties of the Ni-Zn ferrite and the magnetic circuit structure have not been published. The transformer has a primary-to-secondary turn ratio of 2:1, an excitation inductance of 200 nH, and a leakage inductance of 33 nH. The converter efficiency at 96 W rated output is 89.4%. In the case of the Beyond MHz band Ni-Zn ferrite transformer fabricated by the MEMS process for Power Supply on Chip [12], a1. 2 mm high Ni-Zn ferrite was placed inside a 4.1 mm × 2 mm dia. toroidal coil. The transformer with a turn ratio of 15:15 has an inductance of 105 to 115 nH in the 1 to 80 MHz bandwidth, a coupling coefficient of about 0.7 from 1 to 15 MHz, and a maximum primary Q value of 16.7 at 14 MHz when the secondary is open. The inductance is increased by 20% and the coupling coefficient is increased by 40% compared to the empty core.

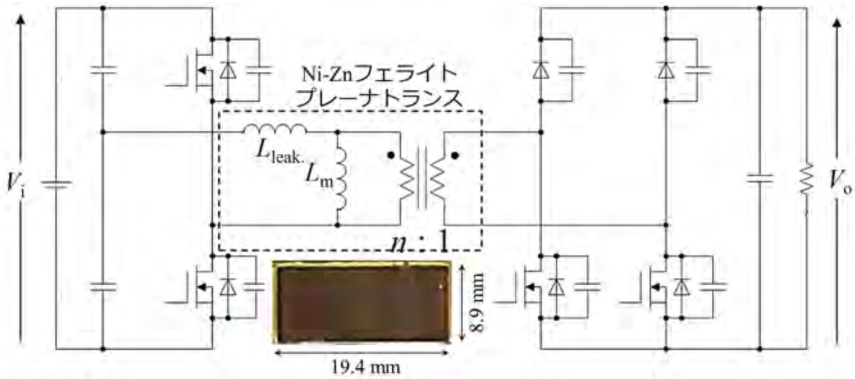

Figure 2.1.5.18 Main circuit topology of a 5 MHz switching current resonant isolated converter [11]

Issue

The saturation magnetization of Ni-Zn ferrite for Beyond MHz with specific permeability below a few tens is 200-300 mT, and the current resonant converter of Hariya et al. [11] excites the transformer positively and negatively symmetrically, whereas the Φ2 resonant converter transformer of Sagneri [10] operates in flyback and is therefore excited in the It is excited in the first quadrant of the B-H coordinate system, and its low saturation magnetization is a major drawback. Furthermore, Ni-Zn ferrite and Mn-Zn ferrite have a temperature at which iron loss is at a minimum, and above that temperature, the temperature coefficient of iron loss becomes positive and there is a risk of thermal runaway [13]. **Figure 2.1.5.19 shows** the temperature dependence of iron loss measured for Mn ferrite at magnetic flux density amplitudes B_m from 100 mT to 300 mT [13]. As B_m increases, the temperature at which the temperature coefficient of iron loss becomes positive decreases and the risk of thermal runaway increases. Therefore, in order to use ferrite in transformers without the risk of thermal runaway, it must be used at a lower B_m, which imposes significant restrictions on the miniaturization of the magnetic core.

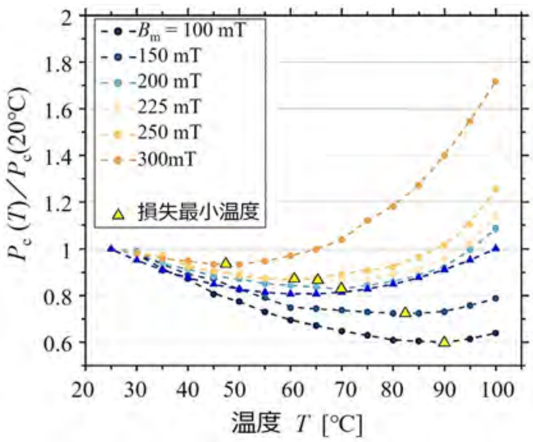

Figure 2.1.5.19 Temperature dependence of iron

b. Example of a particulate composite core transformer

As described in "1.2.2 Magnetic Powder Cores and Fine-Particle Composite Cores," there are many choices of fine-particle powders, such as carbonyl iron powders, Fe-based amorphous powders, and Fe-based nanocrystals. Even if a closed-circuit toroidal transformer is constructed with a low permeability fine-particle composite core and the windings are uniformly wound around the magnetic path, leakage flux generation is inevitable, and like Ni-Zn ferrite transformers, leakage inductance is large, so many transformers are used as leakage transformers.

Carbonyl iron powder bulk composite core transformer

Micrometals has launched a carbonyl iron powder bulk composite toroidal core for the Beyond MHz band, and according to Oliver [14] of Micrometals, hysteresis loss accounts for most of the iron loss in a core with a specific permeability of 10 up to about 10 MHz, and even above 10 MHz, the increase in eddy current loss is small. The increase in hysteresis loss is small even above 10 MHz, and the iron loss is lower than that of the benchmark Ni-Zn ferrite core above 20 MHz.

In their research and development of a MHz band Class-E resonant converter [15], Sekiya et al. applied a carbonyl iron powder bulk composite toroidal core with a permeability of 10 to the resonant inductor and isolation transformer of a 4 MHz operating Class-E resonant converter with a 1 kW output much higher than 100 W and achieved a high converter efficiency of 95.3%. efficiency of 95.3% was achieved. **Figure 2.1.5.20** plots the dependence of hysteresis loss W_h on the maximum flux density B_m for a carbonyl iron powder bulk composite toroidal core with a specific permeability of 10 from the manufacturer's published data sheet. The figure can also be viewed as iron loss per cycle. As shown in the figure, the B_m dependence of the hysteresis loss Wh changes after B_m = 15 mT, and the iron loss is very small when the magnetic flux density amplitude is excited at a level sufficiently smaller than 15 mT. Increasing the magnetic flux density amplitude by reducing the magnetic core volume leads to an increase in iron loss despite the downsizing of the transformer.

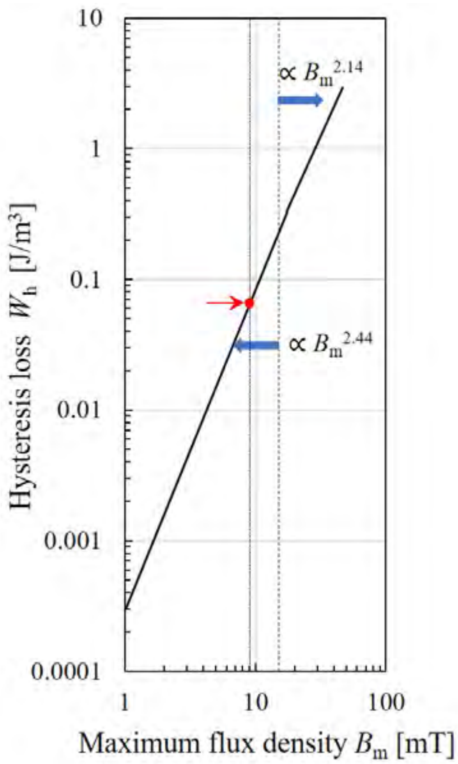

Figure 2.1.5.20 Hysteresis loss of a carbonyl iron powder bulk composite toroidal core with a specific permeability of 10 (plotted based on data sheets published by Micrometals)

As another example of a carbonyl iron powder bulk composite core transformer, Sato et al. (16) fabricated a prototype planar transformer with windings embedded in a casting method carbonyl iron powder/epoxy composite core and implemented it in a flyback converter for evaluation. **Figure 2.1.5.21** shows the circuit topology of the converter and the appearance of the planar transformer. The planar transformer is 40 x 40 x 10 mm and has an outer iron structure with primary and secondary square conductor spiral windings with a turn ratio of 16:8 embedded in a composite magnetic core. The carbonyl iron powder is nearly spherical with an average grain size of 1.6 μm. An oxide film of 25 nm to 65 nm is formed on the surface of the powder by heat treatment of As made non-reduced powder at 200°C for 6 hours in air. The planar transformer was fabricated by pouring a mixed slurry consisting of surface carbonyl iron oxide powder and a two-component epoxy precursor solution into a mold with the primary and secondary windings in place and curing at 120°C for 5 hours. **Figure 2.1.5.22** shows the complex permeability and complex permittivity of the composite core. The saturation magnetization of the composite core is about 1 T. The specific permeability is approximately 6 and remains constant up to 100 MHz, and the loss factor tanδ (μ"/μ') is on the order of 10-3 at frequencies below 50 MHz. The dielectric

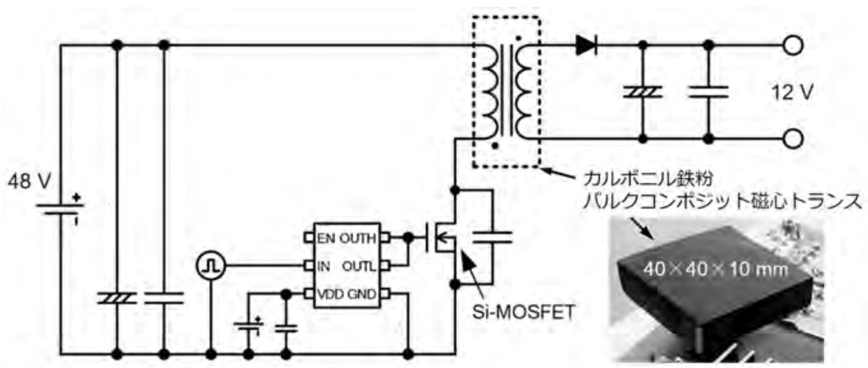

Figure 2.1.5.21 Circuit configuration of a flyback converter and appearance of a carbonyl iron powder composite core transformer [16]

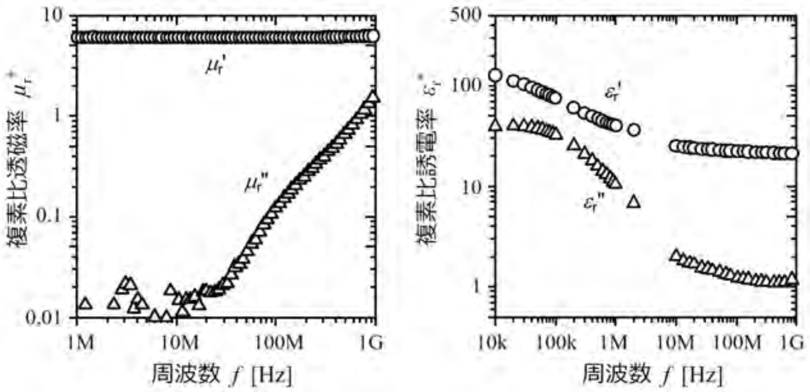

(a) Complex permeability (b) Complex permittivity

Figure 2.1.5.22 Frequency response of complex permeability and complex permittivity of surface carbonyl iron oxide powder composite cores [16]

constant of the epoxy resin itself is about 2.7, but the dielectric constant of the composite core is greatly increased by the dispersion of conductive iron fine powder, and from 100 kHz to 1 MHz, the real part of the complex permittivity ε_r' is about 60 to 40 and the imaginary part ε_r'' was about 25 to 8. The DC volume resistivity of the composite core has a value of 100 Ω-m, which is close to that of Ni-Zn ferrite. However, the interleaved structure, in which the primary and secondary conductors are arranged alternately as primary and secondary square conductor spiral windings with a turn ratio of 16:8, can improve the coupling coefficient between the windings to 0.998. However, the parasitic capacitance between conductors increases, and the resonance frequency drops from 10 MHz to 2 MHz compared to the case with the non-interleaved winding. The prototype planar transformer was applied to a PFM flyback converter with 48 V input and 12 V output in the range of 400 kHz to 1 MHz, and the transformer leakage inductance, parasitic capacitance C_{oss} of the main switch MOS-FET and parallel capacitor between drain and source (100 pF), and an efficiency of about 85% was obtained at 60 W output.

Although the use of interleaved structure windings in low permeability core transformers can increase the coupling coefficient between the windings, this technique is not suitable for Beyond MHz transformers because it leads to an increase in parasitic capacitance.

Fe-based amorphous particulate composite core transformer

Sugimura et al. [17] fabricated a prototype casting method Fe-based amorphous fine particle composite core transformer using 2.56 μm diameter SWAP amorphous Fe-Si-B-C-Cr powder with a saturation magnetization of 1.26 T. The transformer was implemented in a 48 V input - 24 V, 5 A output MHz. The transformer was implemented and evaluated in a 48 V input - 24 V, 5 A output MHz switching LLC resonant converter. The details of the composite core are described in "1.2.2 Powder Core and Fine-Particle Composite Core, (3-3) Fine-Particle Composite Core, " but the saturation magnetization is 0.84 T, the coercive force is 128 A/m, the specific permeability is about 10 and almost constant up to 100 MHz, and tanδ is in the order of 10^{-3} in the MHz band. The iron loss at a frequency of 2 MHz and a flux density amplitude of 20 mT is about 1/6 that of the benchmark Ni-Zn ferrite with a specific permeability of 20. **Figure 2.1.5.23 shows** the main circuit topology and external view of the LLC resonant converter, with 48 V input - 24 V output and an output current rating of 5 A. The primary is a half-bridge configuration with GaN-FETs and a leakage transformer with an Fe-based amorphous particle composite core. The leakage transformer has a turn ratio of 5:4:4 with an intermediate tap on the secondary side, and an SBD full-wave rectifier circuit is used on the output side. **Figure 2.1.5.24 shows** the electrical characteristics of the prototype transformer compared to a Ni-Zn ferrite transformer of the same size and turn ratio but with a permeability of 20. The inductance when the secondary side is open is nearly twice as large, reflecting the difference in excitation inductance due to the two-fold difference in magnetic permeability. The resonant frequency is 30 to 40 MHz, and the coupling coefficient at 1 MHz is about 0.84 for the composite core transformer and about 0.87 for the Ni-Zn ferrite transformer with high permeability. The specific permeability is 10, the core shape is toroidal with outer diameter; 15.5 mm, inner diameter; 9 mm, height; 11.1 mm, and volume; 1.39 cm^3.

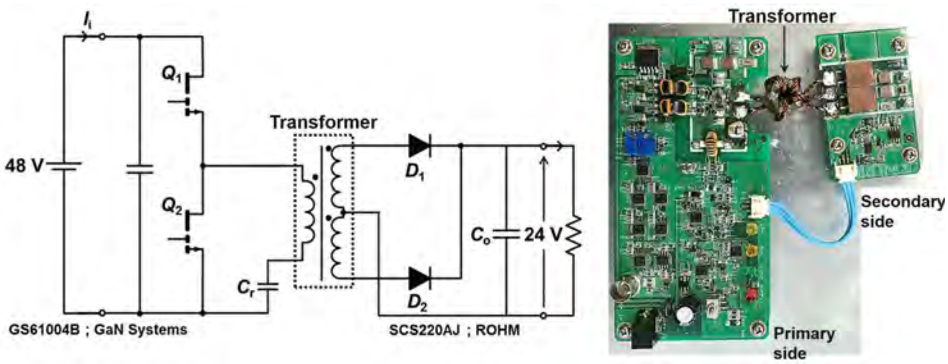

Figure 2.1.5.23 Circuit topology and external view of LLC resonant converter [17]

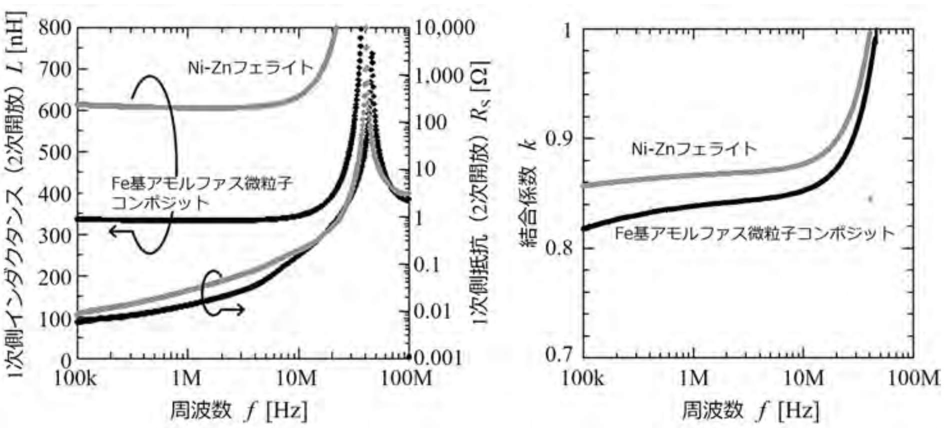

Figure 2.1.5.24 Characteristics of Fe-based amorphous particulate composite core transformers

Table 2.1.5.2 Specifications of Fe-based amorphous particulate composite core transformers

toroidal magnetic core	Fe-based amorphous fine particle composite magnetic cores Specific permeability; 10, OD; 15.5 mm, ID; 9 mm, height; 11.1 mm, volume; 1.39 cm3
number of volumes	*N1: N2:* N3 = 5: 4: 4
primary side	331 nH @ 1 MHz

Figure 2.1.5.25 shows the results of the evaluation of the prototype transformer implemented in a 48 V input-24 V output MHz switching LLC resonant converter. With the composite core transformer, the switching frequency to maintain a constant output voltage of 24 V varied from 5.4 MHz to 4.9 MHz over the range of 1 to 5 A current output, and the efficiency was over 90%, reaching a maximum of 93.1% at 1.5 A (36 W) output. When the output power was increased above 77 W (24 V, 3.2 A), LLC resonance operation ceased due to a rapid increase in permeability caused by thermal runaway of the ferrite. The composite core transformer operated stably even at the 120 W rated output, and the efficiency of the transformer at this time was estimated to be 97% and the transmission power density 90 W/cm^3.

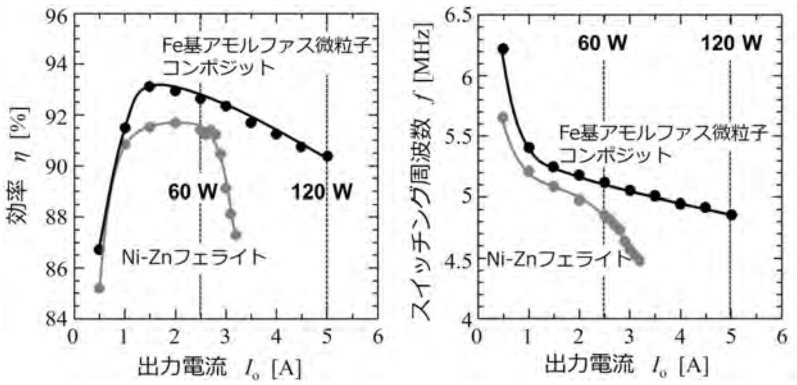

Figure 2.1.5.25 Efficiency, operating frequency, and output current of a 48 V input-24 V output MHz switching LLC resonant

Non-public

in the excitation current. Details of these composite sheet magnetic cores are described in "1.2.2 Powder Core and Fine Particle Composite Core, (3-3) Fine Particle Composite Core".

Figure 2.1.5.28 shows the efficiency characteristics of the prototype LLC resonant converter. The target efficiency is 50%, but the target efficiency is exceeded over a wide load range in the 12 V output case. Recently, the target efficiency can be achieved even with a 5 V output by improving the primary switch.

Micro Transformer

[19] reviewed the trends of microtransformers based on thin-film and MEMS processes from the dawn of the 1980s to the present, including

R&D cases in Japan. The applications of microtransformers are wide ranging, including energy conversion, communications, and sensing, etc. In their review of prototype development cases, about 40% of the published research papers were aimed at energy conversion applications, 46% of which were for frequencies below 10 MHz and 40% for frequencies between 10 and 100 MHz. Since they are fabricated using thin-film or MEMS processes, they are limited to small-capacity output converter applications, and their recent typical application is implementation in isolated converters with a few W output for power device isolated gate drivers in inverters and converters, as described by Kawasaki et al. (18).

Non-public

Non-public

Examples of prototype microtransformers and their application to converters are shown in **Table 2.1.5.3**. The only microtransformer developed by Yue et al. of ADI utilizes a multilayer magnetic thin-film core, and the efficiency exceeds 50%, partly due to the low operating frequency of the converter, showing the advantage of employing a magnetic core.

Table 2.1.5.3 Typical characteristics of prototype microtransformers and converters [20][21][22]

		By Qin et al. [20]	By Yue et al. [21]	by Cheng et al. [22]
frequency (esp. of waveforms)		160 to 210 MHz	16 to 25 MHz	180 to 210 MHz
Micro Transformer	*Q-value*	6.8	12	11
	Size	5.2 mm2	8.4 mm2	8 mm2
converter	output (e.g. of dynamo)	0.8 W	1.1 W	1.25 W
	highest efficiency	34 %	52 %	46.5 % of

Issue

Ni-Zn ferrite, which has been regarded as a benchmark for Beyond MHz magnetic cores, has many applications in transformers, but it is necessary to design transformers for converters by considering that the critical temperature that causes thermal runaway varies with the operating flux density level. As described in "1.2.2 Powder Cores and Fine-Particle Composite Cores, (3-1) Challenges in Ni-Zn Ferrite Cores for Beyond MHz Band Benchmarks," it is desirable to clarify the mechanism of residual loss generation, which is the main cause of high frequency iron loss in ferrite, and to reduce the risk of thermal runaway due to this.

Transformers with fine-particle composite cores, with the exception of carbonyl iron powder composite cores, have not yet entered the stage of practical application, and future developments are expected. As described in "1.2.2 Powder Cores and Fine-Particle Composite Cores, (4) Summary and Future Issues," low-cost production of fine alloy powders from a few micrometers to sub-micrometers is a major issue for practical application, and we look forward to further developments in this area.

Regarding magnetic thin-film transformers, an on-silicon microtransformer/isolation converter for power device isolated gate circuits has been presented by ADI [(21)], but the problem of increased cost has been pointed out for air-core transformers [(22)]. [Toshiro Sato]

1.5.3 Inductor

(1) For converters below 100 kHz (1 kW or more)

Inductors are often used as AC filter reactors for inverters and smoothing reactors for DC-DC converters at any frequency and power, but the materials used differ for each frequency and power. **Figure 2.1.5.29** shows the circuit diagram and operating waveforms of a buck chopper as the most typical circuit. The inductance value is determined from the ripple current (often set at 0.1 to 0.3 times the maximum DC load current) and load regulation response specifications. Since the inductor contains the DC component of the load current, it operates in a loop with a DC magnetic field bias in the first quadrant in the B-H plane. On the other hand, the unique requirements for chopper inductors are DC resistance and DC superposition characteristics according to the current rating. Therefore, low permeability materials are often used to prevent magnetic saturation, or a gap is inserted to lower the effective permeability of the magnetic core.

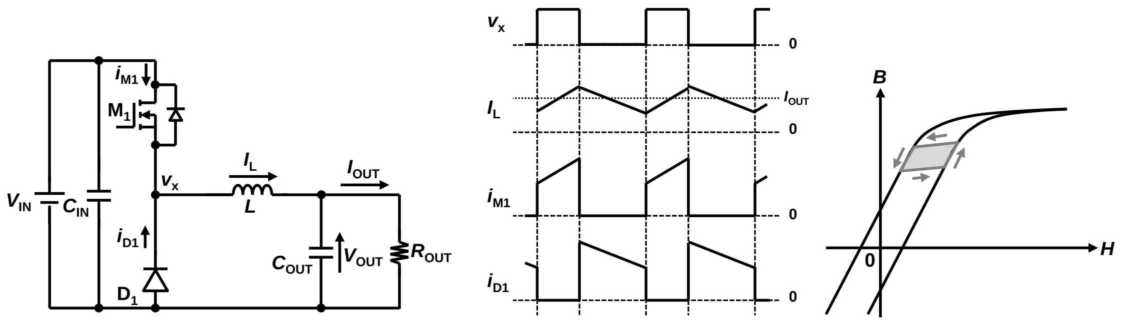

Fig. 2.1.5.29 Buck chopper

As core materials for inductors used in choppers below 100 kHz (above 1 kW), constant permeability characteristics are required to minimize the change in permeability due to the magnetic field corresponding to a large DC load current. Polycrystalline powder cores of Fe-Si, Fe-Ni, and Fe-Al-Si (sendust) systems have constant permeability characteristics by themselves because of the spatial distribution of non-magnetic gaps in the core, and they are sometimes used without gaps. The effective specific permeability is adjusted to be about several tens to several hundreds. Toroidal, EI, EE, and UU types are used as core shapes.

Litz wire or round wire is used as the winding wire when the current capacity is small, while flat wire or thin plate conductor with a high occupancy ratio is often used when the current capacity is large. [Kousuke Miyaji]

(2) 100 kHz to 1 MHz, for 100 W to 1 kW converters

There are not many choices of inductor materials for choppers from 100 kHz to 1 MHz and from 100 W to 1 kW in the frequency range below 100 kHz. Gapped Mn-Zn ferrites, amorphous and nanocrystalline magnetic powders, etc. are used.

Table 2.1.5.4 shows the basic structure and features of the wire-wound embedded inductors, in which the winding is embedded in an amorphous or nanocrystalline magnetic powder core. The horizontal winding arrangement (planar inductor) uses spiral windings and has excellent heat dissipation characteristics, while the vertical winding arrangement has a smaller foot area. As the excitation frequency increases, the resonant frequency of the inductor decreases due to the capacitance between the windings, which may cause ringing or an increase in AC

Table 2.1.5.4 Basic Structure of Wire-wound Embedded Inductors **and** Their Characteristics

項目	横巻線配置（プレーナインダクタ）	縦巻線配置
鉄心材料	アモルファスやナノ結晶系圧粉	
巻線	平角線	
基本構造	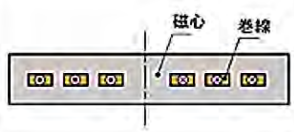	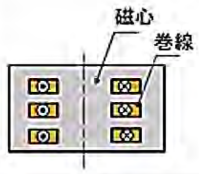
特徴	放熱特性に優れる	フィット面積の減少

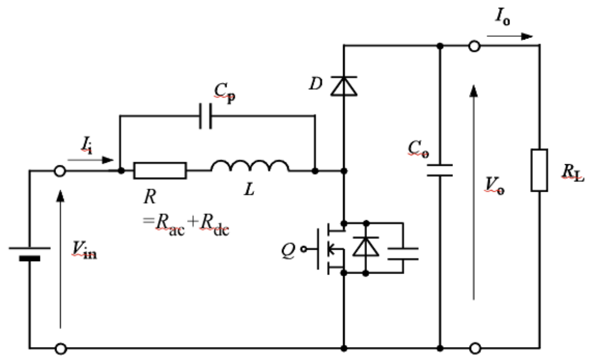

Fig. 2.1.5.30 Circuit Configuration of Non-Isolated Step-up DC-DC Converter

resistance during excitation, so the resonant frequency must be considered in the design. Specific examples of analysis and design of planar inductors are described below.

Figure 2.1.5.30 shows the circuit configuration of a non-isolated step-up DC-DC converter, where the inductor is represented by the three elements *R*, *L*, and *C*. In an ideal state, the inductor has no components other than inductance, and there is no energy loss. However, in actual inductors, in addition to the inductance, there is a parasitic capacitance consisting of the resistance component *R of* the winding and magnetic core, and the interline capacitance *C, etc.* The parasitic capacitance and inductance cause parallel resonance, and the impedance changes from inductive to capacitive at the self-resonant frequency. If the self-resonant frequency is low, a high-frequency resonance current flows in the inductor current during switching of power devices, which increases iron loss and AC copper loss.

The performance of the inductor is expressed by the *Q*value of the coil. The higher the *Q*value, the lower the conduction loss and the higher the efficiency of the converter. As the excitation frequency increases, not only the *Q* value of the coil but also the resonance frequency must be considered.

Figure 2.1.5.31 shows the structure of the inductor. In order to adjust the inductance value by varying the parameter D_s in the straight section, the winding of the inductor has a race-track structure. The leakage flux generated around the conductor penetrates nearby conductors and causes eddy currents inside the conductor [23]. The generated eddy currents increase the AC resistance of the planar inductor. Magnetic sealing technique (MST) [23] is a technique to reduce AC resistance by sealing the winding with magnetic composite material and inducing the leakage flux that causes eddy currents into the magnetic composite material. Magnetic sealing technology can reduce the eddy currents generated in the windings, thereby reducing AC resistance caused by copper loss. Furthermore, inductance is increased by placing magnetic composite material near the conductor. The above two effects improve the Q value of the inductor. However, because the magnetic composite material, which has a higher dielectric constant than air, encapsulates the winding, the parasitic capacitance increases and the self-resonant frequency decreases. Therefore, it is necessary to design an inductor with a high self-resonant frequency to effectively reduce the inductor loss. The distance w_g between the windings was varied so that the resonant frequency is 10 times higher than the excitation frequency of 500

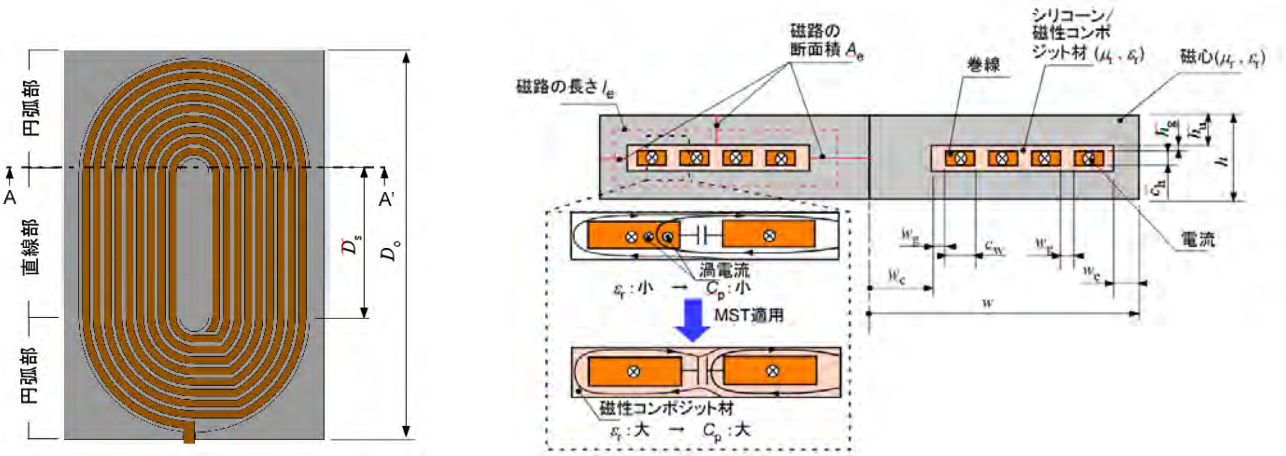

(a) Plan view (b) A-A cross section

Figure 2.1.5.31 Structure of planar inductor with magnetic composite material

kHz.

Figure 2.1.5.32 shows the frequency characteristics of an inductor whose windings are not encapsulated with magnetic composite material and an inductor whose windings are encapsulated with magnetic composite material [24]. As shown in **Figure 2.1.5.32 (a)**, the self-resonant frequencies of the inductors without and with magnetic composite encapsulation were 11.9 MHz and 7.1 MHz, respectively. The self-resonant frequencies of both inductors were more than 10 times higher than the excitation frequency of 500 kHz. As **shown in Figure 2.1.5.32 (b)**, the inductances at 500 kHz were 16.6 μH and 21.8 μH, respectively. Sealing the winding with magnetic composite material increases the inductance due to the formation of a magnetic path of magnetic composite material with a short path length around the outer circumference of the conductor. The DC resistance was 27.8 mΩ, and the resistance at 500 kHz for the planar inductors without and with magnetic composite encapsulation was 843 mΩ and 299 mΩ, respectively . The Q-values of the inductors without and with magnetic composite encapsulation at 500 kHz were 60 and 216, respectively, a 3.6-fold improvement.

Figure 2.1.5.33 compares the heat generation characteristics of the inductors at an excitation frequency of 500 kHz and output power of 800 W. The temperature was reduced by 63 ℃ from 135 ℃ to 72 ℃ by encapsulating the inductors in magnetic composite material. The temperature was reduced by 63 ℃ from 135 ℃ to 72 ℃ by encapsulating the inductor with a magnetic composite material. [Tsutomu Mizuno]

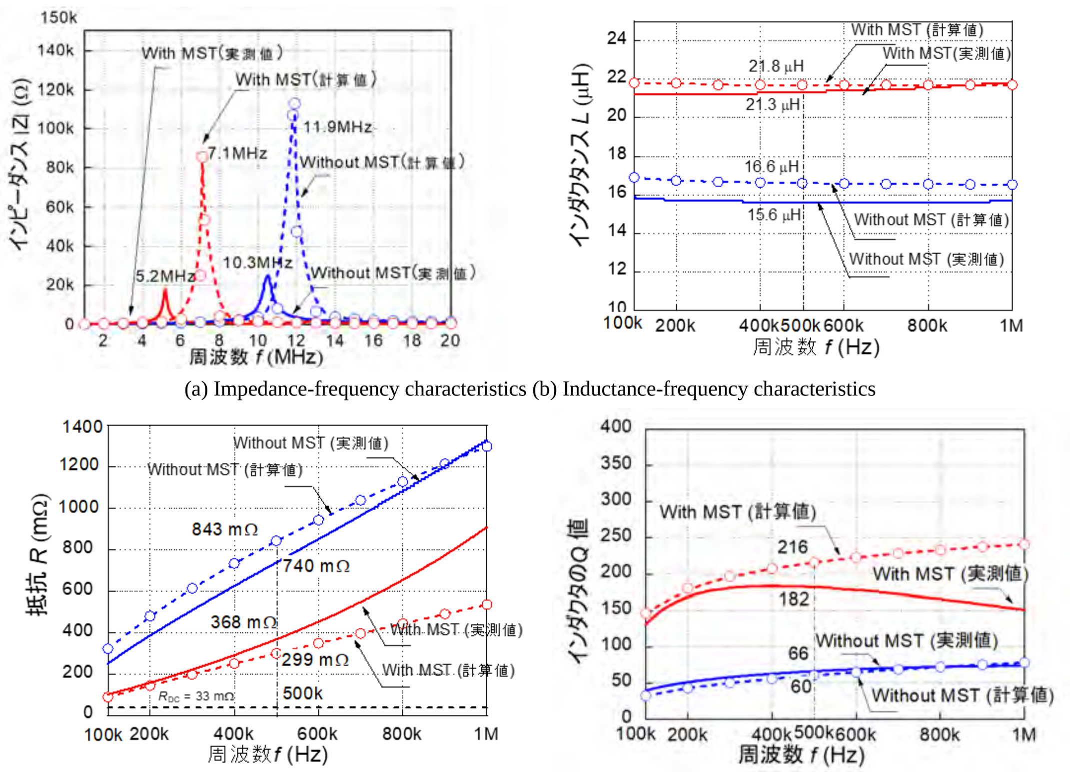

(a) Impedance-frequency characteristics (b) Inductance-frequency characteristics

(c) AC resistance - frequency response (d) Performance index Q value - frequency response

Figure 2.1.5.32 Impedance characteristics of planar inductors

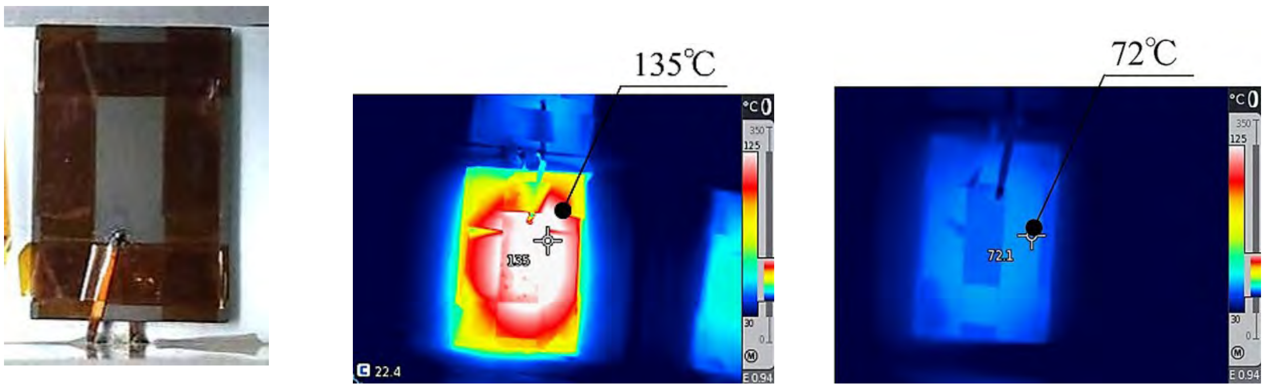

(a) Appearance (b) MST not applicable (c) MST applicable

Figure 2.1.5.33 Inductor heating characteristics (output $_{Po}$ = 800 W, after time t = 40 min)

(3) 1 MHz or higher, 100 W or lower for converters

Inductors for choppers are required to have a small change in inductance with respect to DC current, and the magnetic core must have constant permeability characteristics with a small change in permeability with respect to the DC bias magnetic field. The paper reports on the application of Ni-Zn ferrite and fine composite cores for choppers, as well as inductors and converters using magnetic thin films, and the challenges they face.

a. Ni-Zn ferrite inductors

Bulk Ni-Zn ferrites, including those for EMI countermeasures, are marketed by many domestic and foreign companies, and a large number of inductors using bulk Ni-Zn ferrites, including chip components, have been commercialized.

Hayashi et al. [25] and Sugawara et al. [26] fabricated a thin inductor using a 0.5 mm thick bulk Ni-Zn ferrite with a specific permeability of 200 and a saturation magnetization of 280 mT, and developed a micro DC-DC converter with a CMOS-IC chip mounted three dimensionally above the inductor as shown in **Figure 2.1.5.34.** The converter is a buck chopper type. The converter is a buck chopper type, with 2.7 to 5.5

V input - 0.8 to 2.2 V, 0.5 A (maximum) output, and 2.7 MHz switching frequency. **Figure 2.1.5.35** shows the DC current superposition characteristics of a Ni-Zn ferrite inductor, with inductance evaluated at 2.7 MHz and 50 mA. At a DC current of 0.3 A, the inductance is 1.54 μH and the equivalent series resistance is 0.96 Ω. The DC resistance of the coil is 0.15 Ω. The inductance at zero DC current is almost constant up to 10 MH, and the highest value of *Q* is about 30 per 3 MHz. **Figure 2.1.5.36** shows the efficiency of a micro DC-DC converter with a 3.6 V input. The efficiency at 2.2 V and 0.5 A (1.1 W) output is about 85 %. The output power density of the converter reaches about 90 W/cm^3, which is largely due to the three-dimensional mounting of the CMOS-IC and inductor.

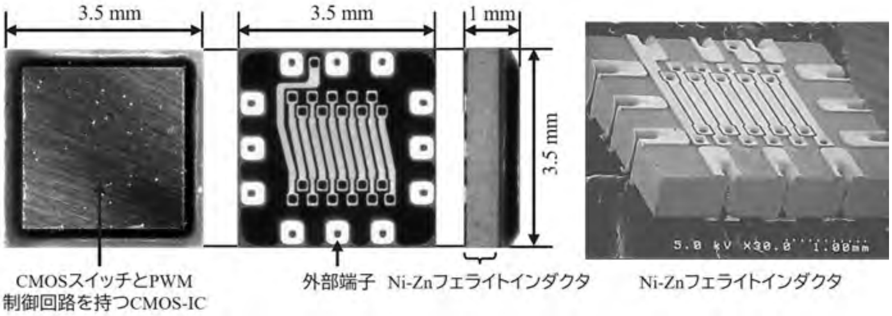

Figure 2.1.5.34 Micro DC-DC converter with CMOS-IC chip mounted three-dimensionally on top of Ni-Zn ferrite inductor

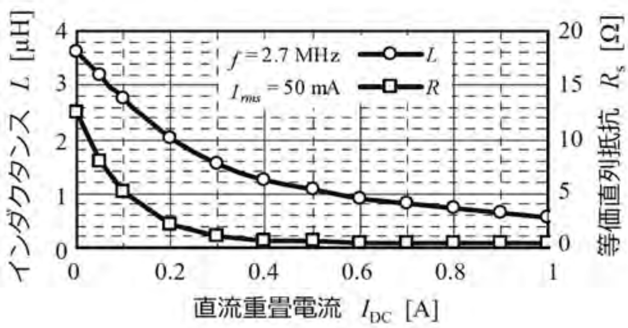

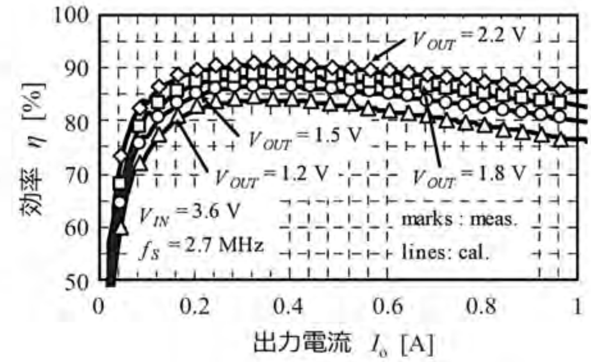

Figure 2.1.5.35 DC current superposition characteristics of Ni-Zn ferrite inductors **Figure 2.1.5.36** Efficiency of micro DC-DC converters

Other prototype planar inductors utilizing 3 μm-thick Ni-Zn ferrite thin films fabricated by electrophoresis have been fabricated for implementation in converters with a power output of a few watts [27], achieving a 35% increase in inductance relative to the empty core and a *Q* value of 53, the highest at 2 MHz.

In Ni-Zn ferrites that follow Snook's limit, low permeability materials have high natural resonance frequencies, so Ni-Zn ferrites with low permeability have constant permeability characteristics and can be used at high frequencies. However, as mentioned above, Ni-Zn ferrite is not suitable for high-current applications because of its low saturation magnetization of 200 to 300 mT, and the large nonlinearity of residual loss with respect to magnetic flux density amplitude and the risk of thermal runaway, so the operating flux density amplitude for inductor applications, as for transformers, must be sufficiently small. Therefore, as with transformers, the operating flux density amplitude must be set sufficiently small for inductor applications, which are often implemented in small-capacity converters.

b. Fine particle composite core inductors

Carbonyl iron powder composite core inductors

Although carbonyl iron powder composite cores have a low specific permeability of less than 10, their permeability does not decrease up to several hundred MHz, and they have constant permeability characteristics for DC bias magnetic fields, so they are being implemented in inductors for buck converters for point-of-load applications.

Figure 2.1.5.37 shows the appearance and electrical characteristics of an inductor with the winding embedded in a 1.6 μm carbonyl iron powder/epoxy composite core with 54 vol.%-thermal oxide film, fabricated by the casting method described in "1.2.2 Powder Core and Fine Particle Composite Core. The specific permeability of the composite core is 6. The self-resonant frequency is above 50 MHz, the inductance is almost constant at about 400 nH up to 10 MHz, and the *Q* value is about 160 at 5 MHz. The inductance does not decrease at all even with a superimposed DC current of 10 A. **Figure 2.1.5.38** shows the efficiency characteristics of a 5 V input-1 V output 1 MHz switching GaN-FET buck chopper, which shows a high efficiency of more than 90 % over a wide load range when an SBD is used in parallel to suppress surge in the main switch. The results show a high efficiency of more than 90 % over a wide range of loads.

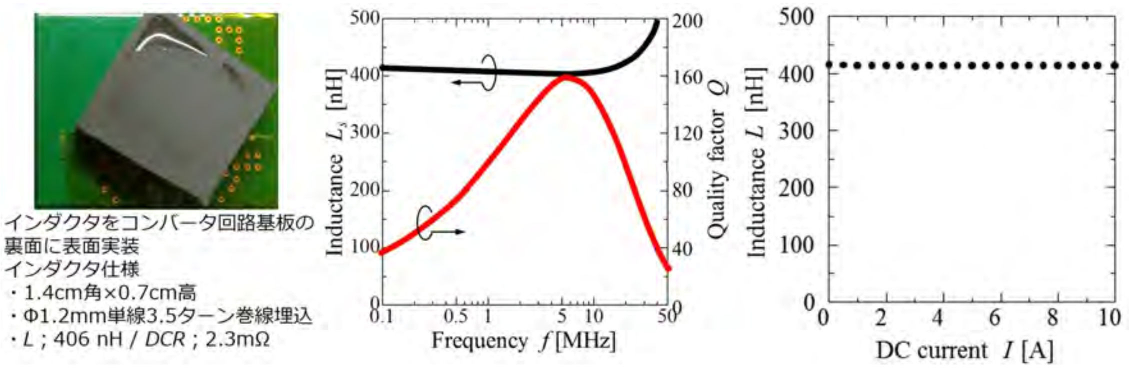

Figure 2.1.5.37 54 vol.% - Winding embedded in 1.6 μm carbonyl iron powder/epoxy composite core with thermal oxide film Appearance and electrical characteristics of inductors

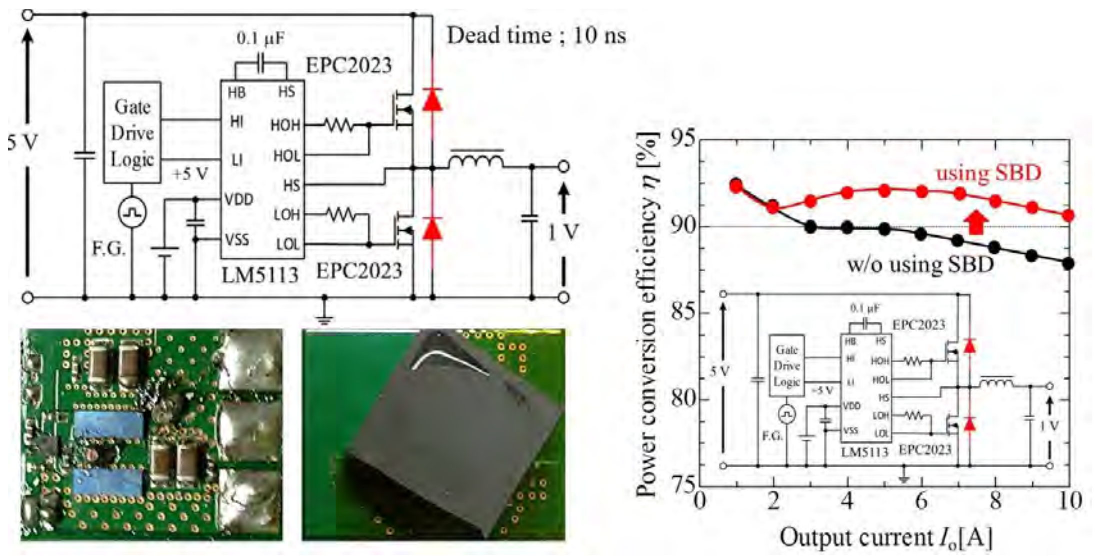

Figure 2.1.5.38 Efficiency characteristics of a 5 V input-1 V output 1 MHz switching GaN-FET buck chopper implemented with a carbonyl iron powder/epoxy composite core inductor

Sankarasubramanian et al. [29] at INTEL have developed a microinductor array for a Fully Integrated Voltage Regulator (FIVR) for 10th generation core SoCs. The target specifications for inductance are shown in **Table 2.1.5.5**. **Figure 2.1.5.39** shows an overview. The inductors are mounted in the gap between the interposer and PCB with a lower profile than the solder balls for connection, and the inductor height is set to 180 μm or less. Four straight conductors are arranged in parallel inside a carbonyl iron powder (CIP) composite magnetic core, and the four straight conductor inductors are collectively called a micro inductor array (MIA). The size of the inductor array is approximately 1.3 mm square, and is used in a four-phase buck chopper as a coupled inductor since the four inductors share a magnetic path. The detailed electrical characteristics of the microinductor array are not disclosed. [30] The INTEL 4th generation core processor (Haswell) used air-core inductors that utilized the wiring inside the package, but now it is changing to magnetic coupled inductors for multiphase PoL (Point of Load) converters. However, the current is shifting to coupled inductors using magnetic materials for multiphase PoL (Point of Load) converters.

Table 2.1.5.5 Target Specifications for Microinductor Arrays [29]

Inductance (approx. 2 times the empty center)	2.5 to 3 nH
Q-value	> 13 @140 MHz
DC resistance (1/2 or less of empty core)	< 20 mΩ

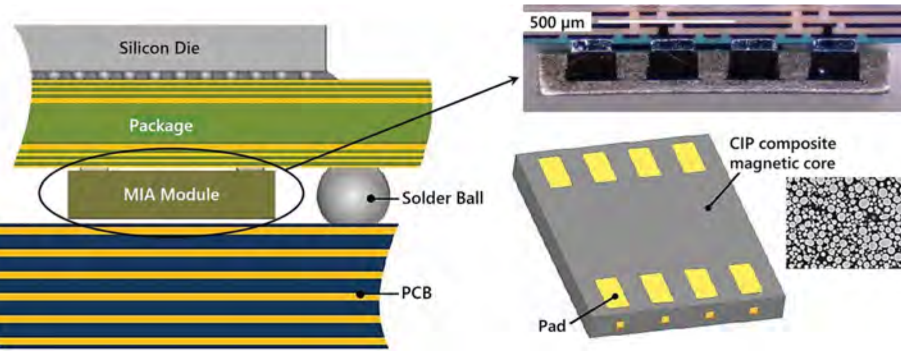

Figure 2.1.5.39 Microinductor Array for FIVR for INTEL 10th Generation Core SoCs (29)

Flat Powder Composite Core Inductors

Tokin's Chatani et al. developed a thin inductor in which the magnetic flux generated by the current in the longitudinal through conductor passes through the high permeability flat powder surface, using a composite sheet magnetic core for high-frequency power supplies (31) made of Fe-Al-Si flat powder (32). The details of the Fe-Al-Si flat powder composite sheet core are described in"1.2.2 Powder Cores and Fine Particle Composite Cores, (3-3) Fine Particle Composite Cores". In thin inductors, the Fe-Al-Si flat powder composite sheet core is embedded in the PCB, and the number of turns varies depending on the number of via conductors that penetrate the Fe-Al-Si flat powder composite sheet core. The high magnetic permeability of the sheet surface can be utilized. The footprint of the inductor is 11 x 12 mm and the height is 1.5 mm. The DC resistance is as low as 2.8 mΩ for 2 turns and 4.4 mΩ for 3 turns due to the combination of the short through-via conductor and the solid conductor for connecting via conductors on the PCB surface layer. The inductance is approximately 135 nH in the 2-turn case and 280 nH in the 3-turn case, and in the case of the 2-turn case, the decrease in inductance is about 30% even at a DC current of 30 A. The thin inductor was used in a 1 MHz step-down chopper DC-DC converter with 12 V input - 3.3 V and 18 A output developed at the Center for Power Electronics Systems (CPES) at Virginia Tech, USA (33). The footprint of the 12 V input -3.3 V output 1 MHz switching single-phase buck chopper module with a flat powder composite core thin inductor is almost the same as the inductor size. Maximum efficiencies of approximately 93 % at 4 A output and 87 % at 18 A output were achieved.

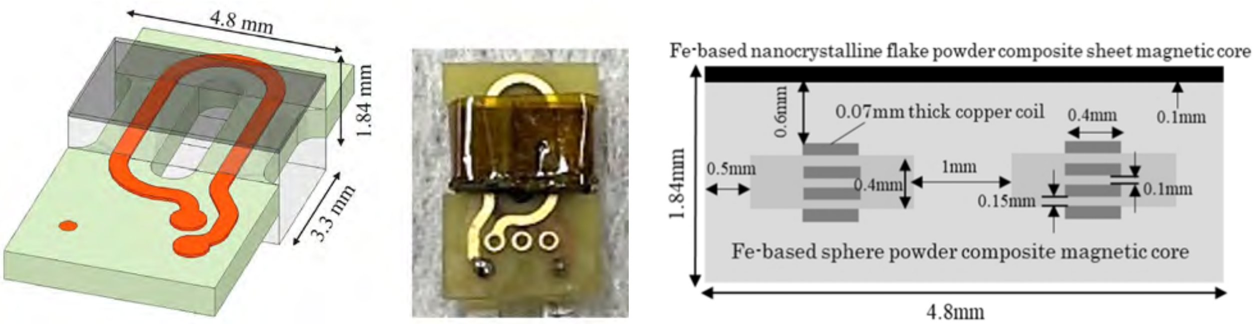

(a) Schematic diagram, external appearance (b) Cross-sectional structure

Figure 2.1.5.40. Hybrid core-coupled inductor (34)

Kimura et al. (34) fabricated a prototype hybrid-core coupled inductor combining a fine nanocrystalline spherical powder composite core and a nanocrystalline flat powder composite sheet core, and reported the results of evaluation in a 24 V input - 12 V, 5 V output 12 MHz switching GaN-FET two-phase the results of the evaluation are reported. The composite core is made of 3.5 μm diameter Fe-Si-B-Nb-Cu-C powder with a thermal oxide film and composited with epoxy resin by the casting method described in "1.2.2 Magnetic Powder Core and Magnetic Particle Composite Core". The specific permeability is constant at 10 up to 100 MHz, and the loss factor tanδ is on the order of 10^{-3} in the range of 3 to 50 MHz. The amorphous flattened powder with a thickness of 1 to 3 μm is then printed with a metal mask using silicone resin as a binder and annealed at 560°C for nanocrystallization to obtain a nanocrystalline flattened powder composite sheet core (see "1.2.2 Magnetic Powder Core and Fine Particle Composite Core" for details). The specific permeability is 150, and the tanδ exceeds 0.1 at frequencies above 10 MHz. The iron loss at a frequency of 3 MHz and a flux density amplitude of 20 mT is 400 kW/m^3 for the fine nanocrystalline spherical powder composite core, which is less than 1/10 of the benchmark Ni-Zn ferrite (67 material, specific permeability 40) from Fair Rite, Inc. The magnetic core is 850 kW/m^3, which is less than 1/5 of Ni-Zn ferrite. **Figure 2.1.5.40 (a)** shows the schematic diagram and appearance of the prototype hybrid core coupled inductor, and (b) shows the cross-sectional structure. The coil for the coupled inductor consists of a 2-turn coil x 2-layer configuration using a 4-layer metal PCB, and the two-layer coil is surrounded by a three-dimensional isotropic fine nanocrystal spherical powder composite core with a specific permeability of 10, which is a closed magnetic circuit configuration. The nanocrystalline spherical powder composite sheet core has a specific permeability of 150 in the flat plane and is placed horizontally on the top surface of one side, as shown in **Figure 2.1.5.40 (b).** The reason for placing the flat powder composite sheet magnetic core on the most surface of the flat powder composite sheet magnetic core is to shield the magnetic flux leaking from the low permeability type powder composite magnetic core, and the inductor is surface mounted on the circuit board with the flat powder composite sheet magnetic core surface down. **Figure 2.1.5.41** shows the electrical characteristics of the prototype coupled inductor. For comparison, the electrical characteristics of a Ni-Zn ferrite chip inductor with similar inductance values are also shown. The figure also shows the difference with and without the flat powder composite sheet magnetic core for magnetic shielding. The self-resonant frequency of both the prototype inductors and the Ni-Zn ferrite chip inductors is above 100 MHz, and the inductance of both is constant up to several tens of MHz. The prototype inductor without magnetic shielding has ahigh *Q* value of about 70 at 24 MHz, and the prototype inductor with magnetic shielding has ahigher *Q* value than the Ni-Zn ferrite chip inductor, with a value of over 40 in the range of 3 to 15 MHz, although the Q value drops due to the loss in the shield layer. The DC superposition characteristics of the prototype inductor show a small decrease in inductance even at 4 A. In two-phase coupled inductor operation, the DC current magnetomotive force is canceled, resulting in a large margin against magnetic saturation. **Figure 2.1.5.42 shows** the circuit topology and external view of a 24 V input-12 V, 5 V output 12 MHz switching GaN-FET two-phase buck converter with prototype coupled inductors mounted. Two coupled inductors are surface-mounted on the back of the converter circuit board, and the converter circuit footprint is 1.5 cm^2 and volume is 0.75 cm^3. **Figure 2.1.5.43** shows the efficiency characteristics of the converter: 81 % at 5 V, 3 A (15 W) output and 92 % at 12 V, 2.5 A (30 W) output.

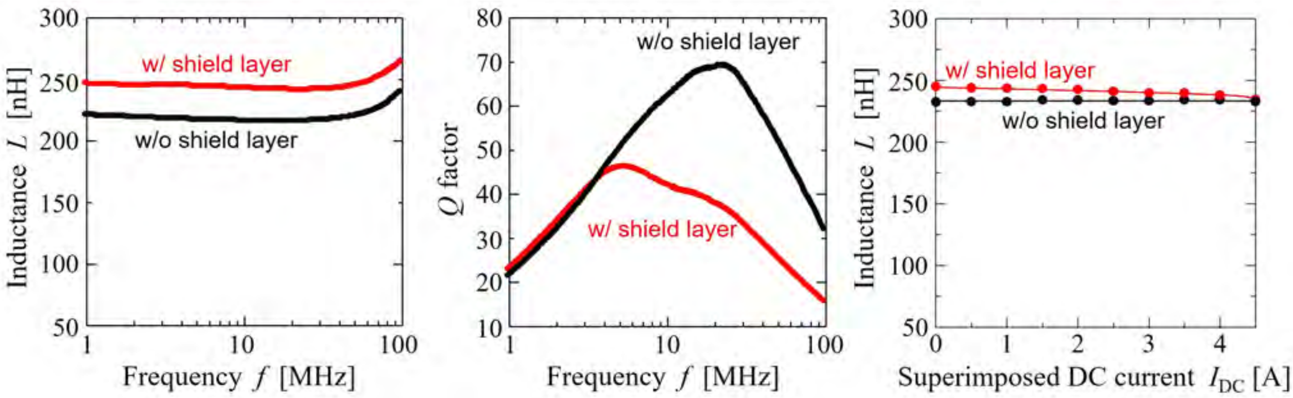

Figure 2.1.5.41 Electrical characteristics of a hybrid core-coupled inductor (34)

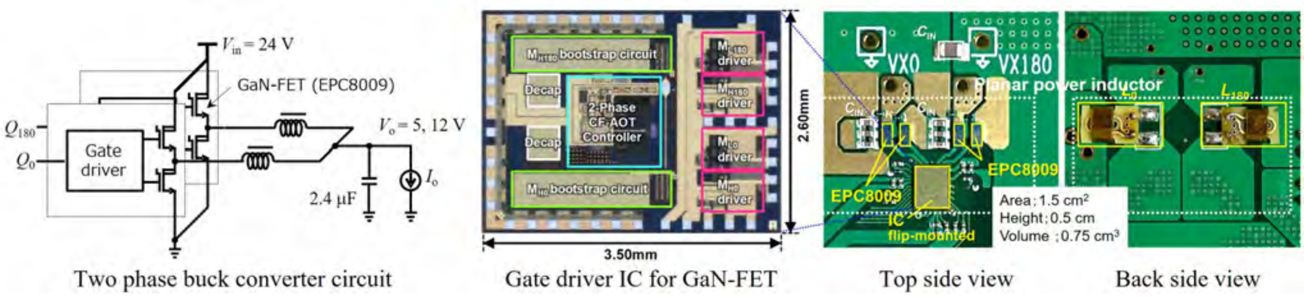

Figure 2.1.5.42 Top view of a 24 V input-12 V, 5 V output 12 MHz switching GaN-FET two-phase buck converter with prototype coupled inductor mounted (34)

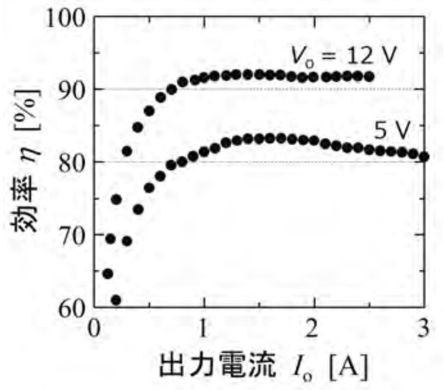

Figure 2.1.5.43 Efficiency characteristics of a 24 V input-12 V, 5 V output 12 MHz switching GaN-FET two-phase buck converter (34)

There are many other examples, such as a fine spherical powder composite core inductor built into a PCB (35), and a converter module with CMOS switches and control system chips mounted in three dimensions (36).

c. Magnetic thin-film inductors

In the 1990s and early 2000s, active research and development of magnetic thin-film inductors and their application to converters was promoted mainly in Japan, and a number of micro power supplies with several W output power were developed and commercialized, including Fe-Co-BC heteroamorphous magnetic thin-film inductors and their application to boost choppers (37) and the monolithic integration of Co-based amorphous magnetic thin-film inductors in CMOS converter IC chips (38). Later, the demand for high-current drive in response to the lower voltages in microprocessors and other LSIs led to the transition to the Power Supply on Chip, a further development of the Point of Load. The transition was made to the Power Supply on Chip, which further developed the Point of Load.

Figure 2.1.5.44 shows the appearance of a magnetic thin-film inductor developed by Ferric in the U.S. (39) It is manufactured in a wafer process at TSMC in Taiwan with specifications of inductance density of 300 nH/mm^2 or higher per footprint area, current density of 12 A/mm^2 or higher, DC resistance 50 mΩ or less, and a coupling coefficient of 0.9 or higher in the case of coupled inductors. The disadvantages of magnetic thin films, which do not allow for a large magnetic path cross-sectional area and are prone to magnetic saturation, are mitigated by the coupled inductor configuration, which is actually used in converters for mobile terminals.

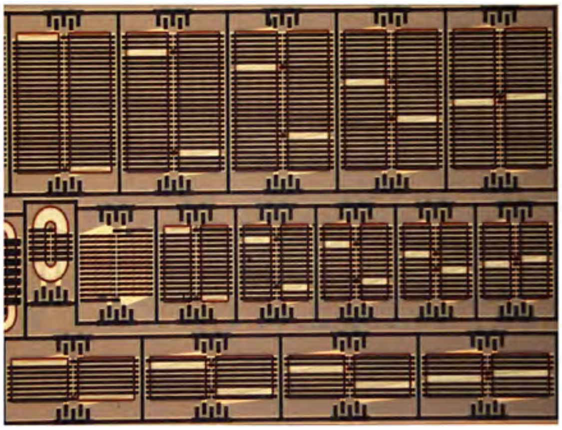

Figure 2.1.5.44 Magnetic thin-film inductors from Ferric, USA

EnaChip of the U.S. is developing thin-film inductors targeting 5 to 30 MHz (40) and possesses technologies for high-throughput plating of Co-Fe amorphous films with high saturation magnetization and layering with insulating films to produce inductors at low cost. **Figure 2.1.5.45** shows an example of the inductor development, which consists of a 1 μm x 6-layer plated magnetic thin film and a Cu solenoid coil.

An international workshop on Power Supply on Chip is held every other year (41), and an independent session on Integrated Magnetics has been established for active discussions. [Toshiro Sato]

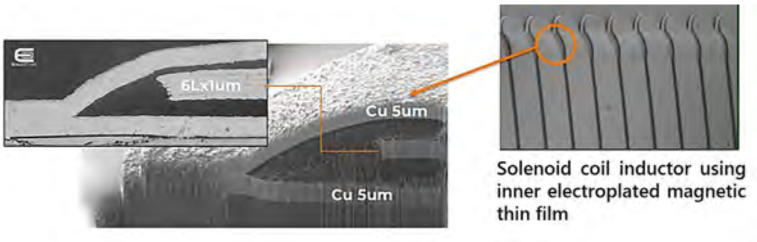

Figure 2.1.5.45 Example of an inductor developed by EnaChip in the U.S. (40)

1.5.4 AC Copper Loss Reduction Technology

With the expansion of wide bandgap semiconductors, compact, lightweight, and highly efficient transformers and inductors are desired. By increasing the excitation frequency to a higher frequency, it is possible to reduce the number of turns of the winding and make it smaller. However, as the excitation frequency is increased, the AC resistance due to skin effect and proximity effect increases. Reducing AC resistance is essential to suppress heat generation and improve efficiency of the winding (42).

(1) Copper loss reduction technology by wire (round wire, flat wire, Litz wire, stranded wire, magnetic flux path control)

Generally, round or flat wires are used, and the AC resistance increases as the frequency increases due to the skin effect and proximity effect. For this reason, it is necessary to select a conductor diameter that is sufficiently smaller than the skin depth determined from the frequency of the current flowing in the excitation, the permeability and resistivity of the wire material. This paper describes the AC copper loss of round, square, Litz, and stranded wires, and introduces magnetic flux path control techniques (magnetic coated wire, magnetic molding, etc.) to reduce the magnetic flux linking the conductor.

Table 2.1.5.6 summarizes the types of wire and the suppression of skin and proximity effects. In general, the AC resistance of round and flat wires increases with increasing frequency due to the skin effect and proximity effect. Therefore, it is necessary to select a conductor diameter that is sufficiently smaller than the skin depth determined from the current frequency and the permeability and resistivity of the wire. To suppress the skin effect and proximity effect, Litz wire, which is made by twisting thin strands, is sometimes used [(43)]. However, in the frequency band above 1 MHz, there is a resonant frequency caused by the capacitance between strands, and the resistance increases due to the resonance. Therefore, the Litz wire loses its advantage in the band above 1 MHz. In addition, the occupancy ratio of Litz wire is as small as 0.4 or less, making it unsuitable for miniaturization and weight reduction of inductors and transformers.

In addition, the structure of conductors to which magnetic flux path control (MPC) technology is applied and its effects are summarized. Magnetic flux path control technology is a general term for technology to reduce AC resistance (copper loss) by suppressing the skin and proximity effects by loading magnetic materials on the conductor. In round conductors, the proximity effect is suppressed by loading a magnetic material on the outer circumference of the conductor [(44)]. Similarly, the proximity effect can also be suppressed by providing a magnetic material on the outer circumference of a litz wire [(45)].

Table 2.1.5.6 Types of wire and suppression of skin and proximity effects

Conductor type		Structure	Suppression of skin effect	Suppression o proximity effe
General wire	Round wire	Round wire	Ineffective	Ineffective
	Rectangular wire	Rectangular wire	Ineffective	Ineffective
AC copper loss reduction wire	Litz wire	Round wire	Effective	Effective
	Round wire with MPC	Magnetic material Round wire	Ineffective	Effective
	Litz wire with MPC	Magnetic material Litz wire	Effective	Effective
	Rectangular wire with MPC	Non-magnetic insulator Rectangular wire Magnetic material	Effective	Effective
	Board pattern with MPC	Magnetic material Substrate Conductor pattern	Effective	Effective

In a flat-angle conductor, nonmagnetic insulators are provided on both sides of the conductor in the width direction, and a magnetic material is further loaded on the outer circumference of the conductor [(46)]. This structure suppresses both the skin effect and the proximity effect. Furthermore, in a square conductor with a conductor pattern on the substrate, the copper loss caused by the skin and proximity effects can be reduced by loading the magnetic material in the form of a cap on the conductor [(47)]. Magnetic materials include Fe, amorphous alloys, and magnetic composite materials, and materials with large magnetic permeability and low iron loss are desirable.

Copper and aluminum are used as conductors. The resistivity of aluminum is 1.6 times that of copper, resulting in higher DC resistance for the same conductor cross-sectional area. However, optimization of the dimensions (width and thickness) of rectangular aluminum wire and application of flux path control technology may reduce AC resistance compared to rectangular copper wire. In addition, the aluminum density is smaller than that of copper, and the mass of the winding is about 1/3.

Magnetic materials for magnetic coating should be selected from silicon iron, nanocrystalline materials, Fe-based amorphous materials, etc., considering specific permeability and saturation magnetization.

Figure 2.1.5.46 shows the magnetic properties of a magnetic tape using nanocrystalline mixed spherical powder (mixed powder with average grain size of 25 μm and 3 μm). As shown in Figure (a), the complex specific permeability is 25.4 and the loss term μ''. Furthermore, the saturation magnetization is 798 mT.

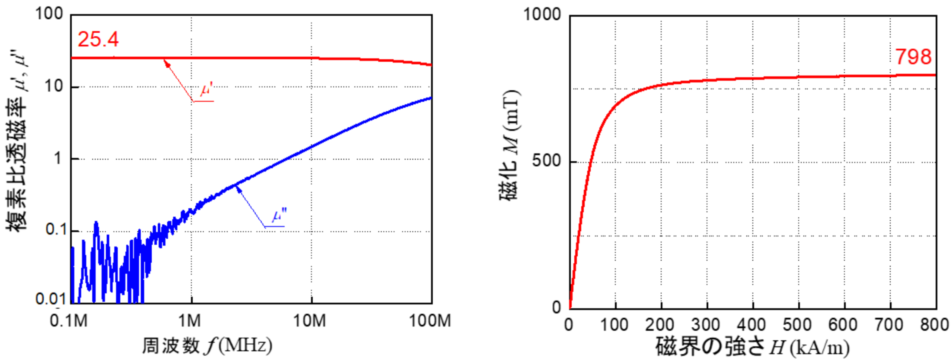

(a) Complex specific permeability characteristics (b) Magnetization characteristics

Figure 2.1.5.46 Magnetic properties of magnetic tape with nanocrystal mixed spherical powder

(2) Copper loss reduction technology by interleaved winding structure

The interleaved winding structure can reduce AC copper losses due to proximity effects. **Figures 2.1.5.47 (a) and (b)** show analytical models of planar transformers [48]. Figure (a) shows a sandwich-wound planar transformer with the secondary winding across the primary winding. Figure (b) shows an interleaved planar transformer with primary winding P and secondary windings S1 and S2 laid out as S1-S1-P-S1-P-S1-P-S1-S2-P-S2-P-S2-S2 from the top.

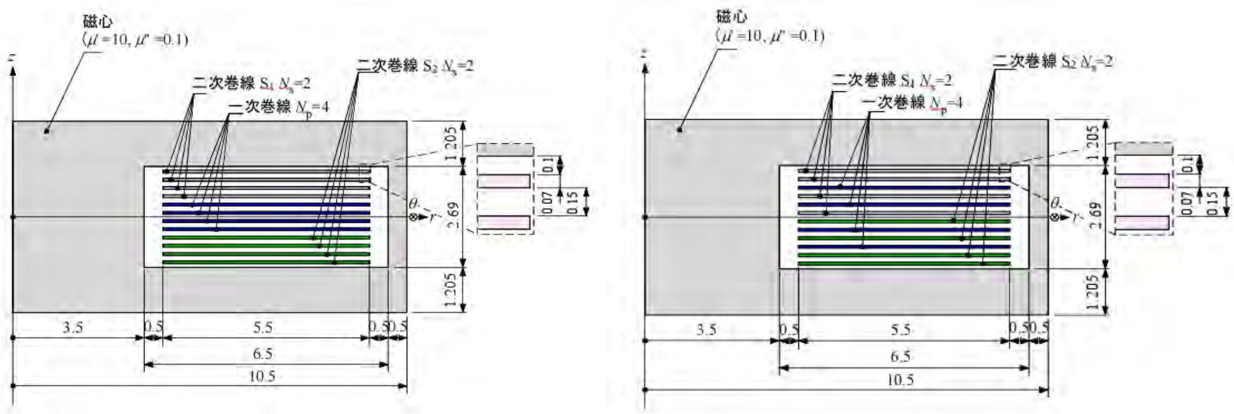

(a) Sandwich winding (b) Interleaved winding

Figure 2.1.5.47 Transformer with sandwich and interleaved windings

Figure 2.1.5.48 compares the resistance of the primary winding of a transformer with sandwich and interleaved windings, showing the primary resistance Rsh1 at secondary S1 short circuit. The results of the analysis for the sandwich and interleaved windings are also plotted. The interleaved winding resistance is smaller than the sandwich winding resistance. The R_{sh1} at a frequency of 5 MHz is 132.9 mΩ, which suppresses the increase in AC resistance due to the proximity effect.

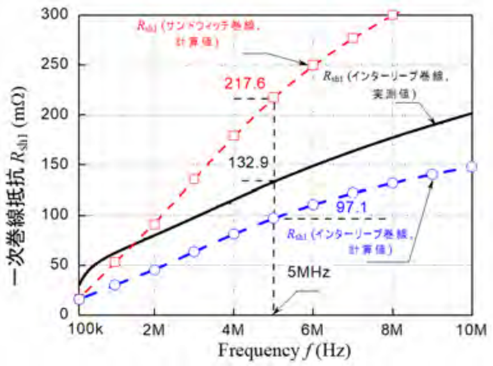

Figure 2.1.5.48 Resistance comparison of primary windings of transformers with sandwich and

(3) Copper loss reduction technology by magnetic circuit structure

AC copper losses increase when the fringing flux links through the winding (49). **Figure 2.1.5.49** shows how to reduce AC copper losses caused by the proximity effect using a curved gap. By making the magnetic core of the gap curved, the fringing magnetic flux acting on the winding is reduced, thereby decreasing the AC copper loss due to the proximity effect. Another method is to provide a large number of gaps and shorten the gap length per gap to shorten the magnetic path of the fringing magnetic flux and prevent the magnetic flux from acting on the winding, thereby reducing the increase in AC copper loss caused by the proximity effect.

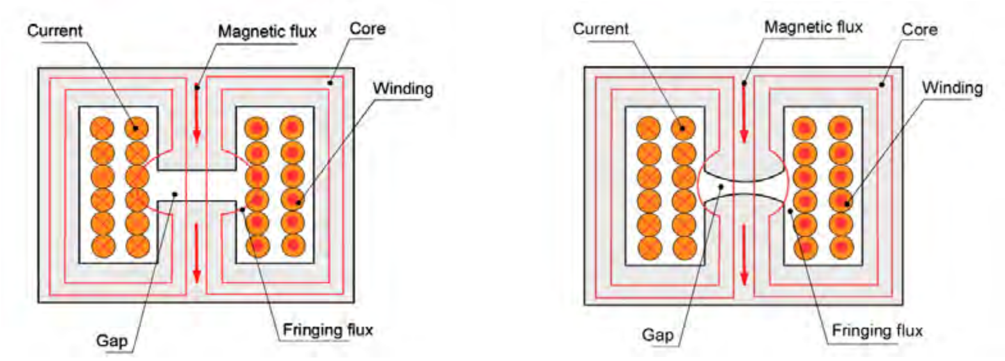

(a) Flat gapped inductor (b) Curved gapped inductor

(Fringing flux reducing inductor)

Figure 2.1.5.49 Reduction of AC copper loss due to proximity effect with curved gap

[Tsutomu Mizuno.]

References

(1) https://www.proterial.com/products/soft_magnetism/non_cut_core.html

(2) h ttps:// detail-infomation.com/transformer-core-type/

(3) https://www.proterial.com/products/soft_magnetism/cut_core.html

(4) Mohamed H. Ahmed, Michael A. de Rooij, Jianjing Wang: "High-Power Density, 900-W LLC Converters for Servers Using GaN FETs: Toward Greater Efficiency and Power Density in 48 V to 6/12 V Converters," *IEEE Power Electronics Magazine*, Vol. 6, No. 1, pp. 40-47, DOI: 10.1109/MPEL. 2018.2886106 (2019)

(5) Yusuke Hayashi, Hajime Toyoda and Akira Matsumoto: "Contactless DC connector based on GaN LLC converter for next generation data centers", *IEEE TRANSACTIONS ON INDUSTRY APPLICATIONS*, Vol. 51, No. 4, pp. 3244-3251, DOI: 10.1109/IPEC.2014.6869792 (2015)

(6) Hwa-Pyeong Park, Hyun-Jun Choi, Jee-Hoon Jung: "Design and Implementation of High Switching Frequency LLC Resonant Converter for High Power Density", *International Conference on Power Electronics-ECCE*, Vol. 9, p. 504, DOI: 10.1109/ICPE.2015.7167832 (2015)

(7) Masato Chigira, Yuichi Nagatsuka, Yasuyoshi Kaneko, Shigeru Abe, Tomio Yasuda and Akira Suzuki: "Small-size Light-weight Transformer with New Core Structure for Contactless Power Transfer System of Electric Vehicle", *2011 IEEE Energy Conversation Congress and Exposition* ", Vol. 17, No. 22, p. 264, DOI: 10.1109/ECCE.2011.6063778 (2011)

(8) Kota NAKANISHI, Kazuhiro SHIMURA, Mitsuhide SATO, Tsutomu MIZUNO: "Efficiency Improvement of 500 kHz Band LLC Resonant Converter by Transformer with Magnetic Tape Wound Plain Square Wire," 36th Symposium on Electromagnetic Force Related Dynamics (SEAD36), OS3-8-3, pp.295- 300 (2024)

(9) Alex J. Hanson, Julia A. Belk, Seungbum Lim, Charles R. Sullivan and David J. Perreault: "Measurements and Performance Factor Comparisons of Magnetic Materials at High Frequency", *IEEE Transactions on Power Electronics*, Vol. 31, No. 11, pp. 7909-7925, DOI: 10.1109/TPEL.2015 .2514084 (2016)

(10) Tony Sagneri: "The challenge of VHF power conversion", *2016 Applied Power Electronics Conference & Exposition*,. Prenarry Session, Long Beach, CA, USA (2016)

(11) A. Hariya, H. Yanagi, Y. Ishizuka, K. Matsuura, S. Tomioka and T. Ninomiya: "5 MHz PWM-controlled current-mode resonant DC-DC converter using GaN-FETs", Proceedings of the *2014 International Power Electronics Conference* (IPEC-Hiroshima -ECCE-ASIA), pp. 3630-3637 (2014)

(12) Haiwang Li, Kaiyun Zhu, Kaibo Lei, Tiantong Xu and Hanxiao Wu: "Integrated MEMS Toroidal Transformer With Ni-Zn Ferrite Core for Power Supply on Chip", *IEEE Transactions on Power Electronics*, Vol. 37, No. 9, pp. 10075-10080, DOI: 10.1109/TPEL.2022.3160698 (2022)

(13) Yibo Wang, Xiaosheng Wang, Liping Mo, K.T. Chau, C.Q. Jiang and Weisheng Guo: "Temperature-dependent magnetic characteristics and thermal runaway assessment in passive-cooled inductive power transfer systems," *Energy*, Vol. 332, 137173, doi.org/10.1016/j.energy. 2025.137173 (2025)

(14) Christopher G. Oliver: "Powder Core Materials for Magnetic Components in GaN and SiC Power Devices", *2016 Applied Power* Electronics *Conference* (APEC2016), Industry Session, IS09.6, Long Beach, CA, USA (2016)

(15) Ryoko Sugano, Yuchong Sun and Hiroo Sekiya: "High-frequency resonant gate driver with isolated class-E amplifier",. *Nonlinear Theory and Its Applications*, *IEICE Japan*, Vol. 9, No. 3, pp. 358-373, doi.org/10.1587/nolta.9.358 (2018)

(16) K. Sato, K. Sato, K. Sugimura, T. Sato, M. Sonehara, and H. Takeuchi: "Trial Manufacture of Surface Carbonyl Iron Oxide Powder Metal Composite Core Transformer and Its Application to Flyback Converter," Special Issue on Transactions of the Magnetics Society of Japan, Vo.1, No. 1, pp. 44-52, doi.org/10.20819/msjtmsj. 17tr110 (2017)

(17) Kanako Sugimura, Daisuke Shibamoto, Naoki Yabu, Tatsuya Yamamoto, Makoto Sonehara and Toshiro Sato: "Surface-Oxidized Amorphous Alloy Powder/Epoxy-Resin Composite Bulk Magnetic Core and Its Application to Megahertz Switching LLC Resonant Converter", *IEEE Transactions on* Magnetics *on Magnetics*, Vol. 53, No. 11, #2801406, DOI: 10.1109/TMAG.2017.2718042 (2017)

(18) Jun Kawasaki, Kazuhiro Shimura, Nanami Kawada, Mitsuhide Sato, Makoto Sonehara, Toshiro Sato, Tsutomu Mizuno, Kosuke Miyaji: "Study of 10 MHz band insulated planar transformer using Fe-based nanocrystalline flat powder and Fe-based amorphous spherical powder," IEEJ Basic, Material and Common Division Magnetics / Industrial Applications Division Linear Drive Joint Workshop Document, MAG22-047/LD22-030, pp. 5-10 (2022)

(19) Fellype do Nascimento, Antonio C. C. Telles, Ednan Joanni and Ricardo C. Teixeira: "A Survey on Microtransformers", *Journal of Integrated Circuits and Systems*, Vol. 16, No. 2, pp. 1-12, doi.org/10.48550/arXiv.2106.04554 (2021).

(20) Wenhui Qin, Xin Yang, Shaoyu Ma, Fang Liu, Yuanyuan Zhao and Tianting Zhao: "An 800mW fully integrated galvanic isolated power transfer system meeting CISPR 22 Class-B Emission Levels with 6dB Margin" , *2019 IEEE* International Solid-State *Circuits Conference* (ISSCC2019), pp. 246-248, San Francisco, CA, USA, DOI: 10.1109/ISSCC.2019.8662349 (2019)

(21) Zhuo Yue, Ma Shaoyu, Zhao Tianting, Qin Wenhui, Zhao Yuanyuan, Guo Yingjie: "A 52% Peak-Efficiency >1W Isolated Power Transfer System Using Fully Integrated Magnetic-Core Transformer", *2019 IEEE* International Solid-State *Circuits Conference* (ISSCC2019), pp. 244-246 , San Francisco, CA, USA, DOI: 10.1109/ISSCC.2019.8662301 (2019)

(22) Lin Cheng, Zuohuan Chen, Daquan Yu and Dongfang Pan: "A high-efficiency transformer-in-package isolated DC-DC converter using glass- based fan-out wafer-level packaging", *Fundamental Research*, Vol. 4, No. 6, pp. 1407-1414, doi.org/10.1016/j.fmre.2023.05.003 (2024)

(23) K. Shimura, T. Kanaya, S. Kobayashi, M. Sato, M. Sonehara, T. Sato and T. Mizuno: "Reduction of Alternating-Current Resistance and Heat Generation of Spiral Inductors with Magnetic Sealing Technique" , *IEEJ Transactions on Electrical and Electronic Engineering*, Vol.18, No. 9, doi.org/10.1002/tee.23873 (2023)

(24) Haruka MUROSAKI, Kazuhiro SHIMURA, Mitsuhide SATO, Tsutomu MIZUNO: "Design of Inductors for Non-Insulating Step-up DC-DC Converters Applying Magnetic Encapsulation Technology Considering Self-Resonant Frequency," 36th Symposium on Electromagnetic Force Related Dynamics (SEAD36), OS3-8-4, pp.301-306 (2024)

(25) Z. Hayashi, Y. Katayama, M. Edo and H. Nishio: "High-efficiency dc-dc converter chip size module with integrated soft ferrite ", *IEEE Transactions on Magnetics*, Vol. 39, No. 5, pp. 3068-3072 (2003), DOI: 10.1109/TMAG.2003.815895 (2003)

(26) Satoshi Sugawara, Kohei Yamada, Haruhiko Nishio, Masaharu Edo, Toshiro Sato, and Kiyoto Yamazawa: "Characteristics Analysis and Improvement of Transient Response of Micro DC-DC Converter for Portable Devices," Journal of the IEEJ Industrial Applications Division, Vol. 128, No. 12, pp. 1373-1380, doi.org/10.1541/ieejias. 128.1373 (2008)

(27) Jae-Jin Lee, Yang-Ki Hong, Seok Bae, Ji-Hoon Park and Jeevan Jalli: "High-Quality Factor Ni-Zn Ferrite Planar Inductor",. *IEEE Transactions on Magnetics*, Vol. 46, No. 6, pp. 2417-2420, DOI: 10.1109/TMAG.2010.2044377 (2010)

(28) Toshiro Sato: "Leading Research on SiC/GaN Power Device MHz-Band Switching DC-DC Converters," SiC Alliance Public Relations Committee and Planning Committee Joint Workshop (2016)

(29) Malavarayan Sankarasubramanian, Kaladhar Radhakrishnan, Yongki Min, William Lambert, Michael J Hill and Ashay Dani: "Magnetic Inductor Arrays for Intel® Fully Integrated Voltage Regulator (FIVR) on 10th generation Intel® Core™ SoCs", *2020 IEEE 70th Electronic Components and* Technology Conference (ECTC), pp. 399-403, DOI: 10.1109/ECTC32862.2020.00071 (2020).

(30) Nasser Kurd, Muntaquim Chowdhury, Edward Burton, Thomas P. Thomas, Christopher Mozak and Brent Boswell: "Haswell: A Family of IA 22 nm Processors," *IEEE Journal of Solid-State Circuits*, Vol. 50, No. 1, pp. 49-58, DOI: 10.1109/JSSC.2014.2368126 (2014)

(31) Shun Mikoshiba, Hiroshi Shima, Ken-ichi Chatani: "Development of Thin Magnetic Core Material for High Frequency Power Supply Using Soft Magnetic Metal Flat Powder," Proceedings of the 42nd Annual Meeting of the Magnetics Society of Japan, 13aC-3 (2018)

(32) Ken'ichi Chata'ni: "Soft magnetic metal-flake composite material suitable for highly integrated power Modules", *2018 International Symposium on 3D* Power Electronics Integration *and* Manufacturing (3D PEIM2018), College Park, Maryland USA (2018)

(33) Dongbin Hou, Yipeng Su, Qiang Li and Fred C. Lee: "Improving the Efficiency and Dynamics of 3D Integrated POL", *Proceedings of the 2015* Applied *Power* Electronics *Conference and* Exposition (APEC2015), pp. 140-145, Charlotte, NC, USA (2015)

(34) Soichi Kimura, Kota Koike, Motohiro Kanai, Ryohei Miyata, Toshitaka Minamisawa, Kousuke Miyaji, Makoto Sonehara and Toshiro Sato:" Fabrication of Fe-based Nanocrystalline Spherical and Flake Powder Composite Magnetic Cores for Tens of MHz and their Application to Planar Power Inductor", *IEEJ Transactions on Fundamentals and Materials*, Vol. 144, No. 6, pp. 199-206, doi.org/10.1541/ieejfms.144.199 (2024)

(35) T. Akiyama, S. Ishida, T. Shirasawa, T. Fukuoka, S. Hara, H. Yoshida, M. Sonehara, T. Sato and K. Miyaji: "Integrated CMOS Switch Buck DC-DC Converter Fabricated in Organic Interposer with Embedded Magnetic Core Inductor", *Journal of the Magnetics Society of Japan*, Vol. 43, No. 3, pp. 64-69 (2009). 3, pp. 64-69 (2019), doi.org/10.3379/msjmag.1905R005 (2019).

(36) Takanobu Fukuoka, Yuki Karasawa, Tomoki Akiyama, Ryoutaro Oka, Shu Ishida, Tomohiro Shirasawa, Makoto Sonehara, Toshiro Sato and Kousuke Miyaji: "An 86% Eficiency, 20MHz, 3D-Integrated Buck Converter with Magnetic Core Inductor Embedded in Interposer Fabricated by Epoxy/Magnetic -Filler Composite Build-Up Sheet," in *Proceedings of the 34th* Applied *Power* Electronics *Conference and Exposition* 2019 (APEC2019), pp. 1561-1566 (2019)

(37) T. Sato, T. Inoue, H. Tomita, S. Yatabe, K. Nishijima, Y. Tokai, M. Nameki, N. Saito and T. Mizoguchi: "5MHz switching micro dc-dc converter using planar inductor," *in Proceedings of the 1996 IEEE International Telecommunications* Energy *Conference* (INTELEC'96), Boston, MA, USA, pp. 399-300. Boston, MA, USA, pp.485-490 (1996)

(38) Masaharu Edo, Haruo Nakazawa, Yoshitomo Hayashi, Yasushi Katayama, Kazuo Matsuzaki and Eiichi Yonezawa: "Ultra-small DC/DC converter with integrated thin-film inductor," Journal of the IEEJ Basic, Material and Common Division, Vol. 120, No. 3, pp. 277-282, doi.org/10.1541/ieejfms1990.120.3_. 277 (2000)

(39) Noah Sturcken: "INTEGRATED POWER MANAGEMENT WITH FERROMAGNETIC THIN-FILM POWER INDUCTORS", *2018 International Workshop on Power Supply on Chip* (PwrSoc2018), Hsinchu, Taiwan (2018)

(40) Trifon Liakopoulos, Matt Wilkowski, Kamyar Ahmadi and Mo Khodadadi: "Scalable Integrated Magnetics : A Cost-Effective and Efficient Solution for Vertical Power", *2023 International Workshop on Power Supply on Chip* (PwrSoc2023), Hannover, Germany (2023).

(41) https://psma.com/conferences/PwrSoC

(42) J.D. Lavers, V. Bolborici : "Loss comparison in the design of high frequency inductors and transformers", *IEEE Transaction on magnetics*, Vol. 35, No. 5, pp. 3541-3543, DOI: 10.1109/20.800583 (1999)

(43) Tsutomu Mizuno, Asahi Kamiya, Yusuke Shimura, Kazutake Iida, Daisuke Yamamoto, Naoki Miyao, Hideaki Sasahira: "Study on the Effect of the Number of Strands of Litz Wire on AC Resistance," Journal of AEM Japan, Vol.18, No.3, pp.300-305(2010)

(44) T. Mizuno, S. Enoki, T. Hayashi, T. Asahina and H. Shinagawa: "Extending the linearity range of eddy-current displacement sensor with magnetoplated wire", *IEEE Transactions on Magnetics*, Vol. 43, No. 2, pp. 543-548, DOI: 10.1109/TMAG.2006.887853 (2007)

(45) Yinggang Bu, Shun Endo and Tsutomu Mizuno: "Improvement in the transmission efficiency of EV wireless power transfer system using a magnetoplated aluminum pipe", *IEEE Transactions on magnetics*, Vol. 54, No. 11, 8401205, DOI: 10.1109/TMAG.2018.2840109 (2018)

(46) Kenta Torishima, Kazuhiro Shimura, Mitsuhide Sato, Tsutomu Mizuno: "Reduction of AC Copper Loss in Flat Copper Wire Using Magnetic Flux Path Control Technique," IEEJ Transactions A, Vol. 140, No. 7, pp. 364-371, DOI: 10.1541/ieejfms.140.364, DOI: 10.14243/jsaem.28. 128 (2020)

(47) Yuta Tokudaiji, Daichi Miura, Yusuke Hattori, Kohei Murasato, Yinggang Bu and Tsutomu Mizuno : "AC resistance reduction of a flexible wireless power trans-mission coil using magnetic path control technology at 13.56 MHz", *IEEE Transactions on Magnetics*, Vol. 55, No. 7, 8401407, DOI: 8401407 8401407, DOI: 10.1109/TMAG.2019.2895239 (2019)

(48) Kazuhiro Shimura, Daito Tanaka, Mitsuhide Sato, Tsutomu Mizuno: "Reduction of Copper Loss in Planar Transformers for LLC Resonant Type Converters by Applying Interleaved Winding," Journal of the AEM Society of Japan, Vol. 28, No. 2, pp. 128-133, DOI: 10.14243/jsaem.28.128 (2020)

(49) Mukuta Shimamoto and Toshihisa Shimizu: "Validation of a Simple Calculation Method for Fringing Losses," IEEJ Transactions A, Vol. 140, No. 11, pp. 522-528,

DOI:10.1541/ieejfms.140.522 (2020)

1.6 Examples of Steinmetz coefficients.

Key words: Steinmetz parameters, core loss

As described in equation (2.1.1.9), the Steinmetz (SE) equation is a typical mathematical expression in iron loss modeling and is a phenomenological expression for iron loss P (W/m^3) in sinusoidal excitation. α and β, expressed in the SE equation, are SE parameters representing powers of frequency and maximum flux density **Table 2.1.1**. **Table 2.1.6.1** summarizes α and β expressed in terms of SE parameters for various soft magnetic materials; both α and β for Fe-based soft magnetic alloy materials and amorphous alloy materials are lower than for ferrite. **Figure 2.1.6.1** shows the frequency dependence of iron loss in a pressed core made of different soft magnetic materials. For all materials, the iron loss increases linearly on a logarithmic scale with frequency. Among these materials, Fe-Si-Al has the lowest iron loss. **Figures 2.1.6.2-2.1.6.4** show the frequency dependence of iron loss for different maximum flux densities measured at sinusoidal excitation and zero bias settings for the Fe-Si, Fe-Si-Al and Fe-Ni magnetic powder cores, as well as α and β represented by the SE parameters. Regardless of the material type and the maximum flux density, the iron loss in all of the cores increases linearly with frequency on a logarithmic scale. In addition, α and β, which are expressed as SE parameters, range from 1.01 to 1.69 and from 1.96 to 2.37 for all the magnetic cores, regardless of the material composition, etc. (1)(2)(3).

This formula is widely used in the design and operational analysis of magnetic elements such as transformers and inductors. It is useful in the initial design and simple evaluation of magnetic elements because the iron loss of a magnetic powder core can be estimated simply and efficiently.

Table 2.1.6.1 Soft magnetic materials in various soft magnetic materials
Steinmetz parameters (α and β)

材料	α	β
Fe-Si	1.1−1.5	2.0−2.2
Fe-Ni	1.0−1.6	2.0−2.2
Fe-Si-Al	1.0−1.5	2.0−2.4
Fe-Ni-Mo	1.3−1.6	~2.1
Ferrite (Proterial)	1.8−3.2	2.4−3.6
Amorphous (Proterial)	~1.4	~2.5

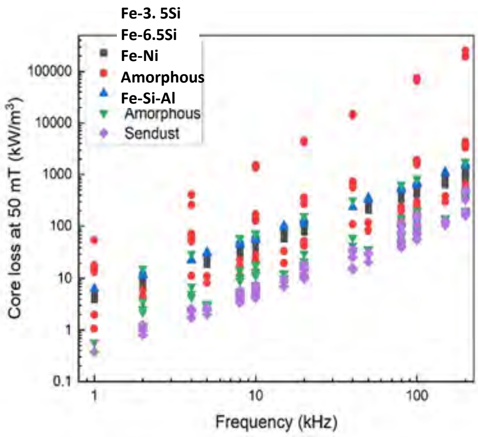

Figure 2.1.6.1 Composed of various soft magnetic materials

Fe-Si cores

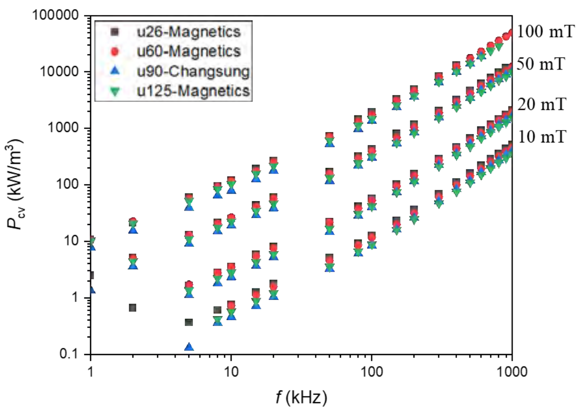

$P_{cv} = kf^{\alpha} B_m^{\beta}$

FeSi cores	*k*	α	β	*f- kHz*
μ26-Magnetics	1218	1.11	2.11	< 50
	140	1.51	1.97	≥ 50
μ60-Magnetics	1272	1.13	2.17	< 50
	156	1.50	2.10	≥ 50
μ90-Changsung	800	1.17	2.17	< 50
	90	1.55	1.98	≥ 50
μ125-Magnetics	1299	1.11	2.21	< 50
	147	1.50	2.05	≥ 50

Figure 2.1.6.2 Frequency dependence of iron loss for different maximum flux densities and SE parameters (α and β) in a pressed magnetic core made of Fe-Si

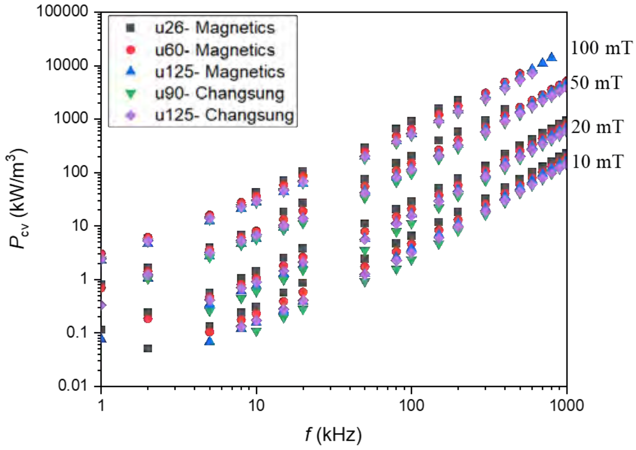

Fe-Si-Al cores	*k*	α	β	*f- kHz*
μ26-Magnetics	161	1.45	2.16	< 100
	109	1.45	2.03	≥ 100
μ60-Magnetics	218	1.31	2.14	< 100
	43	1.58	2.05	≥ 100
μ125-Magnetics	138	1.36	2.13	< 100
	24	1.67	2.07	≥ 100
μ90-Changsung	237	1.33	2.37	< 100
	24	1.63	2.07	≥ 100
μ125-Changsung	192	1.32	2.20	< 100
	39	1.55	2.04	≥ 100

Figure 2.1.6.3 Frequency dependence of iron loss for different maximum flux densities and SE parameters (α and β) in a pressed magnetic core made of Fe-Si-Al

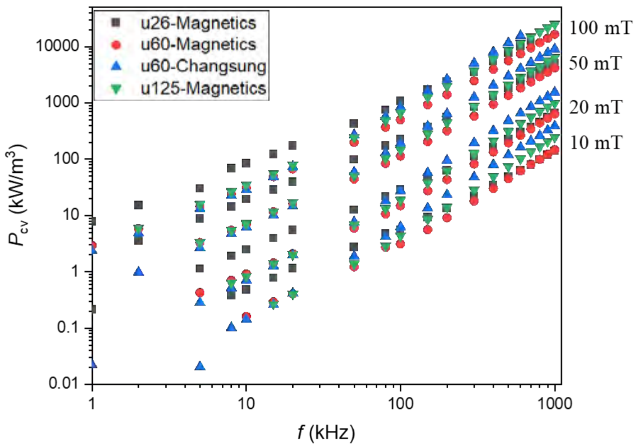

Fe-Ni cores	*k*	α	β	*f- kHz*
μ26-Magnetics	1056	1.01	2.12	< 50
	138	1.41	2.06	≥ 50
μ60-Magnetics	306	1.15	2.15	< 50
	35	1.55	2.01	≥ 50
μ60-Changsung	185	1.40	2.22	< 50
	45	1.62	1.96	≥ 50
μ125-Magnetics	306	1.16	2.15	< 50
	35	1.56	2.01	≥ 50

Figure 2.1.6.4 Frequency dependence of iron loss for different maximum flux densities and SE parameters (α and β) in a pressed magnetic core made of Fe-Ni

For example, in the case of ferrite cores and laminated steel sheets, the prediction of their losses supports the selection of appropriate materials and shapes that satisfy efficiency and thermal design requirements. It is also incorporated into simulation tools and design support software in the power electronics field, and plays an important role in the operational analysis of converters, inverters, and high-frequency magnetic circuits [(4)].

On the other hand, for the design of magnetic elements, it is necessary to consider various requirements in addition to the mere loss estimation by the SE formula [(4)(5)]. Specifically, in the case of a toroidal-shaped magnetic core, leakage flux is suppressed, contributing to miniaturization; in the case of an E-shaped magnetic core (E-core), it is superior in terms of manufacturing; and in the case of an E-shaped magnetic core (E-core), it is superior in terms of loss reduction. In addition, eddy current losses can be suppressed by introducing thin laminates and a segmented structure. The drive frequency of the magnetic element is an important requirement in balancing the performance and volume of the element. In addition, heat dissipation from magnetic elements is mainly caused by iron loss. Therefore, in order to maintain stable operation of magnetic elements over a long period of time, it is necessary to manage the heat dissipation from the elements, and it is important to provide effective cooling measures. Furthermore, in terms of material selection, hysteresis loss and eddy current loss can be reduced by selecting soft magnetic materials with low coercive force and high electrical resistance. Losses can be further reduced by selecting amorphous alloy materials or nanocrystalline alloy materials. Thus, by combining design and material selection for shape, frequency, and heat dissipation, it is possible to realize a high-performance, compact magnetic element and effectively control iron loss.

References

(1) Metal Powder Core HRM series , Proterial , Ltd.
(2) Magnetics®, Magnetics - Powder Cores Manufacturer
(3) Daniela Rodriguez-Sotelo, Martin A. Rodriguez-Licea, Ismael Araujo-Vargas, Juan Prado-Olivarez, Alejandro-Israel Barranco-Gutiérrez and Francisco J. Perez-Pinal : "Power Losses Models for Magnetic Cores: A Review", Micromachines, Vol. 13, p. 418, DOI:org/10. 3390/mi13030418 (2022)
(4) Zenong Li, Weijian Han, Zhen Xin, Qing Liu, Jianliang Chen, Poh Chiang Loh : "A Review of Magnetic Core Materials, Core Loss Modeling and Measurements in High-Power High-Frequency Transformers", CPSS Transactions on Power Electronics and Applications, Vol.7, pp.359-373 , DOI: 10.24295/CPSSTPEA.2022.00033 (2022)
(5) Minkai Mu : "High Frequency Magnetic Core Loss Study", a thesis for a doctorate (PhD), Virginia Polytechnic Institute and State University (2013)

1.7 Trade-offs in materials and manufacturing processes for magnetic components

Keyword: Magnetic powder cores, Soft magnetic properties, Practical applications, Magnetic components

In the materials and manufacturing process of magnetic elements, trade-offs among various factors must be considered. In this section, we focus on the synthesis conditions such as mechanical properties (hardness) of the material, heat treatment process, filling ratio, pressing pressure, and dimensions of the magnetic core used as a magnetic element.

1.7.1 hardness

The hardness of soft magnetic materials used in a pressed core affects its magnetic properties, mechanical properties, and manufacturing process [(1)(2)]. **Table 2.1.7.1** summarizes the hardness of typical soft magnetic materials used in the magnetic powder core. On the other hand, the hardness of Fe-Si alloys tends to be equal to or harder than that of Fe. In addition, soft magnetic composite materials are up to twice as hard as Fe, and ferrite materials are more than three times harder than Fe.

Table 2.1.7.1 Hardness of typical soft magnetic materials

材料	硬さ [HV]
Iron	90－150
Fe-80Ni	~ 100
Fe-Ni-Mo	~ 150
Steel (silicon steel, Fe-Si)	120－250
Soft magnetic composites (SMC)	200－400
Ferrite (Mn-Zn, Ni-Zn)	450－700

In the case of a magnetic core made of a low-hardness material, plastic deformation easily occurs during press forming, resulting in a high filling ratio of the magnetic core. On the other hand, in the case of a pressed core made of a high-hardness material, it is difficult to deform during press forming, making it difficult to improve the filling ratio of the pressed core. In addition, excessive press pressure can easily cause cracks in magnetic cores made of hard materials or large-sized magnetic cores. Thus, the hardness of the material (ease of plastic deformation) is closely related to the filling ratio in a pressed core. Especially for highly ductile materials such as Fe-based powders, further deformation improves the filling efficiency.

From the above, it is necessary to carefully control the optimum process conditions and additive materials according to the hardness of the soft magnetic material used in the magnetic powder core to achieve a balance among magnetic properties, mechanical strength, and manufacturing process.

1.7.2 Heat treatment process

In the heat treatment process of a magnetic core, the heat treatment temperature and the atmosphere during heat treatment are important factors that affect the basic properties of the magnetic core, and precise control of these factors is essential to optimize the magnetic properties and mechanical durability of the magnetic core [(3)-(6)].

For the heat treatment temperature, the temperature as well as the heating and cooling rates are carefully set to prevent heat-induced deterioration of the properties of the soft magnetic materials that compose the magnetic powder core and to optimize the magnetic properties such as saturation magnetic flux density and specific permeability of the materials. Different heat treatment temperatures are required for different types of alloys. On the other hand, soft magnetic materials composed of several elements, such as amorphous alloy materials and nanocrystalline alloy materials, require more rigorous temperature control (heating and cooling rates) to achieve the desired crystal structure and magnetic properties. As shown in **Figure 2.1.7.1**, both the AC coercive force and the loss per cycle in the powder core made of Fe-6.5wt.%Si powder changed significantly depending on the heat treatment temperature. These may be caused by structural changes or thermal degradation of the resin. For amorphous alloy materials, optimization of structural control should be carefully considered, taking into account the glass transition temperature, crystallization temperature, and composition of the raw material.

Regarding the atmosphere during heat treatment, heat treatment is mainly performed under vacuum, argon, nitrogen, hydrogen, or other atmospheres that can prevent oxidation of the magnetic powder core and inhibit diffusion of elements in the core. Heat treatment under a vacuum atmosphere prevents oxidation of the magnetic powder core and maintains the purity of the powder and its magnetic properties. Heat treatment under argon or nitrogen atmosphere not only prevents oxidation of the magnetic powder core, but also promotes phase transformation of the powder itself. Therefore, heat treatment under these atmospheres is widely used. In addition, heat treatment under a hydrogen atmosphere can reduce oxides on their surfaces, mainly in iron-based powders, to promote bonding between particles, activation of reactions with other elements, and to improve magnetic properties. The choice of these atmospheres affects the overall performance of the magnetic powder core and contributes to controlling surface oxidation, inter-particle bonding, and the density of the magnetic core.

In addition to these factors, the controlled cooling rate after heat treatment as described above significantly affects the microstructure and magnetic properties of the magnetic powder core, depending on the type of soft magnetic material that constitutes the core. In particular, controlled cooling can minimize residual stress in the core, prevent cracks in the core for large size cores, and ensure improved mechanical

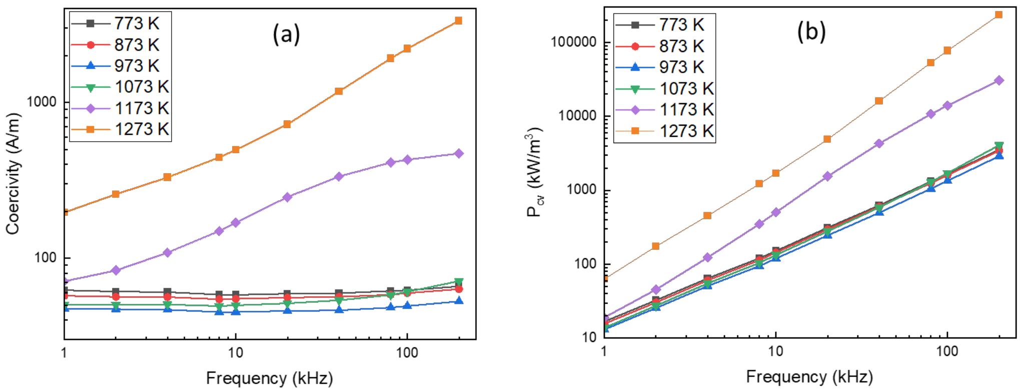

strength and uniform magnetic properties.

Fig. 2.1.7.1 Frequency dependence of AC coercive force and high-frequency loss in a pressed core consisting of Fe-6.5wt.%Si powder at different heat treatment temperatures [(6)]

1.7.3 Fill rate and press pressure

Filling ratio and pressing pressure are important factors affecting the electrical and magnetic properties and mechanical strength of a pressed magnetic core [(7)-(9)]. The filling ratio is an index indicating the percentage of soft magnetic powder in the volume of the magnetic core. The filling ratio is a factor that affects the magnetic permeability μ of the magnetic powder core. As the filling ratio increases, the density of the soft magnetic powder increases, which is expected to improve the permeability in the magnetic powder core. This can be explained by a simple model in which the magnetic core consists of two phases: "soft magnetic powder" and "air gap (or air)". In this model, the effective permeability μ_{eff} in the magnetic core can be approximated as $\phi\mu_{eff} = \mu_{particle} \cdot \emptyset$ (μ_{particle}: permeability of soft magnetic powder, ϕ: filling ratio (ratio of magnetic powder to core volume)), indicating that μ_{eff} increases with increasing filling ratio. However, if the filling ratio is further increased to make the magnetic powder core denser, the magnetostatic interaction between particles becomes more pronounced and nonlinear changes in magnetic permeability may occur, which cannot be explained by this model. Excessive pressing pressure may also deform the powder itself, and the expected permeability may not be obtained.

In general, a high packing ratio increases the permeability, flux flow in the core, and mechanical strength of the magnetic powder core, but it also increases the risk of cracking or breakage during handling, and its effect on hysteresis loss and eddy current loss is more complex. Hysteresis loss is reduced by the reduction of voids due to the high fill factor, while eddy current loss is reduced by the reduction of voids due to the high fill factor. On the other hand, eddy current losses are more likely to increase due to the lower electrical resistance between the particles in the core caused by a high filling factor, especially in the higher frequency range. If the filling factor is too low, the mechanical strength decreases due to the increase of voids in the core, which leads to an increase in high-frequency losses due to an increase in the excitation current.

As for the pressing pressure, [(8)(9)] the pressure range is 500 MPa to 1500 MPa, and the optimum condition depends mainly on the type of soft magnetic material and the application of the magnetic powder core. As a specific example, the dependence of high-frequency magnetic properties on pressing pressure in a magnetic powder core made of Fe-Ni powder is described here. **Figure 2.1.7.2** shows the frequency dependence of complex permeability and high-frequency loss in a pressed core made of Fe-Ni powder formed at different press pressures. The value of the real part of the complex permeability increased from 70 to 75 with increasing pressing pressure. This result is due to the improvement of the filling ratio in the pressed core. The high-frequency loss was lowest at a pressing pressure of 1176 MPa and increased at higher pressing pressures. This behavior is considered to be due to the increase in eddy current loss caused by the breakdown of the insulation layer between the powders due to the densification of the magnetic powder core caused by excessive pressing pressure. This result suggests that it is important to maintain high electrical resistance while maintaining the insulating coating on the powder surface in order to suppress the increase in high-frequency losses caused by high pressing pressure.

From the above, it is essential to optimize the balance between magnetic properties and mechanical strength in a pressed core by adjusting the filling ratio and pressing pressure in order to maximize the magnetic performance of the pressed core.

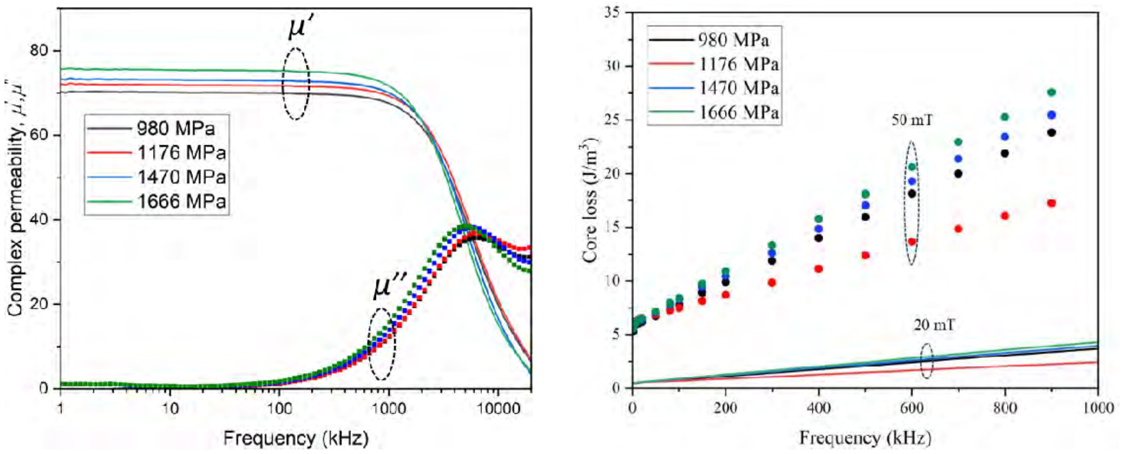

Figure 2.1.7.2 Frequency dependence of complex permeability and high-frequency loss in a magnetic powder core made of Fe-Ni powder formed at different pressing pressures [8]

1.7.4 size limitation

The dimensions (size) of a magnetic core made of soft magnetic powders are limited by factors such as material properties, mechanical strength, heat dissipation performance, and manufacturing feasibility. Small size (10 to 50 mm) magnetic cores are widely used mainly in the power electronics field. For medium-sized pressed cores (50-200 mm), they are commonly used in transformers, etc. For large pressed cores (>300 mm), alternative materials are often chosen to overcome the limitations of cores made of magnetic powders. In addition to the need for advanced materials and cooling facilities, large-sized pressed cores also face challenges such as the non-uniformity of the density of the magnetic powder core, the fragility of the structure, and the size limitation of the molds.

As the size of the magnetic powder core increases, the permeability of the core decreases due to the increased voids between the powders, which affects the magnetic properties. In addition, cracks are more likely to occur due to mechanical stress and thermal expansion. In addition, eddy current loss due to skin effect tends to increase in high-frequency bands, making laminated cores and ferrite cores more suitable in many cases.

[Mai Phuong Nguyen, Satoshi Okamoto, Yasuhi Endo]

References

(1) Lu Lu, Jay Sim and Ruike Renee Zhao : "Mechanics of hard-magnetic soft materials: A review", Mechanics of Materials, Vol. 189, p.104874, DOI: 10.1016/j.mechmat.2023.104874 (2024)

(2) Katie Jo Sunday and Mitra L. Taheri : "Soft magnetic composites: recent advancements in technology", Metal Powder Report , Vol. 72, pp. 425-429, DOI: 10.1016/j.mprp.2016.08.003 (2017)

(3) Tomoyuki Ueno, Hijiri Tsuruta, Tatsuya Saito, Asako Watanabe, Tomoyuki Ishimine and Koji Yamada : "Practical and Potential Applications of Soft Magnetic Powder Cores with Superior Magnetic Properties", SEI TECHNICAL REVIEW, Vol. 82, pp. 9-15 (2016)

(4) M.M. Zhou, Y. Han, W.W. Guan, S.J. Han, Q.S. Meng, T.T. Xu, H.L. Su, X. Guo, Z.Q. Zou, F.Y. Yang and Y.W. Du : "Magnetic properties and loss mechanism of Fe-6.5wt%Si powder core insulated with magnetic Mn-Zn ferrite nanoparticles", Journal of Magnetism and Magnetic Materials , Vol. 482, pp. 148-154, DOI:

10.1016/j.jmmm.2019.03.062 (2019)
(5) Hea-Ran Kim, Dongsup Lee, Sangsun Yang,Young-Tae Kwon, Jongryoul Kim, Yunseok Kim and Jae-Won Jeong : "Optimizing Annealing Temperature Control for Enhanced Magnetic Properties in Fe-Si-B Amorphous Flake Powder Cores, Metals", Vol. 13, p. 2016, DOI: 10.3390/met13122016 (2023)
(6) Mai Phuong Nguyen, Shigeyoshi Yoshida, Satoshi Okamoto, Takamichi Miyazaki and Yasushi Endo : "Magnetic properties and lowering core loss in Fe-Si powder cores in high frequency range", Journal of Magnetism and Magnetic Materials, Vol. 617, p.172816, DOI: 10.1016/j.jmmm .2025.172816 (2025)
(7) Mai Phuong Nguyen, Shigeyoshi Yoshida, Satoshi Okamoto, Sho Muroga, Takamichi Miyazaki and Yasushi Endo : "Soft magnetic properties of Fe -Ni powder cores in the high frequency range", AIP Advances, Vol. 14, p.015034, DOI: 10.1063/9.0000719 (2024)
(8) Mai Phuong Nguyen, Shigeyoshi Yoshida, Satoshi Okamoto, Takamichi Miyazaki and Yasushi Endo : "Effect of Compaction Pressure on Core Loss in Fe-Ni Powder Cores for High-Frequency Applications", IEEE Transactions on Magnetics, Vol. 60, p. 2800104, DOI: 10.1109/ TMAG.2024.3402273 (2024)
(9) Nobuhito Chujo, Fumihiro Kino, Keita Kume, Toshihumi Aoyama and Masakatsu Fukuda : "Effect packing fraction on magnetic properties of the Fe-Si-Al powder cores by coarse powder and fine powder mixing", J. Jpn. Soc. Powder Metallurgy, Vol. 63, pp. 624-629, DOI: 10.2497/jjjspm. 63.624 (2016)

1.8 Modeling of magnetic elements

Magnetic characteristics are evaluated by the response of the magnetic flux density B to an external magnetic field *H*. The response (susceptibility) is defined as B = μH as the magnetic permeability μ. The magnetic element characteristics in circuit simulators and electromagnetic field simulators used in the power electronics field are described as B = μH. However, in actual magnetic materials, μ is not a constant but a nonlinear function of H, and has hysteresis characteristics that vary according to the historical state , making its handling extremely difficult. In addition, reflecting the loss behavior in the high-frequency range,μis highly dependent on the frequency. How to represent such very complicated μ behavior and magnetic hysteresis is a proposition of modeling in magnetic devices.

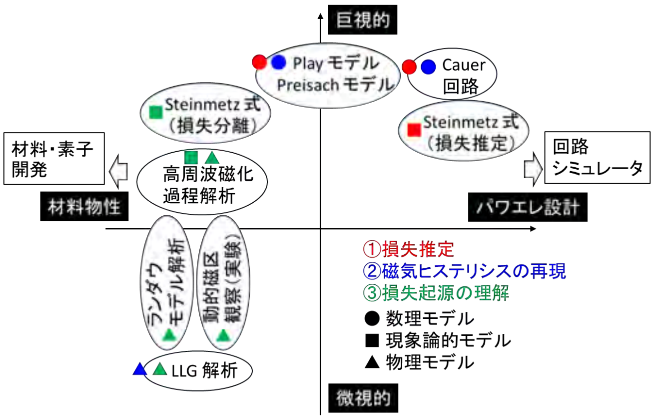

Figure 2.1.8.1 Classification of various modeling methods

The Steinmetz equation is used not only for loss estimation but also for loss separation for phenomenological interpretation of loss origins. Steinmetz equation is used not only for loss estimation but also for loss separation for phenomenological interpretation of loss origins. Furthermore, from this perspective, various types of loss analysis and magnetic domain observation, which have not been generally recognized as modeling, can be positioned as a type of modeling. **Figure 2.1.8.1** shows the classification of these methods, with material properties and power electronics design (electromagnetism) on the horizontal axis and macroscopic-microscopic on the vertical axis. The objectives of the various methods are (1) loss estimation, (2) reproduction of magnetic hysteresis, and (3) understanding of the origin of loss, and the methods are further classified as mathematical models, phenomenological models, and physical models, with the shape and color of each mark. The methods that are closer to power electronics design are expected to be connected to circuit simulators, while the methods that are closer to material properties are expected to be connected to the development of materials and devices. From this perspective, it is expected that the various modeling methods will be coupled in the future to construct an integrated modeling system from material/element development to power electronics design.

In this section, the play model analysis and the high-frequency magnetization process analysis are explained as follows. [Satoshi Okamoto]

1.8.1 Play Model Analysis

The current status of (1) loss estimation and (2) methods for reproducing magnetic hysteresis in magnetic elements and soft magnetic materials mentioned above will be reviewed and future prospects will be discussed.

(1) Hysteresis Model Overview

The Steinmetz [(1)] and Bertotti [(2)] methods are well known for expressing iron loss; the Steinmetz method expresses iron loss as a function of frequency and *B*amplitude and is widely used because of its simplicity. An extended method corresponding to square wave voltage excitation has also been proposed. Bertotti 's method models the abnormal eddy current loss separately, and is applicable to a limited number of frequencies. Bertotti's method models the anomalous eddy current losses separately and can achieve good accuracy with a small number of parameters in a limited frequency range. Since it does not include the skin effect term, it must be combined with another method to cover a wide frequency range, and the frequency dependence of 3/2 power may not be suitable for some soft magnetic materials. It is also possible to apply the method to magnetic field simulations.

The Preisach model [3] and the Jiles-Atherton (JA) model [4] are well-known hysteresis models; the Preisach model can represent a wide range of hysteresis characteristics such as DC superposition characteristics, but has the drawback of a large computational load. The JA model is often used because of its simplicity, but its accuracy in expressing hysteresis characteristics such as minor loops is not necessarily high. The Pray model [5] is a model that reduces these drawbacks. The Pray model is mathematically equivalent to the Preisach model, and is a promising model with high expressive power and a relatively small computational load. However, they are all static DC models, and must be combined with other methods to represent AC hysteresis characteristics.

(2) Combination of Cauer ladder circuit and play model

Therefore, a combination of the Cauer ladder circuit [6] and the Pray model, as shown in Figure 2.1.8.2(a), has been studied to represent the high-frequency characteristics of soft magnetic materials. By using the Pray model to represent inductor characteristics, it is possible to represent a wide range of hysteresis phenomena such as polarization and minor loops with a small computational load. The AC B-H curve corresponding to an arbitrary excitation waveform can be calculated (② in **Fig. 2.1.8.1** reproduces magnetic hysteresis), and as a result, the loss estimation in **Fig. 2.1.8.1** can be performed. This method is expected to be able to predict characteristics under a wide range of operating conditions based on measurement results under limited measurement conditions.

The inductor in the first stage of the Cauer circuit represents static hysteresis characteristics, eddy current loss is represented by a resistive element, etc. Each element has a physical meaning, and the model can be easily extended according to the physical phenomena to be considered. The RL element in the latter stage is responsible for high-frequency characteristics, allowing the model to cover a wide range of frequencies. The advantages of the circuit representation include the ability to handle arbitrary input waveforms such as PWM excitation, the natural representation of frequency characteristics as circuit characteristics, and the ability to be implemented in various general-purpose software such as circuit simulators. Eddy currents in soft magnetic materials flow in the microscopic internal structure, but it is not practical to perform magnetic field analysis considering the microscopic structure due to the computational cost. Therefore, a homogenization method is needed to give homogeneous soft magnetic materials with average magnetic properties reflecting the internal structure, and the Cauer circuit can be used as a homogenization method.

Figure 2.1.8.2 (b) shows the calculated frequency response of the iron loss of sendust. The calculation results reproduce the measurement results over a wide range of frequencies and amplitudes. The calculation has also been successfully implemented in the representation of the characteristics of other soft magnetic materials, in the simulation of iron loss under pulse waveform input, and in the finite element magnetic field analysis method.

(3) Future Development

In the following, we discuss the expected early applications, issues that need to be resolved, and limitations of the known models with respect to future developments.

a. Expected Early Applications It is expected to be incorporated into finite element magnetic field analysis to create a high-frequency magnetic element design tool. In addition, its use in expressing the AC hysteresis characteristics of magnetic elements (rather than materials) will enable its incorporation into power circuit analysis.

For simulation of soft magnetic materials/magnetic element characteristics under real-world conditions, it is desirable to improve the representation accuracy when DC bias is superimposed. To this end, the stop model [5] can be used instead of the play model, and the weight function of the play/stop model can be determined by using the extracted features, etc. On the other hand, another issue is that a ladder circuit of hysteresis inductors and resistors does not express resonance characteristics. In response to this, the resonant response of magnetization can be simulated by introducing a play hystereon with dynamic characteristics, and at the same time, the resonant characteristics due to the element structure can be simulated by inserting a capacitor in the circuit. Expansion of applicable frequencies by expressing resonance characteristics using characteristic separation of magnetic wall movement and magnetization rotation is also expected. On the other hand, improvement of implementability in general-purpose software is also desired.

c. Model Limitations Since it is a phenomenological model, model identification requires measurement results, and *B*-*H* loop data are needed up to the range of *B*required for the calculation. Also, the (static) hysteresis characteristics are fixed and separate from the eddy current-based dynamic characteristics, and changes in the magnetic domain structure with frequency are not taken into account. As a mathematical model, the hysteresis characteristics that can be expressed are theoretically shown, and clear constraints are known to exist. [Tetsushi Matsuo]

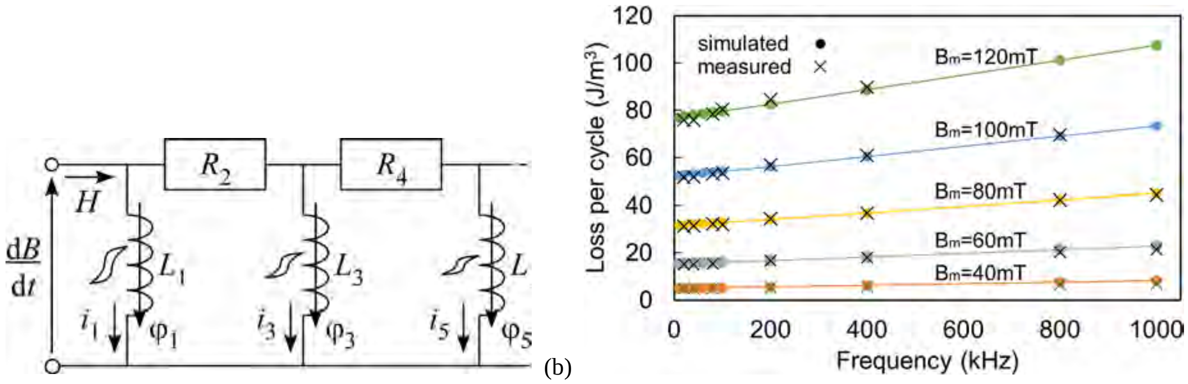

Figure 2.1.8.2 Magnetic property representation by Play model and Kauer circuit: (a) Kauer circuit, (b) Sendust iron loss calculation results

1.8.2 High frequency loss analysis (magnetization rotation and magnetic wall movement)

High frequency loss analysis originated from the Steinmetz equation of 1892, as described in Chapter 2, Section 1.1, which showed that the loss P (W/m^3) can be expressed as $P = kf^{\alpha}{}_{\mathrm{Bm}}{}^{\beta}$ with frequency f and excitation amplitude B_m bekiα, β. The hysteresis loss P_h is proportional to f under the assumption that the hysteresis curve area remains unchanged, not including dynamic effects, which are losses per cycle. The classical eddy current loss P_{cl} is calculated from Maxwell's equation assuming a uniform magnetization state (magnetization rotation) of the entire sample, and is proportional to f^2 in the lower frequency region where skin effects become apparent. Furthermore, there is a loss component proportional to $f^{1.5}$ that cannot be explained by P_h and P_{cl}, and this is considered to be an anomalous eddy current loss due to local eddy currents generated by the movement of magnetic walls, and the basic theory was established in the 1950s with the single magnetic wall model by Williams and others (7) and the periodic magnetic wall model by Pry and Bean (8). 8) by Pry and Bean. In 1981, Sakaki and Imagi explained the loss behavior of $f^{1.5}$ by introducing the magnetic wall number variation with increasing frequency (9), and in 1985, Bertotti's statistical theory. (11)(12) On the other hand, it has long been accepted that high-frequency losses are caused by eddy currents, both classical eddy currents and anomalous eddy currents, but recently, Suzuki's group has experimentally shown that there is a strong correlation between magnetostriction and high-frequency losses (13), and Tsukahara's group has developed a theory of the effect of magnetostriction on high-frequency losses (14), and its formulation has shown that high-frequency loss due to magnetostriction has the same $f^{1.5}$ loss behavior as that of anomalous eddy currents (15). In other words, since the high-frequency losses due to eddy currents and magnetostriction cannot be distinguished in the solution analysis by frequency becking, the loss component of $f^{1.5}$ for both of them combined as excess loss P_{exc} is given by the iron loss formula based on the Steinmetz formula in Equation (2.1.1.10) or Equation (2.1.1.11) in Section 1.1.6 of Chapter 2 (2.1.1.11) is given.

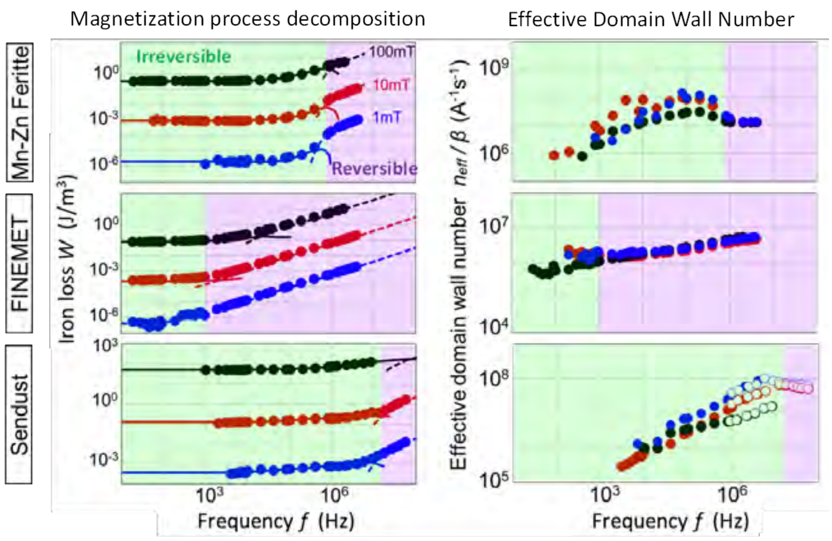

Fig. 2.1.8.3 Results of applying the magnetization process separation model (left) and the effective magnetic wall model (right) to the sendust compact core, FINEMET wound core, and Mn-Zn sintered core. The solid and dashed lines on the left show the loss components of the irreversible and reversible magnetization processes, respectively. Blue, red, and black indicate measurement results at excitation amplitudes B_m = 1, 10, and 100 mT , respectively .

On the other hand, it should be noted that the iron loss formula based on the Steinmetz formula was established in the era when electromagnetic steel plates were driven at low frequencies. Specifically, hysteresis loss is treated as independent of frequency, but in reality, in the high-frequency range, the magnetic domain structure is subdivided and the magnetization process itself changes (16), and the classical eddy current loss, which assumes magnetization rotation, and the excess loss, which assumes magnetic wall movement, are compatible. The iron loss equation based on the Steinmetz equation should be interpreted phenomenologically.

A loss analysis method based on the magnetization process has been proposed by Fiorillo and his group, and it has been shown that the reversible component (magnetization rotation) and irreversible component (magnetic wall movement) of the magnetization process can be separated (17). The model by Sakaki and Imagi, already mentioned above, is also effective as a method to experimentally quantify magnetic domain subdivision in the high-frequency region (9). Hereafter, the former is referred to as the magnetization process separation model and the latter as the effective magnetic wall model. The effective magnetic wall model was originally intended for periodic magnetic walls of electromagnetic steel plates, but it has been shown to be applicable to samples with irregularly shaped magnetic domains, such as ferrite and amorphous thin strips, by treating them as effective periodic magnetic walls (18).

Figure 2.1.8.3 shows the results of applying the magnetization process separation model and the effective magnetic wall model to three types of magnetic cores: sendust compact core, FINEMET wound core, and Mn-Zn sintered core (19). The vertical axis is the iron loss per cycle, W (J/m^3). The magnetization process separation model shows that the irreversible magnetization process is the main component in the low frequency region, and the effective magnetic wall model is the main component in the high frequency region. The iron loss W changes slowly with frequency in the low-frequency region. On the other hand, in the high-frequency region, the reversible magnetization process is the main component and Wincreases significantly. The effective magnetic wall model shows that the effective magnetic wall number n_{eff} tends to increase in the low-frequency region and saturates in the high-frequency region. Furthermore, the frequency at which the magnetization process changes in the magnetization process separation model roughly corresponds to the frequency at which the behavior of n_{eff} changes in the effective magnetic wall model. However, this frequency varies greatly from sample to sample. Furthermore, comparison with the results of the analysis using the equation (2.1.1.7) in Section 1.1, which has been widely used in the past, shows that the loss component in the irreversible magnetization process (magnetic wall movement) is almost equal to the sum of hysteresis loss and excess loss, while the loss component in the reversible magnetization process (magnetization rotation) is almost equal to the classical eddy current loss. Statistical analysis also shows that the effective magnetic wall number corresponds well to the behavior of the magnetic object in the statistical theory. Therefore, the results of this analysis clarify the correspondence between various iron loss analysis models proposed in the past.

On the other hand, the results in **Figure 2.1.8.3** were obtained for samples with relatively small iron loss, and such a clear correspondence was not found especially for samples with large magnetostriction-induced loss, indicating that a more detailed discussion of the magnetic domain structure and magnetization process is needed. This is an issue to be addressed in the future. [Satoshi Okamoto]

*In large amplitude excitation, magnetization rotation occurs after the magnetic wall shift. However, even in this case, the ratio of magnetization rotation to the total magnetization change is very small.

1.8.3 LLG Analysis

As shown in "**Figure 2.1.8.1** Classification of various modeling methods" Landau-Lifshitz-Gilbert (LLG) analysis is aimed at understanding microscopic properties of magnetic materials. It has been used in the fields of magnetic recording and spintronics as a tool for clarifying the dynamic behavior of magnetization at the nanoscale, such as the dynamics of magnetization reversal, but it is difficult to extend it to real-scale electrical devices and magnetic elements. On the other hand, Maxwell's equations, which describe electromagnetic phenomena, have been widely used as a tool to understand the behavior of electromagnetic fields, not only in the electromagnetic properties of materials but also in the analysis and design of electrical devices such as transformers, inductors, and motors. Since there is a big difference in the scale of the analysis space between LLG analysis, which covers the nanoscale region, and Maxwell analysis, which is used for real-scale electrical equipment, various innovations are required to analyze the two in conjunction.

Here, we present an example of LLG/Maxwell coupled analysis for the purpose of analyzing the properties of soft magnetic materials such as transformers and inductors, and also discuss some of the issues involved.

(1) LLG equation and Maxwell equation

The LLG equation describes the dynamic behavior of magnetization and is expressed as

$$\frac{dM}{dt} = -\frac{\gamma}{1+\alpha^2} M \times H_{\mathrm{eff}} - \frac{1}{1+\alpha^2}\frac{\alpha\gamma}{M_{\mathrm{s}}} M \times (M \times H_{\mathrm{eff}}), \quad H_{\mathrm{eff}} = \frac{\delta E_{tot}}{\delta M} \qquad (2.1.8.1)$$

M is the magnetization vector and H_{eff} is the effective magnetic field. γ is the gyromagnetic constant, and α is the damping constant for the dynamic behavior of the magnetization. The effective magnetic field H_{eff} is defined by the partial derivative of the magnetization energy E_{tot}.

$$E_{\mathrm{tot}} = \int dV\{E_{\mathrm{ani}} + E_{\mathrm{ex}} + E_{\mathrm{ext}} + E_{\mathrm{sta}} + E_{\mathrm{ela}}\} \qquad (2.1.8.2)$$

E_{ani}, E_{ex}, E_{ext}, E_{sta}, and E_{ela} are the anisotropic energy per unit volume, exchange energy, Zeeman energy due to external magnetic field, magnetostatic energy, and magnetoelastic energy, respectively. Thermal energy is also added if the behavior at high temperatures is considered. Although all energies should normally be considered, they may be omitted depending on the analytical model under consideration. Nowadays, general-purpose software for LLG analysis is available (20).

Maxwell's equations describe electromagnetic phenomena in the space containing the material, and in the case of metallic magnetic materials, they are expressed as follows

$$\mathrm{div}B = 0,\ \ \mathrm{rot}E = -\frac{\partial B}{\partial t},\ \ \mathrm{rot}H = j,\ \ B = \mu H \tag{2.1.8.3}$$

where B is the magnetic flux density vector, E is the electric field vector, and j is the current density vector. μ is the magnetic permeability. In general, there is a nonlinear relationship between magnetic flux density and magnetic field, and the magnetic permeability is also nonlinear. In the case of ferrite and composite materials, which have dielectric properties, the displacement current component must be taken into account. For transformers, inductors, and motors, Maxwell analysis is now available as general-purpose software that can consider nonlinear *B-H* characteristics including hysteresis and coupling with external circuits (21). At present, there is no general-purpose software that enables simultaneous coupled analysis of LLG and Maxwell, and coupled analysis has been attempted using various methods.

There are not many examples of coupled LLG/Maxwell analysis for soft magnetic materials for transformers and inductors. As shown in **Figure 2.1.8.4**, modeling itself is difficult for isotropic materials with a mixture of magnetic wall movement and magnetization rotation. Based on the guideline that the introduction of the magnetization rotation process by anisotropic induction is effective in reducing high-frequency losses in metallic magnetic materials, the following is an example of high-frequency loss modeling by coupled LLG/Maxwell

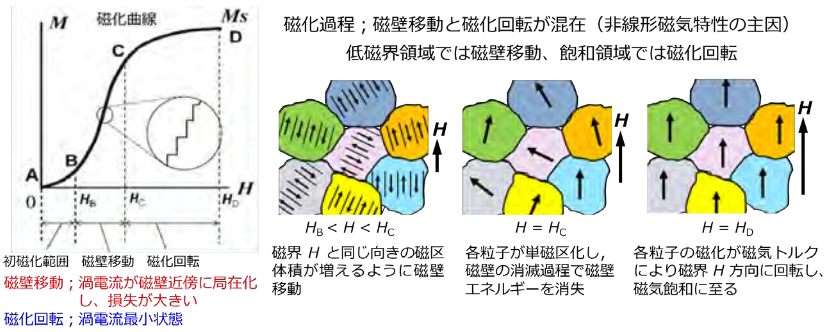

Figure 2.1.8.4 Magnetization characteristics when magnetic wall movement and

analysis assuming magnetization rotation.

(2) Example of LLG/Maxwell Coupled Analysis

a. a previous coupled analysis by Bottauscio et al. (22) and Paakkunainen et al. (23) for anisotropic amorphous thin bands

Bottauscio et al. (22) studied a method for predicting high-frequency magnetic properties by coupling LLG and the diffusion equation of the electromagnetic field by Maxwell analysis for the case of longitudinal magnetization rotation excitation of a thin amorphous strip with induced anisotropy in the width direction. The LLG analysis neglects magneto-elastic energy, eddy currents are included in the effective magnetic field of the LLG analysis, and the LLG analysis and the diffusion equation of the electromagnetic field are analyzed using a one-dimensional model in the longitudinal direction of the thin strip. Although the results do not reflect the inhomogeneity of local magnetic properties in thin strips of actual dimensions, they compare the measured energy loss of annealed Co-Fe-B-Si amorphous thin strips annealed in a magnetic field in the width direction from 0.1 kHz to 1 GHz and find that the analytical results reproduce the trend of the measured values well.

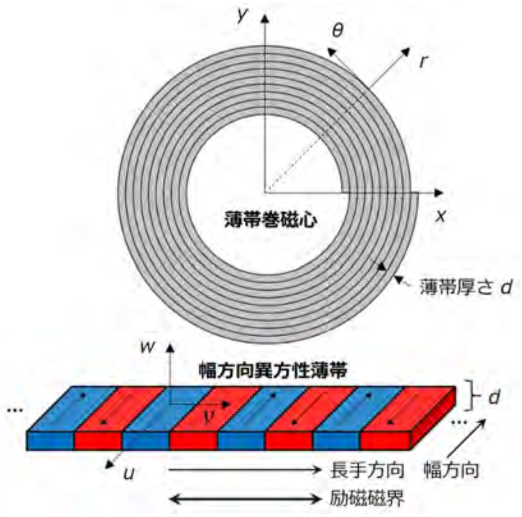

Figure 2.1.8.5 Model of thin strip winding core with anisotropy in the width direction, based on reference (23)

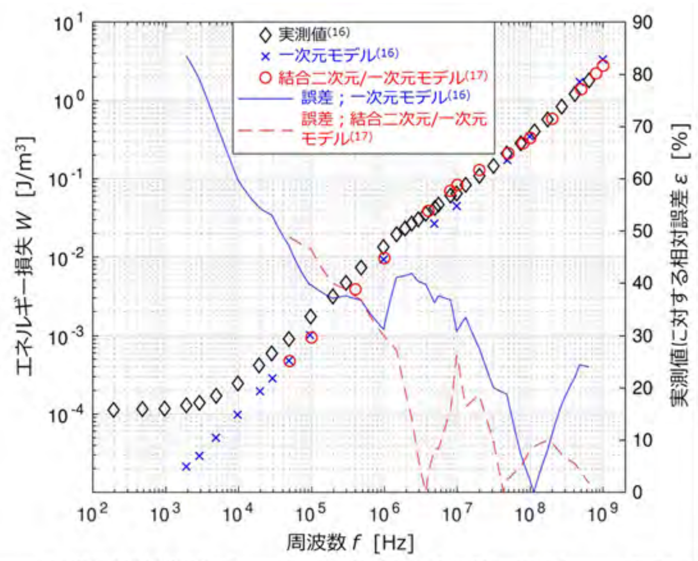

平均磁束密度振幅；B_m = 3 mT，磁化回転ダンピング定数；α = 0.04
電気抵抗率；ρ = 1.41 μΩ・m，厚さ；17 μm

Figure 2.1.8.6 Energy loss of 17-μm-thick widthwise anisotropic Co-Fe-B-Si amorphous thin band, based on Ref. (23)

Paakkunainen et al. [23] proposed a method that combines longitudinal one-dimensional LLG analysis and two-dimensional electromagnetic field analysis for thin strip with width-directed anisotropy. **Figure 2.1.8.5** shows a model of a thin strip core with anisotropic winding in the width direction to be analyzed, assuming a 180° magnetic domain structure aligned in the width direction of the thin strip and assuming that the magnetic walls do not move due to longitudinal excitation of the thin strip and that magnetization reversal occurs only by magnetization rotation. (22), the eddy current magnetic field is included in the effective magnetic field of the LLG analysis. The longitudinal one-dimensional LLG analysis is modeled analytically based on the governing equations in Eq. (2.1.8.1), while the finite element method is used for the two-dimensional electromagnetic field analysis. The results of the one-dimensional LLG analysis are assigned to each mesh of the two-dimensional finite element method (FEM). **Figure 2.1.8.6** plots the energy loss of a 17-μm-thick, widthwise anisotropic Co-Fe-B-Si amorphous thin band, showing the predicted and measured values from the one-dimensional analysis by Bottauscio et al. (23), as well as the relative error to the measured values. The average magnetic flux density amplitude $_{\mathrm{Bm}}$ is 3 mT, the damping constant for the dynamic behavior of magnetization α is 0.04, and the electrical resistivity ρ is 1.41 μΩ-m. Both of them explain the measured values well at frequencies above 1 MHz, where the energy loss is large, and in particular, the two-dimensional FEM/one-dimensional LLG analysis by Paakkunainen et al. In the actual thin band, energy loss involving magnetic wall movement is included in the low frequency region, and the discrepancy in the calculated values at frequencies below 1 MHz is estimated to be due to eddy current loss caused by magnetic wall movement. Based on the report [24] that the damping constant for the dynamic behavior of magnetization depends on the thin-band thickness, the discrepancy in the measured values is reduced by increasing the value of α from 0.04 to 0.1. have been used.

In the examples of Bottauscio et al. [22] and Paakkunainen et al. [23], the coupled LLG/Maxwell analysis reproduces the measured values well because magnetization rotation is dominant at high frequencies where the magnetic walls cannot follow (magnetization rotation is a reversible magnetization process, and the agreement between the predicted and measured values in the high frequency region is a natural consequence). However, at frequencies below 1 MHz, there is a large discrepancy with the measured values, and the measured values include eddy current components due to magnetic wall movement, which is estimated to result in large errors. The influence of the amplitude level of the magnetic flux density is stated to improve the prediction accuracy by adjusting α. Furthermore, the specific method of giving anisotropic energy (anisotropic magnetic field) is not clarified, and there are many ambiguous points. It is also necessary to discuss how the intensity of anisotropy and the dispersion of orientation affect the loss. In addition, both analyses were performed on anisotropic thin strips with a thickness of 13 to 20 μm. Although it is possible to accurately predict high-frequency losses above 1 MHz, it is unlikely that these thin strips will be used in transformers and inductors at frequencies above 1 MHz. In reality, the main application is expected to be up to several hundred kHz, so it is desirable to improve the accuracy of loss calculation in the low-frequency range.

b. A case of coupled analysis for anisotropic thin zones by Oishi et al. [26]

Oishi et al. [26] proposed a coupled LLG/Maxwell analysis for longitudinal magnetization rotation excitation of anisotropic thin strips using a different method. Since eddy currents depend on the shape and dimensions of soft magnetic materials, the eddy currents vary greatly

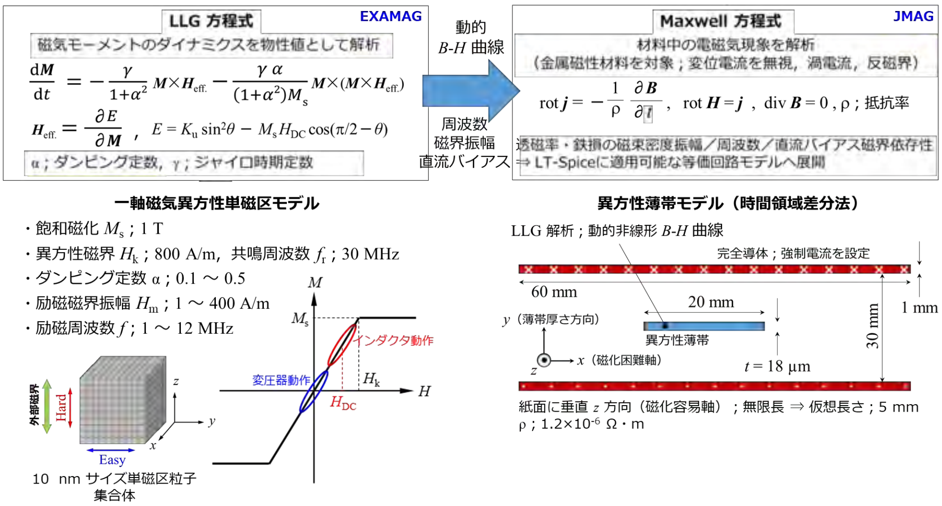

Figure 2.1.8.7 LLG/Maxwell pseudo-coupled analysis for an anisotropic thin band with saturation magnetization of 1 T and an anisotropic magnetic field of 800 A/m

depending on the shape and dimensions of the magnetic cores of actual transformers and inductors. Therefore, we have studied a method to calculate the damping loss due to magnetization rotation by LLG analysis and to use the resulting dynamic *B-H* curve as a parameter of Maxwell analysis as material-specific physical property data. Each analysis was performed using general-purpose software (20)(21). **Figure 2.1.8.7** shows an overview of the LLG/Maxwell pseudo-coupled analysis for an anisotropic thin band. In the Maxwell analysis, eddy current calculations are performed reflecting the shape and dimensions of the real-scale material, so the dynamic loss obtained here is the sum of damping loss due to magnetization rotation and eddy current loss. A pseudo-coupled analysis of dynamic *B-H* curves for an anisotropic thin band with a saturation magnetization of 1 T and an anisotropic magnetic field of 800 A/m is performed for the case of origin-symmetric AC excitation. Although not shown here, the intrinsic resonance frequency of the material of the target model is about 30 MHz. In the LLG analysis, the damping loss increases rapidly at 10 MHz, which is close to the resonance frequency, due to the effect of resonance, and the dynamic *B-H* curve becomes nonlinear. The results of the Maxwell analysis using these material specific dynamic property parameters are shown in **Figure 2.1.8.8**, which shows the frequency characteristics of the dynamic loss, which is the sum of the damping loss and eddy current loss for *α*; 0.1, and the *B-H* curve at each frequency. The material-specific magnetization process shows nonlinear behavior near the resonance frequency, but in the Maxwell analysis, the eddy current braking is dominant, so the rapid increase in damping loss due to resonance is masked, and the results are in good agreement with the calculated values based on classical eddy current loss. Since the dynamic loss consists of damping loss and eddy current loss, the effect of nonlinear damping loss becomes apparent when the eddy current loss becomes relatively small due to the thinning of the thin band. The above analysis can also be performed for inductor operation in which a DC magnetic field is superimposed in the same direction as the AC magnetic field, and it is possible to estimate the strength and orientation distribution of the anisotropic magnetic field (anisotropic dispersion) from the measured magnetostatic properties of magnetic materials using LLG analysis [27], and incorporate these into LLG/Maxwell analysis (27) By incorporating these into LLG/Maxwell analysis, the actual material properties can be predicted with higher accuracy, and for thin anisotropic bands, loss modeling with high accuracy at several hundred kHz, which is regarded as the volume zone, is expected to become possible.

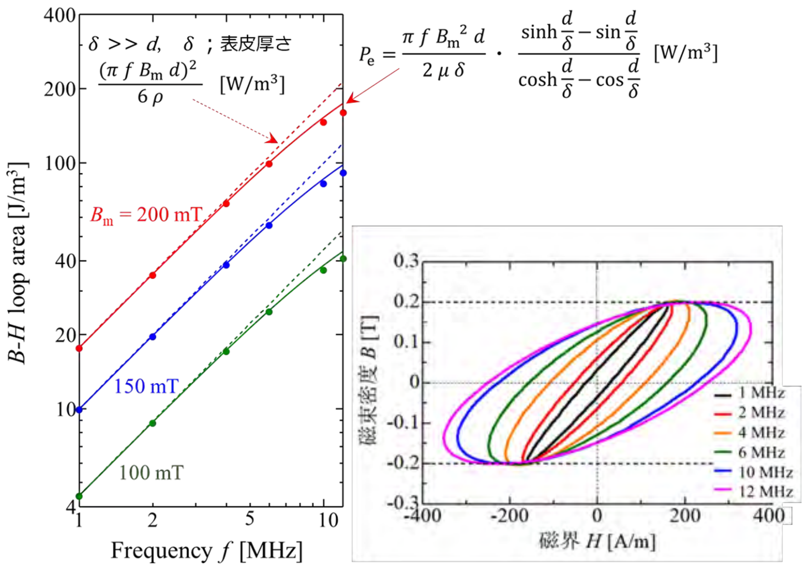

Figure 2.1.8.8 Frequency response of dynamic loss in anisotropic thin band simulating transformer operation, based on Ref. (26)

(3) issue

LLG analysis of soft magnetic materials for transformers and inductors assumes anisotropy-induced hard magnetization axis excitation, which is very difficult to model for many materials with a mixture of magnetic wall motion and magnetization rotation as shown in **Figure 2.1.8.4**. Further study is needed before the coupled LLG/Maxwell analysis can be useful for general soft magnetic materials. For example, it is necessary to devise various methods such as extracting many material-specific property parameters from multiple measured property data, compiling a statistical database of local magnetic properties of materials and using it for LLG analysis, etc. In the future, the introduction of AI approaches using GA, multi-objective optimization, etc. will be essential. In the future, the introduction of AI approaches using GA and multi-objective optimization will become indispensable. Furthermore, it is desirable to develop general-purpose software that can be used by inductor and transformer designers.

[Toshiro Sato]

References

(1) K. Venkatachalam, C.R. Sullivan, T. Abdallah, H. Tacca: "Accurate prediction of ferrite core loss with nonsinusoidal waveforms using onlySteinmetz parameters", Proc. IEEE Workshop Comput. Power Electron. pp. 36-41, DOI: 10.1109/CIPE.2002.1196712 (2002)

(2) G. Bertotti: "Hysteresis in Magnetism", Academic Press, DOI: https://doi.org/10.1016/B978-0-12-093270-2.X5048-X (1998)

(3) I.D. Mayergoyz: "Mathematical Models of Hysteresis and their Applications", Elsevier, DOI: https://doi.org/10.1016/B 978-0-12-480873-7.x5000-2 (2003)

(4) D. C. Jiles and D. L. Atherton: "Theory of Ferromagnetic Hysteresis", J. Magn. Magn. Mater. vol. 61, pp. 48-60, DOI: https:// doi.org/10.1016/0304-8853(86)90066-1 (1986)

(5) S. Bobbio, G. Miano, C. Serpico, C. Visone: "Models of magnetic hysteresis based on play and stop hysterons", IEEE Trans. Magn. ., Vol. 33, No. 6, pp. 4417-4426, DOI: 10.1109/20.649875 (1997).

(6) Y. Shindo, T. Miyazaki, T. Matsuo: "Cauer circuit representation of the homogenized eddy-current field based on the Legendre expansion for a magnetic sheet", IEEE Trans. Magn., Vol. 52, No. 3, 6300504, DOI: 10.1109/TMAG.2015.2478139 (2016).

(7) H. J. Williams, W. Shockley, and C. Kittel : "Studies of the propagation velocity of a ferromagnetic domain boundary", Phys. Rev. Vol. 80, pp. 1090-1094, DOI: 10.1103/PhysRev.80.1090 (1950).

(8) R. H. Pry and C. P. Bean : "Calculation of the energy loss in magnetic sheet materials using a domain model", J. Appl. Phys. 29, pp. 532-533, DOI: 10.1063/1.1723212 (1958)

(9) T. R. Haller and J. J. Kramer : "Model for reverse-domain nucleation in ferromagnetic fonductors ", J. Appl. Phys. .1036-1037, DOI: 10.1063/1.1658805 (1970)

(10) Y. Sakaki and S. Imagi : "Relationship among eddy current loss, frequency, maximum flux density and a new parameter concerning the number of domain walls in polycrystalline and amorphous soft magnetic materials", IEEE Trans. TMAG.1981.1061229 (1981)

(11) G. Bertotti : "Physical interpretation of eddy current losses in ferromagnetic materials. I. Theoretical considerations" , J. Appl. Phys., Vol. 57, pp. 2110-2117, DOI: 10.1063/1.334404 (1985)

(12) G. Bertotti : "Physical interpretation of eddy current losses in ferromagnetic materials. II. Analysis of experimental results ", J. Appl. Phys., Vol. 57, pp. 2118-2126, DOI: 10.1063/1.334405 (1985)

(13) H. Huang, H. Tsukahara, A. Kato, K. Ono, and K. Suzuki : "Origin of excess core loss in amorphous and nanocrystalline soft magnetic materials ", Phys. Rev. B, Vol. 109, 104408, DOI: 10.1103/PhysRevB.109.104408 (2024)

(14) H. Tsukahara, H. Imamura, C. Mitsumata, K. Suzuki, and K. Ono : "Role of magnetostriction on power losses in nanocrystalline soft magnets ", NPG Asia Mater.

(15) H. Tsukahara, H. Huang, K. Suzuki, and K. Ono : "Formulation of energy loss due to magnetostriction to design ultraefficient soft magnets ", NPG Asia Mater.

(16) S. Flohrer, R. Schäfer, J. McCord, S. Roth, L. Schultz, G. Herzer : "Magnetization loss and domain refinement in nanocrystalline tape wound cores", Acta Mater. vol. 54, pp. 3253-3259, DOI: 10.1016/j.actamat.2006.03.011 (2006)

(17) C. Beatrice, V. Tsakaloudi, S. Dobák, V. Zaspalis, and F. Fiorillo : "Magnetic losses versus sintering treatment in Mn-Zn ferrites ", J. Magn. Magn. Mater. vol. 429, pp. 129-137, DOI: 10.1016/j.jmmm.2016.12.121 (2017)

(18) Y. Sakaki and T. Sato : "Large signal eddy current losses beyond 100 kHz," IEEE Trans. Magn. 10.1109/TMAG.1984.1063478 (1984)

(19) N. Ono, Y. Uehara, T. Onuma, T. Taniguchi, N. Kikuchi, and S. Okamoto : "Multimodal iron loss analyses based on magnetization processes for various soft magnetic toroidal cores J. Magn. Magn. Mater.

(20) F-S Technologies website: "EXAMAG LLG Simulator for Large-Scale Multiscale Magnetic Field Simulation," https://www.fsastech.com/ja-jp/products/software/examag/

(21) JSOL Home Page: "Simulation Software for Design and Development of Electrical Equipment," https://www.jmag-international.com/jp/products/

(22) Oriano Bottauscio, Fausto Fiorillo, Cinzia Beatrice, Ambra Caprile, Alessandro Magni: "Modeling High-Frequency Magnetic Losses in Transverse Anisotropy Amorphous Ribbons," *IEEE Transactions on Magnetics*, Vol. 51, No. 3, #2800304, DOI:10.1109/TMAG.2014.2361534 (2015)

(23) Elias Paakkunainen, Lasse Laurson, Paavo Rasilo: "Coupled 2-D FEM and 1-D Micromagnetic Model for Transverse Anisotropy Tape-Wound Magnetic Cores," *IEEE Transactions on Magnetics*, Vol. 59, No. 5, #7400604, DOI:10.1109/TMAG.2023.3239634. (2023)

(24) Alessandro Magni, Oriano Bottauscio, Ambra Caprile, Federica Celegato, Enzo Ferrara, Fausto Fiorillo: "Spin precession by pulsed inductive magnetometry in thin amorphous plates", *Journal of Applied Physics*, Vol. 115, No. 17, #17A338, DOI: 10.1063/1.4867755 (2014)

(25) Cinzia Beatrice, Samuel Dobák, Enzo Ferrara, Fausto Fiorillo, Carlo Ragusa, Ján Füzer, Peter Kollár: "Broadband magnetic losses of nanocrystalline ribbons and powder cores", *Journal of Magnetism and Magnetic Materials*, Vol. 420, pp. 317-323, DOI: 10. 1016/j.jmmm.2016.07.045 (2016)

(26) Kyosuke Oishi, Koshi Saito, Toshiro Sato, Makoto Sonehara, Toshitaka Minamisawa: "Dynamic Magnetization Reversal and Dynamic Loss Analysis of a Single Magnetic Domain Model by LLG/Maxwell Quasi-coupled Simulation," 48th Annual Conference of Magnetics Society of Japan, Symposium "What is Required for Soft Magnetic Materials for the Next Generation Power Electronics? What is required of soft magnetic materials for the next generation of power electronics? (2024)

(27) Kyosuke Oishi, Eiji Teranishi, Akinari Souda, Makoto Sonehara, Toshiro Sato: "Estimation of Anisotropic Dispersion in Co-Pd Substituted FINEMET Thin Bands with Induced Uniaxial Magnetic Anisotropy," Proc. of the IEEJ Magnetics Society, MAG-25-078 (2025)

Section 2 Capacitor

2.1 Using different capacitors for power electronics

Keyword: Energy storage elements, Ripple current, Withstand voltage, Lifetime, Capacitance

In power electronics applications, capacitors play the role of not only a reactance element expressed as $X=1/\omega C$ (Ω), but also an energy storage element expressed as $W=1/2CV^2$ (J). In other words, it is necessary to discuss both the behavior of AC circuits as well as DC circuits simultaneously in power electronics applications. Moreover, the frequency component produced by power electronics circuits is not a single component in most cases, but has a wide bandwidth from low to high frequency regions, and the bandwidth varies depending on the circuit and control scheme.

2.1.1 Radar chart

Looking at the power electronics circuit from the capacitor's point of view, it only accepts the current flowing in from the circuit and the applied voltage without any denial, and the evaluation axes can be classified as follows

- Ripple current rating (low frequency range)
- Ripple current rating (high-frequency range)

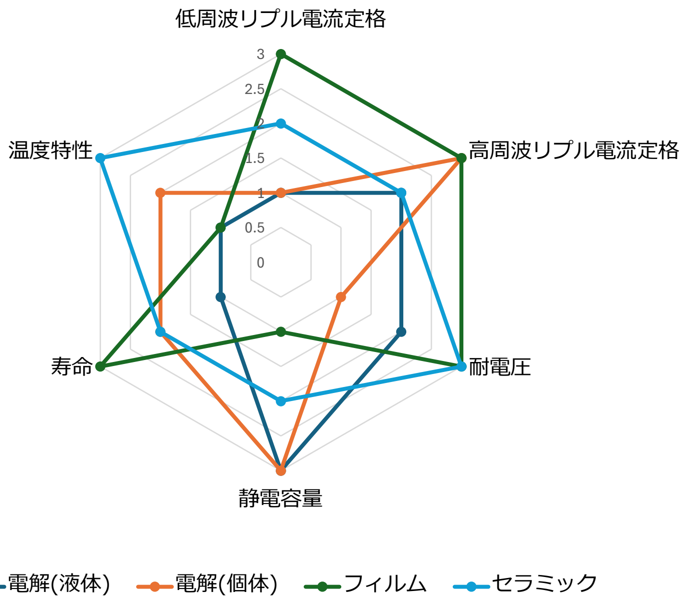

- Withstand voltage
- Capacitance (reactance ωL)
- life span
- cost
- Temperature Characteristics

The ripple current rating is divided into low-frequency and high-frequency regions. This is because when the low-frequency (100 or 120 Hz) current generated by a single-phase converter flows in, not only is capacitance required, but also low loss in the low-frequency region is required. For example, electrolytic capacitors can be easily increased in capacitance, but their ESR increases in the low-frequency range, which is a drawback. **Figure 2.1.1.1** shows a radar chart summarizing the above evaluation axes and the characteristics of each capacitor.

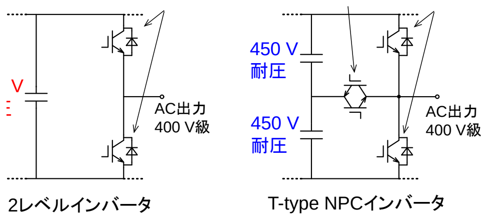

Figure 2.1.1.2 Application of 450 V solid polymer capacitor to a 400 V

However, cost is excluded from the radar chart because there are multiple possible evaluation criteria. For example, the radar chart changes depending on whether it is considered per unit capacitance (JPY/μF) or per unit ripple current rating (JPY/A). It may also be necessary to consider the cost of capacitors in the power electronics circuit, but this is difficult to evaluate because it depends on the other evaluation axes mentioned above.

If the performance of the capacitors given in the above evaluation axes evolves, the circuit technology used may (or should) change along with it. For example, if a 450 V withstand voltage polymer solid capacitor is realized as shown in **Figure 2.1.1.2**, it can be applied not only to 200 V series inverters but also to 400 V series inverters if the circuit configuration is made into an NPC inverter (1). If ESR increase in the low-frequency range is a problem, as is the case with aluminum electrolytic capacitors, a power decoupling circuit can be introduced to actively reduce the low-frequency ripple current (2). Another idea is to connect different types of capacitors in parallel, for example, using liquid electrolytic capacitors in the low-frequency region where capacitance is required and using solid polymer capacitors to handle the switching ripple component in the high-frequency region (3).

The above ideas are similar to the fact that the circuit configuration adopted has been reviewed as power semiconductor devices have evolved, and that there are examples of the adoption of combinations of different types of semiconductors, such as cascode connections, respectively.

2.1.2 Perspectives of the user and the creator

(1) User

Most power electronics circuit engineers look at capacitors as a black box, with electrical characteristics (current rating, withstand voltage, and capacitance), physical size, and lifetime. For physical size, power density (W/cm^3), which is the rated power per unit volume, is often used as an indicator. However, since the actual voltage and current waveforms of power electronics circuits often have a diverse mix of DC, low-frequency, and high-frequency components, it is difficult to accurately estimate the characteristics (loss, life) in actual use by using electrical characteristics based on impedance measurement at a single frequency. As a result, a margin is set for selection.

For these reasons, the user really needs data on actual use (e.g., loss characteristics at square wave ripple current inflow). Or, the user side needs to transmit the method of acquiring data on capacitors in actual use.

(2) Maker

It is possible that the actual use of the capacitor in the power electronics circuit is not clear. For example, it is unclear whether the emphasis should be on increasing capacitance or reducing losses, and since power electronics circuits have (or appear to have) a wide variety of circuit configurations, it appears that it is necessary to provide capacitors suitable for each circuit. It would be desirable to have the requirements from the user side expressed not in terms of application or circuit configuration, but in terms of clear numerical values for how much electrical stress is applied to the capacitor. Specifically, environmental temperature, ripple current (in the low-frequency range and high-frequency range, respectively), capacitance, etc. should be mentioned.

[Kazunori Hasegawa]

References

(1) A. Nabae, I. Takahashi and H. Akagi: " A new neutral-point-clamped PWM inverter", IEEE Trans. Ind. Appl. Appl. Vol. 17, No. 5, pp. 518-523, (1981)

(2) T. Shimizu, K. Wada and N. Nakamura: " Flyback-Type Single-Phase Utility Interactive Inverter With Power Pulsation Decoupling on the DC Input for an AC Photovoltaic Module System", IEEE Trans.

(3) D. Kuba and K. Hasegawa: "Measurement of Loss Sharing by Parallel Connection of Solid and Liquid Aluminum Electrolytic Capacitors in Three-Phase Inverter and Single-Phase PFC Rectifier," IEEJ Joint Seminar on Semiconductor Power Conversion/Home Appliances, Consumer Electronics, and Automotive, SPC-24-226/HCA-24-046/VT-24-071, (December 2024) December 2024)

2.2 Ceramic Capacitors

Keyword: Multilayer ceramic capacitor (MLCC), Paraelectric, Ferroelectric, Antiferroelectric, Reliability, Electrode material

2.2.1 Classification of dielectrics and their application as multilayer ceramic capacitors

Dielectrics are mainly classified into paraelectric, ferroelectric, and antiferroelectric, depending on the symmetry and polarization properties of the material. Their characteristics are outlined below.

(1) paramagnetic substance

The dielectric constant does not change with the application of an electric field. Since the relative dielectric constant is generally low (100 to 101), composition design for low loss and high dielectric strength is fundamental. In general, temperature and time variations (aging) of the relative dielectric constant are extremely small, and materials such as CaZrO3 are used as temperature compensating (Class-I) multilayer ceramic capacitors. In oxides, cations with stable valence, such as Si, Al, Zr, and Hf, are often selected. 102-class high relative dielectric constant can be obtained by using a material system that exhibits special paraelectricity, called quantum paraelectricity or precursor-type ferroelectricity. However, the temperature variation of the relative permittivity is rather large. Typical examples are rutile TiO2, CaTiO3, SrTiO3, and KTaO3.[(1)(2)] A material in which Bi in Bi2SiO5 is partially replaced by La has a high permittivity of class 102, but the temperature change in permittivity is very small.[(3)] By using a phenomenon called the Maxwell-Wagner-Sillars effect [(4)], an exceptionally large relative permittivity of class 104 can be obtained, which has been put to practical use as a grain boundary insulating type capacitor. (In recent years, the number of such capacitors has been decreasing due to the difficulty of stacking them in the trend toward capacitors with larger capacitance and smaller size.)

(2) ferroelectric

The dielectric constant decreases with the application of an electric field, and extremely high dielectric constants of 10^2 to 10^3 can be obtained. $BaTiO_3$, a perovskite-type oxide, is used as a representative material for high dielectric constant (Class-II) multilayer ceramic capacitors. Although the relative dielectric constant has a strong temperature dependence, the temperature change can be weakened by adding appropriate additive elements. Aging, in which the relative dielectric constant decreases with time, is often observed. Typical ferroelectric material systems include perovskite-type oxides, layered perovskite-type oxides, and tungsten bronze-type oxides. Many of them contain Ti, Nb, Pb, Bi, etc. as constituent elements.

(3) antiferroelectric

The dielectric constant increases with the application of an electric field. When the applied electric field is sufficiently small, the dielectric constant is 10^1 to 10^2, which is higher than that of ferroelectric materials. Excluding water-soluble oxides and organic materials, the number of antiferroelectrics reported today is far fewer than that of ferroelectrics. A perovskite-type oxide, $PbZrO_3$, is known as a representative antiferroelectric material [(5)]. Recently, a new antiferroelectric material has been reported in titanite-type oxides, which is expected to be a new material combining high dielectric constant and excellent insulating property under high voltage [(6)(7)].

(4) Reliability (life span, dielectric breakdown strength)

The reliability required of multilayer ceramic capacitors varies widely, but from the standpoint of intrinsic reliability, insulation resistance at high temperatures and high electric fields is important. In general, there is a problem of insulation resistance degradation under high temperatures and high electric fields, and this problem is particularly apparent in the most advanced compact large-capacity multilayer ceramic capacitors, which have a thinner layer thickness. The mechanism of insulation resistance degradation is complex and is strongly affected by defects such as oxygen defects inherent in ceramics and heterogeneity of ceramics, as well as structural defects and heterogeneity of devices.

It is known that there is a negative correlation between dielectric breakdown strength and dielectric constant, but the correlation between high temperature load life and dielectric constant is not well understood.

(5) Electrode Material

For both Class-I and Class-II multilayer ceramic capacitors, noble metal materials such as Pt, Pd, and Ag-Pd were used for the inner electrodes when they were first developed. For both Class-I and Class-II multilayer ceramic capacitors, noble metal materials such as Pt, Pd, and Ag-Pd were used for the internal electrodes, but with the development of reduction-resistant dielectrics, base metals such as Ni and Cu are now mainly used. In PLZT-based multilayer ceramic capacitors, Cu is used as the internal electrode, taking advantage of the technology cultivated in the manufacture of multilayer piezoelectric actuators.

2.2.2 Trade-off between dielectric constant and reliability

Dielectric response is derived from various polarization phenomena such as electronic polarization, ionic polarization, orientation polarization, and even interface polarization due to spatial inhomogeneity of electrical properties in a material. Electronic polarization is a polarization phenomenon that occurs when the electronic state is excited by the application of an external electric field. Therefore, the dielectric constant due to electronic polarization is proportional to the reciprocal of the energy band gap of the material. In general, the higher the energy band gap, the higher the insulating property, and thus there is an inverse relationship between the dielectric constant and the insulating property of a material, resulting in a trade-off between high dielectric constant and good insulating property. Since all polarization phenomena can be regarded as a kind of excitation phenomena, a similar trade-off between dielectric permittivity and insulating property is expected to occur for dielectric permittivity caused by other polarization phenomena, as in the case of electronic polarization.

On the other hand, if the applied electric field is significantly large, dielectric breakdown may occur due to the formation of electron conduction paths as chemical bonds are broken by the local electric field. Since the magnitude of the local electric field in a dielectric is proportional to the dielectric constant, there is also a tradeoff between dielectric breakdown strength and dielectric constant. However, since there are various mechanisms of dielectric breakdown, a unified understanding of the relationship between dielectric constant and dielectric strength has not been established.

Since insulation is an important factor in material reliability, the tradeoff between dielectric constant and insulation leads to a tradeoff between dielectric constant and reliability. However, the relationship between dielectric constant and reliability is highly dependent on the fabrication process, since the reliability of ceramic capacitors is greatly affected by the nature of additives and grain boundaries. In order to prevent dielectric breakdown in actual multilayer ceramic capacitors, the rated voltage is usually set with a margin of sufficient reliability. The rated voltage is often set at about 1/10 of the breakdown strength. Since short-circuit failures due to dielectric breakdown of ceramic capacitors greatly affect the reliability of power electronics devices, the prevention of such failures is an extremely important issue. However, it is difficult to solve this problem only by developing new materials. Therefore, a multifaceted approach is needed, which combines prior avoidance by designing electrode patterns and detecting the precursor phenomena of dielectric breakdown.

For consumer electronics applications, there is little need for superior insulation properties as long as the dielectric loss is small to some extent, but as power electronics applications expand in the future, it is expected that even better insulation properties will be required. However, as power electronics applications expand in the future, it is expected that even better insulation properties will be required. [8]

[Hiroki Taniguchi, Manabu Hagiwara, Sakyo Hirose]

References

(1) R. A. Parker: "Static Dielectric Constant of Rutile (TiO_2), 1.6-1060°K", Phys. Rev. 124, 1719 (1961).

(2) G. Rupprecht and R. O. Bell: "Dielectric Constant in Paraelectric Perovskites", Phys. Rev. 135, A748 (1964).

(3) H. Taniguchi, S. Tatewaki, S. Yasui, Y. Fujii, J. Yamaura, and I. Terasaki: "Structural variations and dielectric properties of ($Bi_{1-x}La_x)_2SiO_5$ ($0 \leq x \leq 0.1$): Polycrystallines synthesized by crystallization of Bi-Si-O and Bi-La-Si-O glasses", Phys. Rev. Materials 2, 045603 (2018)

(4) A. R. Von Hippel: "Dielectrics and Waves", Wiley, (1954)

(5) E. Sawaguchi and K. Kittaka: "Antiferroelectricity and Ferroelectricity in Lead Zirconate", J. Phys. Soc. Jpn. 7, 336 (1952))

(6) Hiroki Taniguchi, Takumi Watanabe, Taro Kuwano, Akitoshi Nakano, Yukio Sato, Manabu Hagiwara, Hiroko Yokota and Kazuhiko Deguchi: " Unconventional Polarization Response in Titanite-Type Oxides due to Hashed Antiferroelectric Domains", ACS Nano 18, 14523 -14531 (2024)

(7) Toshiya Uohashi, Taro Kuwano, Manabu Hagiwara, Kenji Natori, Kazuhiko Deguchi and Hiroki Taniguchi: "Antiferroelectricity of titanite -type oxide SrTiGeO5 and its potential for power electronics applications", Appl. Phys. Lett. 124, 182901 (2024)

(8) T. Correia and M. Stewart: "A. Ellmore, and K. Albertsen, Lead-Free Ceramics with High Energy Density and Reduced Losses for High Temperature Applications", Adv. Eng. Mater. 19, 1700019 (2017).

2.3 Film capacitor

Keyword: Film capacitor, Low loss, Temperature characteristics, Reliability, Self-healing, Thin film

A film capacitor is a capacitor that uses a polymer plastic film as a derivative. (**Figure 2.2.3.1** shows the appearance of a film capacitor element.) There are two types of film capacitor elements: (a) a metal foil type film capacitor in which a film and metal foil such as aluminum are superimposed and wound together to form a capacitor, and (b) a vapor-deposited metal type film capacitor in which a vapor-deposited electrode made of extremely thin metal is wound onto the film.

In recent years, the demand for high security and miniaturization has led to the mainstream of vapor-deposited metal-type film capacitors with self-healing functions and high energy density.

Polypropylene (PP) film and polyethylene terephthalate (PET) film are the most commonly used dielectric films in use today, among which PP film is widely used because of its high reliability and excellent electrical characteristics (low loss, stable temperature characteristics, etc.). **Table 2.2.3.1** shows examples of general characteristics of PP and PET films.

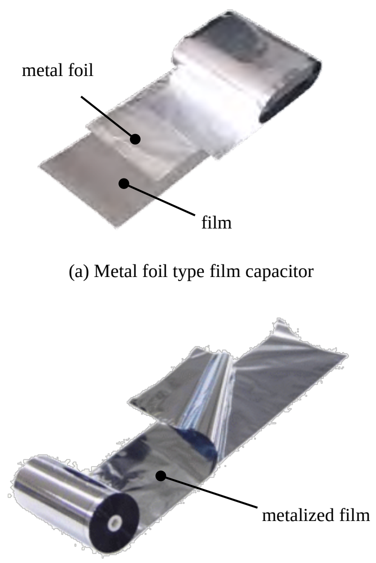

(b) Evaporated metal type film capacitor

Figure 2.2.3.1 Film capacitor element

Table 2.2.3.1 General characteristics of dielectric films

	melting point (℃)	density (g/cm³)	relative dielectric constant (-)	tan δ (%)	dielectric breakdown strength (V/μm)
PP	160-170	0.9	2.2	0.02	550
PET	260	1.4	3.1	0.3	500

2.3.1 High temperature characteristics

Figure 2.2.3.2 shows an example of the capacitance change rate (based on 20 ℃), loss factor, and insulation resistance of PP and PET film capacitors, which are used as dielectric materials in film capacitors, with respect to temperature change.

(1) Capacitance change rate

PP film capacitors are characterized by a gradual decrease in capacitance between -40 ℃ and 100 ℃. The rate of change is approximately 5%, showing excellent stability with respect to temperature. On the other hand, PET film capacitors have a stable capacitance change rate similar to that of PP film capacitors, but the capacitance tends to increase, which is different from the behavior of PP film capacitors.

(2) loss factor

The PP film capacitor shows almost no change with temperature and maintains an extremely low loss factor. On the other hand, the loss factor of the PET film capacitor is more than one order of magnitude higher than that of the PP film capacitor, with a bottom around 80 ℃.

Focusing on the capacitance change rate and loss factor, the temperature characteristics vary depending on the type of dielectric film, so it is necessary to use them in consideration of their characteristics.

(3) Insulation resistance

The insulation resistance of both PP and PET film capacitors tends to decrease as the temperature rises.

These dielectric films are crystalline organic polymer materials, and as the temperature rises, molecular motion becomes more active, and eventually the crystalline portions break down and become fluid (melting point).

Increased molecular motion facilitates the movement of electrons and ions in the polymer, leading to a decrease in the film's insulation resistance, which in turn leads to a decrease in its withstand voltage performance.

In the above, it was shown that the characteristics of film capacitor elements change depending on temperature characteristics (high temperature characteristics). Equivalent Series Resistance (ESR), which is one of the factors that raise the capacitor temperature, will be explained in the following sections.

2.3.2 Equivalent Series Resistance

The main causes of temperature rise in capacitors are ambient temperature and self-heating due to losses generated in the capacitor. This section discusses the losses due to the AC component generated inside the capacitor.

Figure 2.2.3.3 shows the equivalent resistance components. The three resistance components that mainly contribute to the loss are the resistance component R_d associated with the dielectric polarization delay, the conductor component R_c such as electrodes, and the insulation resistance component R_l of the dielectric film.

ESR is an important factor that affects the loss due to the AC current component of a capacitor. In **Figure 2.2.3.3,** the factors that affect ESR are R_d and R_C, except for R_l, which is the insulation resistance component that has almost no effect on loss due to the AC current component.

Focusing on R_d, the circuit is a series circuit of R_d and C (capacitance). When an alternating voltage v (V) of frequency f (Hz) is applied here, currents with the relationship shown in **Figure 2.2.3.** 4 flow, where I_d (A) is the magnitude of the current produced by R_d, I_c (A) is the

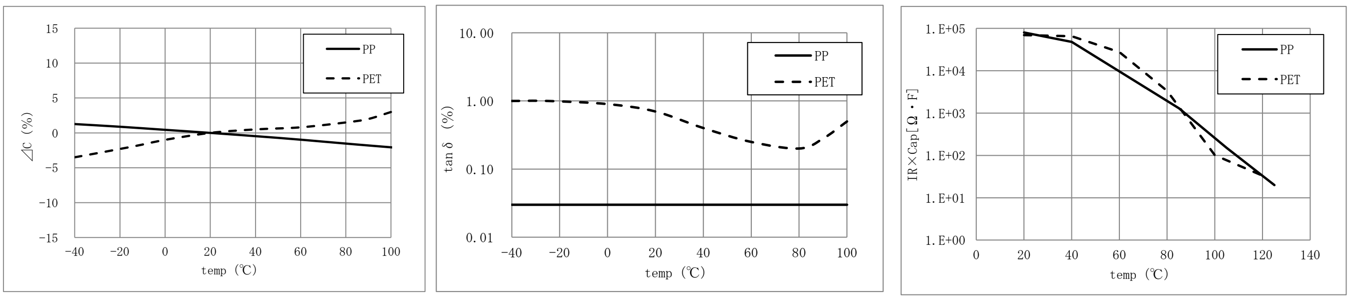

(a) Capacitance change rate - temperature characteristics (b) Loss factor - temperature characteristics (c) Insulation resistance - temperature characteristics current flowing in C, and δ_0 is called the dielectric loss angle, a value determined by the film's characteristics.

Since v is applied to the series circuit configuration of R_d and C, I_d and I_c are

$$I_d = \frac{v}{R_d} \quad (2.2.3.1)$$

$$I_c = 2\pi fCV \quad (2.2.3.2)$$

which is the tangent of δ_0. Taking the tangent of δ_0 in **Figure 2.2.3.4**, we obtain the following equation

$$\tan\delta_0 = \frac{I_d}{I_c} = \frac{1/R_d}{2\pi fC} = \frac{1}{2\pi fCR_d} \quad (2.2.3.3)$$

If the power loss due to R_d is P_0 (W), the product of v and I_d **in Figure 2.2.3.4** is P_0.

I_d can be approximated as $\sin\delta_0 \approx \tan\delta_0$, since δ_0 is usually very small, and is expressed as

$$I_d = I\sin\delta_0 \fallingdotseq I\tan\delta_0 \quad (2.2.3.4)$$

P_0 is the following.

$$P_0 = vI_d = vI\tan\delta_0 \quad (2.2.3.5)$$

Let ESR_0 (Ω) be the equivalent series resistance that causes dielectric losses, and assume that a current I flows through this ESR_0

$$I^2 ESR_0 = P_0 \quad (2.2.3.6)$$

We can think of the equation (2.2.3.6) as Substituting equation (2. 2.3. 5) into equation (2. 2.3.6) and solving, we obtain equation (2.2.3.7).

$$ESR_0 = \frac{P_0}{I^2} = \frac{VI\tan\delta_0}{I^2} = \frac{\tan\delta_0}{2\pi fC} = \frac{1}{(2\pi fC)^2 R_d} \quad (2.2.3.7)$$

This is the ESR associated with the polarization delay of the dielectric film.

Next, the ESR component is also obtained for the conductor component Rc. As in the case of ESR_0, focusing on R_c in **Figure 2.2.3.3**, the model is only R_c with no C present. Let I be the magnitude of the total current flowing when v is applied to it and Ie be the current flowing in R_c

$$I_e = I \quad (2.2.3.8)$$

and if the power loss due to R_C is P_C (W), then

$$P_c = R_c {I_e}^2 = R_c I^2 \quad (2.2.3.9)$$

will be.

If the equivalent series resistance that causes conductor losses is ESR_1 (Ω), then when a current I flows through this ESR_1

$$I^2 ESR_1 = P_c \quad (2.2.3.10)$$

We can think of the equation (2.2.3.10) as Substituting equation (2. 2.3. 9) into equation (2. 2.3.10) and solving, we obtain equation (2.2.3.11).

$$ESR_1 = \frac{P_c}{I^2} = \frac{R_c I^2}{I^2} = R_c \quad (2.2.3.11)$$

Therefore, the overall capacitor resistance component, ESR (Ω), is

$$ESR = ESR_0 + ESR_1 = \frac{\tan\delta_0}{2\pi fC} + R_c \quad (2.2.3.12)$$

It is obtained by

Since there are various possible components of R_c, the ESR components of each component are summed up in the ESR design of film capacitors.

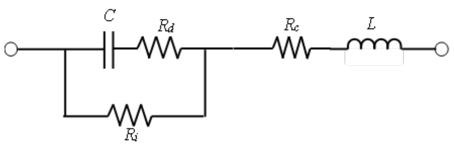

C (F): Capacitance

R_d (Ω): Resistance component due to dielectric loss of the film

Rc (Ω): Conductor resistance component of deposited metal, drawer electrode, etc.

Rl (Ω): Insulation resistance component of film

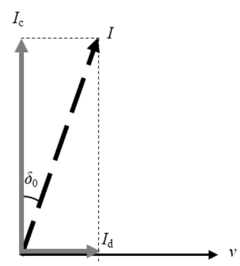

Figure 2.2.3.4 Relationship between

2.3.3 Future of Dielectric Materials, Limitations of Thin Film

In recent years, all products have become smaller and denser, and film capacitors continue to be required to be smaller and denser.

Capacitance is one of the electrical characteristics required of a capacitor, and the body size of a capacitor varies greatly depending on the required capacitance size.

The capacitance of a film capacitor varies with the film thickness and electrode area, and is expressed by the following equation. **Figure 2.2.3.5** shows an image of a film capacitor.

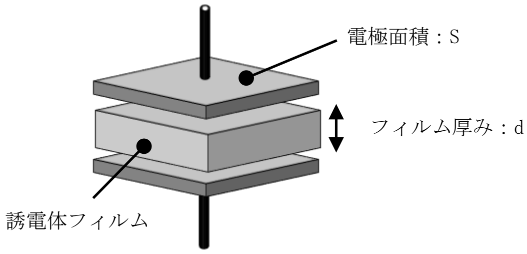

Figure 2.2.3.5 Image of a capacitor

$$C=\varepsilon_0\times\varepsilon_s\times S/d \qquad (2.2.3.13)$$

C(F): Capacitance

ε_0 (F/m): Dielectric constant in vacuum

ε_s : relative permittivity

S(m^2): Electrode area

d（m）: Film thickness

In order to increase the capacitance per unit volume, it is necessary to reduce the size of the film capacitor.

(1) Reduce film thickness d

(2) Increase the dielectric constant of the dielectric

It is necessary to

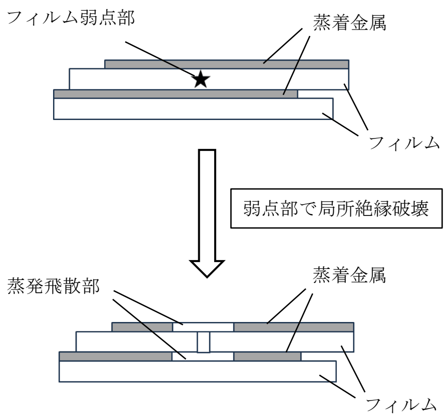

Figure 2.2.3.7 Schematic diagram of self-healing

So far, miniaturization of vapor-deposited metal type film capacitors has been achieved by making the PP film, which is mainly used in the market, thinner (reducing the film thickness d).

Figure 2.2.3.6 shows the PP film size (film thickness) transition with a typical example of a smoothing capacitor for electric railways (1650 V class) and a smoothing capacitor for automotive use (450 V class).

Progress in capacitor technology to use thinner materials through optimization of film forming technology, deposition patterns, and processing has improved withstand voltage performance per unit thickness, resulting in thinner film while maintaining the same operating voltage.

Considering the dielectric breakdown strength of PP film as shown in **Table 2.2.3.1**, 550 V/μm (room temperature: instantaneous withstand voltage), it can be seen that the voltage PP film used in film capacitors is approaching the limit of its withstand voltage performance.

The thinnest PP film currently on the market is 2 μm, which is approaching the limit of thickness in terms of productivity.

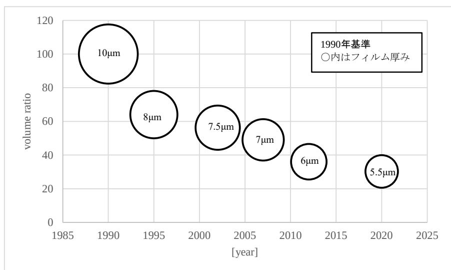

(a) 1650 V class smoothing capacitor for electric railway

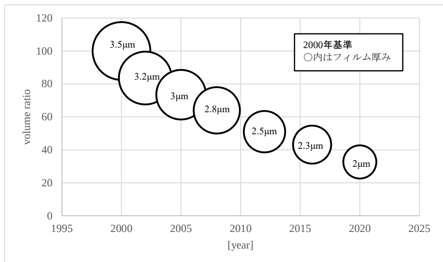

(b) 450 V class automotive smoothing capacitor

Figure 2.2.3.6 Body Size (Film Thickness) Transition

Another approach to increase the dielectric constant of the dielectric is to increase the dielectric constant of the dielectric, but it is difficult to exceed PP film in terms of electrical characteristics and cost. Some film capacitor manufacturers are beginning to market film capacitors that can withstand 125 °C, but it will take some time before they can replace PP film capacitors, including in terms of cost.

2.3.4 Reliability

Film capacitors are characterized by their high reliability. This high reliability is achieved through the self-healing properties of the vapor-deposited electrode type film capacitor and the fuse operation mechanism provided by the vapor-deposited pattern formation.

Therefore, it is common to calculate the expected life of vapor-deposited electrode type film capacitors by assuming a capacitance decrease as the failure mode. The capacitance decrease is often defined as a decrease of 5 to 10% of the initial capacitance.

The following sections describe the self-healing and fuse operation mechanisms related to security.

First, a schematic diagram of self-healing is shown in **Figure 2.2.3.7**. In a vapor-deposited electrode type film capacitor, a very thin metal film is formed on a dielectric film to serve as the electrode. If the dielectric film has an insulation defect or other area where the voltage holding capability is degraded (film weak point), local dielectric breakdown occurs at the weak point when current is passed through the film. At that time, the energy stored in the surrounding area flows into the breakdown point, instantly vaporizing and dispersing the evaporation electrodes near the breakdown point, securing the necessary insulation distance from the breakdown point, and restoring insulation. This is generally called self-healing.

Next, **Figure 2.2.3.8** shows a schematic diagram of the fuse operation mechanism. In a vapor-deposited electrode type film capacitor, a pattern shape consisting of a vapor-deposited electrode and a nonvapor-deposited metal part can be formed arbitrarily to some extent on the vapor-deposited metal surface. This is called a deposition pattern. In a vapor-deposited film with a fuse operation mechanism, the vapor-deposited pattern is divided into groups of small electrodes, and each group of small electrodes is fused. The effect of the fuse is that when a large local dielectric breakdown that cannot be suppressed by self-healing occurs at a weak point in the film, the current flowing into the breakdown point causes the fuse to melt, separating the small electrode and maintaining the capacitor function.

Figure 2.2.4.1 Various types of aluminum

Finally, an example of the security of film capacitors is presented. **Figure 2.2.3.9** shows the rate of capacitance change when a DC voltage is applied to the capacitor for a fixed time in steps with the capacitor temperature set at 105 ^{o}C. As the applied voltage to the capacitor is increased, the capacitance decreases from a certain voltage region. This decrease in capacitance is the result of the small electrodes that have undergone local dielectric breakdown being gradually disconnected from the capacitor electrodes by the self-healing and fusing mechanisms. Continued application of voltage will cause the fuses attached to all the small electrodes to operate, eventually leading to an open state.

The self-healing and fuse operation mechanisms demonstrate excellent performance when PP film is used as the dielectric. However, since the performance of self-healing and fuse operation changes when the dielectric film type is changed, it is necessary to design the deposition pattern with security in mind when changing the dielectric film.

[Ryuhei Koyama.]

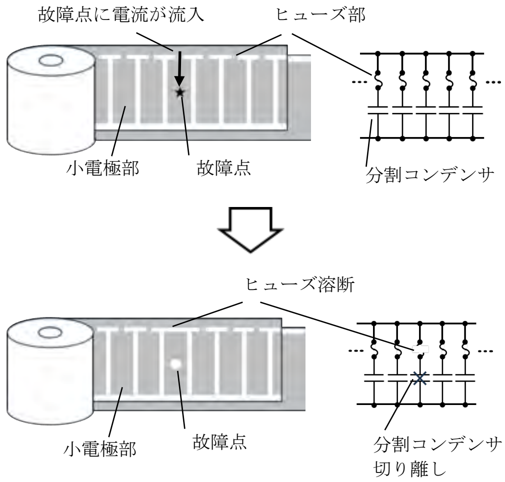

Figure 2.2.3.8 Schematic diagram of fuse operation

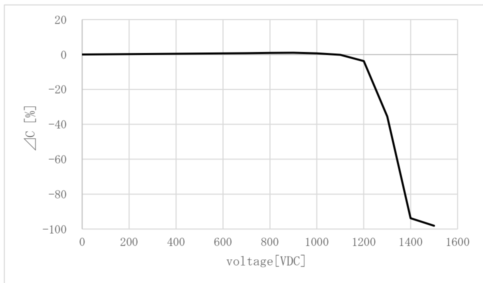

Figure 2.2.3.9 Capacitance change rate - voltage

2.4 Electrolytic capacitor

Keyword: Aluminum electrolytic capacitor, Electrode foil, Etching, Conversion (anode oxidation), Electrolyte, Characteristic comparison radar chart

2.4.1 Electrolytic Capacitor Overview

Among capacitors that are passive components, electrolytic capacitors are characterized by their high capacitance per volume. It is no exaggeration to say that this feature of the electrolytic capacitor is obtained by the surface treatment technology of the metal used for the electrode. In fact, electrolytic capacitors are classified according to the type of metal used for the electrode (e.g., "aluminum electrolytic capacitor" if Al is used, "tantalum electrolytic capacitor" if Ta is used). Among them, aluminum electrolytic capacitors using Al electrodes are available from various companies in various sizes, shapes, and characteristics as shown in **Figure2.2.4.1**, in order to meet various applications in a wide range of fields.

As shown in **Figure 2.2.4.2**, an aluminum electrolytic capacitor is a wound element consisting of a layered anode foil, separator, and cathode foil, impregnated with liquid or solid electrolyte, and sealed with an aluminum case and sealing material.

The structure of the anode and cathode foil is as follows. The surfaces of both the anode and cathode foils are porous, and Al_2O_3 is formed as a dielectric oxide film on the surface of the porous layer of the anode foil. In other words, inside the aluminum electrolytic capacitor, the metal part of the anode foil functions as the anode, the Al_2O_3 on the surface of the anode foil as the dielectric oxide film, and the electrolyte, separator and cathode foil as the cathode.

The capacitance C of the capacitor is proportional to the electrode area S and inversely proportional to the distance d between electrodes as shown in the following equation (2.2.4.1).

$$C = \varepsilon_0 \varepsilon_r \frac{S}{d} \quad (2.2.4.1)$$

Here, ε_0 is the dielectric constant of vacuum (8.854×10^{-12} F/m) and ε_r is the relative dielectric constant of the dielectric oxide film. It is not large compared to other capacitors. However, the surface area of the anode foil can be enlarged by electrochemical treatment to form a very thin dielectric oxide film, which allows aluminum electrolytic capacitors to have a larger capacity per volume than other capacitors.

2.4.2 Electrode Foil

(1) Outline of electrode foil for electrolytic capacitors

As mentioned in 2.4.1, the electrode foil in an electrolytic capacitor is an extremely important material that controls the capacitance per volume, which is its most important feature. Furthermore, the dielectric oxide film on the surface of the anode foil also controls its withstand voltage and loss. Based on the above, the physical properties and functions required for electrode foils are listed below.

(a) The surface area must be large. Equation (2.2.4.1) shows that higher capacitance in capacitors can be achieved by increasing the electrode area, but simply increasing the electrode area will increase the product volume. Therefore, to increase the capacitance per product volume, it is necessary to increase the surface area of the electrode foil by making its surface more porous. Physical etching, chemical etching, electrochemical etching, fine particle deposition, and fine powder sintering are some of the methods used to make the electrode foil surface porous, but electrochemical etching (hereinafter referred to as "etching") is the most common because it can control the amount and speed of dissolution with the amount of electricity, temperature, and other factors, and has industrial advantages compared to other methods. Electrochemical etching (hereinafter referred to as "etching") is the most common.

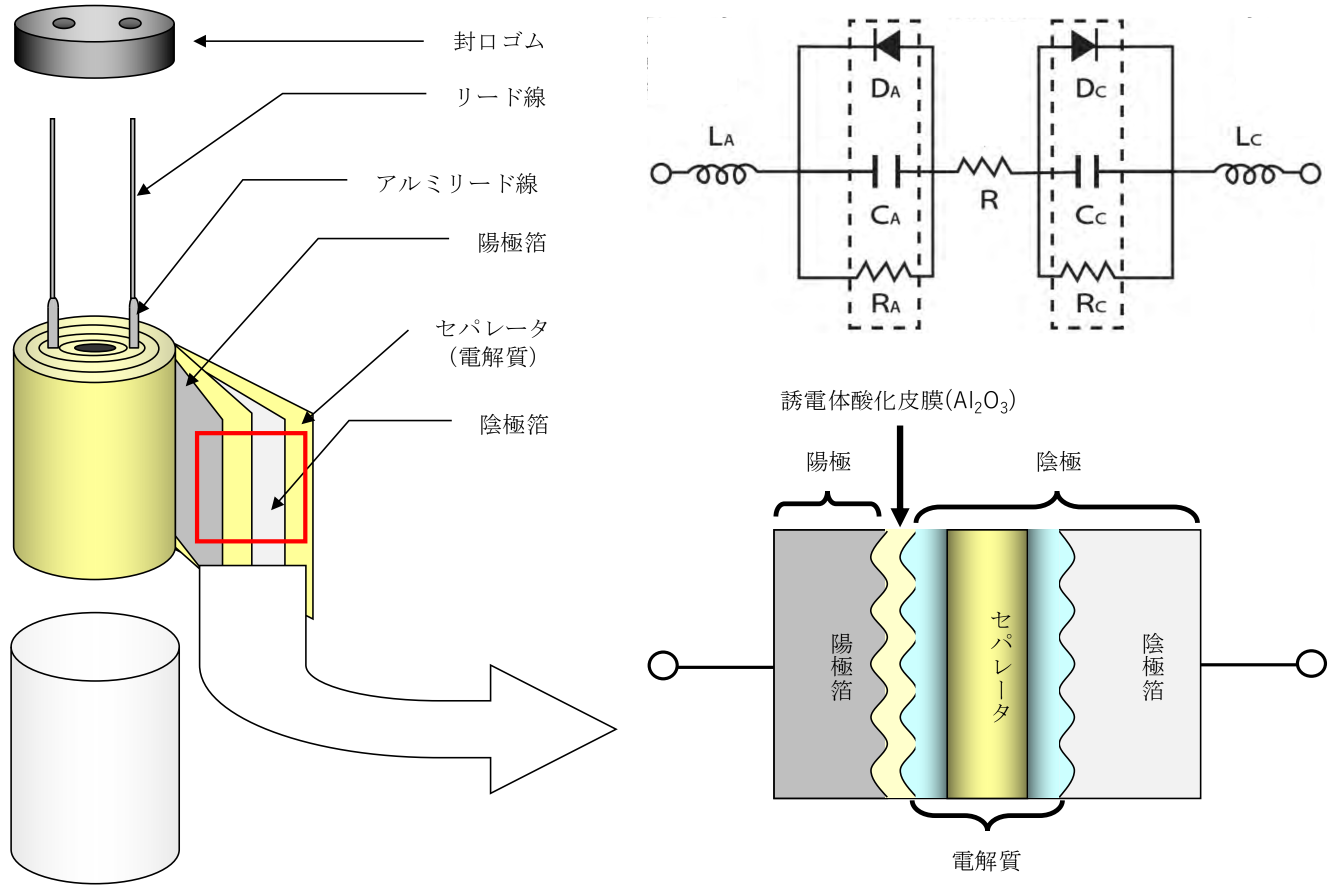

Figure 2.2.4.2 Element structure and basic model of an aluminum electrolytic capacitor

(a) The dielectric oxide film must have a high dielectric constant and a thin film thickness. The dielectric oxide film of the anode foil must be etched to form a porous

The film thickness is obtained by anodic oxidation (a process in which anodic current is applied in an aqueous solution) of an Al foil that has been anodized. The film thickness increases in proportion to the voltage at the time of anodic oxidation (hereinafter referred to as "anodizing voltage"), and this proportionality constant (anodizing ratio, k (nm/V)) has a specific value for each type of dielectric oxide film. **Table 2.2.4.1** shows the relative permittivity ε_r and k of dielectric oxide films obtained by anodic oxidation of various metals. Using this k, equation (2.2.4.2) can be expressed as

$$C = \varepsilon_0 \varepsilon_r \frac{S}{kV_f} \tag{2.2.4.2}$$

where Vf is the voltage of the capacitor. The voltage must be set higher than the rated voltage of the capacitor and cannot be set arbitrarily. Therefore, from equation (2.2.4.2), it can be seen that higher capacitance of the capacitor can also be achieved by increasing the value of ε_r/k. However, with a few exceptions, ε_r and k are basically in a trade-off relationship and they cannot be changed independently They cannot be varied independently. Another point of interest in **Table 2.2.4.1** is that Al_2O_3 has the lowest ε_r/k value among the dielectric oxide films listed here. Therefore, it is possible to increase the ε_r/k values of dielectric oxide films on Al foils by forming composite oxide films containing Al_2O_3 and some of the other dielectric oxide films. Attempts to form (Ti, Ta, Nb, Si, Zr) -Al composite oxide films by Pore-filling [(1)], sol-gel coating/anodic oxidation [(2)-(12)], MOCVD/anodic ox idation [(13)], and liquid phase deposition/anodic oxidation [(14)] have been reported. Al composite oxide film by liquid phase deposition/anodic oxidation (14).

(c) The dielectric oxide film must have a higher withstand voltage. In order to realize a capacitor with a higher rated voltage, anode oxidation should be performed up to a higher voltage with an anode foil to grow a thicker dielectric oxide film. In order to perform anode oxidation up to higher voltages, the anion species in the electrolyte used for anode oxidation must be appropriately selected, and the specific resistance must be increased by lowering the concentration [(15)]. However, the limit of the formation voltage of aqueous boric acid solutions generally used for anode oxidation up to high voltages is 1180 V even if the specific resistance is increased by lowering the concentration to the utmost limit [16], which is one of the reasons why the upper limit of the rated voltage of aluminum electrolytic capacitors is currently limited to about 700 V. In order to overcome this problem, the anode capacitor is used as the capacitor. To overcome this problem, new electrolytes for anode oxidation [17][18] and new pretreatment methods [19][20] for base materials have been studied, and in these studies, the formation of dielectric oxide film at a conversion voltage of 1500 V or higher has been attempted.

Table 2.2.4.1 Dielectric permittivity of dielectric oxide films obtained by anodic oxidation on various metals ε_r and film thickness per conversion voltage k

	Relative dielectric constant, ερ (-)	Anodizing ratio, k (nm/V)	□r/k (V/nm)
SiO_2 (a)	3.5	0.4	8.9
Al_2O_3 (a)	9.8	1.4	7.0
HfO_2 (c)	21	1.9	11.1
ZrO_2 (c)	23	2.0	11.5
Ta_2O_5 (a)	27.6	1.7	16.2
Nb_2O_5 (a)	41.4	2.5	16.6
WO_3 (a)	41.7	1.8	23.2
TiO_2 (c)	90	3.0	30.0

(a) amorphous oxide film, (b) crystalline oxide film

(d) The loss in the dielectric oxide film must be small. The loss W generated inside the capacitor when the ripple current is superimposed on the DC voltage is expressed by the following equation (2.2.4.3).

$$W = V_{DC}I_L + {I_R}^2 ESR \qquad (2.2.4.3)$$

where V_{DC} is the DC voltage, I_L is the leakage current, I_R is the ripple current, and ESR is the equivalent series resistance. The leakage current I_L and equivalent series resistance ESR in equation (2.2.4.3) vary greatly depending on the structure of the dielectric oxide film. However, in the actual use environment of electrolytic capacitors, the leakage current is often very small and $I_L \ll I_R$, so most of the internal loss of the capacitor can be considered as heat generation due to ripple current.

$$W \approx {I_R}^2 ESR \qquad (2.2.4.4)$$

Furthermore, the ESR can be decomposed into the frequency-independent electrolyte resistance R_S and the frequency-dependent loss resistance R_{OX} of the dielectric oxide film [21].

$$ESR = R_S + R_{OX} = R_S + DF_{OX}X_C = R_S + \frac{DF_{OX}}{2\pi f C} \qquad (2.2.4.5)$$

where DF_{OX} is the dielectric tangent of the dielectric oxide film, X_C is the capacitive reactance, and C is the capacitance. Therefore, in the low frequency region where $R_S \ll$ Rox, ESR increases with decreasing frequency. Since the effect of R_{OX} is often larger near the frequency of commercial power supplies, it is necessary to develop dielectric oxide films with small R_{OX} to reduce the internal loss of the capacitor and increase the allowable ripple current.

(e) The chemical stability of the dielectric oxide film must be high. If the chemical stability of Al_2O_3 formed on the surface of the porous layer of the anode foil as the dielectric oxide film is low, Al_2O_3 may react with moisture in the air in the storage condition in the electrode foil and with moisture in the liquid electrolyte inside the capacitor, transforming Al_2O_3 into hydrated oxide, or react with substances in the liquid or solid electrolytes, causing Al_2O_3 may dissolve. If these reactions proceed, the insulating properties of Al_2O_3 will be greatly reduced, resulting in a decrease in the withstand voltage and an increase in leakage current in the capacitor.

(f) High mechanical strength is required. In the winding process of manufacturing aluminum electrolytic capacitors, the electrode foil is subjected to large bending stresses, so it must have the mechanical strength to withstand such stresses. As mentioned earlier, the formation of a porous layer is essential to increase the surface area of the electrode foil in order to increase the capacitance of the aluminum electrolytic capacitor. However, if the proportion of hard dielectric oxide film in the porous layer increases as the surface area expands, the flexibility of the electrode foil decreases, making it difficult to fabricate a wound device. To solve this problem, a technique was developed to improve the flexibility of the electrode foil by creating multiple cracks in the porous layer of the electrode foil as shown in **Figure 2.2.4.3**(22)-(27). **Figure 2.2.4.4** shows an example where the application of this technology suppressed the generation of new cracks due to bending stress in the winding process and enabled the fabrication of a device with smoothly wound electrode foil. As a result, not only the defect rate in the winding process is reduced, but also the capacitance volume efficiency of the wound electrolytic capacitor is improved.

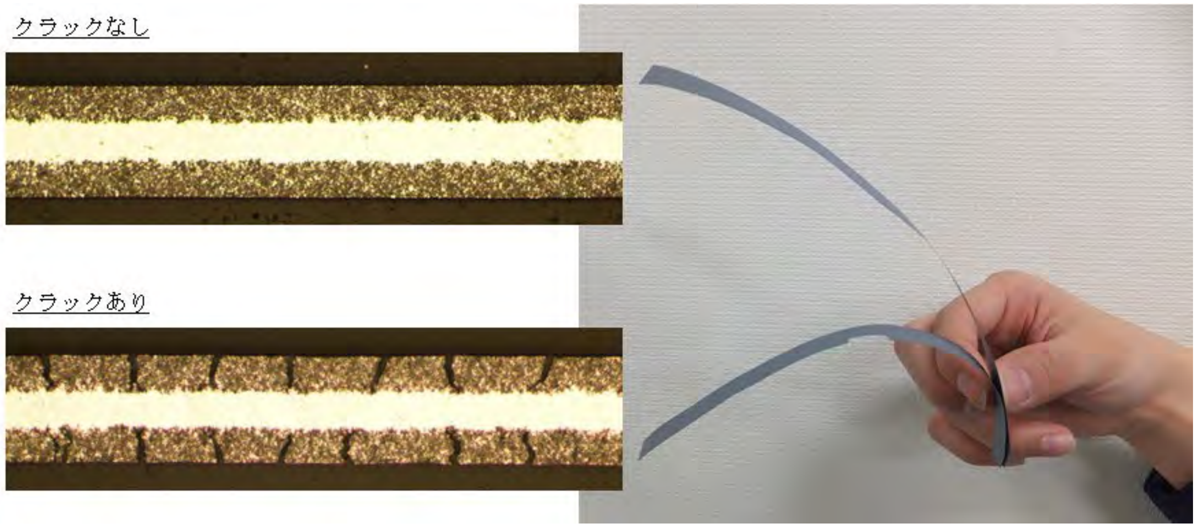

Figure 2.2.4.3 Improved flexibility of electrode foil by crack introduction technique

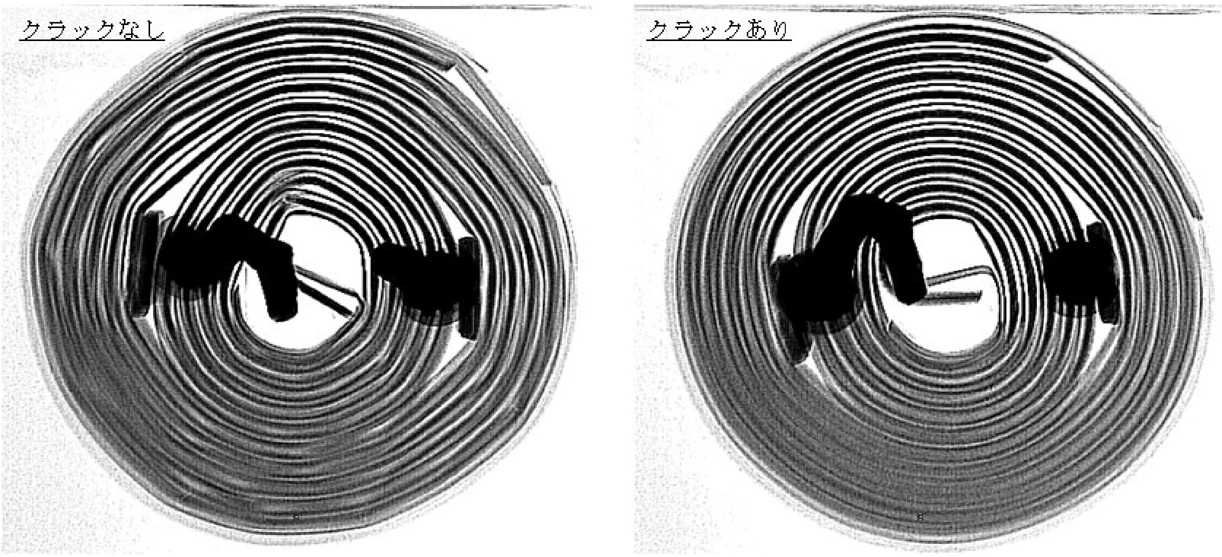

Figure 2.2.4.4 Improved Winding Performance in Aluminum Electrolytic Capacitor Wound Elements Using Crack Introduction Technology

(2) Etching Technology

For anode and cathode foils for aluminum electrolytic capacitors, a sponge-like or tunnel-like porous layer is formed on the front and back surfaces of Al foil by etching high-purity (99.9 to 99.99%) Al foil. In etching, the Al foil is immersed in an acidic solution containing halogens, and AC or DC anodic current is applied to dissolve the Al foil surface to obtain the porous layer. Spongy and tunnel-like structures are generally used depending on the rated voltage of the capacitor. For low voltage applications (rated voltage of 100 V or less), a sponge-like structure consisting of fine cubic pits of 0.1 to 0.5 µm per side connected together is used, and for medium to high voltage applications (rated voltage of 160 V or more), a tunnel-like structure consisting of columnar pits of 1 to 2 µm in diameter growing vertically from the electrode foil surface is used. For medium and high voltages (rated voltages of 160 V and above), a tunnel-like structure is adopted in which columnar pits of 1 to 2 μm in diameter are grown vertically from the surface of the electrode foil.

Figure 2.2.4.5 shows a cross-section of a low-voltage anode foil and an SEM image of the detailed structure obtained by the oxide replica method [28]. The sponge-like structure is obtained by a process in which an alternating current is applied to the Al foil in an aqueous solution containing mainly hydrochloric acid (AC etching). The mechanism by which the spongy structure is obtained by AC etching is generally explained by the etch-pit propagation model proposed by Dyer and Alwitt [29]. In order to obtain a porous layer with a larger surface area by AC etching, it is desirable to grow a finer, more uniform spongy structure with a thicker thickness. To achieve the goal of increasing the surface area of the electrode foil according to this guideline, research and development focusing on the effects of the electrolyte [30] and current waveform [31] used in AC etching on the growth process and propagation behavior of etch pits is still being conducted.

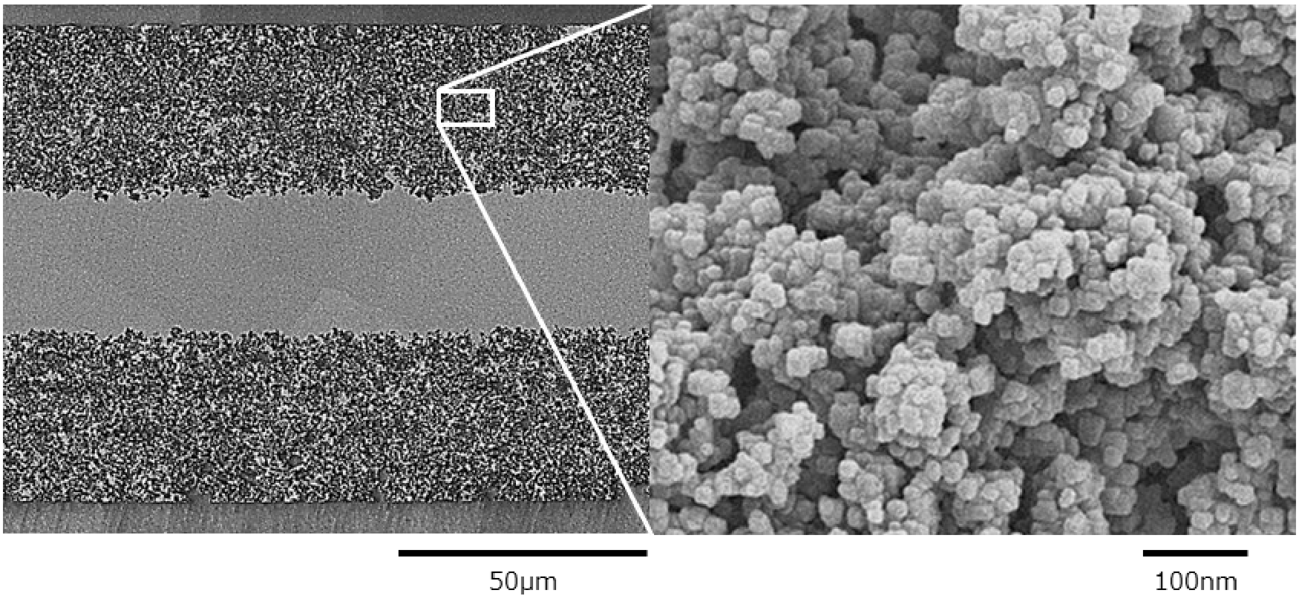

Figure 2.2.4.5 SEM image of cross section and detailed structure (oxide replica) of anode foil for low voltage

Figure 2.2.4.6 shows SEM images of the cross-section (oxide replica method) and surface (surface polished to a depth of about 10 μm by electropolishing) of an anode foil for medium and high voltages. The tunnel-like structure is obtained by a process in which a DC anodic current is applied to the Al foil in an aqueous solution containing mainly hydrochloric acid (DC etching). The columnar pits are approximately 1 μm in diameter and 50 μm long, with a number density of about 10^7 cm^{-2}. Since the columnar pits grow along the <100> orientation, the columnar pits grow perpendicular to the surface of the Al foil [32]-[34] by DC etching of Al foil crystals aligned in the (100) plane by heat treatment. To obtain a porous layer with a larger surface area by DC etching, it is desirable to generate columnar pits on the surface of the Al foil with higher density and more uniform surface distribution, and to grow them with more uniform length. One of the ideal forms is a tunnel-like structure with columnar pits of uniform length grown in a hexagonally close packing on the surface of the Al foil. A method to realize this ideal structure on a laboratory scale has already been devised [35]-[40], and research and development for its mass production is still ongoing [41]. If a tunnel-like structure with uniformly long columnar pits with hexagonal close packing is realized on both sides of the Al foil, it is expected to have approximately four times the capacity at a deposition voltage of 215 V, approximately three times the capacity at a deposition voltage of 335 V, and approximately twice the capacity at a deposition voltage of 650 V or higher compared with the current anode foil for medium and high voltages.

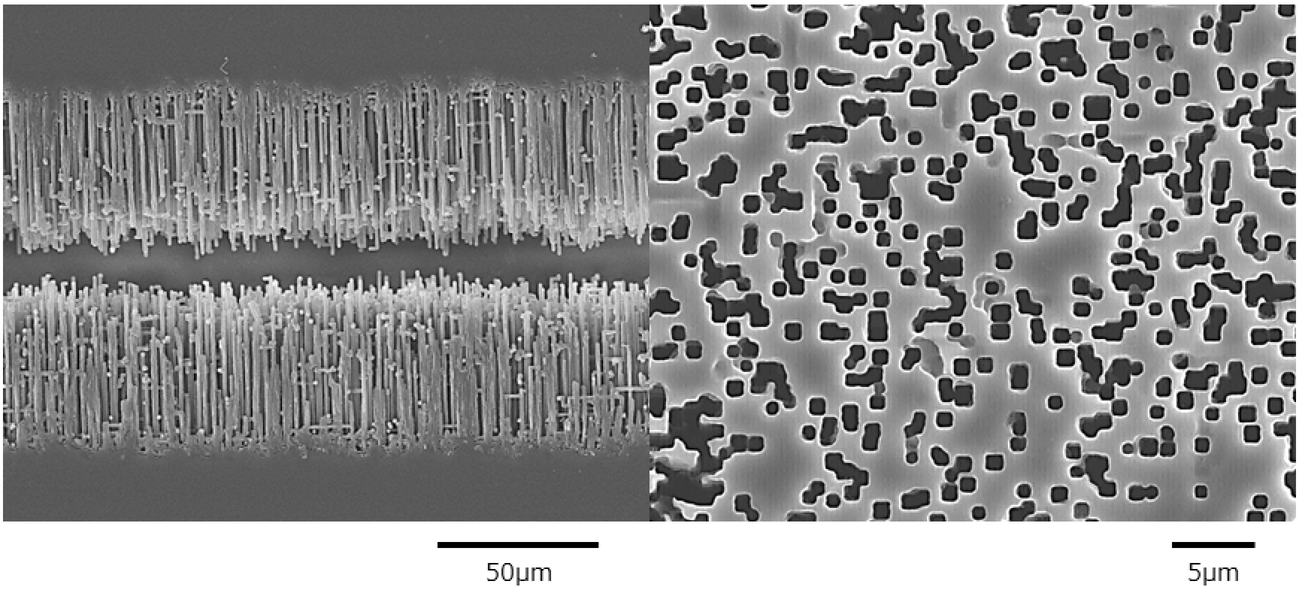

(a) (b)

Figure 2.2.4.6 SEM images of tunnel-like structure of anode foil for medium and high voltage (a) cross section (oxide replica), (b) surface (10 µm electropolished depth)

(3) Chemical conversion technology

In an anode foil for aluminum electrolytic capacitors, a dielectric oxide film is formed on the top surface of the porous layer by anodic oxidation of an Al foil with a porous layer formed by etching or other means. This dielectric oxide film is obtained by applying a DC anodic current to the Al foil immersed in a halogen-free neutral solution to oxidize the top surface of the Al foil. The dielectric oxide film obtained can be classified into amorphous oxide film and crystalline oxide film by changing the pretreatment method of anodic oxidation as appropriate. **Table 2.2.4.2** shows the characteristics of amorphous and crystalline oxide films [(42)]. Amorphous oxide film has lower leakage current and dielectric loss than crystalline oxide film, so it is used when low loss is a priority for electrolytic capacitors. The crystalline oxide film has a higher relative permittivity and thinner film thickness than the amorphous oxide film, so it is used when high capacitance of the electrolytic capacitor is a priority.

Table 2.2.4.2 Comparison of properties between amorphous and crystalline oxide films obtained by anodic oxidation on aluminum

	Amorphous	Crystalline
Relative dielectric constant (-)	8.1	8.4
Anodizing ratio (nm/V)	1.3	0.9
Dissipation factor (-)	0.3 - 0.7% (0.3 - 0.7%)	1.0 - 1.4
Density (g/cm^3)	3.1	3.6
Dissolution rate (relative)	100	1

When an amorphous oxide film is formed as a dielectric oxide film, a porous oxide film is formed by anodic oxidation in an acidic solution containing no halogen, followed by anodic oxidation in a neutral solution to fill the pores of the porous oxide film (pore-filing method). [(43)(44)]. **Figure 2.2.4.7** shows a TEM image of an amorphous oxide film obtained by anodic oxidation of a medium- to high-voltage anode foil in an aqueous oxalic acid solution to form a porous oxide film, followed by anodic oxidation in a 94 ℃ boric acid solution to 500 V to fill the pores of the porous oxide film [(42)]. Generally, it is said that an amorphous oxide film can be grown by removing oil and oxide film adhered to the surface of Al foil during rolling by chemical polishing or electropolishing, and then anodic oxidation is performed at a low temperature of about 20 ℃. However, when anodic oxidation is actually performed at a voltage exceeding 200 V, crystallization in the interior of the amorphous oxide film and the accompanying void formation during its growth are observed. However, when anodic oxidation is performed at voltages exceeding 200 V, crystallization of the amorphous oxide film and accompanying void formation are likely to occur during the growth of the film, and it is not easy to obtain a dense amorphous oxide film. On the other hand, the amorphous oxide film in **Figure 2.2.4.7** formed by the pore-filing method is confirmed to be dense with very few voids.

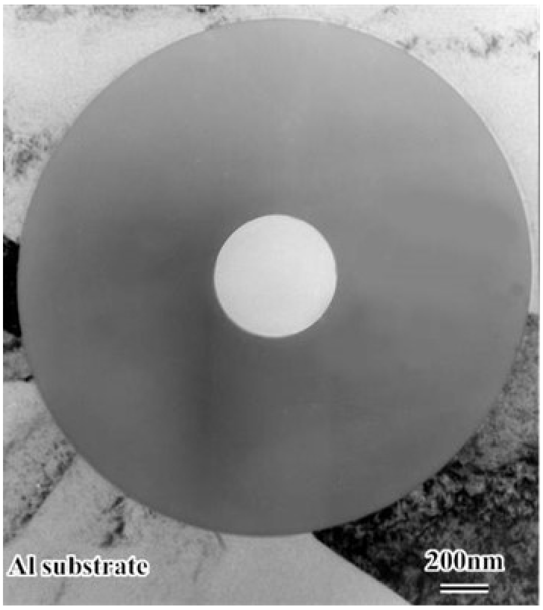

Figure 2.2.4.7 TEM image of amorphous oxide film formed in columnar pit of anode foil for medium and high voltage (500 V conversion voltage)

To form a crystalline oxide film as a dielectric oxide film, the Al foil is immersed in boiling distilled water to form a hydrated oxide (pseudo-behmite) film on the Al foil surface before anodic oxidation, and then anodic oxidation is performed in a neutral solution to change the hydrated oxide film to a crystalline oxide film (γ-Al_2O_3 film) by anodic oxidation in a neutral solution [43][44]. **Figure 2.2.4.8** shows a TEM image of a crystalline oxide film obtained by anodic oxidation of a medium- to high-voltage anode foil in boiling distilled water for 20 minutes to form a hydrated oxide film and then anodic oxidation in a 94 ℃ boric acid solution up to 500 V [42]. The hydrated oxide film consists of two layers, a porous layer and a dense layer, and gradually transforms into a crystalline oxide film as the conversion voltage increases. The hydrated oxide film formed before anodic oxidation is dehydrated at the hydrated oxide film/dielectric oxide film interface during anodic oxidation and transformed into a crystalline oxide, which is simultaneously incorporated into an amorphous oxide film formed at the same location. The amorphous oxide film adjacent to the crystalline oxide is gradually crystallized under the influence of an electric field, and eventually crystallization progresses to the entire dielectric oxide film. Furthermore, it is observed that voids generated during the transformation from the low-density hydrated oxide film or amorphous oxide film to the high-density crystalline oxide film remain in the interior of the crystalline oxide film.

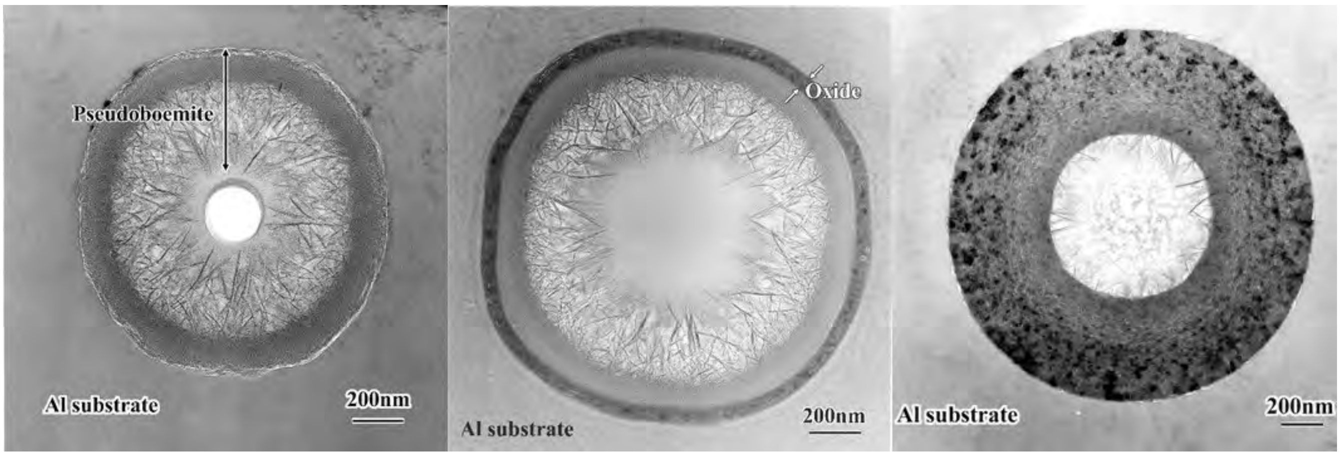

(a) (b) (c)

Figure 2.2.4.8 TEM image of crystalline oxide film formed in a columnar pit of anode foil for medium and high voltage
(a) Hydrated oxide film, (b) 50 V conversion voltage, (c) 500 V conversion voltage

The difference in the amount of voids remaining in the dielectric oxide film is an important cause of the difference in leakage current and dielectric loss between amorphous oxide film and crystalline oxide film, but this alone does not explain everything. As an example, **Figure 2.2.4.9 shows** the change in dielectric withstand voltage and $_{\mathrm{DFOX}}$ of dielectric oxide film caused by heat treatment of Al foil after dielectric oxide film formation.

Figure 2.2.4.9 (a) shows the curve of time variation of voltage values measured by applying a constant current of 4 Am^{-2} to an anode foil immersed in a boric acid solution at 85 ℃ (formation voltage of 640 V). For an anode foil without heat treatment after dielectric oxide film formation, the voltage increases slowly and linearly with time from 640 V. On the other hand, for an anode foil immersed in a boric acid solution, the voltage increases slowly and linearly with time from 640 V to 640 V. On the other hand, for the anode foil that underwent heat treatment after the dielectric oxide film formation, the voltage transiently rises to 695 V, then decreases with time to a minimum, and finally rises along the same straight line as for the anode foil that did not undergo heat treatment. The linear voltage increase measured for the anode foil without heat treatment is explained by the growth of dielectric oxide film due to the application of constant current. On the other hand, the transient voltage increase measured in the anode foil with heat treatment is considered to be caused by a decrease in ionic conductivity due to the transition of interstitial mobile ions, which are carriers of ionic conduction in the dielectric oxide film, to vacancies at lattice points due to heat treatment [(45)-(52)]. In the case of constant current application after heat treatment, ions that have transitioned to the lattice points due to heat treatment are excited to the interstitial positions again due to the electric field, and the ion conductivity is considered to increase, resulting in a decrease in voltage. Furthermore, if the constant current application is continued for a long time, the number of newly excited mobile ions will eventually decrease and the voltage drop will stop, and the voltage rise will occur due to the growth of the dielectric oxide film.

Figure 2.2.4.9 (b) shows the variation of DF_{OX} with electric field strength for a smooth Al foil with an amorphous oxide film of 670 to 700 nm formed as the dielectric oxide film [(21)]. For smooth Al foils that were not heat-treated after the formation of the dielectric oxide film, DF_{OX} shows a value of 1.4-1.5%, independent of field strength. On the other hand, for the smooth Al foil that underwent heat treatment after dielectric oxide film formation, DF_{OX} decreases significantly in the low field strength region, and at the same time, DF_{OX} becomes field strength dependent. Furthermore, when a constant current is applied after heat treatment to grow the dielectric oxide film to some extent, DF_{OX} shows almost the same behavior as in the case where no heat treatment is performed. This difference in DF_{OX} due to the thermal history can be related to the change in the concentration of mobile ions in the dielectric oxide film introduced in the explanation of the behavior in **Figure 2.2.4.9** (a) as shown below. In other words, when the concentration of mobile ions is high after the formation of the dielectric oxide film, $_{\mathrm{DFOX}}$ is high and independent of the electric field strength, but when the concentration of mobile ions decreases due to heat treatment, $_{\mathrm{DFOX}}$ decreases significantly in the low electric field strength region and becomes strongly dependent on the electric field strength. Therefore, in the future development of anode foils with low dielectric loss, it is expected that an approach to significantly reduce the concentration of mobile ions inside the dielectric oxide film will be important.

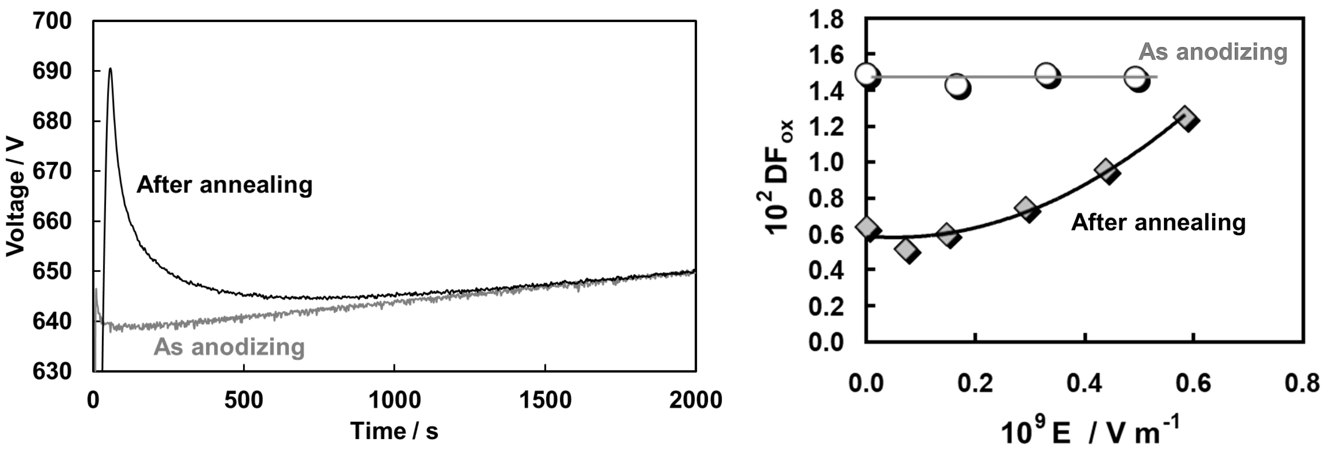

(a) (b)

Figure 2.2.4.9 Change in Dielectric Withstanding Voltage and Dielectric Dissipation Factor (DF_{OX}) of Anode Foil due to Heat Treatment after Dielectric Oxide Film Formation
(a) Time variation curve of voltage when constant current is applied (4 Am^{-2}), (b) DC electric field dependence of DF_{OX}

[Kazuhiro Nagahara]

2.4.3 Electrolyte

(1) Outline of Electrolytes for Electrolytic Capacitors

Electrolyte is an important constituent material that greatly affects the frequency characteristics, temperature characteristics, withstand voltage, heat resistance, life span, price, etc. of electrolytic capacitors. The properties and functions required for electrolytes are listed below.

(a) The electrolyte must be conductive (ionic or electronic conductive and able to carry an electric charge). The more conductive the electrolyte is, the lower the ESR of the electrolytic capacitor. However, the higher the conductivity of the electrolyte, the lower the voltage holding capability tends to be. As will be discussed later, in general, electron conductive materials have higher conductivity than ion conductive materials and provide electrolytic capacitors with lower ESR. However, they are applicable only in low voltage bands.

(a) The capacitor must be chemically stable to the anode foil, cathode foil and other constituent materials. In the case of aluminum electrolytic capacitors, the capacitor must be chemically stable to the anode foil and cathode foil, which are aluminum (chemically stable here means that no chemical reaction occurs with aluminum). The material must be chemically stable not only at room temperature, but also at high temperatures (up to 150 ℃) and for long periods of time (up to several thousand hours). As you know, aluminum is an amphoteric metal, which means that it is prone to chemical reactions in both acidic and alkaline environments, and it is also susceptible to halogenated compounds, which greatly restricts the choice of electrolytes. It must also be chemically stable with respect to materials other than the electrode foil, such as sealing rubber, separators, tabs, and tape.

(c) Anodic oxidation or insulation protection of defective or broken parts of dielectric oxide film is required to reduce leakage current. Dielectric oxide film has defects [(53)] such as defects caused by impurities, defects caused by hydrated oxide film, void defects, etc., which induce leakage current. The electrolyte must have a function to protect the defects in the dielectric oxide film. The first function is to repair defects in the dielectric oxide film by anodic oxidation (chemical conversion), and the second function is to prevent leakage current from the defects by locally insulating the electrolyte itself [(54)]. Liquid electrolytes are mainly the former, while solid electrolytes are mainly the latter.

(d) The electrolyte must be able to maintain conductivity at low temperatures (up to -55 °C). The electrolyte itself must be thermally stable and maintain conductivity for a long period of time at high temperatures (up to 150 °C). In addition, although limited to liquid electrolytes, the electrolyte should be resistant to evaporation outside the capacitor system. The electrolytic capacitor must be stable at the temperature of the substrate environment where the capacitor is installed, as well as at the temperature of self-heating due to the ripple load.

(e) The dielectric oxide film must be infiltrated and filled inside the pores of the dielectric oxide film. As described in the previous section, the dielectric oxide film is porous to increase the capacitance, and if it is not sufficiently filled into the porous material, it will not function as an electrolyte and the capacitor characteristics will deteriorate. In the case of solid electrolytes, filling the porous media is particularly important because it determines the capacitor characteristics. Selection of materials that can be easily filled into the porous media and the filling process are being devised.

(f) The electrolyte should have high wettability and filling ability to the separator. Only when the electrolyte is wetted with the separator and sufficiently impregnated and filled with the electrolyte, the electrolyte will function sufficiently as an electrolyte. Similarly to (e), this also significantly affects capacitor characteristics in the case of a solid electrolyte. In particular, it has a significant effect on ESR in the high-frequency range, so it is important to select a material with high wettability and filling ability to the separator.

(2) Liquid electrolyte

The liquid electrolyte is then described in detail. Liquid electrolytes are mainly composed of a supporting electrolyte dissolved in an organic solvent. Historically, liquid electrolytes were first used, followed by solid electrolytes. Glycerin was used in the past, and ethylene glycol [(55)], γ-butyrolactone [(56)], and sulfolane [(57)] have been used in recent years as organic solvents. Some are used alone, while others are used in mixtures. In addition to organic solvents alone, the addition of a large amount of water has also been studied [(58)]. Water has a high dielectric constant and increases the dissociation of the supporting electrolyte, so adding water to the liquid electrolyte improves conductivity, but it also tends to cause a hydration reaction in the electrode foil, leading to early degradation. As the supporting electrolyte, boric acid or organic carboxylic acid compounds are often used as the anion and ammonium compounds as the cation. The choice of compounds is made in accordance with (a) through (f) described above in (1). For example, (a) select a solvent with high dielectric constant and low viscosity and a support electrolyte with high dissociation to increase conductivity, (b) adjust the support electrolyte to a pH range that does not dissolve the electrode foil, (c) select a solvent and support electrolyte that easily repair dielectric oxide film defects (high chemical compatibility), (d) select a thermally stable (e) selection of a solvent and supporting electrolyte that are thermally stable, (f) selection of a solvent with low viscosity that can be easily impregnated into the porous dielectric oxide film, and (g) selection of a compound that can easily wet the separator.

In some cases, in addition to the solvent and the supporting electrolyte, various compounds may be added in minute quantities as "hanagusuri" (this is the know-how of each electrolytic capacitor manufacturer and is not well publicized). Since charge transfer in liquid electrolytes is by ionic conduction, the temperature dependence of conductivity is larger than that of solid electrolytes, which will be discussed later. In particular, the decrease in conductivity at low temperatures is particularly pronounced. Therefore, electrolytic capacitors using liquid electrolytes have a weak point in low-temperature characteristics, such as an increase in ESR or a decrease in capacitance at low temperatures. In addition, the life of the capacitor depends on the evaporation (dry-up) of the liquid electrolyte.

In the case of liquid electrolytes, it is known empirically that the conductivity of the electrolyte is inversely proportional to the capacitor withstand voltage [(59)], and liquid electrolytes with low conductivity are used when designing capacitors with high withstand voltage. Therefore, electrolytic capacitors with higher voltages tend to have higher ESR.

(3) Solid electrolyte

The first use of solid materials as electrolytes in capacitors is believed to have been in the 1950s. Tantalum electrolytic capacitors were commercialized using manganese dioxide as the solid electrolyte. The solid manganese dioxide electrolyte had a conductivity one order of magnitude higher than the liquid electrolyte, resulting in a low ESR product. Products with this configuration are still manufactured and sold today. In the case of aluminum electrolytic capacitors, products using an organic semiconductor called TCNQ (7,7,8,8-tetracyanoquinodimethane) as a solid electrolyte were marketed by SANYO in the 1980s. [(60)(61)] Because TCNQ has conductivity one to two orders of magnitude higher than liquid electrolytes and has excellent thermal stability, it has been used in the development of Aluminum electrolytic capacitors using TCNQ as a solid electrolyte had low ESR, high heat resistance, and long life. Subsequently, electrolytic capacitors (conductive polymer aluminum solid electrolytic capacitors) using conductive polymers such as polypyrrole [(62)-(65)] and poly(3,4-ethylenedioxythiophene) [PEDOT] [(66)-(69)] as solid electrolytes with one to two orders of magnitude higher conductivity than TCNQ were introduced to the market in the late 1980s and 1990s. (conductive polymer aluminum solid electrolytic capacitors) were launched in the late 1980s and 1990s and are now widely used.

Electrolytic capacitors using solid electrolyte are characterized by low ESR, high heat resistance, and long life, but on the other hand, their capacitance per volume is smaller than that of liquid electrolyte products. The reason for this is that the function of (c) mentioned in （2） above is lower than that of liquid electrolyte, and the anode foil is designed with a higher conversion voltage than the rated voltage of the product (as described in 2.4.1, the capacitance of a capacitor is inversely proportional to the conversion voltage of the anode foil, so a higher conversion voltage results in a lower capacitance). (higher conversion voltage results in a decrease in capacitance). The liquid electrolyte has the ability to repair defects in the dielectric oxide film, minimizing leakage current from the defects. On the other hand, in the case of solid electrolytes, the solid electrolyte itself has no function to repair the defects in the dielectric oxide film, and only a small amount of moisture adsorbed on the solid electrolyte contributes to the repair. The solid electrolyte itself is said to be locally insulated by Joule heat due to leakage current, thereby suppressing current leakage [(54)]. Therefore, it is designed to have a margin by increasing the anode foil conversion voltage relative to the rated voltage of the product, resulting in a smaller capacity for the same volume than a liquid electrolyte.

Another drawback of using solid electrolytes is that it is difficult to apply them to products with high withstand voltages. The upper limit for products on the market is a rated voltage of several tens of volts. One of the reasons for this is the low ability to repair the dielectric oxide film defects mentioned above. Another reason is that when solid electrolytes are used, the failure mode becomes a short circuit when the voltage is increased. In the case of aluminum electrolytic capacitors using conductive polymers, the conductive polymers that have become insulators due to leakage current near the defects in the dielectric oxide film are considered to conduct current when a high voltage is applied, resulting in a short circuit failure mechanism.

(4) Hybrid Electrolyte

A capacitor that uses both the liquid and solid electrolytes described above is called a hybrid electrolytic capacitor. Aluminum electrolytic capacitors using conductive polymers as the solid electrolyte and organic electrolyte as the liquid electrolyte have been on the market since the early 2010s under the product name "conductive polymer hybrid aluminum electrolytic capacitor" [(70)]. The solid electrolyte provides low ESR and high heat resistance, while the liquid electrolyte ensures withstand voltage and leakage current characteristics, thus compensating for the shortcomings of the two. Simply combining both electrolytes does not bring out the best; it is necessary to select a liquid electrolyte that does not interfere with the electrical conductivity of the solid electrolyte, and it is also necessary to formulate a liquid electrolyte that can easily penetrate into the solid electrolyte. Each capacitor manufacturer has its own combination of solid and liquid electrolytes. As a result, electrolytic capacitors with higher withstand voltage than solid electrolytes while maintaining the same ESR as solid electrolytes are being developed. The leakage current is not equivalent to that of liquid electrolytes, but it is greatly improved compared to solid electrolytes, and the failure mode is also open. Low-temperature characteristics are also good because the solid electrolyte part guarantees the low-temperature characteristics. The capacitance per volume is located between the solid electrolyte and the liquid electrolyte. The liquid electrolyte contributes to the repair of defects in the dielectric oxide film, but it is not sufficient, and the anode foil is designed to have a slightly higher conversion voltage. The life time depends on the dry-up time of the liquid electrolyte and is basically not much different from that of the liquid electrolyte. However, since the low ESR suppresses ripple heating, the life time including ripple superposition is longer than that of the liquid electrolyte.

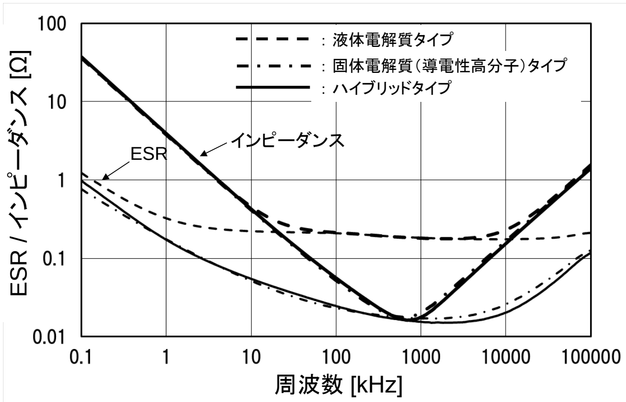

Figure 2.2.4.10 Frequency dependence of ESR and impedance of aluminum electrolytic capacitors with various electrolytes. Data measured at 20℃ product specifications: Φ6.3 x 5.8 L, 35 V/47 μF for liquid electrolyte and hybrid types , 25 V/47 μF for solid electrolyte types)

2.4.4 Comparison of electrolytic capacitor characteristics using different electrolytes

The frequency characteristics of ESR and impedance of aluminum electrolytic capacitors with the three types of electrolytes described in 2.4.3 were compared (**Figure 2.2.4.10**). It can be seen that the liquid electrolyte type has higher ESR and impedance in the high frequency range from 10 kHz onward, while the solid electrolyte and hybrid types have lower ESR and impedance. It can also be seen that there is almost no difference between the solid electrolyte and hybrid types. Next, the durability data at 125 ℃ **is** shown **in Figure 2.2.4.11.** For the liquid electrolyte type, the capacitance drop and ESR increase are noticeable after 2000 h due to evaporation and dry-up of the liquid electrolyte. On the other hand, the solid electrolyte type and hybrid type have high thermal stability of the electrolyte, and both capacitance and ESR are stable over 4000 h, indicating a long life. Compared to the solid electrolyte type, the hybrid type shows a slight decrease in capacitance, but this is due to the effect of the liquid electrolyte. The temperature characteristics were then compared (**Figure 2.2.4.12**). It can be seen that the ESR of the liquid electrolyte type significantly increases at low temperatures below -20 ℃. On the other hand, the solid electrolyte type and the hybrid type are very stable down to -55 ℃, showing good temperature characteristics.

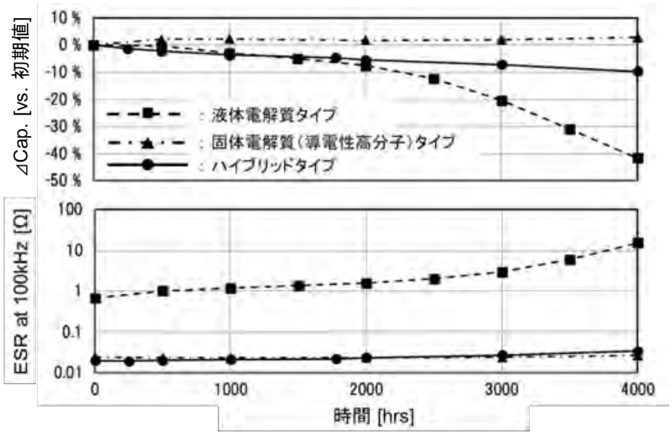

The various properties of aluminum electrolytic capacitors using various electrolytes are compared in a radar chart (**Figure 2.2.4.13**). The solid electrolyte type is represented by the performance of products using conductive polymers, and the hybrid type is represented by the performance of products using conductive polymers and liquid electrolytes. As a relative comparison of the three types, a five-point scale was used. Among the characteristics that are highly dependent on the electrolyte, those that are assumed to be highly important for power electronics applications are shown. The liquid electrolyte type has the largest capacitance, followed by the

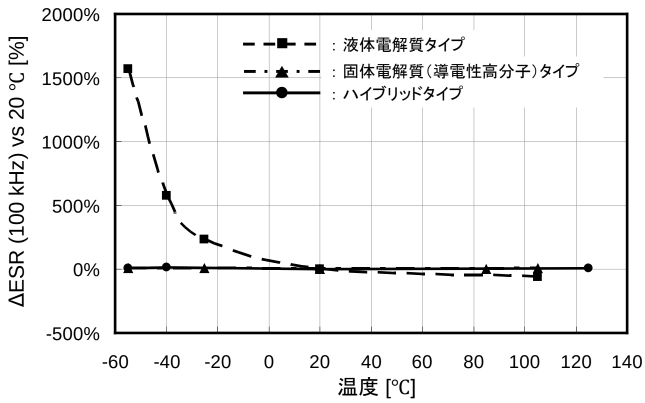

Fig. 2.2.4.12 Temperature characteristics of aluminum electrolytic capacitors with various electrolytes, expressed as a percentage change, with ESR at 20 ℃ as 100. (Product specifications: Φ6.3 x 5.8 L, 35 V/47μF for liquid electrolyte and hybrid types, 25 V/47 μF for solid electrolyte types)

hybrid type, and the solid electrolyte type has the smallest capacitance. The liquid electrolyte type, which has a high dielectric oxide film repair function, has the highest withstand voltage, followed by the hybrid type, and the solid electrolyte type has the lowest withstand voltage. On the other hand, the high-frequency ripple resistance of the liquid electrolyte type is low (due to its high ESR), while the solid electrolyte type and hybrid type are good (due to their low ESR). Temperature characteristics are also poor for the liquid electrolyte type and good for the solid electrolyte and hybrid types. The solid electrolyte type, which does not dry up, has the longest life, followed by the hybrid type, and the liquid electrolyte type has the shortest life. The price is basically the lowest for the liquid electrolyte type, which uses an inexpensive solvent and supporting electrolyte, followed by the solid electrolyte type, which uses a relatively expensive conductive polymer, and the hybrid type, which uses both, which is the most expensive. It can be considered that the characteristics required for capacitors in power electronics applications differ from each other, and it is useful to select the most appropriate electrolyte type. In recent years, life cycle assessment has begun to be conducted for electronic components as well, and although it may depend on how they are used, some have estimated that solid electrolyte type and hybrid type aluminum electrolytic capacitors have a smaller environmental impact than liquid electrolyte type capacitors [71], and there are high expectations for a carbon neutral society in the future. 71), and there are high expectations for a carbon-neutral society in the future.

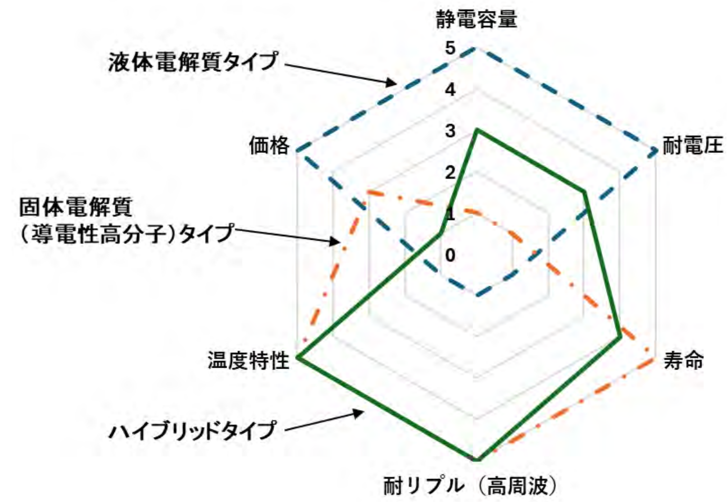

Figure 2.2.4.13 Radar chart comparing the characteristics of aluminum electrolytic capacitors using various electrolytes

[Kenji Machida]

References

(1) M. Shikanai, M. Sakairi, H. Takahashi, M. Seo, K. Takahiro, S. Nagata and S. Yamaguchi : "Formation of Al/(Ti, Nb, Ta)- Composite Oxide Films on Aluminum by Pore Filling", J. Electrochem. Soc. Vol.144, No.8, pp.2756-2766 (1997).

(2) Keiji Watanabe, Masatoshi Sakairi, Hideaki Takahashi, Shinji Hirai and Teie Yamaguchi: "Sol-Gel Coating - Anodic Oxidation of Aluminum Covered with Zr Oxide," Surface Technology, Vol.50, No.4, pp.359-366 (1999).

(3) K. Watanabe, M. Sakairi, H. Takahashi, S. Hirai and S. Yamaguchi : "Formation of Al-Zr composite oxide films on aluminum by sol-gel coating and anodizing", J. Electroanal.

(4) K. Watanabe, M. Sakairi, H. Takahashi, K. Takahiro, S. Nagata and S. Hirai : "Anodizing of Aluminum Coated with Zirconium Oxide by a Sol-Gel Effect of Heat Treatment on the Formation of the Anodic Oxide Film", Electrochemistry, Vol.67, No.12, pp.1243-1248 (1999).

(5) K. Watanabe, M. Sakairi, H. Takahashi, K. Takahiro, S. Nagata and S. Hirai : "Formation of Composite Oxide Films on Aluminum by Sol-Gel Coating and Anodizing - For the Development of High Performance Aluminum Electrolytic Capacitors -", Electrochemistry, Vol. 69, No. 6, pp. 407-413 (2001) .407-413 (2001).

(6) K. Watanabe, M. Sakairi, H. Takahashi, K. Takahiro, S. Nagata and S. Hirai : "Anodizing of Aluminum Coated with Silicon Oxide by a Sol-Gel Method", J. Electrochem Soc. Vol.148, No.11, pp.B473-B481 (2001).

(7) Keiji Watanabe, Masatoshi Sakairi, Hideaki Takahashi and Shinji Hirai: " Anodic Oxidation of Aluminum Coated with SiO_2 by Sol-Gel Method -Preparation of Novel High Voltage Anodic Oxide Films-," Surface Technology, Vol.54, No.3, pp.235-240 (2003)).

(8) Keiji Watanabe, Masatoshi Sakairi, Hideaki Takahashi, Shinji Nagata and Shinji Hirai: "Formation of Al-Nb composite oxide film by sol-gel coating/anodic oxidation," Surface Technology, Vol.55, No.7, pp.471-477 (2004).

(9) S. Koyama, T. Kikuchi, M. Sakairi, H. Takahashi and S. Nagata : " Nb_2O_5 Deposition on Aluminum from $NbCl_5$-used Sol and Anodizing of Nb_2O_5- coated Al", Electrochemistry, Vol.75, No.8, pp.573-575 (2007).

(10) M. Sunada, T. Kikuchi, M. Sakairi, H. Takahashi and S. Hirai : "Dielectric properties of Al-Si composite oxide films formed on Dielectric properties of Al-Si composite oxide films formed on electropolished and DC-etched aluminum by electrophoretic sol-gel coating and anodizing", J. Solid State Electrochem. Vol.11, No.10, pp.1375-1384 (2007).

(11) S-S. Park and B-A Lee: " Anodizing Properties of High Dielectric Oxide Films Coated on Aluminum by Sol-Gel Method", J. Electroceramics, Vol. 13, No.1-3, pp. 111-116 (2004).

(12) Z-S. Feng, J-J. Chen, R. Zhang and N. Zhao: "Formation of Al_2O_3-Nb_2O_5 composite oxide films on low-voltage etched aluminum foil by complexation-precipitation and anodizing" , Ceramics Intle.

(13) H. Takahashi, H. Kamada, M. Sakairi, K. Takahiro, S. Nagata and S. Yamaguchi : Proc. of Intern. Symp. of Dielectric Material Integration for Micro- Electronics, sponsored by Electrochem. Soc. 253-262 (1998).

(14) E. Takahashi, M. Sakairi, T. Kikuchi, and S. Koyama: "Capacitor Handbook," pp. 411-415 (2009).

(15) S. Ikonopisov : "Theory of electrical breakdown during formation of barrier anodic films", Electrochim. 10, pp. 1077-1082 (1977).

(16) Y. Li, H. Shimada, M. Sakairi, K. Shigyo, H. Takahashi and M. Seo : "Formation and Breakdown of Anodic Oxide Films on Aluminum in Boric Acid/ Borate Solutions", J. Electrochem. Soc. Vol. 144, No. 3, pp. 866-876 (1997).

(17) P. Skeldon, G. E. Thompson and G. C. Wood : "Formation of relatively pure alumina films by anodic polarization", Thin Solid Films, Vol. 148, No. 3, pp. 333-341 (1987)

(18) H. Shimada, M. Sakairi, and H. Takahashi: "Formation Behavior of Aluminum Anode Oxide Film in Low Concentration KOH Solution," Surface Technology, Vol.53,

No.2, pp.134-141 (2002).
(19) H. Shimada, M. Sakairi, and H. Takahashi: "An Attempt to Increase the Breakdown Potential of Aluminum Anode Oxide Film by Pore-Filling Method," Surface Technology, Vol.53, No.2, pp.142-148 (2002).
(20) J-H. Cao, Y. Sato, D. Kowalski, C. Zhu, Y. Aoki, Y. Cheng and H. Habazaki : "Highly increased breakdown potential of anodic films on aluminum using a sealed porous layer", J. Solid State Electrochem.
(21) T. Hasebe and R. S. Alwitt : "Nonlinear Dielectric Properties of Anodic Aluminum Oxide Films", J. Electrochem. , No.11, pp.C626-C630 (2007).
(22) Nippon Chemi-Con Corporation, Electrode foil, wound capacitor, method for manufacturing electrode foil, and method for manufacturing wound capacitor, Patent No. 6337998
(23) Nippon Chemi-Con Corporation, Electrode foil, wound capacitor, method for manufacturing electrode foil, and method for manufacturing wound capacitor, Patent No. 6337999
(24) Nippon Chemi-Con Corporation, Electrode foil, wound capacitor, method for manufacturing electrode foil, and method for manufacturing wound capacitor, Patent No. 6338000
(25) Nippon Chemi-Con Corporation, Method for manufacturing electrode foil and method for manufacturing wound capacitors, Patent No. 6723252
(26) Nippon Chemi-Con Corporation, Electrode foil, wound capacitor, method for manufacturing electrode foil, and method for manufacturing wound capacitor, Patent No. 7180049
(27) Nippon Chemi-Con Corporation, Electrode foil, wound capacitor, method for manufacturing electrode foil, and method for manufacturing wound capacitor, Patent No. 7435700
(28) C. G. Dunn and R. B. Bolon : "Technique for a Scanning Electron Microscope Study of Etched Aluminum", J. Electrochem. .116, No.7, pp.1050-1051 (1969)
(29) C. K. Dyer and R. S. Alwitt : "Surface Changes during A.C. Etching of Aluminum", J. Electrochem. Soc. 305 (1981).
(30) S. Ono and H. Habazaki : "Effect of Sulfuric Acid on Pit Propagation Behaviour of Aluminium under AC Etch Process", Corros. ., Vol.51, No.10, pp.2364-2370 (2009)
(31) S. Ono and H. Habazaki : "Pit growth behaviour of aluminium under galvanostatic control", Corros. Sci. Vol. 53, No. 11, pp. 3521-3525 (2011).
(32) N. F. Jackson : "The Tunnel Etching of Aluminium", Electro Component Science and Technology, Vol.2, No.1, pp.33-44 (1975).
(33) R. S. Alwitt, H. Uchi, T. R. Beck and R. C. Alkire : "Electrochemical Tunnel Etching of Aluminum", J. Electrochem. Soc. Vol. 131, No. 1, pp. 13-17 (1984).
(34) Kenshiro Yamaguchi: "High-purity aluminum foil for electrolytic capacitors," Light Metal, Vol. 35, No. 6, pp. 365-371 (1985).
(35) H. Masuda, M. Tajima and K. Nishio : "Site control of tunnel etching of Al for electrolytic capacitors using pretexturing by mold ", Chem. Lett.
(36) K. Nishio, K. Kanezawa and H. Masuda : "Control of anisotropic tunnel etching of Al by indentation", Chem. Vol. 35, No. 10, pp. 1096-1097(2006).
(37) H. Masuda and K. Nishio: "Control of Anode Oxidation Process Based on Texturing Treatment and Its Application to Functional Device Formation," Surface Technology, Vol.54, No.7, pp.442-446 (2003).
(38) K. Nishio, T. Fukushima and H. Masuda : "Control of Pitting Sites on Al for Electrolytic Capacitors Using Patterned Masking Film Solid-State Lett.
(39) K. Nishio, T. Fukushima, A. Takeda and H. Masuda : "Fabrication of Site-Controlled Tunnel Pits with High Aspect Ratios by Electrochemical Etching of Al Using Masking Film", Electrochem, Solid-State Lett.
(40) K. Nishio, T. Fukushima, and H. Masuda: "Formation of Highly Random Al Tunnel Pit Array Based on Masking Process," Surface Technology, Vol.59, No.7, pp.448-451 (2008)
(41) Nichicon Corporation, Manufacturing method of electrode foil for aluminum electrolytic capacitors, Patent No. 2021-27120
(42) Hidenori Uchis and R. S. Alwitt: "Electron Microscopic Evaluation of Electrode Foil," Surface Technology, Vol. 51, No. 11, pp. 1111-1116 (2000).
(43) Nobuyoshi Kanzaki, Ryoichi Shimatani, Hiroshi Takahashi and Hiroyuki Tokumasu: "Long Life and Barrier Film in Aluminum Electrolytic Capacitors," Surface Technology, Vol.41, No.8, pp.808-812 (1990).
(44) Nobuyoshi Kanzaki: "Current Status and Issues of Surface Treatment of Aluminum Electrolytic Capacitors," Surface Technology, Vol.48, No.10, pp.976-981 (1997).
(45) J.F. Dewald : "Transient effects in the ionic conductance of anodic-oxide films at high fields", J. Phys. Chem. Solids, Vol. 2, No. 1, pp. 55-66 (1957).
(46) M. J. Dignam : "Oxide Films on Aluminum: I. Ionic Conduction and Structure", J. Electrochem. Soc. Vol. 109, No. 3, pp. 184-191 (1962).
(47) M. Katoh, T. Kudoh and M. Watase : "Transient Behaviors at a Constant Current for the Tantalum Anodic Oxide Film," DENKI KAGAKU, Vol.40, No.11 DENKI KAGAKU, Vol.40, No.11, pp.792-795 (1972).
(48) M. Kato : "Transient behaviour of the anodic oxide film on tantalum", Electrochimica Acta, Vol. 21, No. 8, pp. 593-597 (1976).
(49) T. Kudo, M. Kato and T. Nagashima: "Transient phenomena of tantalum anodic oxide film under constant voltage," Electrochemistry, Vol.44, No.11, pp.738-742 (1976).
(50) Masayoshi Kato and Tadato Kudo: "Evaluation of Thermal Degradation Degree of Tantalum Anodic Oxide Film by Constant Voltage Excess Phenomenon," Electrochemistry, Vol.46, No.8, pp.449-454 (1978).
(51) Masayoshi Kato, Nobuto Fukushima, Kiyohiro Yokoi and Tadato Kudo: "Effect of Conversion Solution on Properties of Barrier Type Anodic Oxide Films on Aluminum," Metal Surface Technology, Vol.34, No.7, pp.384-390 (1983).
(52) Masayoshi Kato: "Properties of Barrier Type Anodic Oxide Film and Its Evaluation Method," Metal Surface Technology, Vol.39, No.8, pp.420-428 (1988).
(53) Isaya Nagata : "Electrolytic solution cathode aluminum electrolytic capacitors", pp.308-311 (1997)
(54) H. Yamamoto, K. Kanemoto, M. Oshima, and I. Isa : "Self-healing Characteristics of Solid Electrolytic Capacitor with Polypyrrole Electrolyte", Electrochemistry, Vol.67, No.8, pp.855-861 (1999) (in Japanese)
(55) K. Tamamitsu, M. Ue, T. Tsuji, M. Takeda, T. Sato, and M. Ozawa : "Performances of Aluminum Electrolytic Capacitors Using Silica Organo- Sols as Electrolyte Additives", Hyomen-Gijyutsu, Vol.56, No.8, pp.473-478 (2005) (in Japanese)
(56) K. Tamamitsu and M. Ozawa : "Alkali Concentration Mechanism on Cathode Terminal End in Aluminum Electrolytic Capacitor", Zairyo-to-Kankyo, Vol.52, No.8, pp.416-420 (2003) (in Japanese) Zairyo-to-Kankyo, Vol.52, No.8, pp.416-420 (2003) (in Japanese)
(57) K. Tamamitsu : "Sulfolane as an Electrolyte Solvent in Aluminum Electrolytic Capacitors", J. Technology and Education, Vol. .10, No.2, pp.115-120 (2003) (in Japanese)
(58) S. Uzawa, A. Komatsu, and T. Ogawara : "Ultra Low Impedance Aluminum Electrolytic Capacitor with Water based Electrolyte," Reliability Engineering Association of Japan, Vo.24, No.4, pp.276-283 (2002) (in Japanese)
(59) S. Ikonopisov : "Theory of electrical breakdown during formation of barrier anodic films", Electrochimica Acta, Vol.22, No. .10, pp.1077-1082 (1977).
(60) S. Niwa : SANYO TECHNICAL REVIEW, Vol.17, No.1, pp.90 (1985) (in Japanese)
(61) S. Niwa : "Aluminum Solid Electrolytic Capacitor with Organic Semiconductor", Synthetic Metals, Vol.18, pp.665 (1987).
(62) Isao Isa, Minoru Fukuda, Toshio Hosaka, Hideo Yamamoto and Katsumi Yoshino: "Aluminum electrolytic capacitors using polypyrrole as solid electrolyte," IEICE, Vol.J75-C2, No.10, pp.530-537 (1992)
(63) Y. Kudoh : "An Aluminum Solid Electrolytic Capacitor with Electroconductive Polymer Layer Electrode", Hyomen-Gijyutsu Vol.43, No.6, pp.56-60 (1992) (in Japanese)
(64) K. Naoi, Y. Ota, and K. Machida : "Pulse Anodization of Tantalum Oxide / Polypyrrole Film on Nanoporous Tantalum Anode for Solid Electrolytic Capacitors", Electrochemistry, Vol.73, No.7, pp.496-501 (2005) (in Japanese).
(65) K. Naoi, Y. Ota, and K. Machida : "Pulse Anodization of Tantalum Oxide / Polypyrrole Film on Nanoporous Tantalum Anode in Ionic Liquid Media ", Electrochemistry, Vol.74, No.1, pp.53-58 (2006) (in Japanese).
(66) K. Nogami : "Aluminum Solid Electrolytic Capacitor with Functional Polymer", Reliability Engineering Association of Japan, Vo.22, No.7, pp.598-606 (2000) (in

Japanese)
(67) K. Naoi, A. Shimada, and K. Machida : "Simultaneous Electrochemical Formation of Ta_2O_5/Poly (3, 4-ethylenedioxythiophene) Layers ", Electrochemistry, Vol.69, No.6, pp.451-454 (2001).
(68) T. Murakami, S. Endo, and H. Okuzaki, "Fabrication and Characterization of Aluminum Solid Capacitors Using Aqueous Dispersion of Conductive Polymers", Electrochemistry, Vol.80, No.9, pp.636-639 (2012) (in Japanese).
(69) T. Wakabayashi, M. Katsunuma, K. Kudo, and H. Okuzaki : "pH-Tunable High-Performane PEDOT :PSS Aluminum Solid Electrolytic Capacitors ", ACS Applied Energy Materials, Vol. 1, No. 5, pp. 2157-2163 (2018).
(70) T. Aoyama : "Conductive Polymer Hybrid Aluminum Electrolytic Capacitor Using Electrolyte Hybrid Technology", Panasonic Technical Journal, Vol.58, No.1, pp.65-67 (2012) (in Japanese).
(71) C. Zhang, Y. Zheng, J. Jing, Y. Liu, and H. Huang : "A comparative LCA study on aluminum electrolytic capacitors : From liquid-state electrolyte, solid-state polymer to their hybrid", Journal of Cleaner Production, Vol.375, No.15, pp.134044-134056 (2022).